PROBING THE MODAL CHARACTERISTICS OF NOVEL BEAM SHAPES

Areti Mourka

A Thesis Submitted for the Degree of PhD
at the
University of St Andrews

2013

Probing the Modal Characteristics of Novel Beam Shapes

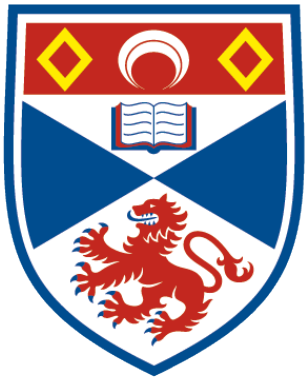

University of St Andrews

A thesis submitted to the University of St. Andrews in application for the degree of Doctor of Philosophy

Areti Mourka

1st supervisor: Prof. K. Dholakia

2nd supervisor: Dr. M. Mazilu

November 2013

Declaration

1. Candidate's declarations:

I, Areti Mourka, hereby certify that this thesis, which is approximately 51.000 words in length, has been written by me, that it is the record of work carried out by me and that it has not been submitted in any previous application for a higher degree.

I was admitted as a research student in May 2009 and as a candidate for the degree of Doctor of Philosophy in May 2009; the higher study for which this is a record was carried out in the University of St Andrews between 2009 and 2013.

Date …… Signature of candidate ……

2. Supervisor's declaration:

I hereby certify that the candidate has fulfilled the conditions of the Resolution and Regulations appropriate for the degree of Doctor in Philosophy in the University of St Andrews and that the candidate is qualified to submit this thesis in application for that degree.

Date …… Signature of supervisor ……

3. Permission for electronic publication:

In submitting this thesis to the University of St Andrews I understand that I am giving permission for it to be made available for use in accordance with the regulations of the University Library for the time being in force, subject to any copyright vested in the work not being affected thereby. I also understand that the title and the abstract will be published, and that a copy of the work may be made and supplied to any bona fide library or research worker, that my thesis will be electronically accessible for personal or research use unless exempt by award of an embargo as requested below, and that the library has the right to migrate my thesis into new electronic forms as required to ensure continued access to the thesis. I have obtained any third-party copyright permissions that may be required in order to allow such access and migration, or have requested the appropriate embargo below.

The following is an agreed request by candidate and supervisor regarding the electronic publication of this thesis:

Access to printed copy and electronic publication of thesis through the University of St Andrews.

Date …… Signature of candidate ……

Date …… Signature of supervisor ……

Στον Νιόνιο και την Δήμητρα

Acknowledgements

I would first like to thank my supervisor Prof. Kishan Dholakia for this opportunity to work in the Optical Manipulation Group and for all his help, support and encouragement throughout my PhD studies. Special thanks to my co-supervisor Dr. Michael Mazilu, to whom I owe a lot of the ideas presented in this thesis. It was his initiative to use the principal component analysis (PCA) algorithm for the modal characterization of novel beam shapes and I greatly appreciate his help and constant support through discussions and suggestions.

I would like to thank Prof. Malcolm H. Dunn and Prof. Miles J. Padgett that agreed to be my examiners.

I would also like to thank and express my gratitude to the people that I have worked with directly for their help and advice: Dr. Joerg Baumgartl, Prof. Ewan. M. Wright, Chris Shanor, Dr. Tom Vettenburg and Dr. Mingzhou Chen.

Furthermore, my thanks go to: Dr. Mark R. Dennis, James D. Ring and Dr. Jari Lindberg in the Theoretical Physics Group of the Physics Department in University of Bristol, for the collaboration in the Pearcey beam study (the corresponding experiments unfortunately did not make it into the thesis).

I also want to thank Dr. Yuanjie Yang and Dr. Yi-Dong Liu in the School of Astronautics & Aeronautics and School of Physical Electronics in University of Electronic Science and Technology of China, for the collaboration in the partially coherent vortex field study.

Moreover, I would like to thank everyone else in the Optical Manipulation group who gave help or advice at any stage. Special thanks to Praveen, Anthi A., Catherine and Jonathan, who helped me polish the content of the thesis by proof reading and suggesting corrections.

For all the great lunch/coffee breaks and entertainment outside the lab, thanks to: Jill, Fiona, Sebastian, Anna Chiara, Ronan, Lani, Bavishna, Helen, Claire, Mathieu, Anisha, Nicola, Alison and Sayantan. To my flatmates: Helen, Catherine, and Neetika: it was great living with you. To Anthi A., Maria, Xenia, Eleni, Thanasis, Vaggelis, Stamatis, Eugenia, Jesse, Elena, and Christos: thanks for all the support and for making the Greek Society of St. Andrews University possible. Special thanks also to Meropi, Aliki, and Anthi T., it is great to know you are always there.

Acknowledgements (continuation)

Last but certainly not least, I would like to thank my family for all of the support over the years; I really couldn’t have done this without you all!

Ένα απέραντο ευχαριστώ πηγαίνει στους γονείς μου για όλη τους την αγάπη και την υποστήριξη που μου δείξανε σε όλη την διάρκεια των σπουδών μου, και που χωρίς εκείνους δεν θα είχα φτάσει ως εδώ.

List of Publications

• Peer reviewed journals

1. A. Mourka, J. Baumgartl, C. Shanor, K. Dholakia, and E. M. Wright. 'Visualization of the birth of an optical vortex using diffraction from a triangular aperture', *Opt. Express* **19**, 5760-5771 (2011), Highlighted on the home page of Optics Express.

2. M. Mazilu, A. Mourka, T. Vettenburg, E. M. Wright, and K. Dholakia. 'Simultaneous determination of the constituent azimuthal and radial mode indices for light fields possessing orbital angular momentum', *Appl. Phys. Lett.* **100**, 231115 (2012).

3. J. Ring, J. Lindberg, A. Mourka, M. Mazilu, K. Dholakia, and M. R. Dennis. 'Auto-focusing and self-healing of Pearcey beams', *Opt. Express* **20**, 18955-18966 (2012).

4. A. Mourka, M. Mazilu, E. M. Wright, and K. Dholakia, 'Modal Characterization using Principal Component Analysis: application to Bessel, higher-order Gaussian beams and their superposition', *Sci. Rep.* **3**, 1422 (2013).

5. Y. Yang, M. Chen, M. Mazilu, A. Mourka, Y. D. Liu, and K. Dholakia, 'Effect of the radial and azimuthal mode indices of a partially coherent vortex field upon a spatial correlation singularity', accepted in *New J. Phys.* (2013).

• Conference publications

6. A. Mourka, M. Mazilu, C. Shanor, E. M. Wright, and K. Dholakia, 'Characterizing the azimuthal and radial mode indices of a Laguerre-Gaussian beam using diffraction from a triangular aperture', *Conference paper, Frontiers In Optics (FiO), Laser Science (LS), Orbital Angular Momentum and Applications IV,* San Jose, California, USA, October 16th – 20th (2011).

7. M. Mazilu, A. Mourka, T. Vettenburg, E. M. Wright, and K. Dholakia, 'Determination of the azimuthal and radial mode indices for light fields possessing orbital angular momentum', *Conference paper, Frontiers In Optics (FiO), Laser Science (LS), Wavefront Engineering and Sensing II*, Rochester, NY, USA, October 14th - 18th (2012).

Conferences / Workshops participation

1. Participation in the Photonics 4 Life Network, 1st Fast-Dot Summer School 'Photonics meets Biology', Heraklion, Crete, Greece, 15th - 18th September 2011.

2. A. Mourka, M. Mazilu, C. Shanor, E. M. Wright and K. Dholakia, 'Characterizing the azimuthal and radial mode indices of a Laguerre-Gaussian beam using diffraction from a triangular aperture', *Frontiers In Optics (FiO), Laser Science (LS), Orbital Angular Momentum and Applications IV*, San Jose, California, USA, 16th – 20th October 2011, Oral Presentation.

3. M. Mazilu, A. Mourka, T. Vettenburg, E. M. Wright and K. Dholakia, 'Detecting the radial and azimuthal components of Laguerre-Gaussian beams', *SPIE Photonics Europe, Nanophotonics*, Brussels, Belgium, 16th - 19th April 2012, Poster.

4. A. Mourka, M. Mazilu, T. Vettenburg, E. M. Wright and K. Dholakia, 'Probing the orbital angular momentum of Laguerre-Gaussian and Bessel beams', *4th Summer Workshop on Optoinformatics*, NUI Maynooth, Ireland, 14th – 16th June 2012, Poster.

5. J. D. Ring, J. Lindberg, A. Mourka, M. Mazilu, K. Dholakia, and M. R. Dennis, 'The Pearcey beam: aberration, propagation and auto-focusing', *5th International Conference, Singular Optics (SO) 2012*, Sevastopol, Crimea, Ukraine, 16th – 21st September 2012, Oral Presentation.

6. M. Mazilu, A. Mourka, T. Vettenburg, E. M. Wright and K. Dholakia, 'Determination of the azimuthal and radial mode indices for light fields possessing orbital angular momentum', *Frontiers In Optics (FiO), Laser Science (LS), Wavefront Engineering and Sensing II*, Rochester, NY, USA, 14th – 18th October 2012, Oral Presentation.

7. Participation in the FP7 Support Action 'SMETHODS' training session of Domain 4, Diffractive Optics, 8th – 12th April 2013 in Jena, Germany.

Conferences / Workshops participation (continuation)

8. A. Mourka, M. Mazilu, E. M. Wright and K. Dholakia, 'Modal Characterization using Principal Component Analysis: application to Laguerre-Gaussian beams and their superposition', *ICOAM 2013, Second International Conference on Optical Angular Momentum*, Glasgow, UK, 3rd – 5th June 2013, Poster.

9. M. Chen, Y. Yang, M. Mazilu, A. Mourka, Y. D. Liu and K. Dholakia, 'Experimental study on the cross-correlation function in partially coherent Laguerre-Gaussian beams', *ICOAM 2013, Second International Conference on Optical Angular Momentum*, Glasgow, UK, 3rd - 5th June 2013, Poster.

10. A. Mourka, M. Mazilu, E. M. Wright and K. Dholakia, 'Probing the Modal Characteristics of Novel Beam Shapes'. Participation in the Photonics 4 Life Network, 2nd Fast-Dot Summer School 'Photonics meets Biology', Heraklion, Crete, Greece, 30th September – 3rd October 2013, Poster.

Scholarships & Awards

2011

1. Photonics 4 Life Network, 1st Fast-Dot Summer School 'Photonics meets Biology', Heraklion, Greece, 15th - 18th September 2011. A scholarship was awarded from the organization committee to cover the cost of my participation.

26/05/2009 - 30/11/2012

2. PhD funding for 3.5 years from UK EPSRC (Engineering and Physical Sciences Research Council).

2013

3. 3rd Best student poster presentation award at the Photonics 4 Life Network, 2nd Fast-Dot Summer School 'Photonics meets Biology', Heraklion, Greece, 30th September – 3rd October 2013 (100€ prize funded by Nature Photonics journal). A scholarship was also awarded from the organization committee to cover the cost of my participation.

4. The SUPA (Scottish Universities Physics Alliance) Graduate School Management Committee has agreed to support my research proposal on the exchange for Postdoctoral or Early Career Researchers and offered me the total of 1500£. I spent a month (September '13) at the Institute of Electronic Structure & Laser (I.E.S.L.) in the Foundation for Research and Technology Hellas (F.O.R.T.H.) (in Heraklion, Crete, Greece), where novel beam shapes were used with two-photon polymerization (2PP) technique to directly generate 3D structures that can be further used as scaffolds for biological applications.

SUPA Courses attended (1st Semester 2009-10)

1. Hot Topics in Photonics (SUPAHTP)

Hours equivalent credit: 14, Assessment: Project pitch

This was a two-day residential course, held in 4th - 5th November 2009 at the Forest Hills Hotel near Aberfoyle. The course ran in a summer school format. Lectures were presented and placed in the context of world activity some of the latest research within the Photonics community in Scotland: such as, the optical manipulation of atoms, colloids and cells, the fluorescence resonance energy transfer (FRET) technique, microdevices for DNA analysis and the single photon detection, generation and quantum cryptography.

2. Photonic Crystals & Plasmonics (SUPAPTC)

Hours equivalent credit: 11, Assessment: Exam

A discussion of the properties of photonic crystals and plasmonic metamaterials, which can be designed to a significant extend via their structure, took place. While photonic crystals are made of dielectric materials, plasmonic structures are typically made of metals. Many of their properties can be understood from their dispersion diagram or optical bandstructure, which is a core tool that was explored in this course. Familiar concepts such as multilayer mirrors and interference effects were used to explain more complex features such as slow light propagation and high Q cavities in photonic crystal waveguides. Finally, superlensing and optical cloaking in plasmonic metamaterials were also discussed.

3. Biophotonics (SUPABIO)

Hours equivalent credit: 15, Assessment: Exam

In this course, topics like fluorescence microscopy, optical tweezers for cell sorting and DNA manipulation, photodynamic therapy, lab–on–a–chip concepts and bio-MEMS were discussed. This course was a very good introduction to the exciting opportunities offered by applying photonics methods and technology to biomedical sensing and detection.

Abstract

In this thesis, an investigation into the modal characteristics of novel beam shapes is presented. Sculpting the phase profile of a Gaussian beam can result in the generation of a beam with unique properties. Described in this thesis are Laguerre-Gaussian (LG), Hermite-Gaussian (HG) and Bessel beams (BBs).

The diffraction of LG beam modes from a triangular aperture is explored and this effect can be used for the efficient measurement of the azimuthal mode index ℓ that indicates the number of multiples of 2π of phase changes that the field displays around one circumference of the optical axis. In this study, only LG beams with zero radial mode index p, with $p + 1$ denoting the number of bright high intensity concentric rings around the optical axis, were considered. Then, a powerful approach to simultaneously determine both mode indices of a pure LG beam using the principal component analysis (PCA) algorithm on the observed far-field diffraction patterns was demonstrated. Owing to PCA algorithm, the shape of the diffracting element used to measure the mode indices is in fact of little importance and the crucial step is 'training' any diffracting optical system and transforming the observed far-field diffraction patterns into the uncorrelated variables (principal components). Our PCA method is generic and it was extended to other families of light fields such as HG, Bessel and superposed beams. This reinforces the widespread applicability of this method for various applications. Finally, both theoretically and experimentally investigations using interferometry show the definitive linkage between both the radial and azimuthal mode indices of a partially coherent LG beam and the dislocation rings in the far-field cross-correlation function (CCF).

‘Αἰὲν ἀριστεύειν’

‘Ever to excel’

Homer (850 BC), Iliad

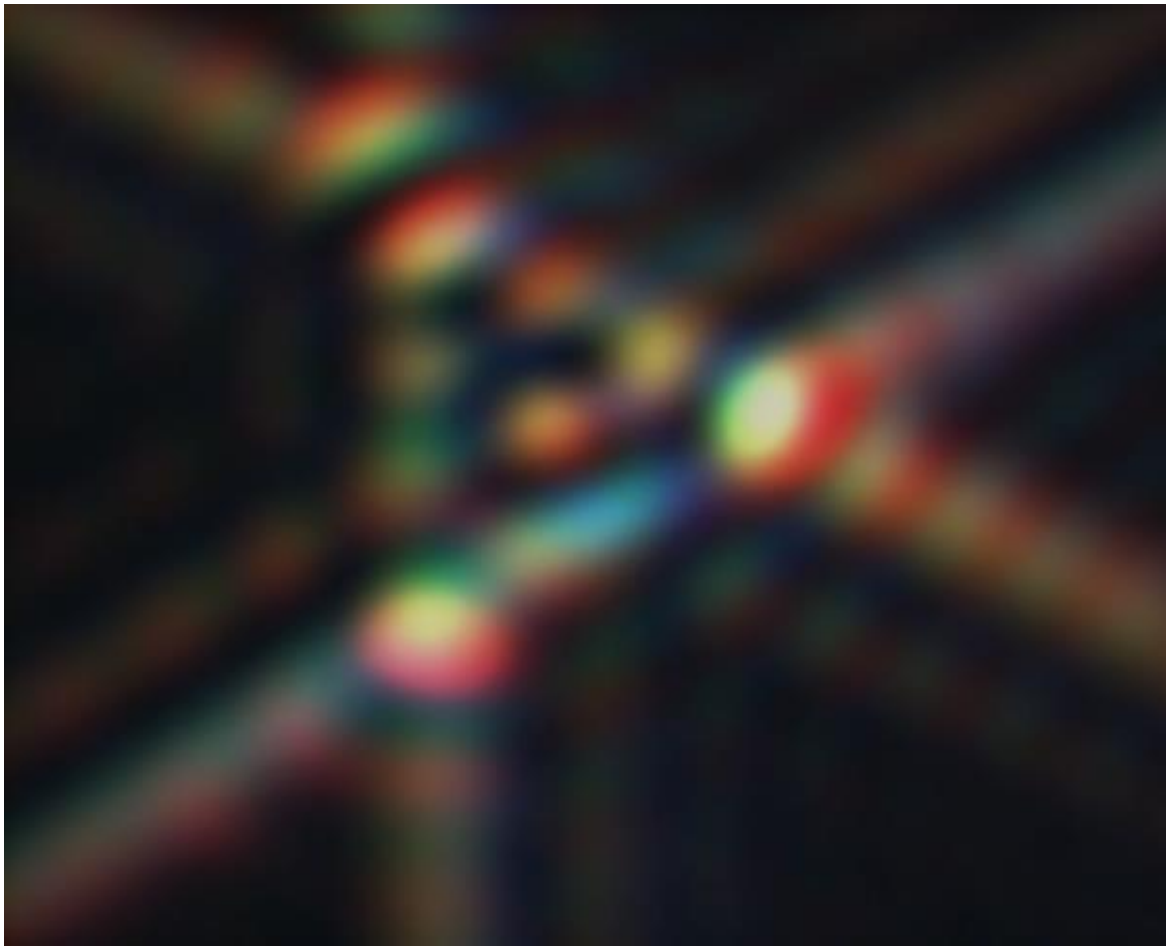

‘Rainbows are caused by light reflected at a fixed angle’

Aristotle (384 BC – 322 BC), Metaphysics

List of Symbols

Unless otherwise, the following symbols have the meanings listed below:

B	Magnetic field vector
d_{lens}	Diameter of a lens
d_a	Diameter of an annulus used for Bessel beam generation
E	Electric field vector
E_0	Field Amplitude
E_f	Efficiency of a hologram
f_{lens}	Focal length of a lens
h	Planck's constant
h_{SPP}	Height of spiral phase plate
$\hbar$	$h/2\pi$
I	Intensity
I_{max}	Maximum intensity
I_{min}	Minimum intensity
i	$\sqrt{-1}$
J_n	Bessel function of order n
k	Wavenumber (or wavevector)
k_z	Longitudinal wavevector
k_r	Radial wavevector
L_c	Coherence length
ℓ	Azimuthal index of an optical vortex
N_d	Number of the dislocation rings (dark zones)
N_F	Fresnel's number
N_r	Number of nodal (concentric bright) rings in an optical vortex
n	Refractive index
n_{lens}	Refractive index of a lens
n_{ax}	Refractive index of an axicon
P_0	Imprinted power on the hologram
p	Radial index of an optical vortex
R	Radius of curvature
R_{lens}	Radius of a lens
r	Radial coordinate or radius vector

List of Symbols (continuation)

r_{Imax}	Radius of maximum intensity of an optical vortex
S	Poynting vector
t	Time
$t(x,y)$	Aperture transmission function
$w(z)$	Beam waist at position z
w_0	Beam waist at focal plane
w_{inc}	Incident beam waist on an axicon
w_{SLM}	Incident beam waist on an SLM
x	Cartesian coordinate
y	Cartesian coordinate
z	Cartesian coordinate
z_R	Rayleigh range
z_{max}	Maximum diffraction-free propagation distance of a Bessel beam
z_{min}	Minimum reconstruction distance of a Bessel beam after an obstruction
α	Base angle of an axicon
γ_{12}	Degree of coherence
δ	Azimuthal optical phase delay (when a SPP is used)
η	Ratio of the beam waist of the incident OV to the aperture's size
θ	Cylindrical polar coordinate
Λ	Period of a grating
λ	Wavelength
π	3.14159265....
ρ	Cylindrical polar coordinate
υ	Visibility of fringes
φ	Azimuthal angle
$\psi(r)$	Phase imposed on a beam by a hologram displayed on an SLM

List of Acronyms

2D	Two-dimensional
3D	Three-dimensional
BB	Bessel beam
CCD	Charged coupled device
CCF	Cross-correlation function
CGH	Computer generated hologram
CW	Continuous wave
DM	Deformable mirror
DNA	Deoxyribonucleic acid
DOE	Diffractive optical element
DP	Dove prism
EM	Electromagnetic
EMCCD	Electron multiplying CCD
FP7	Seventh framework programme
FWHM	Full width half maximum
GB	Gaussian beam
GS	Gerchberg-Saxton algorithm
HeNe	Helium-Neon
HG	Hermite-Gaussian
IR	Infrared
LCoS	Liquid crystal on silicon
LED	Light emitting diode
LG	Laguerre-Gaussian
LUT	Look up table
MEMS	Micro-electro-mechanical systems
MP	Multipoint (or multipinhole)
MPI	Multipoint (or multipinhole) interferometer
OAM	Orbital angular momentum
OCT	Optical coherence tomography
OEi	Optical eigenmode
OT	Optical tweezers
OV	Optical vortex

List of Acronyms (continuation)

PBS	Polarizing beam splitter
PCA	Principal component analysis
PCs	Principal components
SAM	Spin angular momentum
SC	Supercontinuum
SLM	Spatial light modulator
SPIE	Society of Photographic Instrumentation Engineers
SPP	Spiral phase plate
SUPA	Scottish Universities Physics Alliance
UV	Ultra-violet
WFF	Wavefront folding

Table of Contents

CHAPTER 1

Introduction

1.1 Introduction

Light is our primary means of observing the world in which we live. Nowadays light can not only be used in its raw form, but can also be used as a tool, when 'harnessed' and 'sculptured'. In this thesis, light will be manipulated and shaped into novel beam shapes with unique properties that can then be applied to many exciting applications. Hence, different methods will be discussed for measuring their transversal properties.

A light beam can carry angular momentum that has a spin part when every polarization vector rotates that is commonly referred to as spin angular momentum (SAM); in case the light beam's phase structure rotates, its angular momentum has an orbital part, which is known as orbital angular momentum (OAM).

It has only been realized in the past two decades that light beams carrying OAM can easily be made in the laboratory. Allen et al. reported the first experimental studies in 1992 which recognized that laser beams can carry OAM [1]. The light beams carrying OAM were realized as Laguerre-Gaussian (LG) beam modes and have an optical vortex (OV) along the beam axis. These light beams appear as annual rings with zero on-axis intensity and are characterised by two mode indices: ℓ and p. The radial index, p, denotes the number of nodal (concentric bright) rings, N_r, about the beam axis such that $N_r = p + 1$. The azimuthal index, ℓ, indicates the number of multiples of 2π of phase changes around one circumference of the optical axis. It is sometimes denoted as the topological charge or winding number of the LG beam. The wavefronts - that is, surfaces of constant phase - of light beams with azimuthal phase dependence are helical, resulting in a Poynting vector also possessing an azimuthal component [1]. The spiral motion of the Poynting vector around the optical axis indicates an OAM component of $\ell\hbar$ per photon, where $\hbar$ is the Planck's constant/2π. The intensity vanishes at the position of the phase singularity, forming a dark hole in the intensity profile of the vortex beam. Two-dimensional (2D) intensity plots and phase structures for LG beams with different (azimuthal and radial) mode indices are shown in Figure 1.1. For a given value of ℓ, the LG beam has ℓ intertwined helical phase structures (helicoidal twists along a wavelength) possessing a screw singularity on the beam axis (Figure 1.1b). As metaphorically explained by Padgett: 'if there is a single helix, the wavefront looks like a screw thread; if there are two helices, the wavefront looks like DNA; and for three helices, the wavefronts have the shape of fusilli pasta. In fact, LG beams can be made with any number of helices' [2].

The history of this subject dates to the early 1900s, when Poynting's work on the wave motion of a revolving shaft suggested that a circularly polarized light beam carries an angular momentum that would exert torque on a cascaded array of

quarter-waveplates [3]. Furthermore, the circularly polarized light beam carries SAM of -$\hbar$ or +$\hbar$ per photon and thus it can be described as being right-handed or left-handed, depending on the rotation's direction. The waves of the optical field at every point in the cross-section of a circularly polarized light beam are in step and rotate together. Schematically this can be illustrated by the use of a 'plane wave', in which the wavefronts are parallel planes; each separated from the next by a distance of one optical wavelength [2]. This fact contrasts with the helical wavefronts of light beams carrying OAM, as seen in Figure 1.1b below.

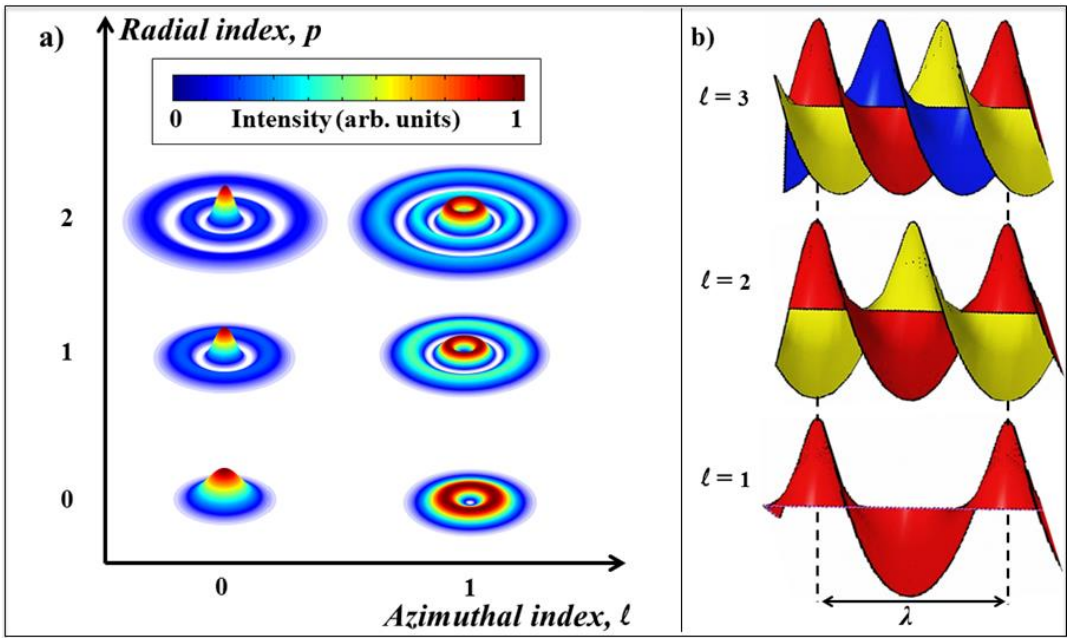

Fig. 1.1. Laguerre-Gaussian (LG) beams. a) The 2D intensity plots of LG beams for different mode indices (numerically simulated) are shown. The rows and columns define the azimuthal and radial mode indices, respectively. The hue colour chart coded for the intensity is also highlighted where the blue and red colours accordingly indicate the lower and higher intensity. b) The helical wavefronts of LG beams with ℓ = 1 to 3 increasing in integer step while the radial index was kept zero, p = 0, are presented. A horizontal propagation axis was considered and λ is the wavelength.

Additionally, in early 1930s, Sir C. G. Darwin (the grandson of Charles Darwin) in his '*Notes on the Theory of Radiation*' made the first assumption that linear momentum at a radius exerts a torque [4]. Moreover, providing the lever is long enough, a fixed linear momentum can exert an arbitrary high torque.

A few years later, Beth followed up Poynting's suggestion in his classic measurement of the torque arising from photon spin [5]. Beth was able to measure the torque that was exerted by a circularly polarized light on a birefringent half-waveplate suspended from a filament, reacting as a torsional pendulum. His measurements were performed by assigning an angular momentum of $\hbar$ (or -$\hbar$) per

photon of left-handed (or right-handed) circularly polarized light in vacuum and assuming the conservation of angular momentum holds at the plate's surface (Figure 1.2). Beth observed that a circularly polarized light beam reverses the handedness of its polarization when passing through a half-waveplate, thus transferring angular momentum to it.

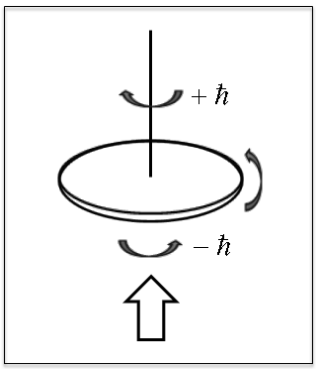

Fig. 1.2. Beth's experiment performed in 1936. It was based on measuring the torque as a circularly polarized light beam was passing through a birefringent half-waveplate suspended from a filament (schematic reproduced based on Ref. [1]).

Therefore, after light beams carrying OAM have been successfully generated in the laboratory, the apparent challenge was the OAM transfer to matter. But how to do so? The answer was to use optical tweezers [6].

Optical tweezers (OT) is a term used for the single beam optical trap, which has been the most popular form of optical manipulation over the last few decades. In 1970, Ashkin reported the first observation of acceleration of freely suspended micron sized particles via the forces of radiation pressure from a continuous wave (cw) visible laser beam [7]. When a laser beam is tightly focused, a large electric field gradient will result. Thus, the illuminated freely suspended small transparent particle will experience an electric field gradient that acted as a force directed towards the beam focus. Only a few years later, Ashkin et al. presented the first experimental observation of a single-beam gradient radiation pressure optical trap [8].

The first demonstration of angular momentum transfer to micron sized particles was reported by He et al., in 1995 [9]. The absorption of the linear momentum caused the highly absorbing ceramic powder particles to rotate at several Hz. However, the particles could only be confined in 2D near the intensity null on the beam axis. So, in a refined experiment by Simpson et al., this problem was overcome by comparing the transfer of both SAM and OAM components in the trap beam to partially absorbing Teflon particles [10]. Due to the fact that these particles were largely transmitting, the gradient force was sufficient to trap them in 3D; thus,

the apparatus acts as an 'optical spanner'. A laser power of a few tens of milliwatts could result in a rotation speed of the trapped particle of a few Hz. By altering the handedness of a circularly polarized LG beam with an OAM of $\ell = 1$, the total angular momentum was changed from $\hbar - \hbar = 0$ to $\hbar + \hbar = 2\hbar$ per photon. The spin and orbital components give torques in opposite senses so there is no overall torque on the particle and, as predicted, a LG beam with an azimuthal index $\ell = 1$ has a well-defined OAM of $\hbar$ per photon.

Therefore, LG beams can be extensively used in the field of optical micromanipulation, where they may trap low refractive index particles, set microscopic particles into rotation, and create micropumps [11-13]. These experiments are receiving considerable attention in cell biology [14, 15]. Furthermore, the use of fabricated light driven micromachines [16, 17] or the transfer of SAM and OAM components of the trap beam to the optically trapped particles has been widely explored earlier [18-20]. As a final note, these experiments have also elucidated the intrinsic and extrinsic nature of OAM [21, 22].

Owing to their unique characteristics, such as helical wavefronts and their dark core [23], OVs have also been applied to light microscopy [24] and wireless communication [25-28], where LG beams have created much interest for data transmission. In this case, OAM can represent a fundamentally new optical degree of freedom of light that arises as a consequence of the spatial distribution of the intensity and phase of the optical field. It has been demonstrated that the wireless communications with OAM multiplexing can work in both optical and radio frequency domains [29, 30]. Thus, the topological charge of a LG beam can be used in optical information encoding, which has advantages such as high capacity and security [31, 32].

Recently, more and more photonic applications have evolved which also use light fields deviating from the fundamental Gaussian beam profile. OVs have also been used for stellar detection [33, 34], and nanometre precision metrology by using the effect of OAM on beam shifts [35]. To conclude, light beams carrying OAM are of great interest and the reader is guided to two recent reviews on the advantages in OAM where the exciting applications of LG beams are discussed in detail [36, 37].

In general, how can such novel beam shapes be generated? After the first realization of the LG beam, many different generation techniques have been introduced. The first demonstration used the so-called $\pi/2$-mode converter, which belongs to a family of astigmatic mode converters that applies the appropriate Gouy phase to appropriate HG modes to create well defined mode indices of LG beams [38]. This was soon followed by the demonstration of a spiral phase plate (SPP) to directly transform a Gaussian beam to an OV [39]. At the same time, computer

generated holograms (CGHs) were applied to convert Gaussian beams into LG beams [40]. Diffractive optical elements (DOEs) made by state-of-the-art photolithographic techniques to etch small scale structures on an optical element can also be used for the generation of LG beams [41, 42]. Finally, q-plates can be applied to convert SAM to OAM in an anisotropic and inhomogeneous media to create LG beams [43]. A detailed description on the generation of OVs will follow in Chapter 2.

Now that the importance of LG beams has been explained, let us consider how a physicist knows when he/she has actually created a LG beam mode. Finding a simple and direct way that can be used for the characterization of a pure LG beam is a key area of this study. A commonly used technique is based on the interference between the helical wavefront under study with its mirror image [44] or a plane wavefront [45]. If a LG beam is interfered with a co-linear plane wavefront, then the resultant interference pattern would comprise of $|\ell|$ dark spokes. Likewise, when a LG beam interferes with its own mirror image, the resultant interference pattern has $2|\ell|$ dark spokes or fringe dislocations (Figure 1.3).

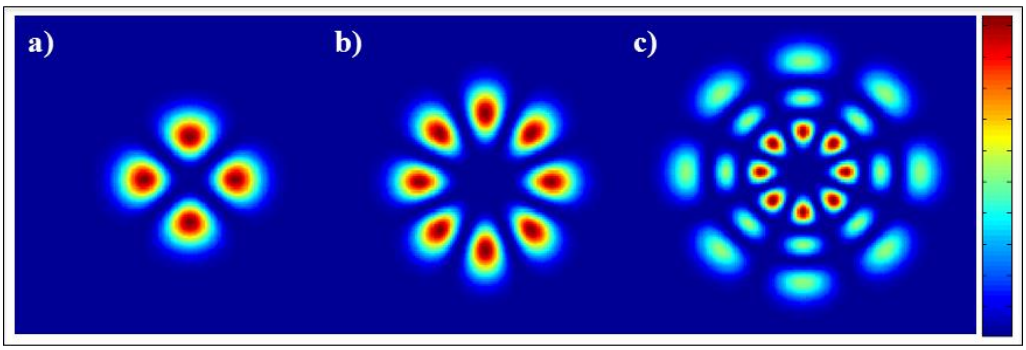

Fig. 1.3. Interference between a LG beam and its mirror image produces $2|\ell|$ dark spokes or fringe dislocations. Numerically simulated a) interference between a LG beam with $\ell = 2$ and its mirror image results in four dark radial fringes, while b) for a LG beam with $\ell = 4$, eight dark radial fringes will be produced. c) Finally, nodal rings will appear if the radial index is also considered, in the present case for the LG beam with $\ell = 4$, $p = 2$. The colour coded for the intensity is highlighted on the right-hand side where the blue and red colours indicate the lower and higher intensity, respectively.

Hence, these interferometric methods allow one to distinguish between infinitely many OAM states [44, 45]. However, if the size of the vortex beam is large compared to the detector area, the measurement of the phase distribution becomes difficult since the dark region around the singularity will accordingly increase, leaving less light to interfere with. Other approaches that can identify the azimuthal

mode index, ℓ, of an incident LG beam, include parametric downconversion [25, 46] and Mach-Zehnder interferometers [47]. However, these approaches are difficult to implement, are sensitive to alignment, or are not programmable.

Diffraction of OVs past a variety of apertures and obstacles can also be used to measure the azimuthal mode index, ℓ, of an unknown vortex beam, as will be presented in Chapter 3 where a detailed description of classical and quantum (single photon) measurements of ℓ will take place. The far-field diffraction of an OV from a triangular aperture results in a well-shaped truncated intensity lattice that can determine both the sign and the magnitude of the azimuthal mode index of the incident vortex beam [48]; it is a simple and reliable method that we focus on in Chapter 4 [49]. However, an adjustment is required so that the size of the triangular aperture is chosen to be of the order of the beam waist of the LG beam under study. Additionally, the far-field diffraction pattern gets more complicated when both the azimuthal and radial mode indices are considered and no clear rules can be established for the characterization of a pure LG beam directly from the complex far-field diffraction pattern as will be discussed in Chapter 3.

Therefore, we developed a new method using the principal component analysis (PCA) algorithm in Chapter 5. Whilst PCA has been established for over one hundred years (a technique dating back to 1901) [50], for the first time, this method is used here in the case of diffraction theory and the analysis of the transverse state of a light field. PCA has been widely used in various areas, such as in face recognition [51].

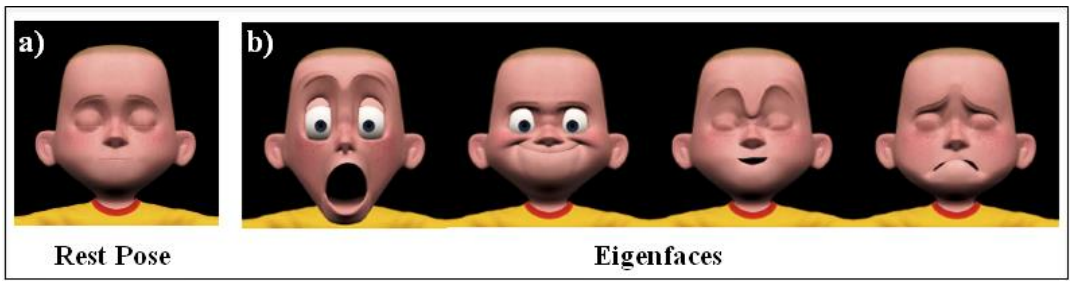

Fig. 1.4. An example of some of the basis motions computed from a facial articulation application. b) Raw basis vectors ('eigenfaces') computed by PCA in order to lead to an easy selection of representative points for (as an example) the a) rest pose (figure reproduced based on Ref. [52]).

The first step of the procedure is concerned with creating a database of all the possible faces that need to be detected. After subtraction of the common mean intensity, the covariance matrix of the test faces is calculated. Its eigenvector with the largest eigenvalue is termed the first 'eigenface' or principal component (PC), corresponding to the largest variability of the test faces set. In the same way, one can

introduce the second ‘eigenface’ as the image corresponding to the second largest eigenvalue of the covariance matrix and so on. Thus, a set of ‘eigenfaces’ is created that represents the most significant features from a sample of pictures of test faces. Then, a picture of the face that one wants to identify is projected onto this subset of ‘eigenfaces’, delivering projection coefficients to approximate the given face (Figure 1.4) [52]. This enables comparison to identify a face, which is much faster than comparing the face to every single face in the database picture by picture, while reducing the dimensionality of the analysed data. By the same token, PCA is used here in order to determine the largest variations between the different far-field diffraction intensity patterns of pure LG beams, even when a random aperture is used. Our approach is robust and it is shown that it can tolerate a certain degree of beam misalignment and beam waist variations [53].

This powerful method can be generalized to other orthogonal mode families as will be seen in Chapter 6. In this regard, Hermite-Gaussian (HG) beams are of major interest in laser resonator output analysis [54] and spectroscopy [55]. Pure HG beams are characterized by nodes in orthogonal direction in a cartesian coordinate space as is well documented [56]. On the other hand, Bessel beams (BBs) offer new directions in manipulation [57], nanosurgery [58], and microscopy [59] and can be delineated by an azimuthal index ℓ and a radial wavevector (k_r), since BBs can have vortices embedded. Both of these fields are also of interest for information processing [60]. It is important to establish the validity of our method for the other families of light fields to demonstrate its full applicability [61]. Finally, BBs are one example of ‘non-diffracting’ waves and their ‘self-healing’ property makes them very useful in OT and many other areas [62-65].

It is noteworthy that all of the previously stated studies have assumed that the optical field is fully spatially coherent. However, the interest for partially coherent fields has recently grown, since they are used in many cases, such as optical coherence tomography (OCT), optical communication, imaging science and astronomy [66, 67]. The preservation of the vortex structure during propagation makes partially coherent beams good candidates for various applications; accordingly, a better understanding of the spatial coherence properties is of fundamental importance. Recently, the coherent OVs or the phase singularities of a partially coherent field have been studied by optical coherence theory [68, 69]. The cross-correlation function (CCF) of a partially coherent vortex beam has also been studied theoretically and experimentally [70-73]. It has been shown that spatial correlation functions have interesting topological properties associated with their phase singularities, and there exist correlation singularities (denoting nulls of the cross-spectral density function) in the regions where the phase is ill-defined.

Therefore in Chapter 7, attention is paid to the dependency of the far-field CCF on both the radial and azimuthal mode indices of a partially coherent vortex field.

1.2 Thesis outline

This thesis describes an investigation into the parameters that can delineate the properties of novel beam shapes. Described in this thesis are Laguerre-Gaussian (LG), Hermite-Gaussian (HG) and Bessel beams (BBs). The current chapter provides a brief introduction to these novel beam shapes and to the numerous fields that can be applied to. Chapter 2 explores the considered beam shapes and describes the existing methods used to generate these beams. The relevancy of technology in spatial light modulators (SLMs) to produce these beam shapes in an easy manner will be also pointed out. Chapter 3 describes previous studies investigating diffraction of OVs past a variety of apertures and obstacles that have revealed interesting structural phase properties of the wavefronts of the considered beams and can be employed to measure the azimuthal mode index ℓ of an unknown vortex beam. Chapters 4 - 7 present the experiments carried out during this research.

I began by investigating the diffraction of an OV from a triangular aperture. Chapter 4 describes how the resultant far-field diffraction pattern can extract information about the azimuthal index, ℓ, which characterizes the incident OV in a simple and direct way (while keeping the radial index zero, $p = 0$): by counting the number of external points (interference lobes) of the resultant far-field diffraction pattern [48]. The number of the interference lobes on any side of the far-field diffraction intensity pattern is equal to the modulus of the azimuthal index plus one $(|\ell|+1)$. As will be seen, there are $(|\ell|+1)$ parallel rows or lines of interference lobes making up a truncated optical lattice. Furthermore, the effect of changing the sign of the azimuthal mode index, $\ell \rightarrow -\ell$, is to rotate the orientation of the truncated optical lattice by 180^{o}. Thus, the number of the interference lobes in the truncated optical lattice (far-field diffraction intensity pattern) and its orientation can be used as a detector of the azimuthal mode index, ℓ, of an incident OV.

In addition, the far-field diffraction patterns for incident OVs possessing non-integer values of ℓ are explored, resulting in the visualization of the birth of an OV. For fractional (non-integer) values of the azimuthal index, ℓ, there is a phase discontinuity which gives rise to a line of low intensity. Our experimental data are in agreement with the key theoretical prediction of Berry, that the birth of a vortex within the light beam takes place as the fractional phase step reaches and passes a half-integer value [74]. Finally, this method was further extended to explore the diffraction of a broadband OV from a triangular aperture. These results demonstrate

the extended versatility of a triangular aperture for the study of an OV for both monochromatic and broadband light fields [49].

The previously discussed diffraction based method encouraged an investigation into the possibility of finding an aperture that can extract information for both (azimuthal and radial) mode indices that characterize a LG beam. Thus, in Chapter 5 the far-field diffraction intensity pattern for LG beams of various mode indices, ℓ and p, was numerically and experimentally explored to ascertain the performance of a triangular aperture. It is shown that the inclusion of the radial index, p, makes a dramatic difference to the form of the far-field diffraction intensity pattern, but no clear rules may be established for determining both mode indices directly from the complex far-field diffraction patterns. Therefore, a new method is developed using the principal component analysis (PCA) algorithm. This method is used for the simultaneous determination of both the azimuthal and radial mode indices (ℓ and p) of both pure and mixed (superposed) LG light fields. It is shown that the shape of the diffracting element used to measure the mode indices is in fact of little importance and the crucial step is 'training' any diffracting optical system and transforming the observed pattern into uncorrelated variables (principal components). Modest fluctuations in the beam parameters such as beam waist and alignment variations can be tolerated in this scheme. Additionally, preliminary results demonstrate reliable decomposition of superpositions of LG beams, yielding the intensities and relative phases of each constituent mode. These results demonstrate the complete characterization of LG beams, including both independent degrees of freedom corresponding to the radial and azimuthal mode indices [53].

Initially our approach was generic, but was then extended to other families of light fields, such as the Hermite-Gaussian (HG) and Bessel beams (BBs), and represents a powerful method for characterizing the optical multi-dimensional Hilbert space. The experimental procedure and results are detailed in Chapter 6 [61].

All of the previously presented studies (Chapters 4 - 6) have assumed that the optical field is fully spatially coherent, however in Chapter 7 the dependency of the far-field cross-correlation function (CCF) on both the radial and azimuthal mode indices (p and ℓ) of a partially coherent vortex beam is demonstrated through an observation of the dislocation rings in the far-field CCF. A well-defined relationship between the number of the dislocation rings (dark zones), N_d, of the far-field CCF and both the radial and azimuthal mode indices in the partially coherent vortex beam can be established, i.e. $N_d = 2p + |\ell|$, and this relationship is verified experimentally. These results may contribute to a better understanding of the connection between the correlation vortices of a partially coherent field and the OVs of the corresponding fully coherent field.

Furthermore, the dependency of the CCF upon both the radial and azimuthal mode indices of a partially coherent vortex beam may create new ways to study other topological phenomena for the complex coherence function.

Finally, Chapter 8 summarizes this thesis, while future work and applications are suggested.

CHAPTER 2

Optical Phase Singularities

2.1 Synopsis and Motivation

According to the terminology, introduced in the wave theory by Nye and Berry [75], the crystallographic term ‘dislocation’ may be used to describe wavefront imperfections. The three main kinds of wavefront dislocations in a monochromatic wave are the edge, screw and mixed edge-screw dislocations. An edge dislocation is a defect where an extra half-plane is introduced mid-way through the wavefront; on the other hand, a screw dislocation takes its name from the helical path which the phase covers around the dislocation line. Finally, when a simple edge dislocation ends in a screw one, a mixed edge-screw dislocation is created.

The clearest example of a screw dislocation is the vortex, which is certainly the most fascinating and commonly studied phase singularity. Vortices can be found in many branches of physics [76-78]. Since Nye and Berry’s seminal paper on wave dislocations, these phase singularities in optics are commonly known as optical vortices (OVs) and as previously discussed, OVs were deeply investigated because of their manifold applications [36, 37]; OVs have been also applied in astronomical studies [79, 80]. In the current chapter, different aspects of OVs will be discussed, focusing on their generation and characteristics.

Other novel beam shapes can also find many applications due to their unique characteristics. The transverse intensity profile of a Bessel beam (BB) does not spread over a finite range and is therefore termed as ‘diffraction-free’ [81, 82]. Consequently, a BB’s central core is immune to transverse spreading and thus it can be used for the extended optical guiding of objects [57, 62]. Additionally, the transverse intensity profile of a BB is able to reform around objects, i.e. it ‘self-heals’, so a BB can be used to reduce scattering artefacts while simultaneously increase image quality and penetration depth in dense media [59]. Furthermore, BBs are also of interest for information processing [60]. Recently, entanglement in the BB basis has been measured, showing an increased spiral bandwidth [83]. In the present chapter, the properties of BBs and methods to generate them, including the use of computer generated holograms (CGH), will be presented. The CGH can be designed to imprint any phase profile on an incident light beam [84]. Finally, the device which displays CGHs, the spatial light modulator (SLM), will be introduced.

2.2 Introduction

Light beams can be described as superpositions of many plane waves propagating in different directions [85]. In general, when three or more plane waves interfere, light vanishes at some points, where the phase becomes undefined (singular); these points have received different names, such as: wave dislocations, phase singularities, nodal

points and optical vortices (OVs). The dislocation axis produces a dark region captured inside the light beam [1]. The screw dislocation is presented in Figure 2.1.

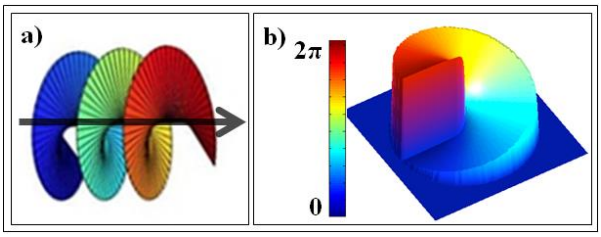

Fig. 2.1. Screw dislocation. a) Helical wavefront and b) phase singularity in an OV, where the hue colour chart shows the corresponding phase.

2.3 Optical vortex (OV)

An optical vortex (OV) is the optical analogue of a fluid vortex [86-89]. As previously stated, the light beams carrying OAM were realized as LG beams and have an OV along the beam axis [1]. Thus, the LG beam has an annular shaped transverse intensity profile [90]. The (numerically simulated) intensity profiles of several LG beams are presented below in Figure 2.2. The intensity profile of an LG beam with ℓ azimuthal index is identical to the $-\ell$ case. The equation describing the scalar field of a LG beam is a solution to the paraxial wave equation in cylindrical coordinates and the amplitude of a LG beam is given by [91]:

$$u_{p,\ell}^{LG}(r,\phi,z) \propto \exp\left(\frac{ikr^2}{2R(z)}\right)\exp\left(-\frac{r^2}{w^2(z)}\right)\exp\left(-i\left(2p+|\ell|+1\right)\Phi\right)\exp(i\ell\varphi)(-1)^p \times\left(2\frac{r^2}{w^2(z)}\right)^{|\ell|/2} L_p^{\ell}\left(\frac{2r^2}{w^2(z)}\right) \quad (2.1)$$

where $k = 2\pi/\lambda$ is the wavenumber, λ is the wavelength, r, φ and z are the cylindrical coordinates, ℓ is the azimuthal mode index, p is the radial mode index, $L_p^{\ell}(x)$ is the generalized Laguerre polynomial, $\exp(-i\ell\varphi)$ is the azimuthal phase term and $w(z)$ is the beam waist measured at the propagation distance z. The Gouy phase shift is contained in the term $\exp\left(-i\left(2p+|\ell|+1\right)\Phi\right)$, with $\Phi = tan^{-1}(z/z_R)$ where $z_R = \pi w_0^2/\lambda$ is the Rayleigh range and w_0 is the beam waist in the focal plane. The radius of curvature of the wavefront, $R(z)$, and the beam waist as a function of z, $w(z)$, are given by the following Equations (2.2) and (2.3), respectively:

$$R(z) = z\left(1+\left(\frac{z_R}{z}\right)^2\right) \quad (2.2)$$

$$w(z) = w_0 \sqrt{\left(1 + \left(\frac{\lambda z}{\pi w_0^{\,2}}\right)^2\right)} \tag{2.3}$$

The $L_p^{\ell}(x)$ is a generalized Laguerre polynomial obtained from [92]:

$$L_p^{\ell}(x) = \frac{x^{-\ell} e^{x}}{p!} \frac{d^{|p|}}{dx^{|p|}} \left(e^{-x} x^{\ell+p}\right) \tag{2.4}$$

The transverse intensity profile for a Laguerre-Gaussian beam is given by:

$$I(r,z) \propto \left(u_{p,\ell}^{LG}(r,\phi,z)\right)^2 \propto \frac{P_0}{w^2(z)} \left(-2\frac{r^2}{w^2(z)}\right)^{|\ell|} \exp\left(\frac{2r^2}{w^2(z)}\right) \left\{L_p^{\ell}\left(\frac{2r^2}{w^2(z)}\right)\right\}^2 \tag{2.5}$$

where P_0 is the incident power and the radius of the maximum intensity, $r_{I_{\max}}(z)$, varies as a function of ℓ according to the following equation [93]:

$$r_{I_{\max}}(z) = \frac{\sqrt{2} w(z)}{2} \sqrt{\ell} \tag{2.6}$$

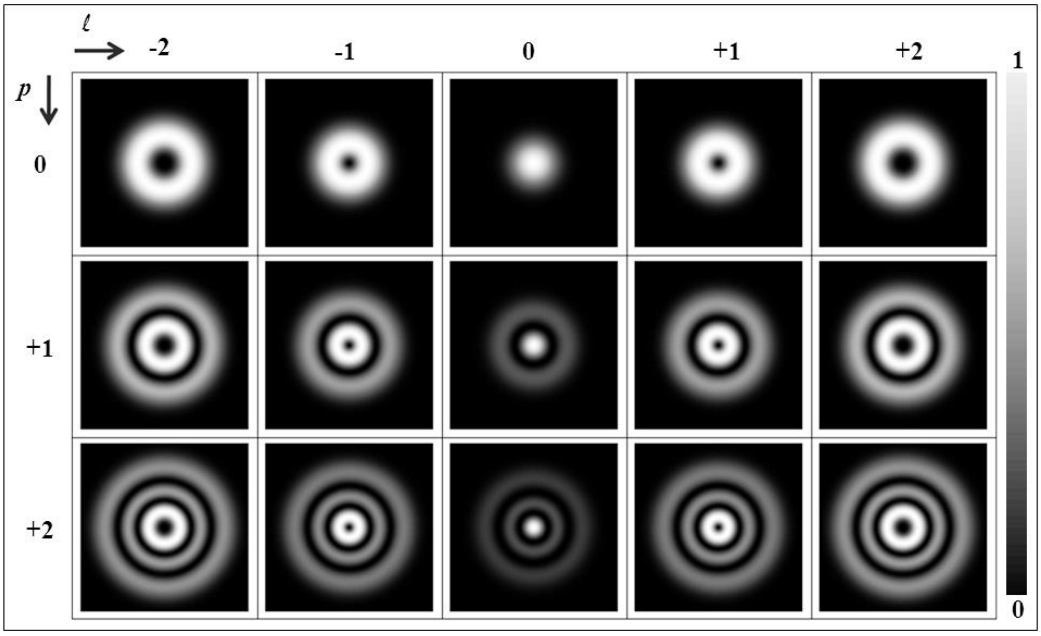

Fig. 2.2. The transverse intensity profiles of LG beams with different radial and azimuthal mode indices (numerically simulated). The intensity profiles for absolute values of OAM are the same and the rows and columns define the azimuthal and radial mode index, respectively. For visualization purpose higher intensity is represented by lighter side, while gray scale is used.

The following Figure 2.3 illustrates how the transverse intensity profile and azimuthal phase of an OV change with ℓ value. In terms of its intensity cross-section, a LG beam with $\ell > 0$ comprises $p + 1$ concentric rings with zero on-axis intensity. Higher order Bessel [82] and Mathieu beams [94] can have similar phase structure.

As a final note, when LG beams interfere, they produce vortex structures resulting in complex patterns of bright and dark regions [95] (see Figure 1.3).

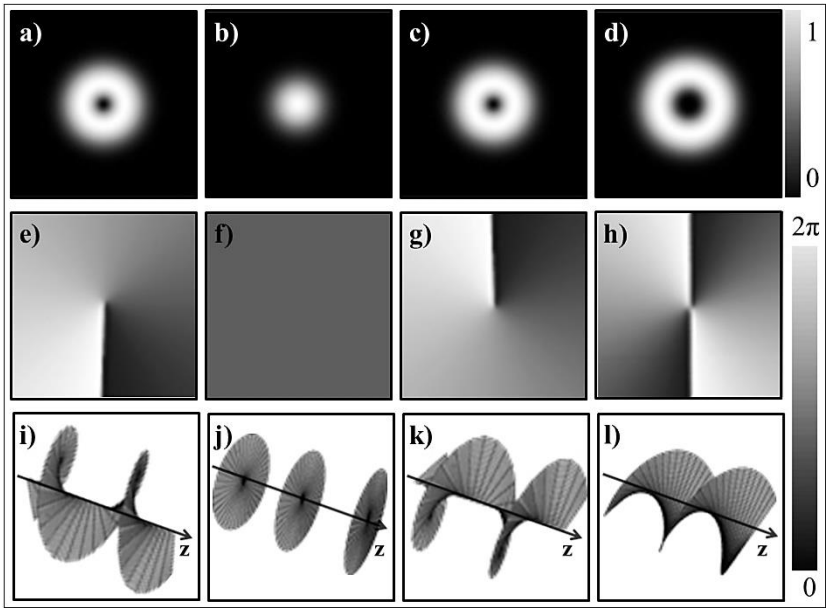

Fig. 2.3. Numerically simulated intensity profiles of LG beams with p = 0, a) ℓ = -1, b) ℓ = 0, c) ℓ = 1 and d) ℓ = 2 are shown. The corresponding azimuthal phase is presented below the intensity profile in e), f), g) and h), respectively. The 3D representations of the helical wavefronts along the propagation axis z are accordingly shown in i), j), k) and l). The gray scale is used, where higher intensity is represented by lighter side.

2.3.1 Generating an optical vortex

In the present subsection, an expression for the Hermite-Gaussian (HG) modes will be introduced as it is essential for an understanding of the direct generation of an OV in a laser cavity, as well as the generation through mode converters, discussed afterwards. The HG modes arise as solutions of the paraxial wave equation in cartesian coordinates [56, 96]. The solutions are expressed in terms of Hermite polynomials multiplied by a Gaussian envelope. These HG beams are categorized by their mode indices n and m and have an amplitude given by:

$$u_{n,m}^{HG} \propto \exp\left(\frac{-\left(x^2+y^2\right)}{w^2(\zeta)}\right)\exp\left(\frac{-ik\left(x^2+y^2\right)z}{2\left(z^2+\left(z/\zeta\right)^2\right)}\right)\exp\left(-i\left(n+m+1\right)\Phi\right)$$

$$\times H_n\left(\frac{x\sqrt{2}}{w(\zeta)}\right)H_m\left(\frac{y\sqrt{2}}{w(\zeta)}\right) \qquad (2.7)$$

where $\zeta = \frac{z\lambda}{\pi w_0^2}$, $w(\zeta) = w_0\left(1+\zeta^2\right)^{1/2}$, w_0 is the beam waist at the focal plane, H_n is the n^{th} order Hermite polynomial and *x*, *y* and *z* are the cartesian coordinates. The 2D (numerically simulated) intensity plots of the first nine HG modes are shown in Figure 2.4 below. The values of *n* and *m* correspond to the number of nodes in the electromagnetic field. The Hermite polynomials obey the following recursion relation:

$$H_{n+1}(x) = 2x \cdot H_n(x) - \frac{d}{dx}H_n(x) \tag{2.8}$$

This can provide a useful way of calculating the higher order polynomials in numerical computations. The n^{th} order function has *n* nulls and *n + 1* peaks. Likewise, the m^{th} order function has a similar behaviour.

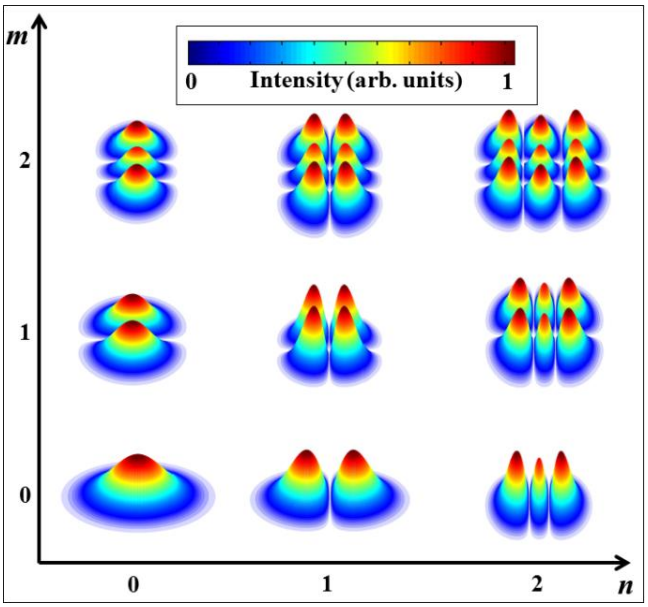

Fig. 2.4. The 2D intensity plots of HG beams with different mode indices (numerically simulated). The rows and columns define the *n* and *m* mode indices in the *x* and *y* directions, respectively. The blue and red colours are accordingly indicating the lower and higher intensity.

2.3.1.1 Direct generation from a laser cavity

In the early 90s, Tamm and Weiss developed the first optical system that gave experimental evidence for the bistability and optical switching of a transverse pattern of a Helium-Neon (HeNe) laser source [97]. The operation principle for this will be explained in the next subsection, where the mode converters for OV generation are presented. Similar laser systems that directly emit LG beams have been developed including Ishaaya et al. [98] and Okida et al. [99]. The latter demonstrated direct production of high power LG beam mode and suggested the

possibility of the production of high power OVs in the visible and ultra-violet (UV) regimes.

2.3.1.2 Mode converters

The key point of Allen et al. [1] was that OAM is a natural property of spiral phased beams and thus it could be generated in a laboratory. Hence, Beijerbergen et al., following the work of Tamm and Weiss on low-order modes, dealt with suitable astigmatic elements which conserve the mode character and thus operate as beam mode converters [38]. In 1999, Allen et al. developed a matrix formulation describing transformations of the phase and intensity structure for monochromatic light beams possessing OAM based on one particular basis set of orthogonal laser modes, namely HG beam modes [100]. The matrix formulation based on HG beam modes was then derived in full by O'Neil and Courtial [101]. A mode converter consisting of two cylindrical lenses of focal length f separated by $f\sqrt{2}$ can transform suitably oriented HG beams into simply related LG beams with $\ell = \pm|m-n|$ and p = min(m, n), acting as a π/2-converter in analogy with a quarter-waveplate for polarization; leaving the mode order ($N = n + m = 2p + |\ell|$) unchanged (Figure 2.5b). When the cylindrical lenses are separated by $2f$ then they act as a π-converter that only rotates the LG beam by 180° and the apparatus works by direct analogy with the half-waveplate for polarization [45] (Figure 2.5a).

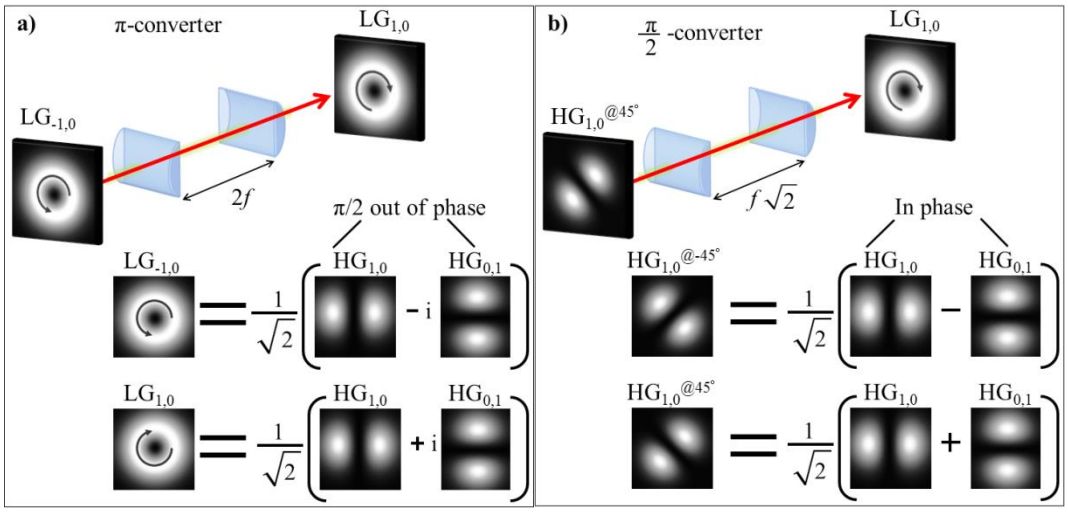

Fig. 2.5. The schematics of cylindrical lenses operate as π- and π/2- mode converters. The distance between two cylindrical lenses and the decomposition of the considered LG beam modes in the HG basis are indicated. The sample intensity cross-sections are those of a HG beam at 45° and -45° with mode indices n = 0, 1 and m = 0, 1 and a LG mode with mode indices ℓ = ±1, p = 0.

The combination of π/2- and π-converters provides considerable freedom in manipulating the LG beam and its OAM. The reader is guided to Ref. [102] where a general prescription for transforming combinations of HG beams into any particular LG beam is given. The main drawback of this mode transformation is that a higher order HG beam is required as an input and any imperfection in the specification or alignment of the cylindrical lens leads to a residual astigmatism in the resulting LG beam. This is manifested as a non-circular beam cross-section as well as in the fact that higher index LG beams tend to split upon propagation in a series of OVs with unity charge [103, 104]. However, mode converters can be used with high power laser sources.

The analogy between transverse light beams and polarization states extends to a description of light beams and their transformation with an equivalent to the Pointcaré sphere that is a graphical tool for visualizing different types of polarized light (Figure 2.6) [105]. The coordinates of the point, on or within a unit sphere centred on a rectangular (*x*, *y*, *z*) coordinate system, describe the state of polarization. Orthogonal polarizations are located diametrically opposite on the sphere. As shown in Figure 2.6a below, linear polarizations are located on the equator and circular states are located at the poles with intermediate elliptical states continuous distributed between the equator and the poles. For OAM, the states $|\ell\rangle$, $|-\ell\rangle$ are represented by the poles of the sphere, while equally weighted superposition of $|\ell\rangle$ and $|-\ell\rangle$ correspond to points around the equator, an example for $\ell = 1$ is shown in Figure 2.6b.

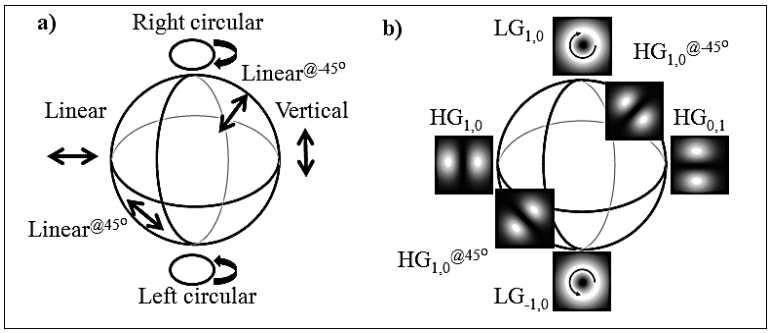

Fig. 2.6. a) The Pointcaré sphere and b) sphere of first-order LG beams. The encountered polarization states and beam modes are indicated. Schematic was produced based on Ref. [105].

2.3.1.3 Spiral phase plates (SPPs)

The use of spiral phase plates (SPPs) is another approach for generating beams with phase singularities [39]. A SPP is an optical element constructed from a piece of transparent material in the form of a disc with refractive index *n* and optically

variable height h_{SPP} that increases linearly with azimuthal angle φ resembling a spiral staircase. This can convert a Gaussian beam into a LG beam [106]. The relation between height and azimuthal angle is given by:

$$h_{SPP} = h_S \frac{\varphi}{2\pi} + h_0 \tag{2.9}$$

where h_S is the step height and h_0 is the base height of the SPP. The spiraling thickness variation imprints an azimuthal retardation on the incident light beam, resulting in the spiraling phase distribution of an OV. The azimuthal optical phase delay, δ, is given by:

$$\delta = \frac{2\pi}{\lambda}\left[\frac{(n-n_0)h_S\varphi}{2\pi} + nh_0\right] \tag{2.10}$$

where n_0 is the refractive index of the surrounding medium. If the height of the step corresponds to a phase difference of 2π, a SPP inserted in the waist of a Gaussian beam will imprint an azimuthal phase profile generating the OV along the beam axis. The optical thickness of the SPP increases with azimuthal position according to: $\ell\lambda\varphi / 2\pi(n-1)$. If the step height of a SPP is not an integer, in addition to the on-axis OV, a radial phase discontinuity is created [74, 107]. SPPs with half-integer step heights have been deliberately fabricated for experiments in quantum optics [108]. The SPP must be smooth and accurately shaped to a fraction of a wavelength, so precise micro-machining techniques have been employed to manufacture SPPs [109]. However, if the SPP is successfully produced, it is only applicable to one wavelength of light and one topological charge ℓ. Even though, achromatic SPPs have been also developed for use with broadband sources [110]. As with mode converters, a SPP can be used with high power beams.

A more versatile way to create OVs is by means of an adjustable SPP [111]. A twisted piece of cracked Plexiglas is used in order to create an adjustable SPP. The Plexiglas is then oriented so that one tab of the SPP is directly perpendicular to the incident light beam, and the other tab is bent at some angle φ away from the other. An incident light beam at the end of the crack will then result in an OV because of the azimuthally varying tilt around the centre of the SPP. If the elastic limit of the plate material is not exceeded, the twisting process is controllable and versible. These adjustable SPPs can be used with multiple wavelengths and produce a range of topological charges.

2.3.1.4 Diffractive optical elements (DOEs)

The use of diffractive optical elements (DOEs) to transform spatially coherent beams into beams containing OVs have also began to be explored in the early 1990s.

For example, computer generated holograms (CGHs) can be used to imprint a phase profile on an incident light beam and produce novel beam shapes. Bazhenov et al. demonstrated a simple technique of generating optical beams with an isolated screw dislocation using the diffraction by lithographically defined CGHs [112]. They reconstructed the helical wavefront by using the diffraction of a plane wave by a synthesized grating. It looks like the usual holographic technique, however in this case a hologram is not reconstructed by optical waves, but is computer generated. They discovered that when a diffraction grating is modified to include an edge dislocation at its centre, in the form of a fork, an optical singularity appears in the first order diffracted beam. Thus, the resulting hologram has a 'forked' dislocation with an imprinted ℓ-value that corresponds to the difference between the number of lines above and below the dislocation. This difference depends on the value of ℓ, as seen in Figure 2.7. For example, for $\ell = 1$ there is one more line at the top of the grating than at the bottom. Similarly, for $\ell = 2$ there are two more lines at the top of the grating than at the bottom and so on (number of prongs = desired topological charge $\ell + 1$).

In general, there are two possible kinds of holograms: amplitude and phase. An amplitude hologram transmits the light in the transparent fringes and absorbs it in the opaque ones. However, the phase hologram does not absorb light. Instead, it changes the optical retardation spatially based on the printed phase pattern. A hologram can be characterized by its efficiency, which is a fraction of power located in the first order of diffraction, P_1, to the imprinted power on the hologram, P_0, i.e. $E_f = P_1/P_0$. In average, an amplitude hologram absorbs about half of impinging power assuming total absorption in the opaque fringes. Hence, amplitude holograms result in lower efficiency compared to the phase holograms that can be designed to ideally achieve 100% efficiency by blazing the used grating. The blazed phase holograms theoretically diffract all incident light into one of the first order LG beams and the pattern for such a blazed hologram is calculated based on the following Equation (2.13).

In general, the complex amplitude, $u(r)$, that the generated beam has (after being incident on the CGH), is described by:

$$u(r) = u_0(r)\exp\left(i\psi(r)\right) \tag{2.11}$$

where $u_0(r)$ is the complex amplitude of the beam incident on the SLM and $\psi(r)$ is the phase imprinted on the beam by the CGH. In order to apply a spiral phase when no diffraction grating is added to the hologram, the phase imprinted on the incident light beam will be given as:

$$\psi(r) = \mathrm{mod}\left(\ell\varphi, 2\pi\right) \tag{2.12}$$

where mod(*a*,*b*) gives the remainder of *a*/*b* and when a spiral phase front with a diffraction grating are added to the hologram in use, the phase imprinted on the incident light beam becomes [91]:

$$\psi(r) = \mathrm{mod}\left(\ell\varphi - \frac{2\pi}{\Lambda} r\cos\varphi, 2\pi \right) \tag{2.13}$$

where Λ is the grating period. The blazed CGHs designed to create a single-ringed LG beam with topological charge, $\ell = \pm 1$ and 2, are respectively shown in Figure 2.7 below, where the spiral phase distribution of the desired hologram is typically added to a linear phase ramp (phase grating) and the sum is expressed as mod(2π). The resulting hologram is a blazed phase grating that has a 'fork' feature in its centre.

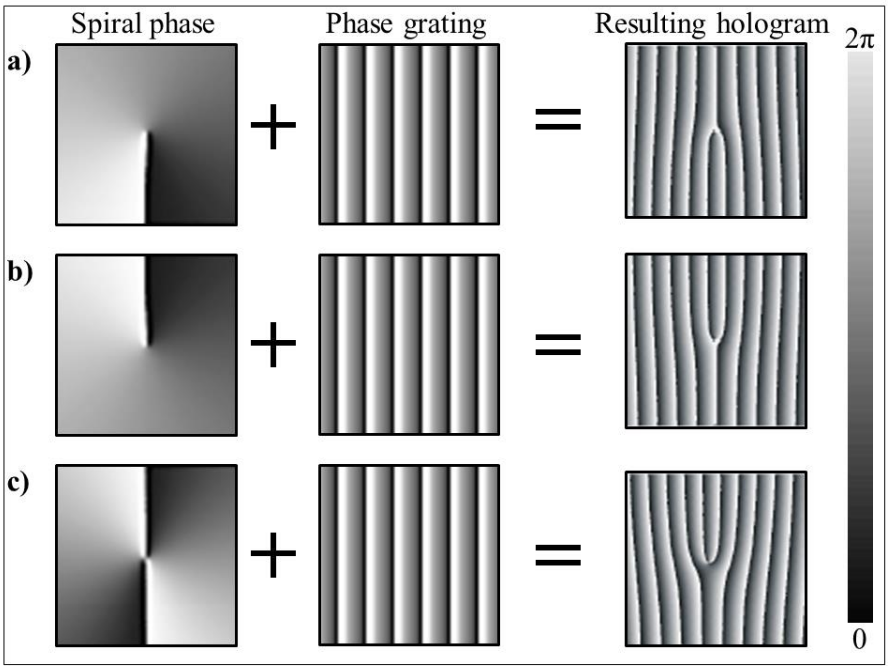

Fig. 2.7. Typical 'forked' CGHs used to generate OVs with $p = 0$ and a) $\ell = -1$, b) $\ell = 1$, and c) $\ell = 2$. Also shown are the spiral phase (first column) and the linear phase ramp (second column) that are combined to give the 'forked' holograms (third column). The hologram is reversed for opposite signed but same magnitude helical beam. The CGH (that is displayed on the SLM) is an 8-bit per pixel bitmap image where black (grayscale level 0) represents a phase of 0 and white (grayscale level 255) represents a phase of 2π.

DOEs made by state-of-the-art photolithographic techniques to etch small scale structures on an optical element can be also used for the generation of LG beams [113]. An incident light beam on the DOE diffracts from the microstructures and the resulting beam profile is the superposition of the diffracted waves. There is no fundamental limit to the mode purity of beam shapes created with this method; it is only limited by the resolution of the lithographic techniques used to etch the DOEs

[41]. Furthermore, a helical mirror can be also used to create OVs of various azimuthal mode indices [114]. A piezoelectric actuator controls the mirror shape in order to provide a continuous phase variation along the azimuthal direction. However, it also introduces radial phase variations because of unavoidable material stresses, thus lowering the quality of the generated OVs. Likewise, a deformable mirror (DM) can be used to generate an OV [42]. By using this method, one can apply any azimuthal index to the incident light beam, up to the mechanical limits of the DM. This allows a great variability of the azimuthal mode index and even fractional (non-integer) values. Finally, q-plates can be applied to convert SAM to OAM in an anisotropic and inhomogeneous media to create LG beams [43]. To conclude, DOEs give freedom to generate OVs at any wavelength and from a GB which makes them more versatile.

2.4 Bessel beam (BB)

Next, let us move on another novel beam shape. A new type of solution to the paraxial wave equation in terms of Bessel function was spotted by Durnin in 1987 [81] and the first experimental realization of the equivalent optical beam, the Bessel beam (BB), soon followed [82]. A complete discussion on BBs is presented in this section.

2.4.1 Introduction to the Bessel beam

From a mathematical point of view, BBs are particular solutions to the paraxial equation in cylindrical coordinates [81]. The electric field of the ℓ^{th} order BB can be described by the formula:

$$E(r,\varphi,z) = E_0 \exp\left(i\left(k_z z - \ell\varphi\right)\right) J_\ell\left(k_r r\right) \tag{2.14}$$

where J_ℓ is the ℓ^{th} order Bessel function, and k_r and k_z are the radial and longitudinal wavevector components of the free-space wavevector, such that $k = 2\pi/\lambda = k = \sqrt{k_r^2 + k_z^2}$, and r, φ and z are the radial, azimuthal and longitudinal components of the cylindrical coordinates and E_0 is the field amplitude. The transverse intensity profiles of BBs with different ℓ values are shown in Figure 2.8. The zeroth order BB has a central maximum, whereas all the higher order BBs have zero on-axis intensity surrounded by concentric rings of light. The central zero of the higher-order BBs is due to the phase singularity of charge ℓ associated with the azimuthal phase term $\exp(-i\ell\varphi)$ [115].

In theory, the intensity profile of a zeroth order BB can propagate for an infinite distance without spreading. It is obvious, that in the laboratory, one deals with an approximation of a BB or a 'quasi-BB', which can propagate 'diffraction-free' for

only a finite distance and it is surrounded by a certain number of rings. Finally, another surprising property of this 'diffraction-free' beam is that a BB can reconstruct beyond obstructions placed in its optical path, thus BB 'self-heals' [116, 117]. The reason for this will be explained in the next subsection, where different methods for BB generation are presented.

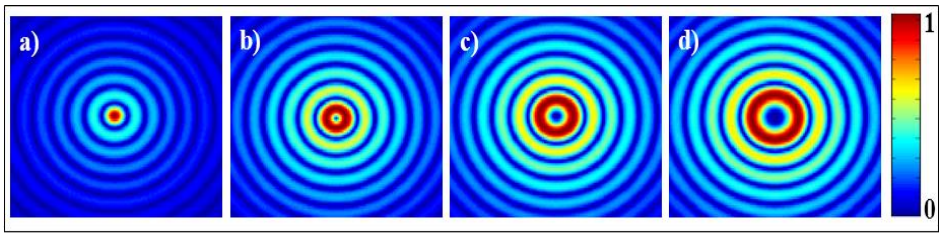

Fig. 2.8. The transverse intensity profiles of BBs (numerical simulated). BBs with ℓ^{th} order Bessel function of the first kind, where ℓ = 0 to 3 increasing in integer step are shown in a) to d), respectively. All BBs have the same k_r value.

2.4.2 Generating a Bessel beam

Experimentally, there are a number of methods to generate a BB. As first demonstrated by Durnin et al., a BB can be generated by illuminating an annular aperture situated at the back focal plane of a lens [82]. Thus, the resulting Fourier transform of this annulus will provide a BB. The maximum 'diffraction-free' propagation distance of the resulting BB, z_{max}, depends on the focal length, f_{lens}, and the radius, R_{lens}, of the lens and also the diameter of the annular aperture, d_a, such that:

$$z_{\max} = \frac{R_{lens}}{\tan\gamma} \quad \text{and} \quad \tan\gamma = \frac{d_a}{2 f_{lens}} \tag{2.15}$$

where γ is the opening angle. However, this approach is an inefficient method because the most of the incident power from the Gaussian beam (GB) is blocked by the opaque part of the annular aperture used. A more efficient method for generating a BB is to use a conical lens, known as axicon [118]. As illustrated in Figure 2.9, by illuminating an axicon with a GB, a conical wavefront is generated that interferes to produce a zeroth order BB. Higher order BBs can be produced by illuminating an axicon with a LG beam [119]. The maximum 'diffraction-free' propagation distance of the resulting BB by this method depends on the beam waist of the incident beam, w_{inc}, the refractive index of the axicon material, n_{ax}, and the base angle of the axicon, α, such that:

$$z_{\max} = \frac{k}{k_r} w_{inc} \approx \frac{w_{inc}}{(n_{ax} - 1)\alpha} \tag{2.16}$$

Thus, a larger beam waist, w_{inc}, results in a larger maximum 'diffraction-free' propagation distance, z_{max}. Also, a smaller value of the base angle of the axicon, α, will result in a larger value of z_{max}. Finally, the most flexible method for generating a BB is the use of a hologram that is computer generated or through microfabrication [120-122]. This allows direct control over the parameters of the resulting BB and is the method employed in the experiments discussed in Chapter 6. The function $\psi(r)$ that can be substituted into Equation (2.11) to generate a BB is given by:

$$\psi(r) = \mathrm{mod}\left(\ell\varphi - \frac{2\pi}{\Lambda} r \tan\alpha, 2\pi\right) \tag{2.17}$$

where the base angle of the axicon is α and ℓ is the order of the BB.

2.4.3 Self-healing property of a Bessel beam

Now that the generation of a BB has been explained, another remarkable feature of the BB will be discussed, i.e. the self-healing property of the BB. An axicon generated BB is seen to reform after striking an opaque obstruction that blocks a part of the incident BB (Figure 2.9).

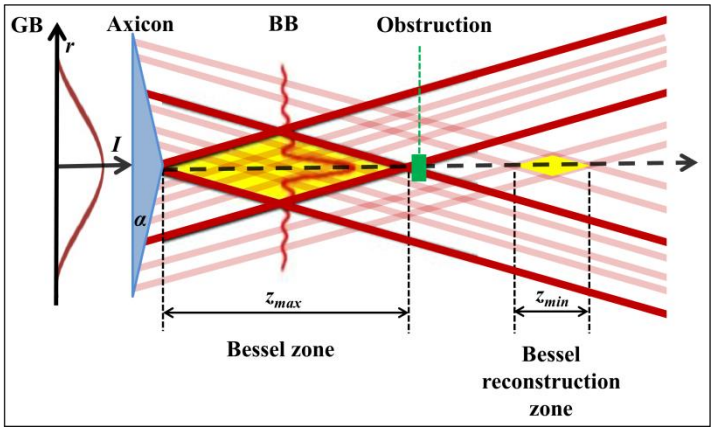

Fig. 2.9. Generation of a BB making use of an axicon lens. The 'Bessel zone' is the region where the waves interfere to produce a BB and the 'Bessel reconstruction zone' is the area where the BB reforms after the obstruction placed in the beam's path.

Furthermore, the BB can be thought as an interference pattern generated by waves propagating on a conical wavefront. If an obstruction is placed in the Bessel beam's path, the BB will reform at some distance after the obstruction, thus the BB 'self-heals'. The previously presented Figure 2.9 clearly illustrates that the optical rays illuminating the axicon close to the optical axis are responsible for the construction of the BB nearest to the axicon. While the optical rays illuminating the axicon away from the optical axis construct the BB further away from the axicon. Hence, the

waves that pass the obstruction are able to interfere and reform the BB. Finally, the minimum distance that it takes the BB to reconstruct around an obstruction, z_{min}, is related to the radius of the obstruction measured from the centre of the beam, r_{obs}, and the wavevectors k_r and k, such that:

$$z_{\min} \approx \frac{r_{obs}k}{k_r} \approx \frac{r_{obs}}{(n_{ax}-1)\alpha} \tag{2.18}$$

Equation (2.18) can be compared to the Equation (2.16) when the refractive index, n_{ax}, and the base angle, α, of the axicon are considered.

2.5 The Spatial Light Modulator (SLM)

The generation of novel beam shapes carrying phase singularities has been made easier through the use of the spatial light modulator (SLM). The commercial availability of SLMs has massively enhanced the popularity of DOEs for generating novel beam shapes. The SLM is a real-time computer controlled pixelated device that has a liquid crystal (LC) display where the spatial variations of phase can be transferred on an incident light beam [123]. One of the main advantages of the SLM is that the parameters of the light beam can be easily altered. The size of the incident GB is a compromise between resolution and power efficiency. On one hand, if the incident GB has a large beam waist, it will make a better use of the active area of the SLM, which in turn results in a higher resolution of the generated beam shape. On the other hand, if the beam waist of the incident GB is too large, a part of the incident power will miss the active area of the SLM and will therefore be either lost or go into the unmodulated zeroth order. Thus, the standard compromise is to use a beam waist that roughly matches to the size of the active area of the SLM. Additionally, any significant incident beam power must be distributed, so as to avoid boiling or damaging the LC active element of the SLM.

A LC-SLM can be either nematic or ferroelectric. Nematic SLMs can modulate the phase by a range of values (in phase steps of $2\pi/256$) between 0 and 2π, but are slow (in practice, an update rate for a near-IR nematic SLM would typically be 20Hz). Ferroelectric SLMs have only two phase levels (phase shift 0 and π), which limits the choice of algorithms for the calculation of the hologram patterns and the diffraction efficiency. However, with update rates of typically tens of kilohertz, ferroelectric SLMs are significantly faster. During this research only electrically addressed nematic SLMs are used since a more precise control over the applied phase can be achieved and the high repetition rate of a ferroelectric device was not required.

Commercial LC-SLMs are either optically or electrically addressed. A photosensor allows the optically driven SLMs to sense the brightness of each pixel

and replicate an image using LCs. The display of an electrically addressed nematic SLM consists of a layer of birefringent LCs. There is a transparent electrode on one side and silicon pixilated electrodes on the other side of the LCs. The magnitude of the voltage applied to the nearest pixelated electrode can alter the orientation of the LCs at a location. Thus, when there is no electric field present, the LCs line up in a preferred orientation. However, as an increasing electric field is applied the orientation of the LCs begins to align accordingly with the considered electric field. Therefore, the refractive index of each pixelated electrode can be controlled by modulating the voltage applied to each silicon pixelated electrode in the LC displays (Figure 2.10) [123].

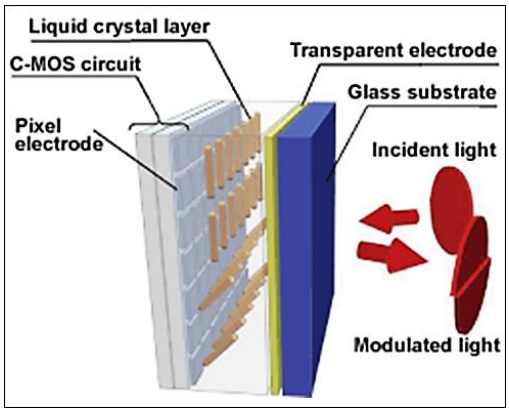

Fig. 2.10. A liquid crystal on silicon (LCOS) spatial light modulator (SLM). The individually addressed pixel electrodes, which act as one electrical contact layer are shown at the left-hand side and a transparent second electrical contact layer is placed above the LC layer. When an electric field is applied the LCs rotate and change the local refractive index, thus altering the retardation imparted to the wavefront in that pixels area. Image adapted from Ref. [123].

	SLM1	SLM2	SLM3
Number of pixels:	1024x768	800x600	1920x1080
Pixel pitch:	19µm	20µm	8µm
Display area:	19.6x14.6mm	16x12mm	16,39x10.56mm
Repetition rate:	72Hz	60Hz	60Hz
Wavelength:	400-700nm	400-700nm	400-800nm
Fill factor:	93%	95%	90%

Table. 2.1. The specifications of the three SLMs used during this study. SLM1 is the Holoeye LC-R 2500, SLM2 is the Hamamatsu x10468-01 and SLM3 is the Holoeye 1080P.

Table 2.1 details the specifications of the three SLMs that were used during this research. SLM1 is the Holoeye 2500, SLM2 is the Hamamatsu X10468-01 and

SLM3 is the dual-head Holoeye 1080P. All considered SLMs use a liquid crystal on silicon (LCOS) display.

2.6 Discussion and Conclusions

In this chapter, different aspects of LG beams were presented, focusing on their generation and characteristics. An expression for the HG beams was also introduced which is essential for the understanding of the direct generation of a LG beam in a laser cavity, as well as generation through mode converters. Next, a thorough discussion on BBs followed. The properties of BBs and methods to generate them, including the use of computer generated holograms (CGH), were presented. The CGH can be designed to imprint any phase profile on an incident light beam [84]. Finally, the device used to display CGHs, the spatial light modulator (SLM), was introduced.

Quantitative measurement of the parameters that can delineate the properties of the Laguerre-Gaussian (LG), Hermite-Gaussian (HG) and Bessel beams (BBs) is essential for the studies and potential ground-breaking applications that these beams have found over the last few decades. Consequently, the modal characterization of the novel beam shapes under consideration here will be studied in this thesis.

Finally, the following chapter will detail the previous studies investigating diffraction of OVs past a variety of apertures and obstacles that have revealed interesting structural phase properties of the helical wavefronts of LG beams and can be employed to measure the azimuthal mode index ℓ of an unknown vortex beam. This forms a theoretical basis for the diffraction of an OV from a triangular aperture presented afterwards in Chapter 4.

CHAPTER 3

Analysis of Optical Vortices based on the Diffraction Theory

3.1 Synopsis and Motivation

Quantitative measurement of the OAM is essential for the studies and potential ground-breaking applications that LG beams have found over the last decades (see Chapter 1). A key issue is the simple, direct measurement of the OAM content of the LG beams. Therefore, measuring the topological charge, ℓ, of a vortex beam becomes a task of great significance.

Diffraction of OVs by a variety of apertures and obstacles can reveal interesting structural phase properties of their spiral wavefronts and can be employed to measure the azimuthal mode index, ℓ, of an unknown vortex beam. The present chapter provides an overview into the analysis of OVs based on the diffraction theory, where an analytical description of classical and quantum (single photon) measurements of ℓ will take place.

3.2 Analysis of LG beams

Two commonly used techniques for the identification of the azimuthal mode index of a vortex beam are based on the interference between the vortex beam under study with its mirror image [44] or a plane wave [45]. The interference pattern through the appearance of fringes clearly reveals the OAM state of the considered OV and these interferometric methods allow one to distinguish between many states. In the first case, the most striking feature of the resultant interference pattern is the fringe splitting or 'forking' arising from the phase discontinuity at the centre of the OV (see Figure 1.3).

On the other hand, for example when a LG beam with $\ell = 3$, $p = 0$ interferes with an obliquely plane wave, at the beam waist the 6π phase change around the circumference gives rise to three fringe dislocations. Away from the beam waist, spiral fringes are observed. Thus in this case of study, the number of radial fringes is equal to $|\ell|$ [45]. This method can be also applied to less symmetric OVs such as those occurring in speckle patterns, where the resultant interference pattern can be used to trace their position and OAM state [124]. However, if the size of the OV is large compared to the detector area, the measurement of the phase distribution becomes difficult, since the dark region around the singularity will accordingly increase, leaving less light to interfere with.

3.2.1 Young's double slit experiment

In 1802, the English polymath Thomas Young performed a celebrated experiment demonstrating interference from two closely spaced slits [125]. Furthermore, Thomas Young was the first to observe the phenomenon of interference and his

experimental apparatus is depicted in the Figure 3.1 below. A monochromatic light beam is incident on the first screen which contains a slit, S_0. The diffracted light beam then arrives at the second screen which has two parallel slits, S_1 and S_2. Hence, the diffracted light beams from the two slits interfere and result in a far-field diffraction pattern of bright bands due to constructive interference, interlaced with dark bands due to destructive interference on the viewing screen, C. The bright bands (fringes) correspond to interference maxima, and similarly the dark bands correspond to interference minima which are highlighted by white or dark spots, respectively shown in Figure 3.1.

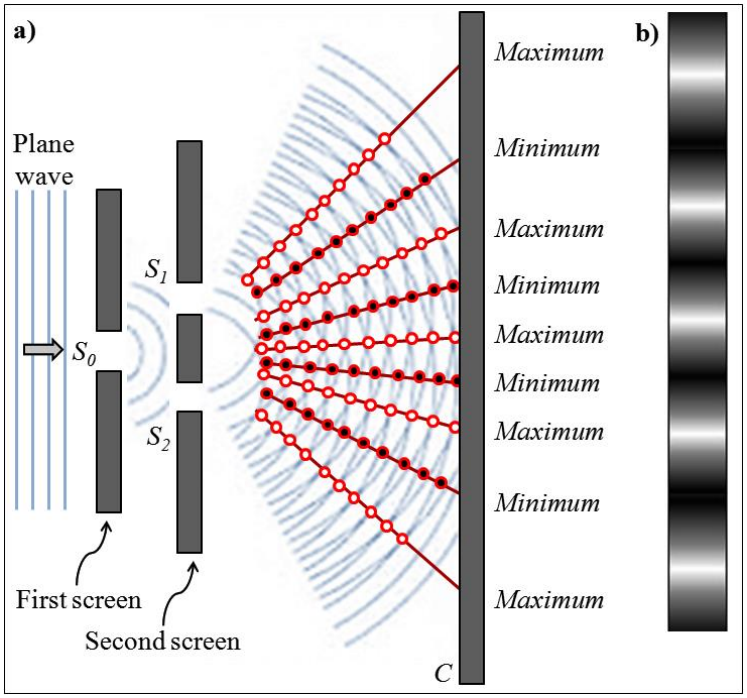

Fig. 3.1. Schematic of Young's double slit experimental apparatus. a) The diffracted light beams from the two slits interfere and result in a far-field diffraction pattern of bright bands due to constructive interference, interlaced with dark bands due to destructive interference on the viewing screen. b) The resulting far-field diffraction intensity pattern is presented.

The ubiquitous Young's double slit experiment, which has been quoted as the most beautiful experiment in physics [126], may be used to determine the phase structure of OVs [127]. In this case, the length of the double slits has to be of the order of the size of the beam waist of the incident vortex beam and as the distance from the centre of the slit increases, the phase difference between opposite points on the slits decreases. Thus, the interference fringes exhibit a diagonal shift in the centre causing the formation of bent interference fringes with either a maximum (for even ℓ) or minimum (for odd ℓ) at the centre (Figure 3.2). The sign of ℓ can be determined

by observing the direction of the bend in the *x*-direction as one looks from the top of the interference pattern to the bottom, and the modulus of the topological charge can be determined by measuring the magnitude of the bend [127] (Figure 3.3).

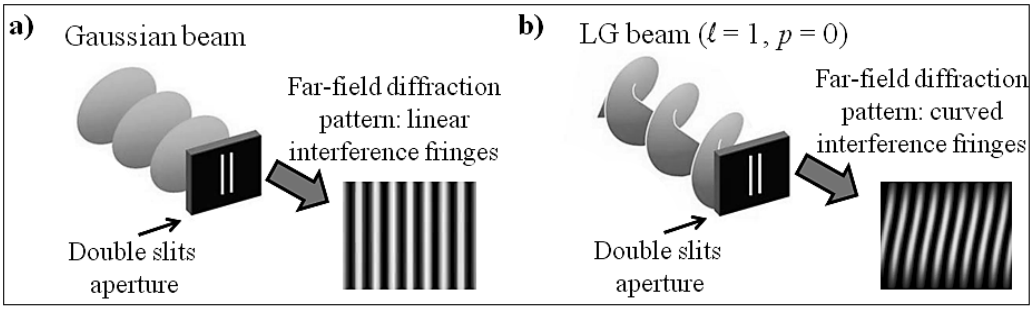

Fig. 3.2. Illustration of the Young's double slit experiment. a) An incident Gaussian beam on Young's double slit apparatus produces the familiar linear interference fringes. b) The bent interference fringes in the far-field intensity diffraction pattern that results for an incident LG beam, can be employed to characterize the azimuthal mode index of the OV ($\ell = 1$ in this case) [127].

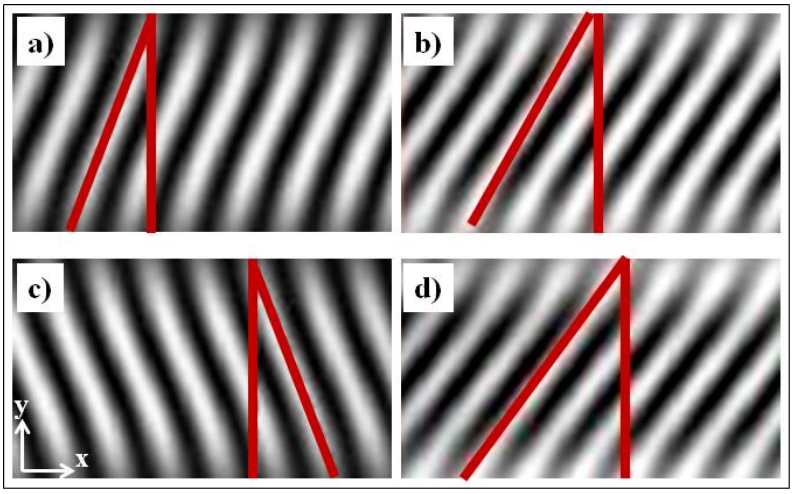

Fig. 3.3. Numerically simulated far-field diffraction intensity patterns for vortex beams incident on double slits aperture based on Equation (6) in Ref. [127]. For incident LG beam with a) $\ell = 3$, b) $\ell = 6$, c) $\ell = -3$ and d) $\ell = 7$ while $p = 0$ (linear gray scale is used, white corresponds to high intensity). The sign and the modulus of ℓ can be determined by observing the direction and the magnitude of the bend as indicated by the red solid lines.

In fact, the interference effect will have some correlation to the width of the double slits, because the wider the slits are, the more the phase varies across the slits. Consequently, an adjustment of the size of the beam waist of the incident LG beam should be done such that the double slits are located at the peak intensity of the LG beam. Using Young's double slits one can measure the azimuthal mode index, ℓ, of

the incident vortex beam, even for polychromatic vortices generated by broadband supercontinuum (SC) radiation [128].

3.2.2 Multipoint interferometer (MPI)

In 2008, Berkhout and Beijersbergen presented an efficient method for probing the OAM of OVs of arbitrary sizes [129]. In this method, based on a multipoint (or multipinhole) interferometer (MPI), the OAM of a vortex beam was recognized according to the fact that OVs with different azimuthal mode indices, ℓ, will result in a different far-field diffraction intensity pattern after the OVs pass through a multipoint (or multipinhole) (MP) plate, in which the pinholes are uniformly distributed in a ring.

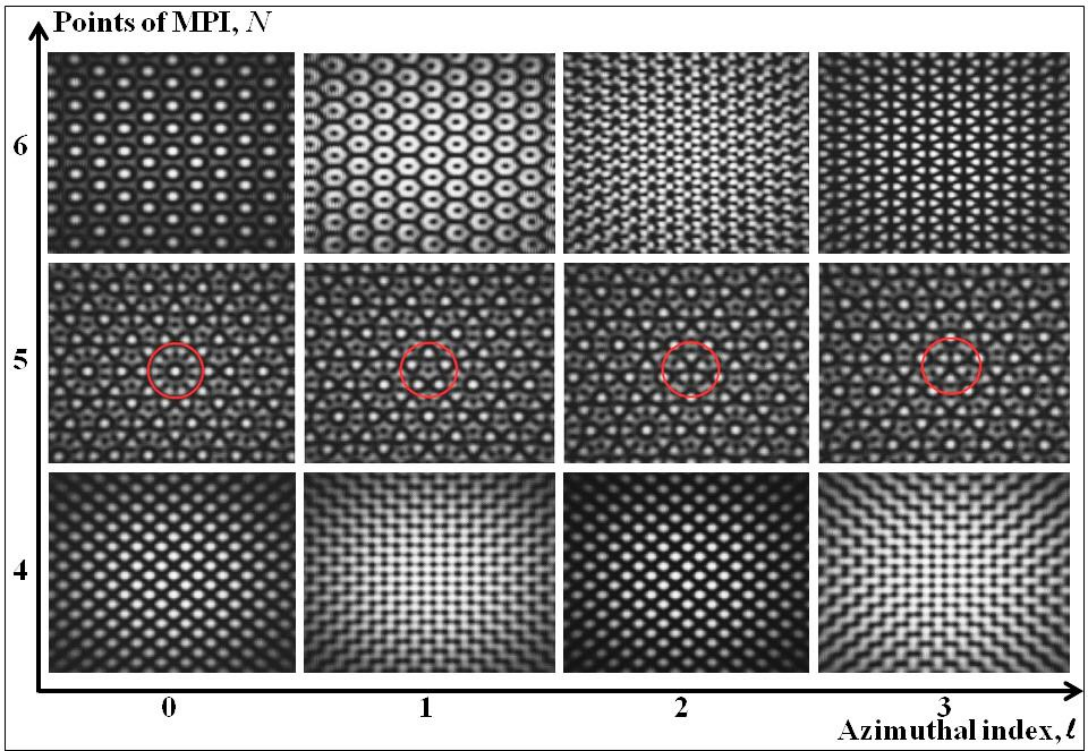

Fig. 3.4. Numerically simulated far-field diffraction intensity patterns for vortex beams incident on a MPI of *N* points based on Equation (2) in Ref. [129]. The columns and rows define the MPI points and the value of the azimuthal mode index of the incident LG beam, respectively. The different far-field diffraction intensity patterns can be employed to measure ℓ (linear gray scale is used, white corresponds to high intensity). Finally, the red circled line indicates an example of an area where the different azimuthal mode indices can be easily identified (in case of $N = 5$).

Some examples of the far-field diffraction intensity patterns are presented in Figure 3.4 above that have been numerically calculated based on Equation (2) in Ref. [129]. The size of the MPI was chosen to be of the order of the beam waist size of the LG

beam in order to collect maximum intensity from the ring-shaped intensity profile of an LG beam with $\ell = 1$. The far-field diffraction intensity patterns for opposite signed ℓ values are mirrored in the *x*-axis and one can determine the sign of ℓ for an odd number of points of the MPI. Nevertheless, for an even number of points there is no difference between the pattern for positive and negative ℓ, making it impossible to differentiate between negative and positive OAM states. However, this method can decompose a superposition of LG beams, which is potentially useful for application in free space communication [130]. The resultant far-field diffraction intensity patterns have a high sensitivity to noises and phase deviations and this may result in some difficulty in distinguishing the OAM state of the OVs directly from the intricate interferometric patterns; nevertheless, the OV can be identified as long as the singularity is enclosed by the MPI.

Guo et al. also studied the OAM of OVs through extracting the phase values sampled by a MP plate [131]. In this case, the phase of an OV passing through a MP plate can be directly extracted from the Fourier transform of a single far-field intensity diffraction pattern according to a simple algorithm and hence the azimuthal mode index, ℓ, can be quantitatively measured. Moreover, triangular and non-uniformly distributed MP plates can be also used for characterizing the OAM of an OV [132, 133].

3.2.3 Coordinate transformation

Berkhout et al. have also presented another efficient method to sort OAM states of light using two static optical elements [134]. The optical elements perform a cartesian (*x*, *y*) to log-polar (*u*, *v*) coordinate transformation (where $u = -a\ln\left(\sqrt{x^2 + y^2}/b\right)$ and $v = \arctan(y/x)$) converting the incident helically phased light beam corresponding to OAM states into a beam with a transverse phase gradient and *a*, *b* are scaling coefficients. Each input OAM state is focused to a different lateral position. Two spatial light modulators (SLMs) are used to create the desired optical elements, and this method based on the coordinate transformation has been also applied to measure OAM superpositions [135]. Furthermore, a mapping of this type transforms a set of concentric rings at the input plane into a set of parallel lines in the output plane. This efficient approach is limited by the fact that the resulting spots can slightly overlap. However, this can be corrected by adding a binary phase grating to the transforming elements, producing different diffraction orders. Nevertheless, there is approximately a three quarters light loss associated with the two used SLMs that can be eliminated by replacing the SLMs with the equivalent custom-made refractive optical elements.

As a consequence, Lavery et. al. showed that the conversion of OAM states into transverse momentum states can be also achieved by replacing the previously used SLMs with refractive optical elements [136]. In this case, the transmission efficiency is approximately 85%, which makes this approach attractive for use with single photons.

Hence, it was demonstrated that this approach is also efficient for single photon experiments by using an electron multiplying camera (EMCCD) in single photon counting mode and a laser source that was attenuated such that on average there is less than one photon present within the system per measurement period. This method was recently improved, extending the measurement bandwidth to > 50 OAM states and showing a simultaneous measurement of the radial component [137], making it an effective measurement technique that can be implemented as a tool in the fields of optical communication and quantum optics.

3.2.4 Diffraction gratings

As previously introduced in Chapter 2, the generation of LG beams is most often accomplished using a hologram, the design of which is a diffraction grating containing a 'fork' dislocation on the beam axis [112].

In 2009, Moreno et al. proposed a technique to characterize the azimuthal mode index, ℓ, of an OV through its diffraction intensity pattern after a fork-shaped grating [138]. The advantage of this system is that it is compact, completely programmable and appears to be valid even for fractional values of the azimuthal mode index, ℓ [139]. However, this technique allows photons to be tested for only one particular OAM state. A more complex CGH could be adopted to detect several different OAM states, but its efficiency will be low.

3.2.5 Fourier transform of the intensity distribution of an OV

Another method that can discriminate between the different topological charges of the OVs was recently proposed by Prabhakar et al. [140]. They showed that the number of dark rings in the logarithm of the Fourier transform of the intensity distribution of an OV is equal to the magnitude of the azimuthal index, ℓ. The strong point of this technique is its simplicity. One can get the topological charge of an OV in real time; however, this method cannot determine the sign of the azimuthal mode index. Recently, this method was also used in order to study the effect of spatial coherence on determining the azimuthal index of an OV [141].

3.2.6 Far-field diffraction of OVs past a variety of apertures and obstacles

There is a lot of research on the diffraction characteristics of a vortex beam passing through a variety of apertures and around obstacles. The far-field diffraction intensity pattern of an OV passing through a slit hexagon [142] or an annular ellipse aperture [143] was recently investigated theoretically and experimentally. It was found that the number of the dark spots or stripes in the far-field diffraction intensity pattern is just equal to the magnitude of the azimuthal mode index, ℓ, of the incident LG beam, and that the centre of each dark spot or stripe is a phase singularity. Hence, the modulus of the azimuthal mode index can be identified but no information can be extracted for the sign of ℓ. Likewise, circular and diamond-shaped apertures may be used but also cannot distinguish between LG beams of opposite helicity but the same magnitude of the azimuthal mode index, ℓ [144, 145].

Moreover, the far-field diffraction intensity pattern of an incident LG beam on a slit aperture has been studied for two different cases; in one, it is incident slightly above the slit aperture, and in the other it is centred on the slit. The symmetry and the fringe formation in the far-field diffraction pattern can give information of the magnitude of ℓ [146]. Additionally, the far-field diffraction intensity pattern of an OV passing through a square aperture can result in an intensity square truncated lattice. It can be seen that there is a relation between the number of lateral spots or interference lobes, N, and the azimuthal index, ℓ, i.e. $|\ell| = 2N - 2$, but only for even values of ℓ. For odd values of ℓ, the square lattice is not very well formed [147]. However, these methods cannot determine the sign of the azimuthal index.

In 2010, Hickmann et al. showed that the far-field diffraction of a vortex beam by an equilateral triangular aperture results in a truncated optical lattice, which has correlations with the OAM of the incident OV [48]. To have a physical insight, Hichmann et al. used a simple qualitative argument to analyze the effect of the azimuthal phase over each edge of an equilateral triangular aperture. When the diffraction patterns corresponding to each edge in the considered equilateral triangular aperture are superposed, i.e. they interfere, one recovers the truncated optical lattice.

Some examples of the stated research in the current subsection are shown in the Figure 3.5 below. The presented far-field diffraction intensity patterns were calculated based on the Matlab code presented in Appendix A, where the propagation was performed in two steps. The field was first propagated to the aperture plane, where the field distribution was multiplied by the relevant transmission function. The transmission function has a unity transmission inside the

considered aperture and zero outside the aperture. Then, the resultant field distribution was propagated to the far-field. As a final note, for the numerical implementation of the far-field diffraction intensity pattern, the scalar field of each LG beam is discretized over a square grid and aperture by the used aperture.

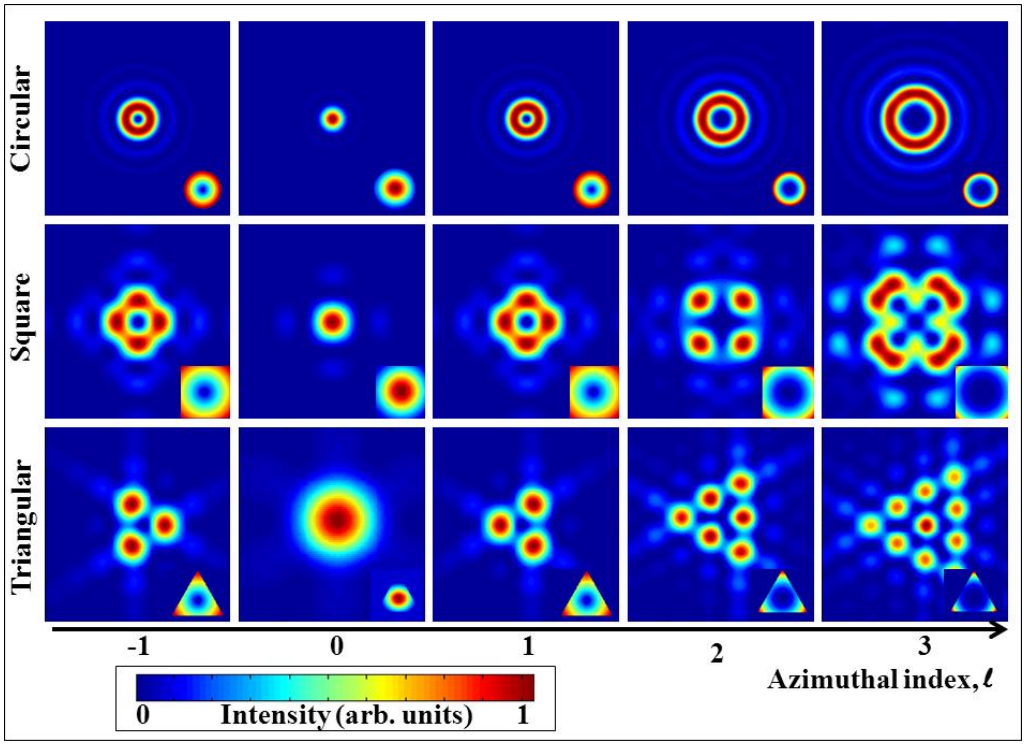

Fig. 3.5. Numerically simulated far-field intensity distributions of OVs of order ℓ = -1 to 3 increasing in integer step (from left to right). The rows present different results for the circular, square and triangular aperture. The hue colour chart coded for the intensity is also highlighted. The aperture plane is presented as inset to the images and the scale is the same for all images.

When a triangular aperture is used, a well-shaped truncated intensity lattice is generated in far-field for any value of the OAM that can determine the magnitude of the azimuthal mode index, ℓ, of the incident vortex beam in a simple and direct way, just by counting the number of external points (interference lobes), N, of the triangular lattice, namely $|\ell| = N - 1$. Changing the sign of ℓ will result in a rotation by 180^{o} of the far-field diffraction patterns. This effect can be used for the determination of the sign of ℓ and proves that a triangular aperture illuminated with an OV is a simple and reliable technique for the determination of both the magnitude and the sign of the topological charge of the vortex beam. Figure 3.5 shows a comparison between three apertures, where the far-field diffraction intensity pattern is numerically calculated for OVs with ℓ = -1 to 3 increasing in integer step. The triangular aperture is shown to be a direct approach that can extract information for

both the sign and the magnitude of the azimuthal mode index, so prevails over the other apertures. Moreover, in 2011, de Araujo and Anderson measured the vortex charge via the approach of the triangular aperture for vortex beams up to charge of $\ell = \pm 7$. They also demonstrated the use of this technique for measuring femtosecond vortices, but care must be taken when interpreting the results for fractional (non-integer) values of the azimuthal mode index, ℓ [148]. Then, Liu et al. proposed a simple and feasible method to determine the magnitude and the sign of ℓ of an OV through its far-field diffraction intensity pattern after an annular triangle (or triangular slits) aperture [149].

These studies demonstrate the extended versatility of a triangular aperture for the study of OVs and set the scene for a further investigation into this diffraction effect, such as whether this is valid for fractional (non-integer) values of the azimuthal index. In our study presented in the next chapter, we address this issue together with a demonstration that the rotation of the far-field diffraction pattern is related to the Gouy phase component of the incident vortex beam [49]. It is also shown that this is valid for both monochromatic and broadband light fields.

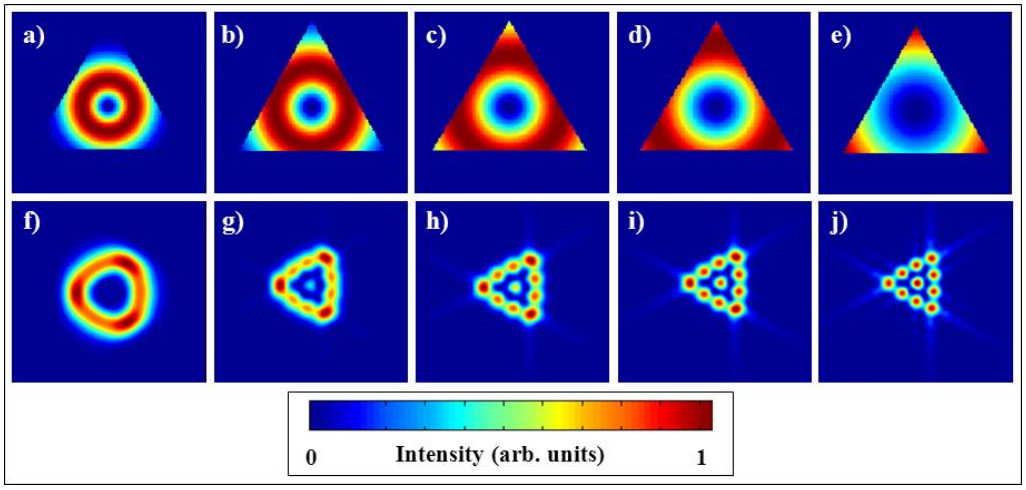

Fig. 3.6. Numerically simulated far-field intensity distributions of OVs with $\ell = 3$ diffracted by a triangular aperture. The OV falls in the centre of the aperture and the ratio of the beam waist of the incident OV to the aperture's size, η, is given by a) $\eta = 0.2$, b) $\eta = 0.3$, c) $\eta = 0.4$, d) $\eta = 0.5$ and e) $\eta = 1$. The aperture plane is presented in the first row, a) to e), while the far-field diffraction intensity pattern is accordingly presented in the second row from f) to j), for the different considered ratios. If the ratio is lower or higher than the presented conditions in a) and e), this effect of diffraction is negligible. The hue colour chart coded for the intensity is also highlighted and the scale is the same for all images.

Finally, one important point about the methods discussed here, is that the phase singularity must fall in the centre of the aperture used and the edges of the aperture

should be illuminated by the inner border of the incident LG beam. As illustrated in Figure 3.6 above, the far-field diffraction intensity pattern is blurred and deformed if the size of the triangular aperture is not commensurate with the beam waist of the considered LG beam.

3.2.6.1 Which is the optimal aperture that can determine simultaneously the azimuthal and radial mode indices of an OV?

As previously described, a wide array of diffractive structures have all recently been used to measure the azimuthal index of LG beams. To date, all these experimentally realized approaches have only been considered when irradiated with LG beams of zero radial index, $p = 0$. In the present subsection, the far-field diffraction intensity pattern for LG beams of various mode indices, ℓ and p, is numerically explored to ascertain the performance of a triangular aperture.

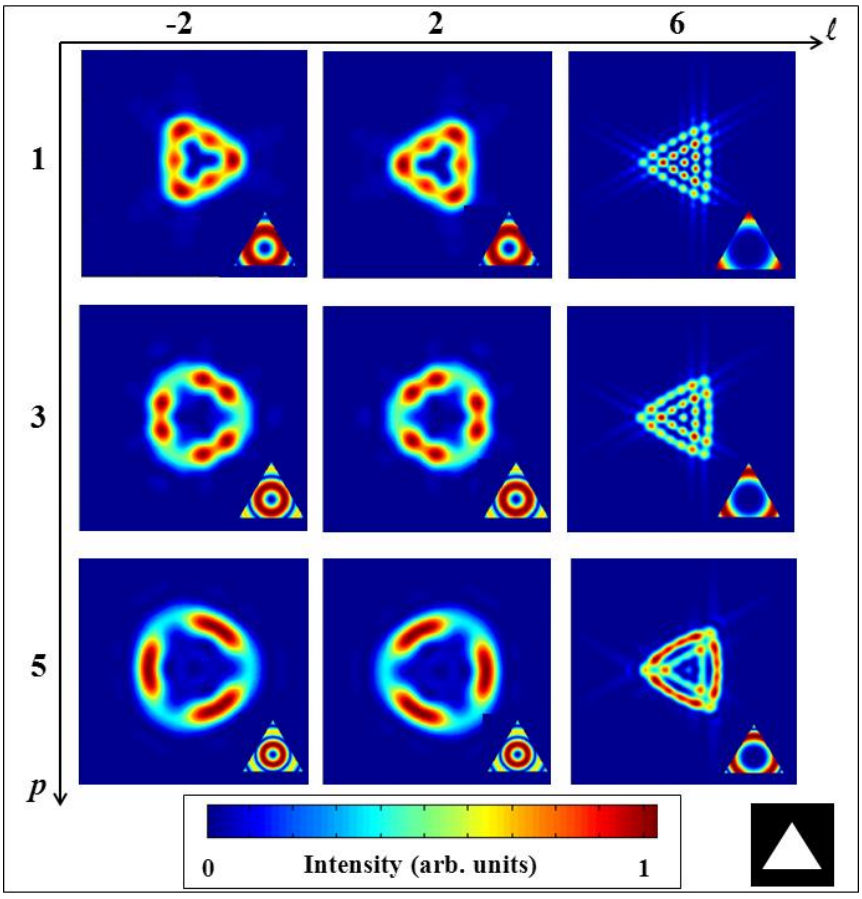

Fig. 3.7. Numerically simulated far-field intensity distributions of OVs with different mode indices diffracted by a triangular aperture. The rows and columns define the azimuthal and radial mode indices, respectively. The aperture plane is presented as an inset in every image. The hue colour chart coded for the intensity is highlighted and the scale is the same for all images. The considered triangular aperture is also highlighted at the bottom right corner.

It is shown that the inclusion of the radial index *p* makes a dramatic difference to the form of the far-field diffraction pattern. Furthermore, no clear rules may be established for determining both mode indices directly from the complex far-field diffraction patterns (Figure 3.7). However, it should be noted that regardless of the radial mode index, the orientation of the far-field diffraction intensity pattern does depend on the sign of the azimuthal mode index. The far-field diffraction intensity pattern rotates for opposite sign but same magnitude of the azimuthal index, ℓ.

Thus, an interesting question is addressed that is raised by the previously presented numerical simulations: which is the optimal aperture that can determine simultaneously the azimuthal and radial mode indices of an OV? Therefore, our aim in the present subsection, is to examine the potential of determining both ℓ and *p* mode indices simultaneously in any measurement.

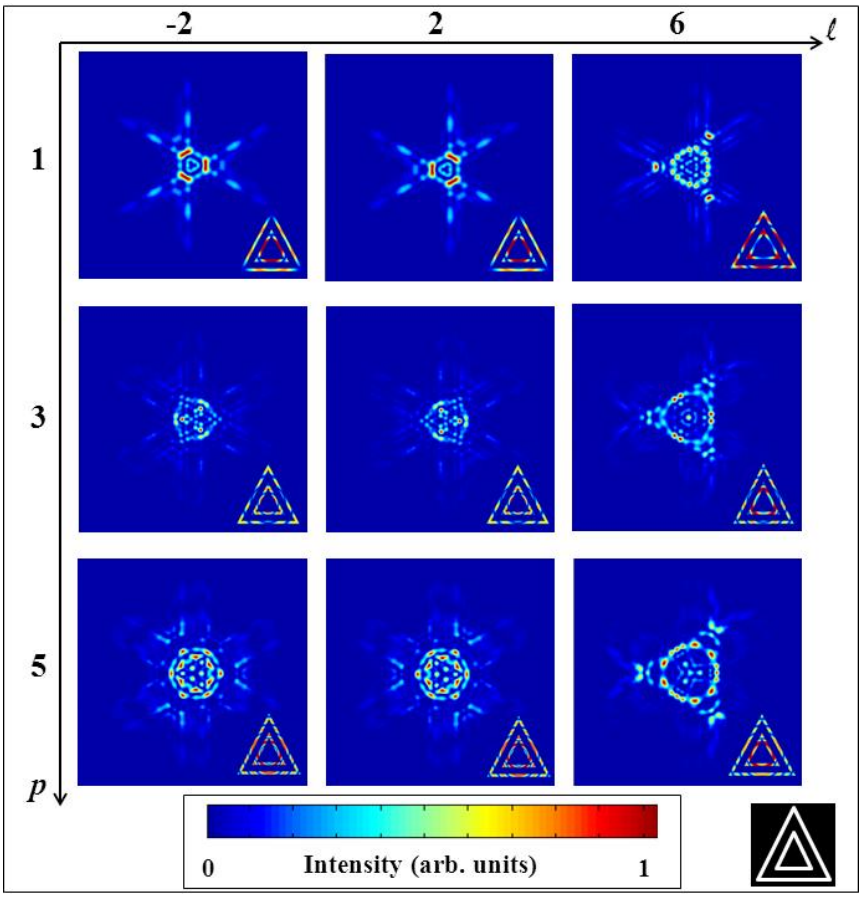

Fig. 3.8. Numerically simulated far-field intensity distributions of OVs with different mode indices diffracted by a double concentric triangular slits aperture. The rows and columns define the azimuthal and radial mode indices, respectively. The aperture plane is presented as an inset in every image. The hue colour chart coded for the intensity is highlighted and the scale is the same for all images. The considered double concentric triangular slits aperture is also highlighted at the bottom right corner.

Since the far-field diffraction from a triangular aperture is one of the most powerful methods for determining the azimuthal mode index by simply counting the number of interference lobes in the far-field diffraction intensity pattern [48, 49, 148, 149]; superposing multiple such apertures might appear, at the first glance, an appropriate method to determine both the radial and azimuthal mode indices of an incident LG beam (Figure 3.8). Furthermore, in order to extract the information of the radial concentric rings present in the LG beam profile when the radial index is considered, a tailored aperture such as a triangular slits aperture with radial spokes was also used (Figure 3.9). Although, it cannot be excluded that there exists a specifically designed aperture that would deliver a simple rule for the detection of both ℓ and p, this is not the case for the double concentric triangular slits aperture or a triangular slits aperture with radial spokes.

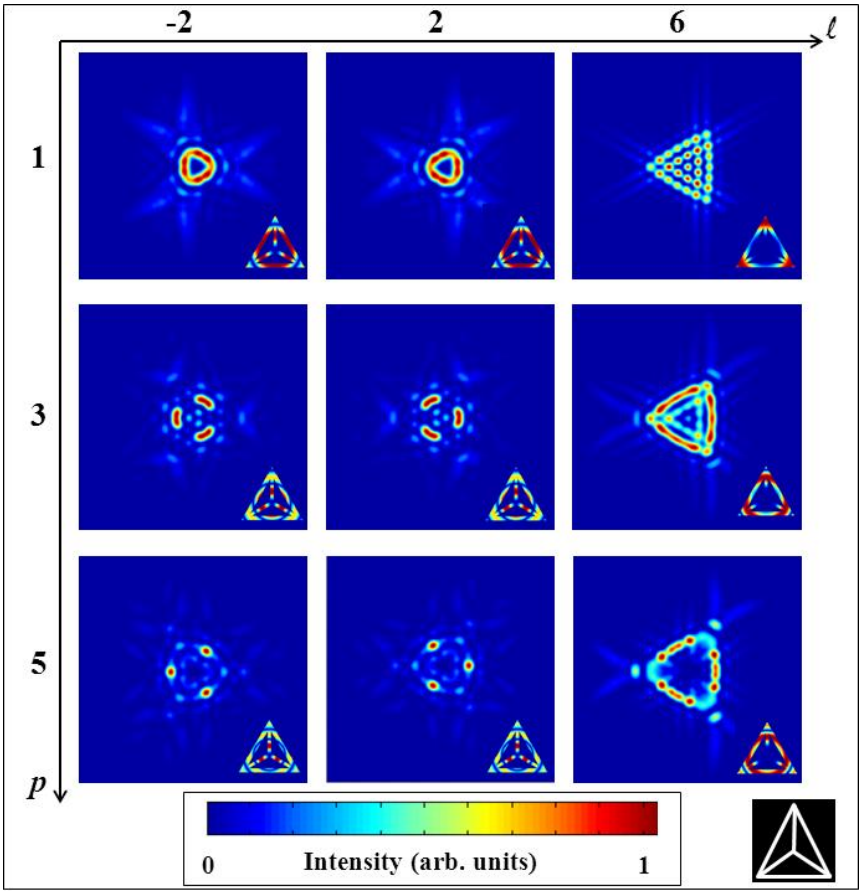

Fig. 3.9. Numerically simulated far-field intensity distributions of OVs with different mode indices diffracted by a triangular slits aperture with radial spokes. The rows and columns define the azimuthal and radial mode indices, respectively. The aperture plane is presented as an inset to every image. The hue colour chart coded for the intensity is highlighted and the scale is the same for all images. The considered triangular slits aperture with radial spokes is also highlighted at the bottom right corner.

Finally, (as discussed in the previous subsection) the incident LG beam must fall in the centre of the considered aperture and the edges of the aperture should be illuminated by the inner border of the incident LG beam, in order to simulate distinct far-field diffraction patterns. These regulations were also kept when a double concentric triangular slits aperture and a triangular slits aperture with radial spokes were used (see Figures 3.8 and 3.9). The ratio of the beam waist of the incident OV to the aperture's size was $\eta = 1$.

3.3 Discussion and Conclusions

In the present chapter, different methods that can be employed to measure the azimuthal mode index ℓ of an OV are presented. The methods are briefly reviewed here. Details of the methods and operation are found in the reference papers.

To date, all of these approaches have neglected the radial index, in spite of the efficient method of the coordinates transformation [136] that has recently been extended to > 50 OAM states and also showed a simultaneously measurement of the radial component [137]. This could be beneficial for increased bandwidth quantum cryptography applications, where the unlimited range of ℓ gives an unbounded state space, and hence a large potential information capacity [25-32].

Since the far-field diffraction from a triangular aperture can give information about the sign and the magnitude of the azimuthal index by counting the number of interference lobes in any side of the resultant truncated optical lattice [48, 49, 148, 149]; the far-field diffraction intensity pattern for LG beams of various mode indices, ℓ and p, is numerically explored to ascertain the performance of a triangular aperture. It is shown that the inclusion of the radial index makes a dramatic difference to the form of the far-field diffraction pattern and no clear rules may be established for determining both mode indices directly from the complex resultant far-field diffraction intensity patterns. However, it should be noted that regardless of the radial mode index, the orientation of the far-field diffraction intensity pattern does depend on the sign of the azimuthal mode index. The far-field diffraction intensity pattern rotates for opposite sign but equal magnitude of the azimuthal index, ℓ.

As a consequence, superposing multiple triangular apertures might appear, at the first glance, an appropriate method to determine both the radial and azimuthal mode indices of an incident LG beam. Furthermore, in order to extract the information of the radial concentric rings present in the LG beam profile when the radial index is considered, a tailored aperture such as a triangular slits aperture with radial spokes is also used. Although, it cannot be excluded that there exists a specifically designed aperture that would deliver a simple rule for the detection of

both ℓ and p, this is not the case for the double concentric triangular slits aperture or a triangular slits aperture with radial spokes. Finally, it is shown that the far-field diffraction intensity pattern is blurred and deformed if the size of the triangular aperture is not commensurate with the beam waist of the incident LG beam.

In the next chapter, our approach to measure the phase singularity of LG beams is explored, based on the diffraction by a triangular aperture that is shown to be one powerful method for the characterization of an OV. The results of this study are within an agreement with the already stated studies and reveal that the form and orientation of the far-field diffraction pattern, i.e. a truncated optical lattice, can be used as a simple and direct way for the determination of ℓ.

CHAPTER 4

Diffraction of an Optical Vortex from a triangular aperture

4.1 Synopsis and Motivation

The study and application of optical vortices (OVs) have gained significant prominence over the last two decades [36, 37]. The determination of the azimuthal index (topological charge), ℓ, of a vortex beam for a range of applications remains an interesting challenge. In this chapter, the diffraction of such beams from a triangular aperture is explored. It is shown that the form of the resultant far-field diffraction pattern is dependent upon both the magnitude and the sign of the azimuthal index, ℓ, and this is valid for both monochromatic and broadband light fields. In the present study, only LG beams with zero radial mode index are considered. For the first time, it is demonstrated that this behaviour is related not only to the azimuthal index, ℓ, but crucially to the Gouy phase component of the incident light beam. In particular, the far-field diffraction patterns for incident LG beams upon a triangular aperture, possessing fractional (non-integer) values of the azimuthal mode index, ℓ, are explored. Such optical fields have a complex vortex structure. This study is able to infer the birth of an OV which occurs at the half-integer value of the azimuthal index, ℓ, and explore its evolution by observations of the far-field diffraction intensity patterns. These results demonstrate the extended versatility of a triangular aperture for the study of OVs [49].

4.2 Introduction

In the current chapter, our approach to measure the phase singularity of LG beams is explored, based on diffraction by a triangular aperture. The results of this work are within agreement with the already stated studies in Chapter 3 [48, 148, 149], and reveal that the orientation of the far-field diffraction pattern from a triangular aperture illuminated by a LG beam, which is a triangular optical lattice, depends crucially upon the sign and the magnitude of the azimuthal mode index, ℓ, which characterizes the incident vortex beam. The azimuthal mode index, ℓ, can be determined in a direct way from the form of the far-field diffraction intensity pattern. It is also shown that the Gouy phase shift causes the 180^{o} rotation of the far-field diffraction intensity pattern as observed by Hickmann et al. when changing the sign of the azimuthal mode index [48].

Recently, there has been significant interest in fractional azimuthal index dislocations embedded within optical beams for studies of entanglement and quantum information processing [108]. For fractional (non-integer) values of the azimuthal index, ℓ, there is a phase discontinuity which gives rise to a line of low intensity. To date, for the generation of an optical beam of half-integer fractional azimuthal index, ℓ, both SPP and off-axis holograms, have been used. Basistiy et al.

made use of a computer generated hologram (CGH), based on a half-integer screw dislocation, to generate a monochromatic fractional LG beam [150]. In 2004, Berry discussed mathematically the evolution of waves with phase singularities of $2\pi\ell$, where ℓ may now be either integer or fractional [74]. For the case of the fractional phase step ($2\pi\ell$) being non-integer, a key theoretical prediction of Berry is the birth of a vortex within the light beam as the fractional phase step reaches and passes a half-integer value. One important characteristic is its instability upon propagation, which was explained by a propagation mechanism that involves an infinite chain of OVs annihilating in pairs during the propagation. The vortex instability is characterized by the OVs breaking into fundamental units in the Fourier plane, where the OVs are spatially separated [74].

Thus, to experimentally investigate such fractional topological charges we need to both generalize the range of fractional phase steps available as well as find a way of studying the evolution. Experimental studies have been performed using interference [151]; however observation of the far-field diffraction pattern from a triangular aperture offers a simple route for exploration of this topic and one can deduce the birth and evolution of a vortex within the light field upon the triangular aperture [49]. This remarkable result is discussed here and is valid for both monochromatic and broadband light fields.

4.3 Theoretical background

In the present section, the theoretical background necessary for discussing the experimental results is given. The basic model involves diffraction of an incident monochromatic OV of wavelength λ and azimuthal index ℓ that is centred on a triangular aperture located at $z = 0$, where z being the propagation axis. In the present study, the propagation was performed in two steps in order to introduce the aperture into the propagation. The same configuration was applied for the numerical calculations previously presented in Chapter 3. The field was first propagated to the aperture plane, where the field distribution was multiplied by the relevant transmission function. This field distribution was then propagated to the far-field. Denoting the transverse coordinates on the aperture plane as $(x, y) = (\rho, \theta)$ in either cartesian or cylindrical polar coordinates, the aperture transmission function is written as $t(x, y) = t(\rho, \theta)$.

4.3.1 Basic equations

For the specific case studied here, $t(x, y)$ describes an equilateral triangular aperture which has unity transmission inside the aperture and zero outside the aperture, and

over the spatial extent of the aperture the slowly varying electric field envelope of the incident OV at $z = 0$ is written as:

$$E^{(\ell)}(x,y,0) = A\cdot(x+i\cdot\mathrm{sgn}(\ell)y)^{|\ell|} \equiv E^{(\ell)}(\rho,\theta,0) = A\cdot\rho^{|\ell|}\cdot e^{i\ell\theta} \tag{4.1}$$

where A measures the field strength, and we hereafter set $A = 1$. In the study at hand, the far-field diffraction patterns were created using a standard $2f$ Fourier transforming optical system based on a lens of focal length f, and the transverse cartesian coordinates were denoted in the focal plane as (ξ, η) (Figure 4.1).

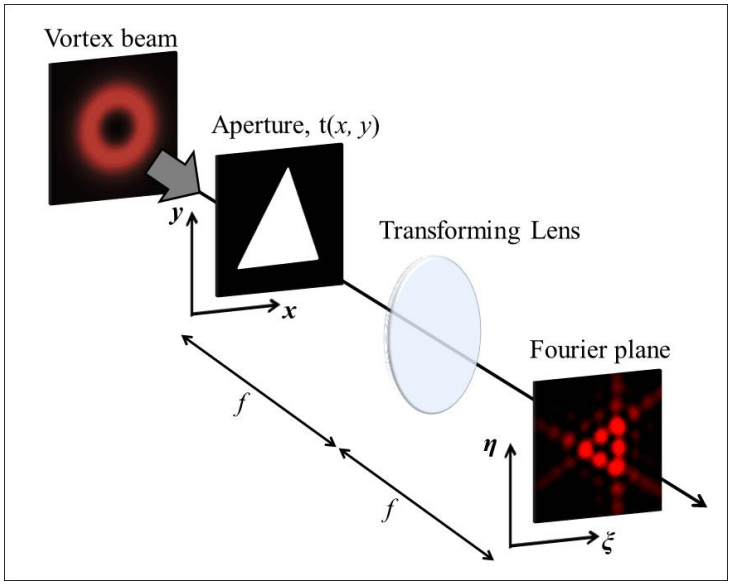

Fig. 4.1. Geometry for the transforming lens. The Fourier plane is always at the image plane of the illuminating source, in this case a triangular aperture illuminated by a vortex beam with $\ell = 2$.

The diffracted field at the distance $z = 2f$ past the aperture is then proportional to the Fourier transform of the product of the OV times the aperture transmission function yielding the following result [48, 152]:

$$E^{(\ell)}(X,Y,z) \propto \int_{-\infty}^{\infty} dx \int_{-\infty}^{\infty} dyt(x,y)(x+i\cdot\mathrm{sgn}(\ell)y)^{|\ell|} e^{-i(Xx+Yy)} \tag{4.2}$$

where $X = 2\pi\xi/\lambda f$ and $Y = 2\pi\eta/\lambda f$ are scaled transverse coordinates in the observation plane. The Equation (2) was numerically solved using the discrete Fourier transform algorithm for the case of a triangular aperture and for a variety of input azimuthal indices, ℓ, both of integer and fractional values. The numerical code was checked against the known analytical solution for the uniformly triangular aperture [152]. In Appendix B, the numerical calculations of the far-field intensity profile $\left|E(X,Y,z)\right|^2$ are presented for a variety of conditions.

4.3.2 Far-field diffraction intensity profile for integer azimuthal indices

As already stated in Chapter 3, Hickman et al. have explored the properties of diffraction of OVs of integer azimuthal indices by a triangular aperture and their use for measuring the azimuthal mode index, ℓ, of an incident LG beam [48]. Some of their findings are repeated here for completeness in presentation. In particular that the far-field diffraction pattern is rotated by 180^o upon reversing the sign of the azimuthal index, while the origin of this rotation is explored which has not been done before.

In Figure 4.2, the numerical simulations of the far-field diffraction intensity profiles are presented for integer azimuthal mode indices, ℓ = 2, 3, 4 in the upper row, and ℓ = -2, -3, -4 in the lower row. One observes what Hickmann et al. refers to as truncated optical lattices [48]. The red-black colour palette is used in the following Figures 4.2 and 4.3 for direct comparison with our experimental results for which the CCD uses this palette. From these numerical simulations one can verify the rule that the number of the interference lobes on any side of the far-field diffraction intensity pattern is equal to the modulus of the azimuthal mode index plus one $(|\ell|+1)$. As can be seen, there are $(|\ell|+1)$ parallel rows or lines of interference lobes making up a given truncated optical lattice. Furthermore, the effect of changing the sign of the azimuthal index, $\ell \to -\ell$, is to rotate the orientation of the truncated optical lattice by 180^o, as can be verified by inspecting the upper and lower rows in Figure 4.2. Thus, the number of interference lobes in the truncated optical lattice and its orientation can be used as a detector of the azimuthal mode index, ℓ, of an incident OV.

It has been previously shown in Chapter 3 that other apertures can be used to detect the modulus of the azimuthal index of an OV. The triangular aperture is even more flexible in that it can reveal both the magnitude and the sign of the azimuthal index using the orientation of the far-field diffraction intensity pattern. This begs the question of the physical origin of the 180^o rotation of the intensity pattern upon reversing the sign of the azimuthal mode index, and here, an answer to this question is provided by demonstrating that the 180^o rotation may be traced to the Gouy phase-shift. This explains the fact that the diffraction of an OV from a polygonal aperture in general depends upon the sign of the azimuthal index, and furthermore exposes that this dependence stems from the Gouy phase-shift, giving new physical insight into this problem, compared to previous studies [49]. An analytical study on the Gouy phase-shift dependence is discussed in Appendix B.

Theoretically, the intensity profile of an OV with ℓ azimuthal index is identical to the $-\ell$ case (see Chapter 2). This makes it impossible to deduce the azimuthal

mode index directly from the intensity profile of the vortex beam. The triangular aperture breaks this symmetry and any mask that is not inversion symmetric would be able to distinguish between the two different signs of ℓ.

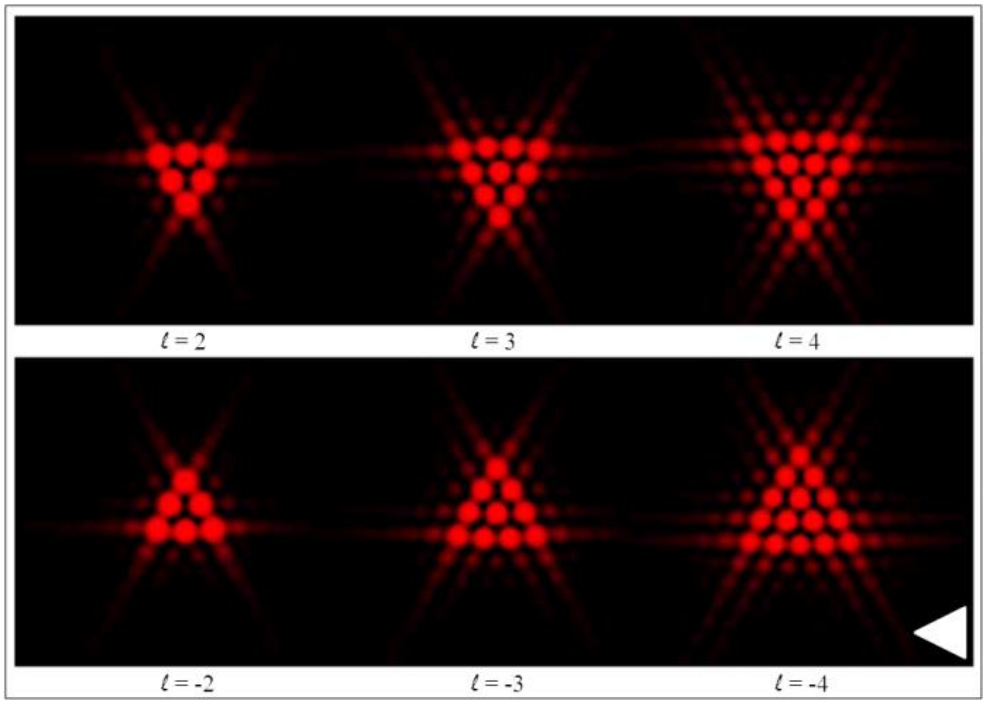

Fig. 4.2. Numerical simulations of the far-field diffraction intensity profile for integer azimuthal mode indices. Where ℓ = 2, 3, 4 in the upper row, and ℓ = -2, -3, -4 in the lower row (from left to right). These far-field diffraction intensity patterns reveal the truncated optical lattice generated by the triangular aperture for incident OVs with integer azimuthal mode indices, and the fact that the far-field diffraction intensity patterns are rotated by 180^{o} under reversal of the sign of the azimuthal index, ℓ. The orientation of the triangular aperture is indicated on the right-bottom corner of the patterns [49].

In conclusion, for example the far-field diffraction intensity pattern produced by a circular aperture is also rotated but this is clearly not observable, and the triangular aperture is likely the simplest aperture that can act as a detector of both the magnitude and sign of the azimuthal mode index. As a final remark, Arlt has previously considered diffraction of an OV by a knife edge as a detector of the absolute handedness of vortex beams [153].

4.3.3 Far-field diffraction intensity profile for fractional azimuthal indices

The second novel topic of the present chapter is now discussed, namely the far-field diffraction intensity patterns obtained for incident OVs possessing fractional

azimuthal mode indices, ℓ. The following Figure 4.3 shows the far-field diffraction intensity patterns obtained for ℓ = 2 to 3 increasing in fractional steps of 0.1. The main feature that should be pointed out is that for azimuthal indices in the range 2 < ℓ < 2.3 the far-field diffraction intensity pattern remains largely unchanged and close to that for ℓ = 2 in that it has ($|\ell|$ + 1) = 3 rows of interference lobes in the truncated optical lattice. In contrast for $\ell \geq$ 2.4 one can see that the far-field diffraction intensity pattern starts to distort on the left side as indicated by the circled region in the far-field diffraction intensity pattern for ℓ = 2.4 in Figure 4.3 below.

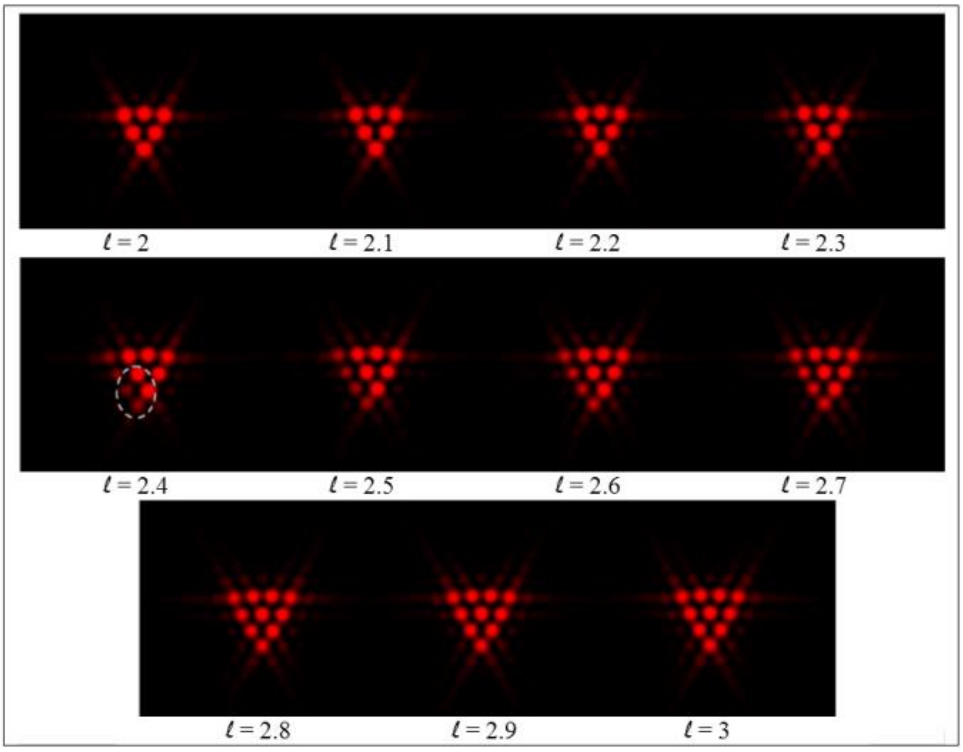

Fig. 4.3. Numerical simulations of the far-field diffraction intensity profile for fractional azimuthal mode indices. Far-field diffraction intensity patterns obtained for ℓ = 2 → 3 increasing in fractional steps of 0.1. These far-field diffraction intensity patterns illustrate the birth of an OV (region indicated by white dashed ellipse) as the azimuthal mode index passes through a half-integer value [49].

This distortion is the beginning of a new row of interference lobes that develops for ℓ < 2.4, and for ℓ = 3 the new row is fully formed and there are ($|\ell|$ + 1) = 4 rows in the truncated optical lattice in the far-field diffraction intensity profile. What the sequence of the intensity profiles in Figure 4.3 reveals is how the birth of an OV is manifested in the truncated optical lattice generated by the triangular aperture, and in particular how the optical lattice deforms from having three to four rows of interference lobes as ℓ = 2 → 3 in this example: there is little distortion of the

truncated optical lattice from its $\ell = 2$ form with 3 rows for $2 < \ell < 2.3$, and the birth of the $\ell = 3$ vortex with its 4 rows is clearly evident for $\ell \geq 2.5$ until it is completed for $\ell = 3$. This sequence of events is perfectly in keeping with the prediction due to Berry [74] that the birth of a vortex occurs at the point where the fractional azimuthal mode index passes a half-integer value. The numerical results are easily generalized to higher azimuthal mode indices, ℓ, with the same general result: as the azimuthal index of the incident OV passes ($|\ell| + 1/2$) the birth of an OV is revealed in the optical lattice produced by diffraction of the OV by the triangular aperture, in keeping with Berry's prediction [74]. To illustrate this, Figure 4.4 provides an animation in which the intensity pattern is shown as the azimuthal mode index is varied from $\ell = 2 \rightarrow 5$, so that several examples can be viewed. To aid viewing the animation pauses at integer values of ℓ so that the reader can view the different examples involving variation between the integer values of the azimuthal index. The animation paints a fascinating picture in which starting from an integer ℓ azimuthal index, the optical lattice has ($|\ell| + 1$) rows which persist until the azimuthal index reaches ($|\ell| + 0.3$) at which point the optical lattice appears to move to the right as a new row of lobes starts to appear on the left. This process culminates when the azimuthal index reaches ($|\ell| + 1$) for which the optical lattice has ($|\ell| + 2$) rows, and this scenario is seen in each example displayed in the animation (Figure 4.4).

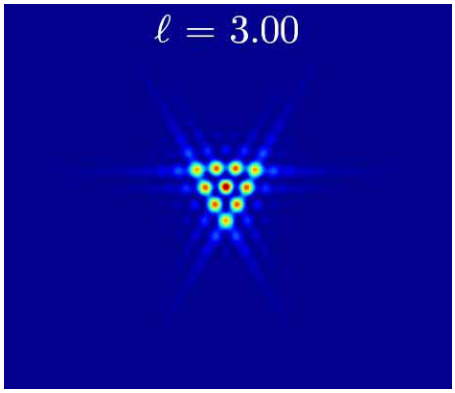

Fig. 4.4. Numerical simulations of the far-field diffraction intensity profile for azimuthal mode indices $\ell = 2 \rightarrow 5$ in steps of 0.01. The figure includes an animation in which the intensity pattern is shown as the azimuthal index is varied from $\ell = 2 \rightarrow 5$ in steps of 0.01, so several examples can be viewed. To aid viewing the animation pauses at integer values of ℓ so that the reader can view the different examples involving between integer values of the azimuthal index [49].

To access the animation, see the published work in Ref. [49]. As a final remark, Jesus-Silva et al. have recently presented a new ingredient to the studies of the birth

of an OV at the Fraunhofer zone, where it was shown that the birth of an OV occurs at a fractional value a, i.e. $a = n + \varepsilon$, where n is an integer number and ε is a small fraction [154].

4.4 Experiments

The above numerical simulations demonstrate that the optical lattice revealed in the intensity profiles generated from the far-field diffraction of an OV by a triangular aperture can provide a visualization of the birth and evolution of an OV as the azimuthal mode index, ℓ, is varied. In this section, the experimental realization of these results will take place for both monochromatic and broadband light fields.

4.4.1 Experimental setup

The experimental setup is shown in the following Figure 4.6. A Helium-Neon (HeNe) laser source (JDS Uniphase, 633nm, P_{max} = 4mW) served for the monochromatic measurements, while for the broadband while light measurements a commercially available supercontinuum (SC) source (Fianium Ltd, 4ps, 10MHz) was used, which delivers radiation across a spectral range of 464-1750nm and a maximum average power of 6W. An IR mirror was used in order to reflect the IR component of the beam, so a bandwidth of 464-700nm was selected (shown in the spectrum displayed in Figure 4.5). The white light beam was additionally sent through a photonic crystal fiber (Thorlabs LMA-25) in order to obtain a beam featuring a homogeneous Gaussian intensity profile.

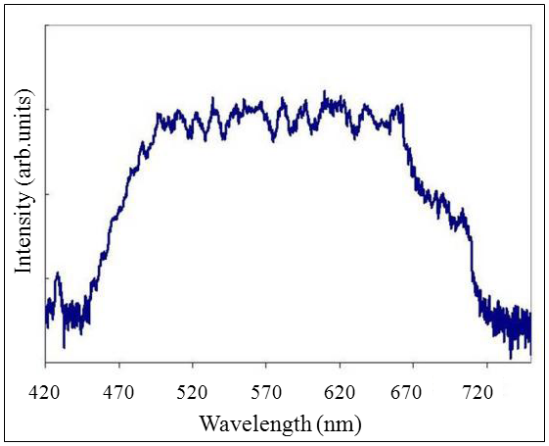

Fig. 4.5. The spectrum of the white light supercontinuum laser source used. The Avaspec 3648 spectrometer was used to take the spectrum in the range from 420nm to 750nm.

A half-waveplate ($\lambda/2$) was used in order to rotate the polarization of the incident light beam to the optimum angle for the SLM so as to maximize the power

diffracted into the first-order. The polarization state was verified by the use of a polarized beam-splitter (PBS) after the $\lambda/2$ plate.

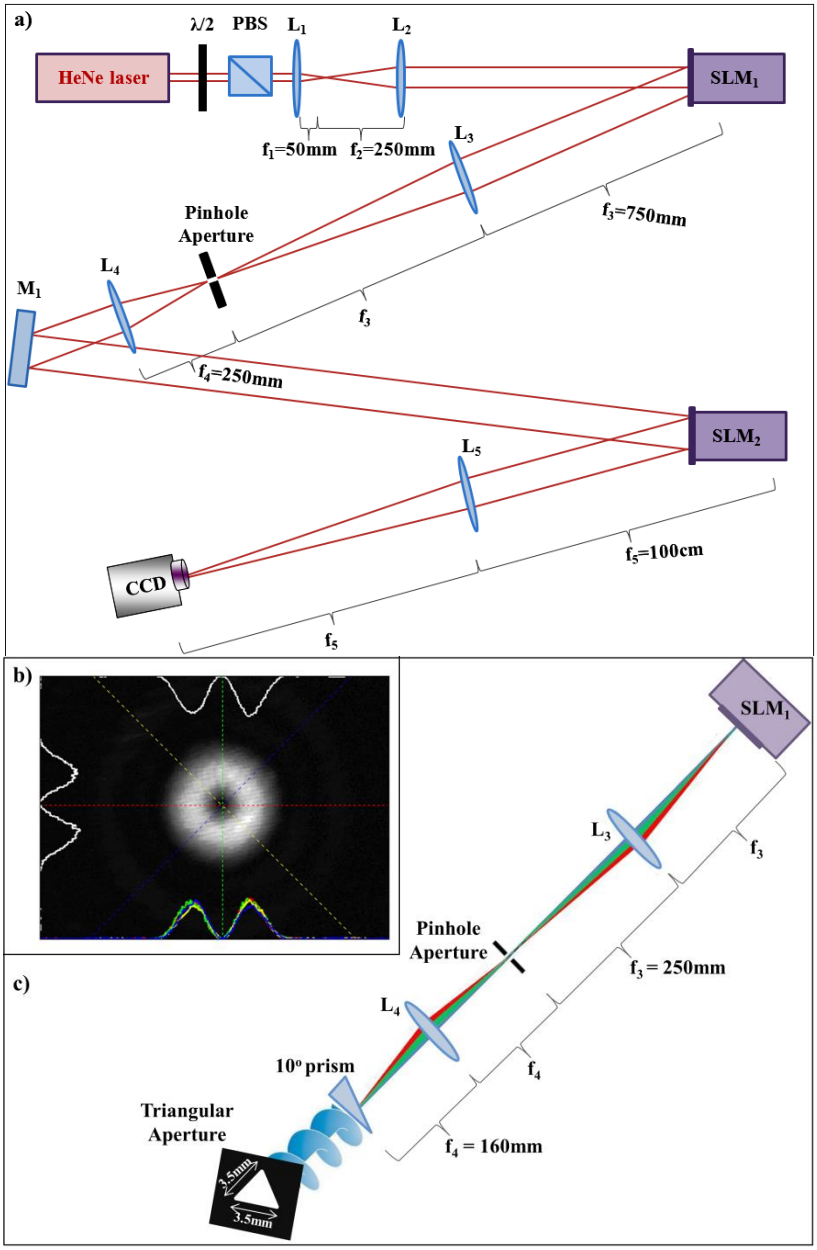

Fig. 4.6. Experimental apparatus. a) Experimental setup for the monochromatic studies: L = lens, SLM = spatial light modulator, M = mirror, CCD = charge coupled device camera, PBS = polarizing beam splitter. Focal widths of lenses: f_1 = 50mm, f_2 = 250mm, f_3 = 750 mm, f_4 = 250mm and f_5 = 100cm. b) The beam profile of the resulting monochromatic LG beam with ℓ = 2. For visualization purposes the LG beam is presented in grayscale. c) For the broadband studies, the dispersion introduced by the SLM is compensated by using an $f_3 - (f_3 + f_4) - f_4$ imaging scheme on a glass prism (10^o) in the back focal plane of L_4, where f_3 = 250mm and f_4 = 160mm. Finally, a static equilateral triangular aperture (each side was 3.5mm) was used instead of the second SLM to avoid issues related to dispersion.

The incident laser beam was subsequently expanded with a telescope in order to slightly overfill the chip of a spatial light modulator (SLM) which was a Holoeye LC-R 2500 with LCoS display area ≈ 1.5cm. The LG beam was created in the far-field of the SLM. As previously presented in Chapter 2, the holograms were of the form of forked diffraction gratings in order to impose a $2\pi\ell$ phase shift on the incident GB, where ℓ is the azimuthal mode index of the LG beam. The SLM was calibrated and wavefront corrected using the optical eigenmode (OEi) technique (see Appendix C) [155, 156]. Moreover, a pair of lenses were used (lenses L_3 and L_4 in the Figure 4.6) so as to filter the first-order diffracted beam carrying the vortex, from the unmodulated zero-order diffracted beam using an aperture located in the back focal plane of lens L_3. For the broadband studies a prism (10^o) (shown in Figure 4.6c) was situated in the back focal plane of the lens L_4. With this configuration, a compensation was achieved, for the dispersion mediated by the linear phase shift imposed onto the incident laser beam by the SLM in order to separate the first-order from the zero-order diffracted beam. The two lenses (L_3 and L_4) are not necessary for the monochromatic studies, but we intended to perform both the monochromatic and the broadband studies on the basis of the same experimental setup. After L_4, the generated LG beam was incident onto a triangular aperture.

The triangular aperture was realized in a different manner for the monochromatic and broadband studies. A second SLM (Hamamatsu X10468-01) was used for the monochromatic studies. This allowed us to flexibly change the geometry of the triangular aperture using dedicated LabVIEW software. In particular, the change in size of the LG beam when changing ℓ was taken into account for the monochromatic studies. In contrast, a static triangular aperture imprinted onto a photographic film was used for the broadband measurements. With this configuration, further dispersion onto the broadband LG beam was avoided, that would require further prism compensation. Each side of the printed equilateral triangular aperture has a length of 3.5mm; the aperture was mounted on an *x-y-z* translation stage that permitted positioning to an accuracy of 5.5μm in order to be carefully aligned with the vortex beam. Finally, lens L_5 was used to create the far-field diffraction pattern in the respective back focal plane where a colour CCD camera (Basler piA640-210gc, pixel size: 7.4 μm x 7.4μm) served to record and save the images of the far-field diffraction patterns onto the hard drive of a computer.

On a final note, the quality of the prism dispersion compensation critically depends on the beam diameter. To account for this, the size of the broadband LG beam was reduced by extracting a central part of the beam using the first SLM. Satisfactory results in terms of dispersion were obtained when reducing the beam diameter by a factor of two. Additionally, since the diffraction angle from the

grating is dependent on wavelength, the white light vortex splits up into its constituent monochromatic vortices [157]. As previously mentioned, to compensate for this dispersion, an $f_3 – (f_3 + f_4) – f_4$ imaging scheme (shown in Figure 4.6c) was used to image the SLM plane onto a prism (10^o) with opposite dispersion to that of the SLM, in order to give a 3.5mm diameter white light LG beam with $\ell = 3$. The period of the diffraction grating was altered until the magnitude of the dispersion introduced by the SLM exactly matched that of the prism.

This compensation scheme worked well for most of the spectrum of the beam, although dispersion in the blue part of the spectrum could not be completely compensated. This can be seen in the far-field diffraction patterns for all the beams, but is most clearly visible in the intensity profile of the LG beam with azimuthal index, $\ell = 6$ in the following Figure 4.7: the blue vortex is shifted slightly to the left and the red vortex slightly to the right.

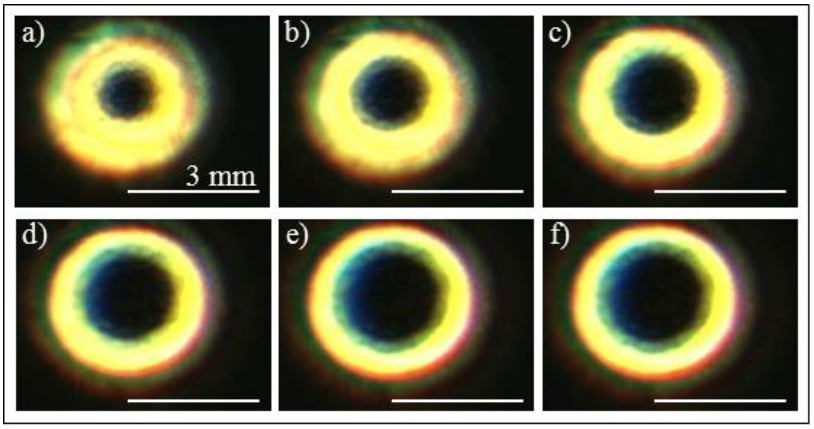

Fig. 4.7. Intensity profiles of white light vortices. White light LG beams with azimuthal index of $\ell = 1$ to 6 increasing in integer step, were all generated and are depicted in a) to f), respectively.

To record distinct images of the monochromatic far-field diffraction intensity patterns, an adjustment was made between the size of the triangular aperture and the size of the LG beam under consideration, since the diameter of the bright ring depends on the azimuthal mode index, ℓ [91, 158]. The far-field diffraction pattern is blurred and deformed if the size of the triangular aperture is not commensurate with the beam waist of the incident LG beam (see Figure 3.6). Moreover, the far-field diffraction intensity pattern is larger for a large thickness while the pattern gets more distinct for a small thickness, when an annular triangular aperture is used [149]. The CCD exposure time was also adjusted in order to best highlight the pattern morphology for each recorded pattern.

4.4.2 Experimental results

4.4.2.1 Far-field diffraction intensity profile for integer azimuthal indices using monochromatic light field

The experimental results obtained for the far-field diffraction intensity patterns for integer azimuthal indices using monochromatic light fields are seen in Figure 4.8. The triangular aperture was the same for $\ell = 2$ and $\ell = 3$ and it was adjusted to a larger size for $\ell = 4$. The experimental results are in excellent agreement with the theoretical prediction shown in Figure 4.2: the number of interference lobes on any side of the diffraction pattern is equal to ($|\ell| + 1$), so there are ($|\ell| + 1$) parallel lines of interference lobes in any of the three directions, and the pattern orientation is flipped when the sign of the azimuthal mode index is changed.

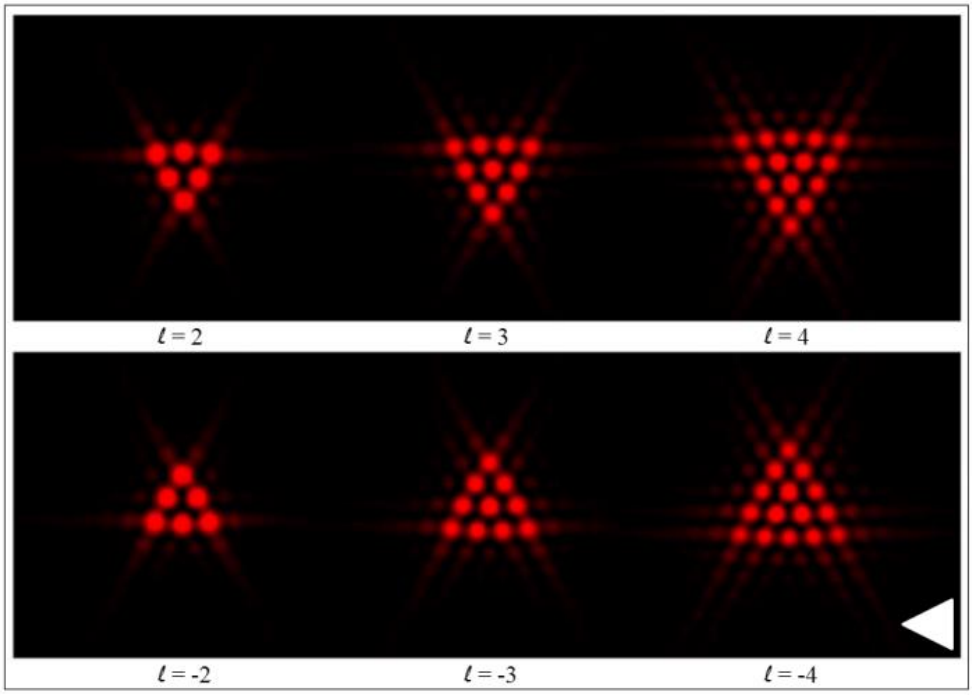

Fig. 4.8. Measured monochromatic far-field diffraction intensity profile for integer azimuthal indices. Where $\ell = 2, 3, 4$ in the upper row, and $\ell = -2, -3, -4$ in the lower row (from left to right). The orientation of the triangular aperture is indicated on the right-bottom corner of the patterns. This should be compared to the theoretical prediction seen in Figure 4.2 [49].

4.4.2.2 Far-field diffraction intensity profile for fractional azimuthal indices using monochromatic light field

The experimental data obtained for the far-field diffraction intensity patterns for fractional azimuthal mode indices using monochromatic light fields are also in an excellent agreement with the theoretical prediction. This is best seen through

comparison of Figures 4.9 and 4.3, where the former shows far-field intensity diffraction patterns recorded with the CCD camera for $\ell = 2 \rightarrow 3$ in fractional steps of 0.1. The experimental data clearly manifest the expected distortion of the far-field diffraction pattern for $\ell > 2.4$ as indicated by the white circled region. A new row arises that develops for $\ell > 2.4$, and finally the $\ell = 3$ far-field diffraction pattern is formed. The experimental data therefore verify Berry's prediction [74] of the birth of a vortex occurring at half-integer values of the fractional azimuthal mode index.

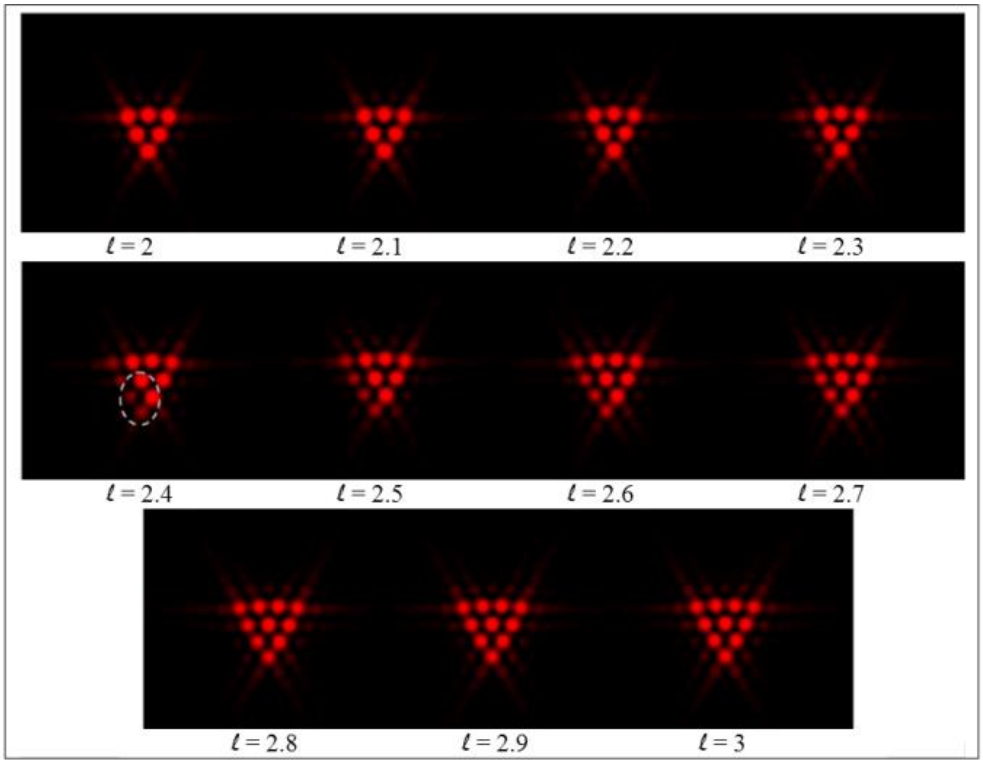

Fig. 4.9. Measured monochromatic far-field diffraction intensity profile for fractional azimuthal indices. Far-field diffraction intensity patterns obtained for $\ell = 2 \rightarrow 3$ in fractional steps of 0.1. The white dashed ellipse indicates the region where the birth of the vortex is observed. Compare to theoretical prediction in Figure 4.3 [48].

4.4.2.3 Far-field diffraction intensity profile for integer azimuthal indices using broadband light field

In the present subsection, a study was performed in order to investigate whether the characteristic far-field diffraction intensity patterns may be observed for broadband 'white light' source. By placing the CCD camera on a translation stage that permitted positioning to an accuracy of 5mm and translation steps of 20cm, we follow the creation of the diffraction pattern as the LG beams with azimuthal indices $\ell = \pm 3, \pm 4$ propagate in a distance z from the triangular aperture. In general, the

Fraunhofer region occurs when the Fresnel number, N_F, is given by: $N_F = \frac{W^2}{z\lambda} \ll 1$, where W is the aperture or slit size (3.5mm), λ is the wavelength of the incident beam (0.6μm) and z is the distance from the aperture [159]. For the case studied here, the Fraunhofer region can be employed if the viewing distance is almost equal to two metres (≈ 2m). In the following Figures 4.10 and 4.11 the recorded diffraction intensity patterns for LG beams with ℓ = ±3, ±4 in different distances from the triangular aperture plane to the detector plane are presented.

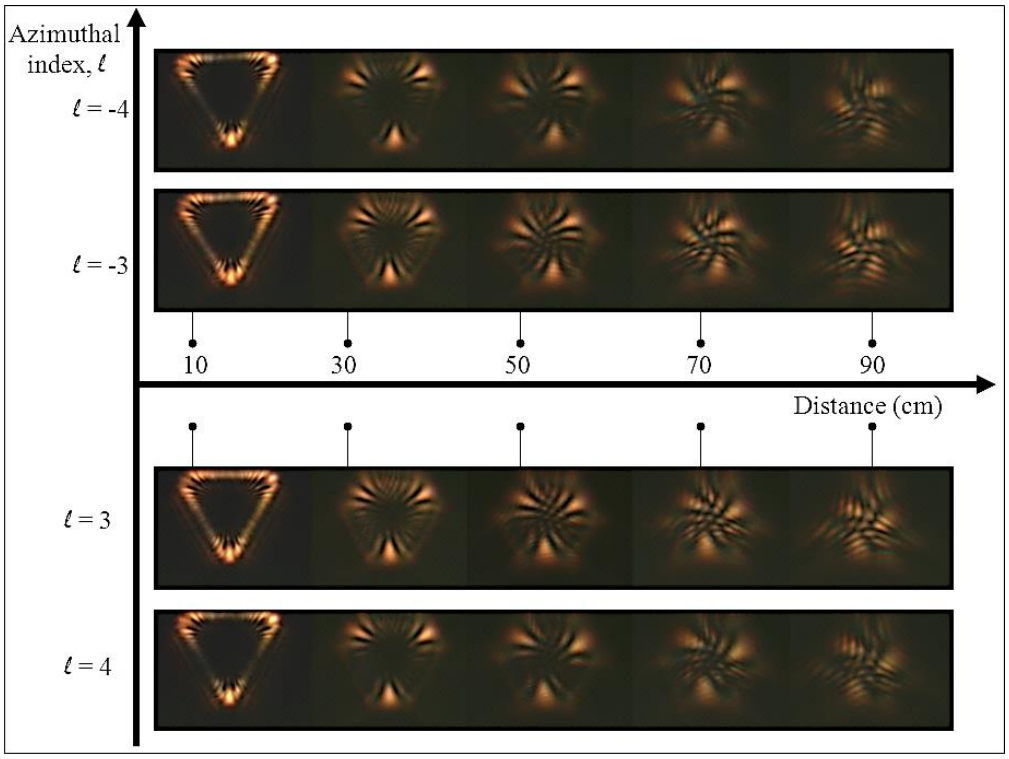

Fig. 4.10. Diffraction intensity patterns in near-field. Diffraction intensity patterns obtained for LG beams with ℓ = ± 3, ± 4 at different distances from the aperture plane. The orientation of the triangular aperture is the same as shown in the following Figure 4.12.

The far-field diffraction pattern is created in a distance close to two metres (≈ 190cm), and the experimental results also verify that the orientation of the far-field diffraction pattern depends on the sign of the azimuthal mode index that characterizes the considered LG beam (Figure 4.11). The CCD exposure time was adjusted in order to best highlight the pattern morphology for each recorded diffraction pattern.

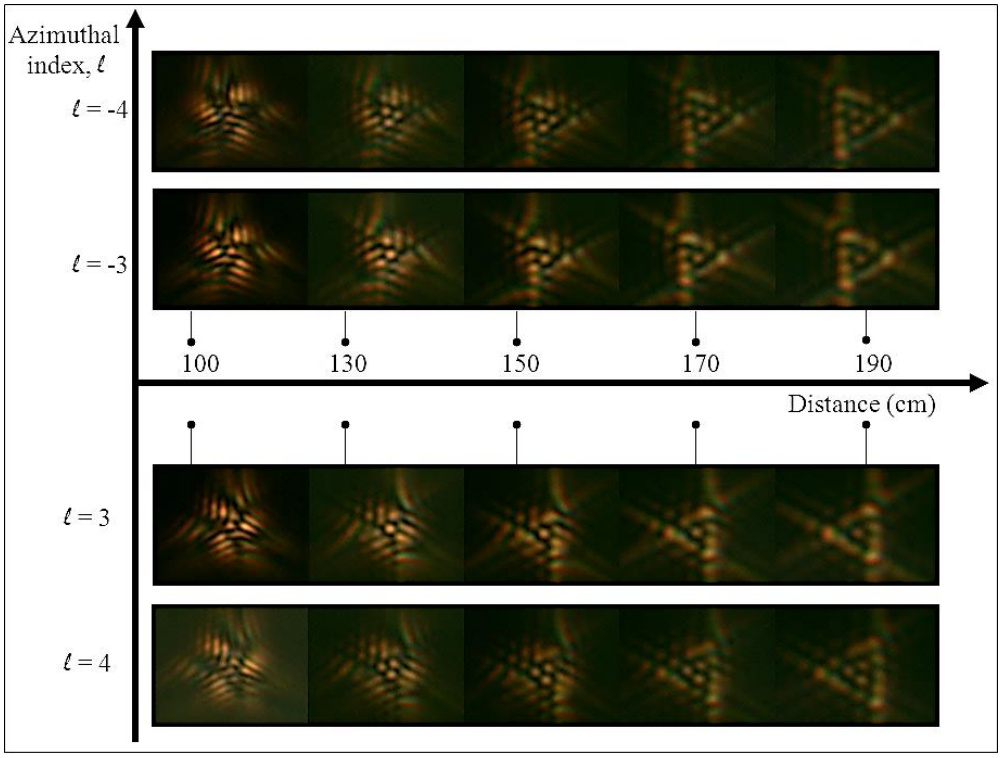

Fig. 4.11. Measured diffraction intensity profiles for different propagation distances close to far-field. Diffraction intensity patterns obtained for $\ell = \pm 3, \pm 4$. The far-field diffraction pattern is created in a distance ≈ 190cm, and the dependence of the orientation of the diffraction pattern on the sign of the azimuthal index can be noticed.

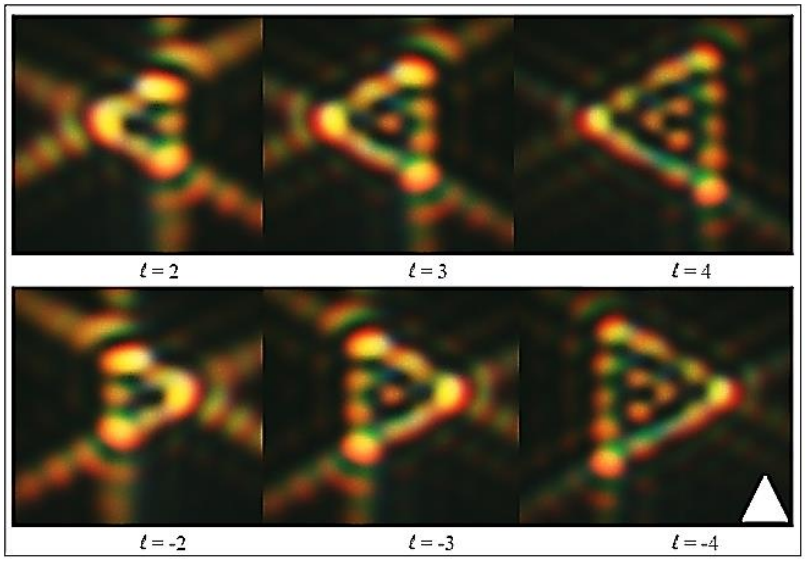

Fig. 4.12. Measured broadband far-field diffraction intensity profile for integer azimuthal mode indices. Where $\ell = 2, 3, 4$ in the upper row, and $\ell = -2, -3, -4$ in the lower row. The orientation of the triangular aperture is indicated on the right-bottom corner of the patterns. This may be compared to the theoretical prediction seen in Figure 4.2.

It was previously demonstrated that the triangular aperture can reveal both the magnitude and the sign of the charge of a vortex beam, and in the current subsection it is also applied to white light OVs with integer values of the azimuthal indices (Figure 4.12). The magnitude of ℓ is directly related to the external interference lobes forming the sides of the far-field diffraction intensity pattern and it is given by $\ell = (N - 1)$, where N is the number of interference lobes on any side of the far-field diffraction intensity pattern. For example, in the case of LG beam with $\ell = 3$, one can observe in the far-field intensity diffraction pattern that the number of lobes in any side of the pattern are $N = 4$, and therefore the azimuthal index is equal to $\ell = 4 - 1 = 3$, which is the case (as seen in Figure 4.12).

4.4.2.4 Far-field diffraction intensity profile for fractional azimuthal indices using broadband light field

In the present subsection, the far-field diffraction of a white light vortex beam with a fractional phase step from a triangular aperture will be studied. To generate these vortex beams, differing fractional topological charge variations were imprinted within an incident GB using a SLM. The same scheme was previously used for the monochromatic measurements. The OAM carried by the LG beam is a continuous function of the azimuthal mode index, ℓ, and it is not restricted to take only integer values. The fractional white light LG beams, due to a phase discontinuity seem to have a missing point at their ring-like intensity structure [160]. This point seems to reassemble for the next integer value of ℓ (Figure 4.13). Here, the diffraction of the fractional white light LG beams from a triangular aperture is presented. The experimental data obtained are also in an excellent agreement with the theoretical prediction. This is best seen through comparison of Figures 4.14 and 4.3.

The far-field diffraction intensity patterns are less distinct compared to the monochromatic data previously shown in the Figures 4.6 and 4.7, which apart from the broadband nature of light, must be attributed to the reduced LG beam size (only half of the SLM display used due to dispersion compensation) and the use of static triangular apertures imprinted onto photographic film which did not allow the adjustment of the considered aperture size to the beam waist of the incident LG beam as flexibly as in the monochromatic studies.

Nevertheless, the birth of the vortex can be clearly identified in the broadband data as well and all the characteristic effects can be observed, that is a new row of interference lobes arises for $\ell > 2.4$. The discrepancy between the broadband and monochromatic data in terms of pattern orientation and region of vortex birth is explained in the final section of this chapter. On a final note, the same diffraction based method was recently used to measure ultra-broadband OV beams and it was

shown that the topological charge is constant, and can be consistently measured across a wide range of colours [161].

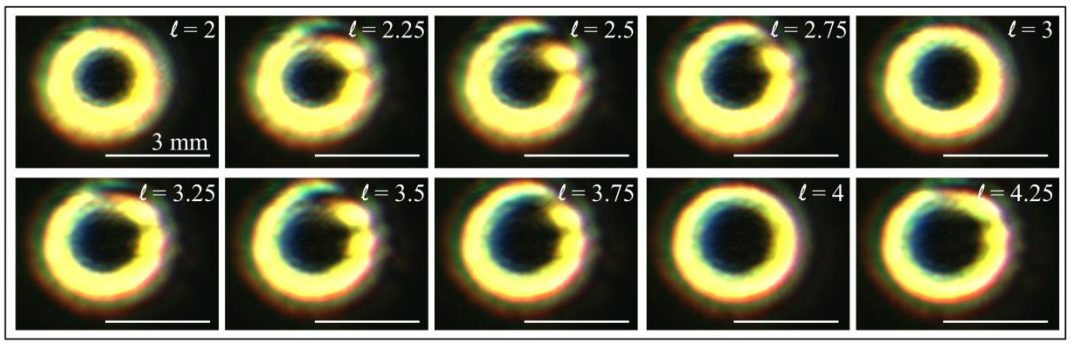

Fig. 4.13. Intensity profile of fractional white light OVs. Fractional white light LG beams with azimuthal index $\ell = 2 \rightarrow 4.25$ with a fractional step of 0.25 are presented.

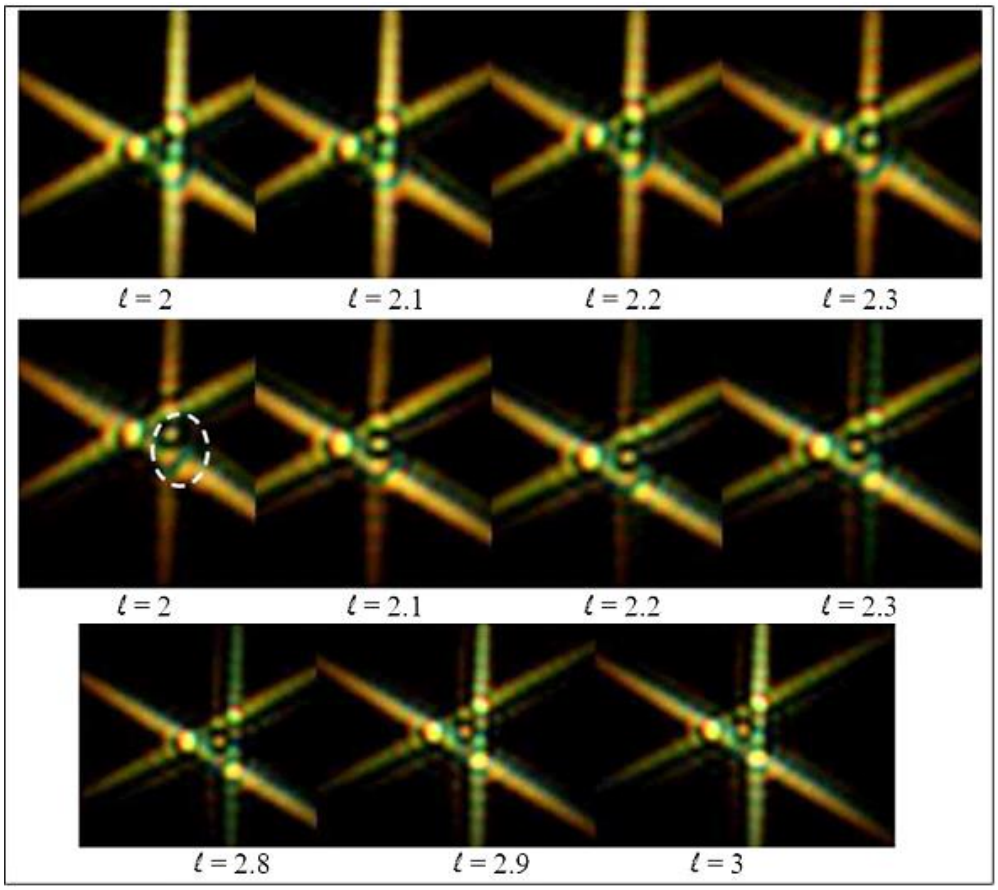

Fig. 4.14. Measured broadband far-field diffraction intensity profile for fractional azimuthal indices. Far-field diffraction intensity patterns obtained for $\ell = 2 \rightarrow 3$ in fractional steps of 0.1. The white dashed ellipse indicates the region where the birth of the vortex is observed [49]. The orientation of the triangular aperture is the same as previously shown in Figure 4.12.

4.4.3 What decides the side of the optical lattice that distorts and finally leads to the birth of an optical vortex?

In the present section, an interesting question is addressed that is raised by our simulations and experiments: what decides the side of the optical lattice that distorts and finally leads to the creation of the new row following the birth of an OV? In particular, for the case of integer azimuthal indices, the generated optical lattice is found to depend only on the orientation of the triangular aperture, and does not depend on any rotation of the OV around its axis, thus amounting to a trivial homogeneous phase-shift of the field. This is, however, not the case for fractional azimuthal mode indices for which the phase of the OV, $\exp(-i\ell\varphi)$, exhibits a discontinuity at a definite azimuthal angle that can be physically identified, so that the relative orientation of the triangular aperture and azimuthal position comes into play and indeed dictates the spatial direction in which the optical lattice distorts and the lattice symmetry is broken. Thus, experimentally it should be the case that if the triangular aperture is rotated keeping the azimuthal mode index and orientation of the OV fixed, then the orientation of the optical lattice should also rotate. Moreover, the optical lattice should melt and reassemble at a different spatial location.

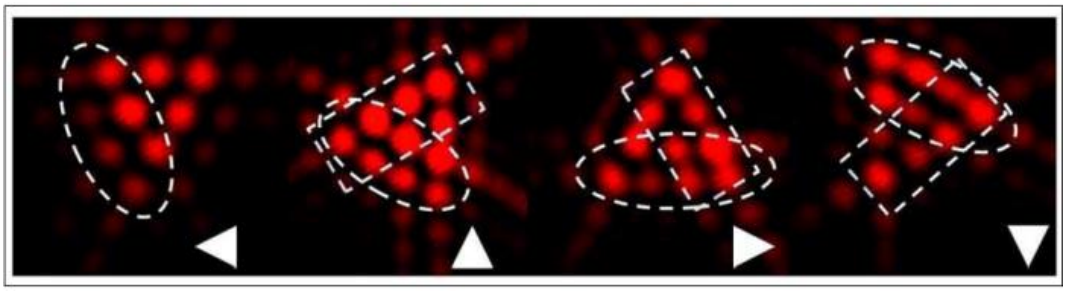

Fig. 4.15. Spatial dependency of the birth of the vortex on the orientation of the triangular aperture. The figure shows measured monochromatic far-field diffraction intensity patterns obtained for ℓ = 2.6 and different orientations of the triangular aperture as indicated on the right-bottom corner of the patterns. The white dashed rectangles indicate where the birth of the vortex should be observed according to the rotation of the diffraction pattern. The white dashed ellipse shows the spatial location where the birth of the vortex is actually observed [49].

This is indeed observed as it is demonstrated in Figure 4.15 on the basis of experimentally recorded monochromatic far-field diffraction intensity patterns. As the triangular aperture is rotated in steps of 90^o so does the far-field diffraction intensity pattern. However, the region of the vortex birth does not follow the rotation as indicated by the white dashed rectangles indicating the expected regions and the white dashed ellipses indicating the actual regions where the birth of the vortex is

observed. This observation also explains why the broadband data would not coincide with the monochromatic data if rotated accordingly.

4.5 Discussion and Conclusions

In the current chapter, the diffraction of OVs with various azimuthal mode indices from a triangular aperture was explored. The results of this study are within an agreement with the previously discussed studies [48] and reveal that the orientation of the diffraction intensity pattern in far-field from a triangular aperture illuminated by a LG beam, which is a triangular lattice, depends crucially upon the sign and the magnitude of the azimuthal index ℓ which characterizes the incident vortex beam. The number of the interference lobes on any side of the far-field intensity pattern is equal to the modulus of the azimuthal index plus one $(|\ell|+1)$. As can be seen, there are $(|\ell|+1)$ parallel rows or lines of interference lobes making up a given truncated optical lattice. Furthermore, the effect of changing the sign of the azimuthal index $\ell \rightarrow -\ell$ is to rotate the orientation of the truncated optical lattice by 180^{o} and in the Appendix B, it is demonstrated that the 180^{o} rotation may be traced to the Gouy phase-shift. This analysis explains the fact that the diffraction of an OV from a polygonal aperture in general depends upon the sign of the azimuthal index, and furthermore exposes that this dependence stems from the Gouy phase-shift, giving new insight into this problem, compared to previous studies [49].

Thus, the number of lobes in the truncated optical lattice and its orientation can be used as a detector of the azimuthal index ℓ of an incident OV. The behaviour of the far-field diffraction pattern is shown to be dependent upon the Gouy phase of the light field for the first time. For fractional (non-integer) values of the azimuthal index, ℓ, there is a phase discontinuity which gives rise to a line of low intensity. The evolution and form of the far-field diffraction pattern from the triangular aperture for incident fields of fractional values of azimuthal index has also been explored. Our experimental data were in agreement with the key theoretical prediction of Berry, that the birth of a vortex within the beam takes place as the fractional phase step reaches and passes a half-integer value [74]. Our experimental data show that the methodology is applicable to both monochromatic and broadband light sources.

Theoretically, the intensity profile of an OV with ℓ azimuthal index is identical to the $-\ell$ case. This makes it impossible to deduce the azimuthal index from the intensity profile of the beam. The triangular aperture breaks this symmetry and any mask that is not inversion symmetric would be able to distinguish between the two different signs of ℓ. In conclusion, for example the far-field diffraction intensity pattern produced by a circular aperture is also rotated but this is clearly not

observable, and the triangular aperture is likely the simplest aperture that can act as a detector of the magnitude and sign of the azimuthal index.

In the current study, the values of ℓ are limited by our present setup to no more than 7 or less than -7. For example, the annular intensity profile may go out of range of the CCD chip when $|\ell|$ is larger. Actually, the values of the azimuthal mode index, ℓ, can go up to higher values while one can still determine the ℓ, by simply counting the number of interference lobes in the far-field diffraction intensity pattern, if for example a larger CCD could be used or a different telescope with a higher magnification. As a final note, the size of the triangular aperture should be chosen to be of the order of the waist size of the LG beam in order to collect maximum intensity from the ring-like intensity profile of the considered LG beam and observe a distinct far-field diffraction pattern.

This method allowed photons to be tested for one particular OAM state, but recently it was used for the measurement of the OAM at photon level via the spatial probability distribution, where it was also shown that by changing the aperture size it is possible to discriminate OAM state superpositions [162].

However our approach, discussed here, has only been considered for LG beams of zero radial index, *p*. Some prior results in Chapter 3 presented the resultant complex far-field diffraction patterns when both mode indices are considered. Moreover, in the next Chapter 5, the far-field diffraction intensity pattern for LG beams of various mode indices ℓ and *p* will be numerically and experimentally explored to ascertain the performance of a triangular aperture.

---

*A significant portion of this chapter was reprinted with permission from [A. Mourka et al, Opt. Express **19**, 5760-5771 (2011)]. Copyright 2011 Optical Society of America.*

A. Mourka designed the considered triangular apertures and performed the experimental work. Dr. J. Baumgartl assisted with the setup, calibration and wavefront correction of the used SLMs. Prof. E. M. Wright and C. Shanor performed the theoretical study. A. Mourka also contributed to the writing of the manuscript.

CHAPTER 5

Towards the complete modal characterization of LG beams: Azimuthal and Radial indices

5.1 Synopsis and Motivation

The determination of the azimuthal mode index, ℓ, of a LG light field is of a key importance in a number of fields. Recently, a wide range of diffractive structures, such as an array of pinholes [129-133], triangular apertures [48, 49, 148, 149], slits [127, 146] and holograms [134, 135], have shown much promise in this regard, as previously presented in Chapter 3. However, to date, the far-field diffraction pattern of the system has only been considered when irradiated with LG light fields of zero radial index *p*. Thus, all these experimentally realized approaches measure only one degree of freedom of LG beams, neglecting the radial component or *p* index, so are therefore not applicable for *a priori* unknown beams. Chapter 3 set the scene for an examination of the potential of the simultaneous determination of both mode indices in any measurement. Additionally, it is unclear which is the optimal aperture and scheme needed to determine simultaneously the azimuthal and radial mode indices (ℓ and *p*), nor the extent with which such an aperture can tolerate deviations in beam parameters. As a consequence, in the present chapter the far-field diffraction intensity patterns for LG beams of various mode indices, ℓ and *p*, are numerically and experimentally explored to ascertain the performance of a triangular aperture. As seen in prior results in Chapter 3, the inclusion of the radial index *p* makes a dramatic difference to the form of the far-field diffraction pattern and is an important consideration in using a triangular aperture for measuring the azimuthal index ℓ, but no clear rules may be established for determining both mode indices directly from the complicated far-field diffraction patterns. Therefore, a novel method is developed using the principal component analysis (PCA) algorithm [50]. This method is used for the simultaneous determination of both the azimuthal and radial mode indices (ℓ and *p*) of both pure and mixed (superposed) LG light fields. It is shown that the shape of the diffracting element used to measure the mode indices is in fact of little importance and the crucial step is 'training' any diffracting optical system and transforming the observed pattern into uncorrelated variables (principal components). Modest fluctuations in the beam parameters, such as beam waist and alignment variations, can be tolerated in this scheme. Additionally, preliminary results demonstrate reliable decomposition of superpositions of LG beams, yielding the intensities and relative phases of each constituent mode. These results demonstrate the complete characterization of LG beams, including both independent degrees of freedom corresponding to the radial and azimuthal mode indices. The approach is generic and may be extended to other families of light fields (e.g. Bessel or Hermite-Gaussian (HG) beams) as will be discussed in the next chapter, and represents a powerful method for characterizing the optical multi-dimensional Hilbert space [61].

5.2 Introduction

In virtually all experimental realisations of LG beams, we are presented with light fields that are appropriately described as superpositions of LG modes, each of the same ℓ index but of different p index [163]. Thus, it is crucial to include the influence of both mode indices on the diffraction pattern of any aperture or slit and further ascertain whether by using any diffracting aperture we are able to determine both the azimuthal and radial mode indices simultaneously. Additionally, the radial index itself adds a major new degree of freedom that may be exploited for quantum communication in its own right. The need for both azimuthal and radial mode analysis is reinforced by recent theoretical work on the angular and radial mode analysis of optical beams that deals with decomposition of beam into LG components by using a Mach-Zehnder scheme [164]. However, this interferometric method does not measure the relative phase between the modes and needs multiple exposures.

In the current chapter, a powerful approach to simultaneously measure the radial and azimuthal mode indices of LG beams, using the algorithm of PCA, is presented [53]. Principal component analysis (PCA) refers to an orthogonal transformation that converts multiple measures into a set of linearly independent and uncorrelated variables called principal components (PCs) or 'eigenfaces'. The first principal component (PC1) accounts for the largest variance within the set of measures and each subsequent component reflects the next highest variance whilst ensuring no correlation (orthogonality) to the preceding PCA components. Whilst established for over one hundred years [50] and widely applied in various areas (e.g. data analysis for spectroscopy, face recognition, data compression), this method has never been considered nor used in the case of diffracting theory. Furthermore, by employing the PCA approach, modest fluctuations in beam parameters such as beam waist size and alignment variations can be tolerated.

To begin with, a triple concentric triangular slits aperture is illuminated by LG light fields with non-zero azimuthal and radial mode indices. This is an extension of the single triangular aperture already considered in Chapter 4, which is presently one of the most powerful techniques for determining the azimuthal index by simply counting the number of interference lobes in the far-field diffraction intensity pattern. Superposing multiple such apertures might appear, at the first glance, an appropriate method to determine both the radial and azimuthal mode indices of an incident vortex field (as previously discussed in Chapter 3). Our aim is to explore how the form of the far-field diffraction pattern is altered by the radial index, p, as well as to examine the potential of determining both ℓ and p mode indices simultaneously in any measurement. Furthermore, open questions include the

optimal aperture to use and the robustness of the determination of mode indices in the presence of any misalignment.

The generic PCA approach implemented here addresses all these issues. In the last part of this chapter, the applicability of the PCA method is considered for the modal characterization of the complex superposition of LG beams, i.e. the detected beams are not pure modes but the result of a general linear superposition of these modes. Here, the PCA method is generalized by using an optical eigenmode (OEi) [155, 156] decomposition together with a Gerchberg-Saxton (GS) algorithm [165]. It is shown that our extended PCA method is able to measure the complex amplitudes of the different LG components in a limited superposition of LG beams, key for practical applications. In the next section, the theoretical background necessary for discussing the experimental results is given.

5.3 Numerical implementation

For the numerical implementation of the far-field diffraction pattern, the scalar field of each LG beam is discretized over a square grid and apertured by the triple concentric triangular slits aperture, in the same way as it was numerically simulated in Chapter 3, where the Matlab code presented in Appendix A was used. The choice of the aperture is based on the properties of the triangular aperture to distinguish between different azimuthal mode indices [48, 49] and the need to extract the information of the radial concentric rings present in the LG beam profile when the radial index is considered.

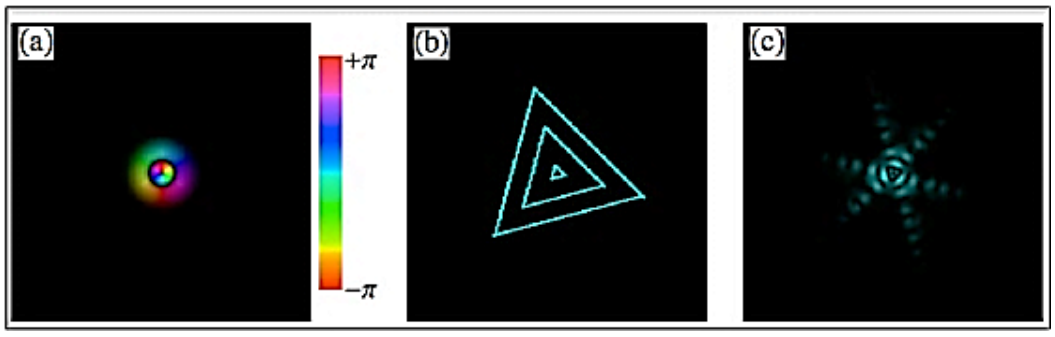

Fig. 5.1. Numerical simulation of the far-field diffraction of an LG beam from a triple concentric triangular slits aperture. (a) Cross-section of the LG beam with mode indices, $\ell = 1$ and $p = 1$, (b) the triple concentric triangular slits aperture, and (c) far-field diffraction intensity pattern of the LG beam represented in part (a) diffracting of the triple concentric triangular slits aperture represented in part (b). The phase is represented by the hue.

Figure 5.1 shows an example LG beam (with ℓ = 1, p = 1), the triple concentric triangular slits aperture and the associated far-field diffraction intensity pattern and Figure 5.2 depicts the far-field diffraction intensity patterns that were observed for different LG beams. In general, these far-field diffraction intensity patterns show a complex interference interaction between the beam waist, the size and width of the triple concentric triangular slits aperture, the number of concentric triangular slits apertures, and the azimuthal and radial mode indices of the incident LG beams (see Chapter 3). From Figure 5.2, one may deduce that the far-field diffraction patterns from the triple concentric triangular slits aperture do not offer any simple way to determine the ℓ and p beam mode indices. Nevertheless, it should be noted that regardless of the radial index, the pattern orientation does depend on the sign of the azimuthal index. The far-field intensity diffraction pattern rotates for opposite sign but same magnitude of the azimuthal index ℓ.

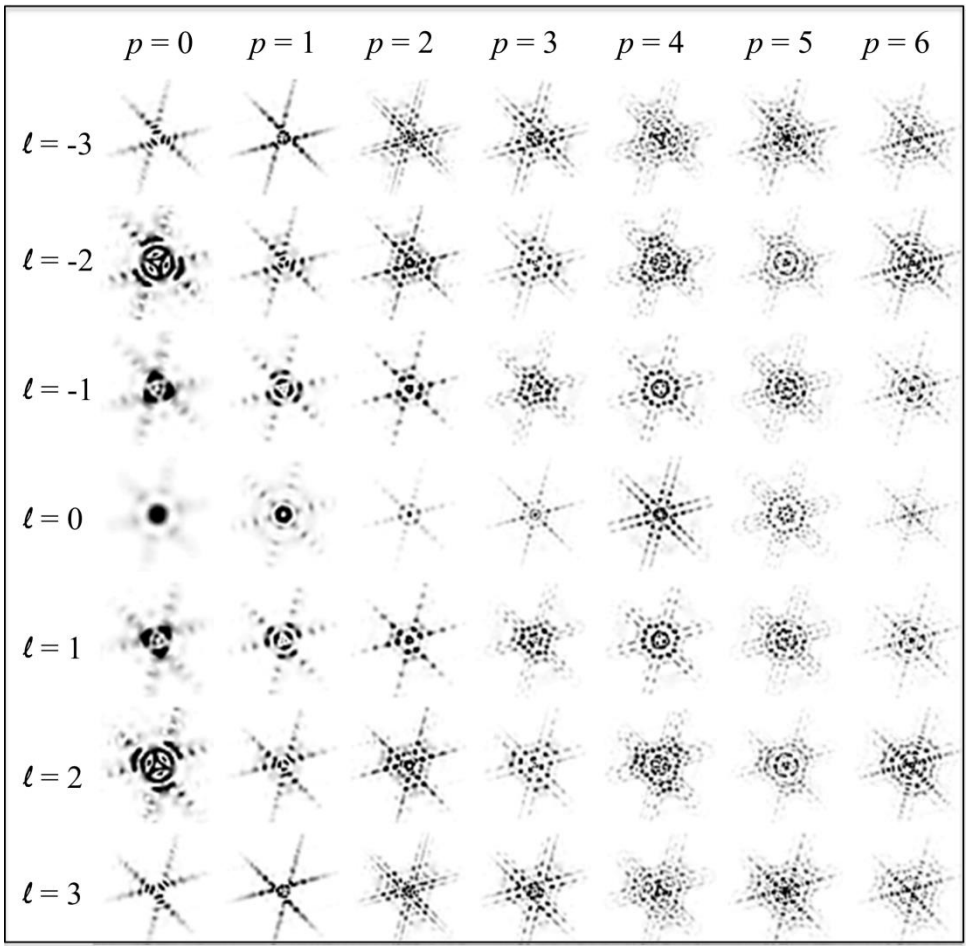

Fig. 5.2. Numerical simulations of the far-field diffraction intensity patterns of LG beams with different radial and azimuthal mode indices after diffraction from a triple concentric triangular slits aperture. The columns and rows define the azimuthal and radial number, respectively. The colour scale is inverted for clarity, where black and white accordingly define the higher and lower intensity.

Although, it cannot be excluded that there exists a specifically designed aperture that would deliver a simple rule for the detection of both ℓ and p, this is not the case for the triple concentric triangular slits aperture. Importantly, the deduction of a complicated ℓ and p retrieval rule can be replaced by considering a face-recognition algorithm readily employed in biometric identification [53].

5.4 Principal component analysis (PCA) algorithm

The main goal of the PCA algorithm is to reduce the dimensionality of the data set while accounting for as much of the original variation as possible present in the data set [51]. Hence, the data set is rotated according to the PCA algorithm, around its centre in order to find the orientation that delivers the largest variation along an axis (Figure 5.3). This axis corresponds to the first principal component (PC1).

In the second step, the PCA algorithm further rotates the data set, leaving PC1 invariant, in order to find a second axis, perpendicular to PC1, showing the second largest variation. This corresponds to the second principal component (PC2). This process can be repeated until all major variance of the dataset are taken into account. The number of the PCs is less than or equal to the number of the original observed data.

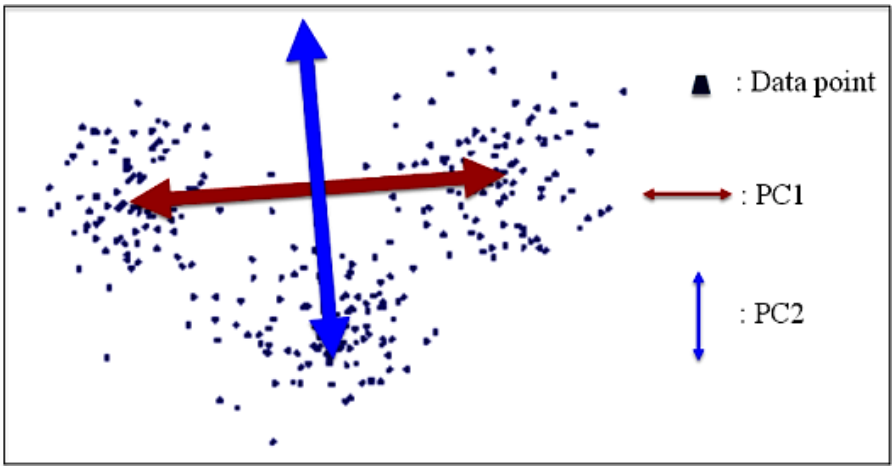

Fig. 5.3. The PCA algorithm. The data set is rotated according to the PCA algorithm, around its centre in order to find the orientation that delivers the largest variation along an axis. This axis corresponds to the first principal component (PC1). In the second step, the PCA algorithm further rotates the data set, leaving PC1 invariant, in order to find a second axis, perpendicular to PC1, showing the second largest variation. This corresponds to the second principal component (PC2). This process can be repeated until all major variance of the dataset are taken into account.

Furthermore, this orthogonal transformation is defined in such a way that the first principal component (PC1) has the largest possible variance within the set of

measures and each subsequent PC reflects the next highest variance possible under the constraint that it be orthogonal to the components considered. The resultant PCs, or 'eigenfaces' (see Figure 1.4), are ordered such that few of them can be used in order to account for most of the variation in all the original data set. Thus, a simpler basis can be provided for the multivariate analysis of the data [166]. Whilst PCA has been established for over one hundred years (a technique dating back to 1901) [50] and widely applied in various areas, e.g. face recognition [51, 52, 167] and cancer detection [168], for the first time, this method is used here in the case of diffraction theory and the analysis of the transverse state of a light field.

5.4.1 Detection through 'eigenface' classification

In the present study, the PCA approach is used in order to determine the largest variations between the different far-field diffraction intensity patterns from the triple concentric triangular slits aperture. The first step of the procedure corresponds to creating a database of all the possible beams that need to be detected. After subtraction of the common mean intensity, the covariance matrix of these intensity patterns is calculated. Its eigenvector with the largest eigenvalue is termed the first 'eigenface' or principal component (PC), corresponding to the largest variability of the LG beam training set. In the same way, one can introduce the second 'eigenface' as the image corresponding to the second largest eigenvalue of the covariance matrix and so on.

From mathematical point of view, after observing a set of N sample images corresponding to the different illuminations, every rectangular image, $\boldsymbol{I}_i$, can then be represented as a column image vector, A_{ij}.

$$\Psi_j = \frac{1}{N}\sum_{i=1}^{N} A_{ij} \tag{5.1}$$

where $i = 1, 2, \ldots N$ is the index number of each image. Each rectangular image, $\boldsymbol{I}_i$, has a size of $(W*L)$, where W, L correspond to the width and length of the rectangular image in pixel number, respectively. Hence, the array containing all the column image vectors, A_{ij}, will have dimensions of (N x $W*L$). New feature vectors can be defined by subtracting the mean image vector, such as:

$$\Phi_{ij} = A_{ij} - \Psi_j \tag{5.2}$$

So next, the covariance matrix, C, can be computed by the following tensor product:

$$C_{jk} = \sum_{i=1}^{N} \Phi_{ij}\Phi_{ik} \qquad (W*L \text{ x } W*L) \text{ matrix} \tag{5.3}$$

The eigenvectors u_j of the covariance matrix are then calculated by solving the eigenvalue equation:

$$\sum_{j=1}^{W*L} C_{ij} u_{jk} = K_k u_{jk} \tag{5.4}$$

where K_k are the eigenvalues. The eigenvectors u_{jk} are reordered by the corresponding eigenvalues. The resultant eigenvectors are referred to as principal components (PCs), or 'eigenfaces', as it was previously discussed, and build the analysis space with them as the axes (Figure 5.4a). To project a new image, U_j, into the analysis space, we need to first centre the image by subtracting the mean of the training data, Ψ_j. Then, a simple projection operation follows:

$$\omega_k = \sum_{j=1}^{W*L} \left(U_j - \Psi_j \right) u_{jk} \tag{5.5}$$

The vector ω can be seen as the new encoding of the image in the analysis space.

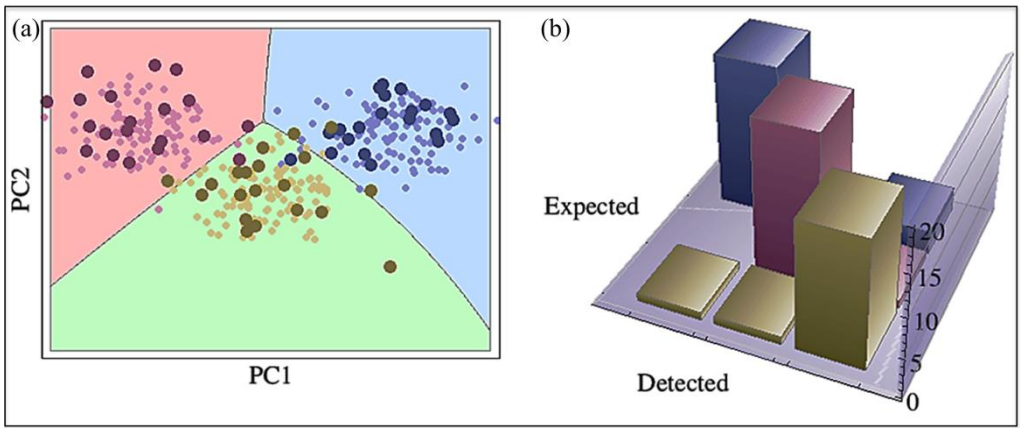

Fig. 5.4. The PCA detection method. This figure includes an animation in which the PCA algorithm is presented. (a) To aid viewing the animation pauses after the 'training' step (cluster identification) and the classification of the 'unknown' data, so that the reader can view the construction of the 3D chart of the confusion matrix which depicts the efficiency of this method in (b). To access the animation, see the published work in Ref. [61].

The measured beams are then projected onto the new coordinate system defined by the 'eigenfaces', so the first and the subsequent principal components (PCs) representation of the measure will be delivered. The LG beams having the same ℓ and p form tight clusters (Figure 5.4a) and the different LG beams can be depicted by using a different colour based on a chosen colour scheme.

Finally, a classification algorithm of the nearest neighbour is applied in order to classify the 'unknown' data [169]. Under this scheme, an 'unknown' LG beam is recognized (classified) by assigning to it the values (for ℓ and p mode indices) of the closest LG beam in the 'training set', where distances are measured in the image space. If all of the images (far-field diffraction intensity patterns) are normalized to have zero mean and unit variance, then this procedure is equivalent to choosing the

LG beam in the 'training set' that best correlates with the 'unknown' LG beam. However, other methods such as Mahalanobis distance can be also applied [170]. Figure 5.4b shows the 3D chart of the confusion matrix, displaying the efficiency of this method, i.e. whether all the 'unknown' beam modes have been correctly identified as the expected beam modes. The ideal confusion matrix is the identity matrix. Finally, if the images in the 'training set' are gathered under small vibrations of the optical system, the points in the projected space will not be well clustered. Nevertheless, correct identification still results if the 'training set' samples the possible illumination or vibration conditions being in the data set.

5.5 Experiments

Our approach is to consider the intensity profile of an LG beam after diffraction of a triple concentric triangular slits aperture and a glass diffuser (random aperture). The far-field diffraction intensity patterns are in general complicated and contain information for the different mode indices for the considered LG beam modes. First, the 'training' step is applied in which the response of the optical diffracting system is measured for every single LG beam considered. Then, the second step followed where the classification algorithm is used that corresponds to the actual identification or measurement of an 'unknown' LG beam, delivering simultaneously its radial and azimuthal mode indices. In this section, the experimental results will be presented. Additionally, beam superpositions of LG beams can be experimentally decomposed, delivering the intensity and relative phases of each constituent mode.

5.5.1 Experimental setup

The experimental apparatus (see Figure 5.5) uses a Helium-Neon (HeNe) laser source (JDS Uniphase, λ = 633nm, P_{max} = 4mW). A half-waveplate was used in order to rotate the polarization of the incoming beam to the optimum angle for the SLM (Holoeye LC-R 2500) so as to maximize the power diffracted into the first order. The polarization state was verified by the use of a polarized beam-splitter (PBS) after the half-waveplate. The laser beam was additionally sent through a 50μm pinhole in order to obtain a beam featuring a homogeneous Gaussian intensity profile and was then subsequently expanded with a telescope (L_1 and L_2) to slightly overfill the chip of a spatial light modulator (SLM). The SLM operated in the standard first-order diffraction configuration and was used to imprint the vortex phase on the incident laser beam. Thus, the LG beam was created in the far-field of the SLM. The SLM was wavefront corrected using the OEi technique (see Appendix C) [155, 156]. In order to filter the first-order beam carrying the vortex, from the unmodulated zeroth-order beam, a pinhole aperture F was located in the back focal

plane of lens L_3. Lenses L_4 and L_5 were then used to image the ℓ and p beam mode onto a diffracting aperture with feature sizes roughly matching the beam waist. Two different apertures were used, namely a triple concentric triangular slits aperture imprinted onto a photographic film and a glass diffuser (Edmund Optics, 0.5^o diffusing angle). Finally, Lens L_6 served to create the far-field diffraction pattern in its back focal plane where a CCD camera (Basler pi640-210gm, pixel size: 7.4μm x 7.4μm) was used to record and save the pattern onto the hard drive of a computer.

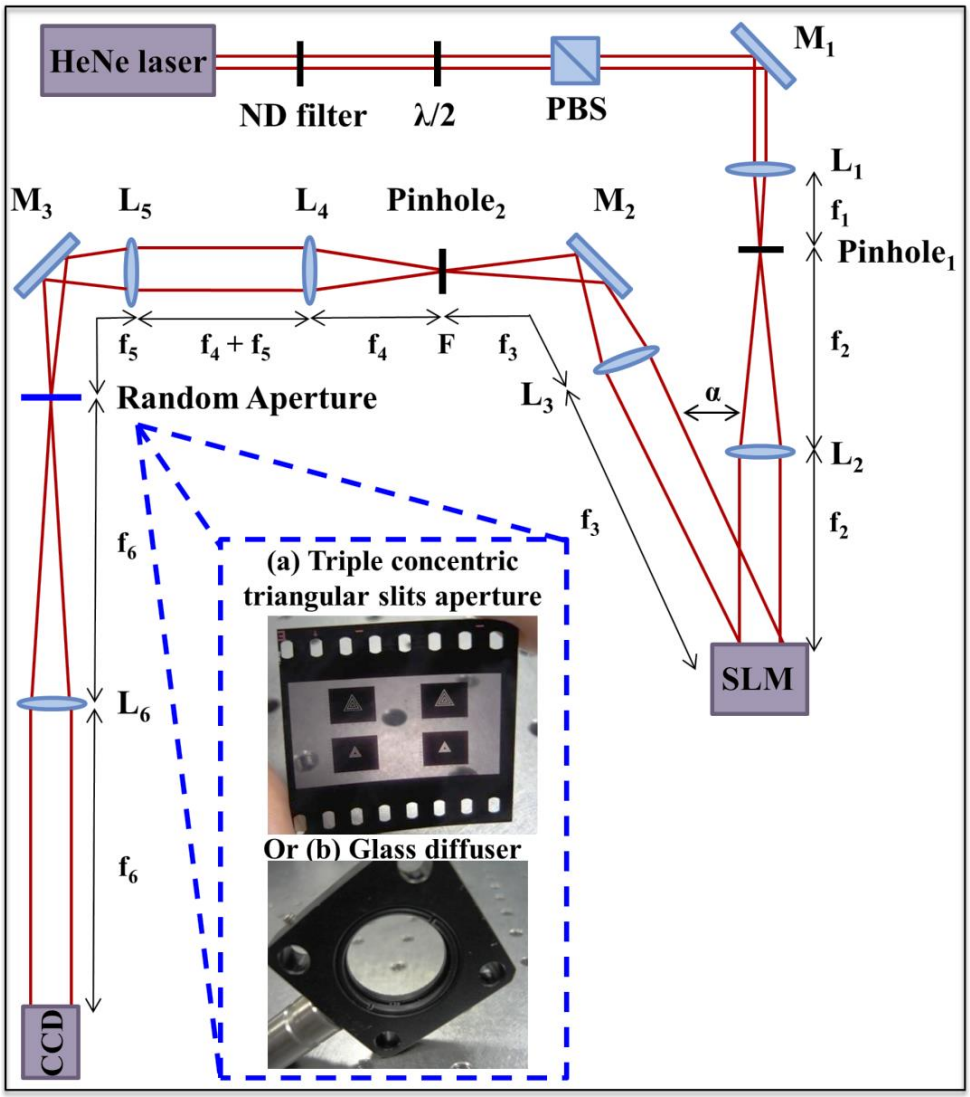

Fig. 5.5. Schematic of the experimental apparatus. L = lens, SLM = spatial light modulator, CCD = charge coupled device camera, and PBS = polarizing beam splitter, $\alpha < 10^o$. Focal lengths of lenses: f_1 = 25mm, f_2 = 1000mm, f_3 = 680mm, f_4 = 400mm, f_5 = 400mm, and f_6 = 800mm. Two different apertures were used: (a) a triple concentric triangular slits aperture, or (b) a glass diffuser (random aperture).

To record distinct images, there should be an adjustment between both the size and the thickness of the used triangular aperture to the size of the beam waist of the

incident LG beam (see Figure 3.6). The triple concentric triangular slits aperture was mounted on an *x-y-z* translation stage with a precision of ±0.005mm, in order to be carefully aligned with the incident vortex beam.

5.5.2 Experimental results

Forty-nine different LG beam modes were considered owing to our present setup, the values of $|\ell|$ and p are limited to no more than 7. For example, the annular intensity profile may go out of range of the CCD chip when $|\ell|$ is larger. Thus, we explored LG beams where the azimuthal mode index, ℓ, varied from -3 to 3 increasing in integer step, and for seven different values of the radial mode index, p, that could vary from 0 to 6, with integer step. The LG beams considered here are presented in Figure 5.6 below and were generated using phase CGHs of type 2, as demonstrated by Arrizon et al. [171].

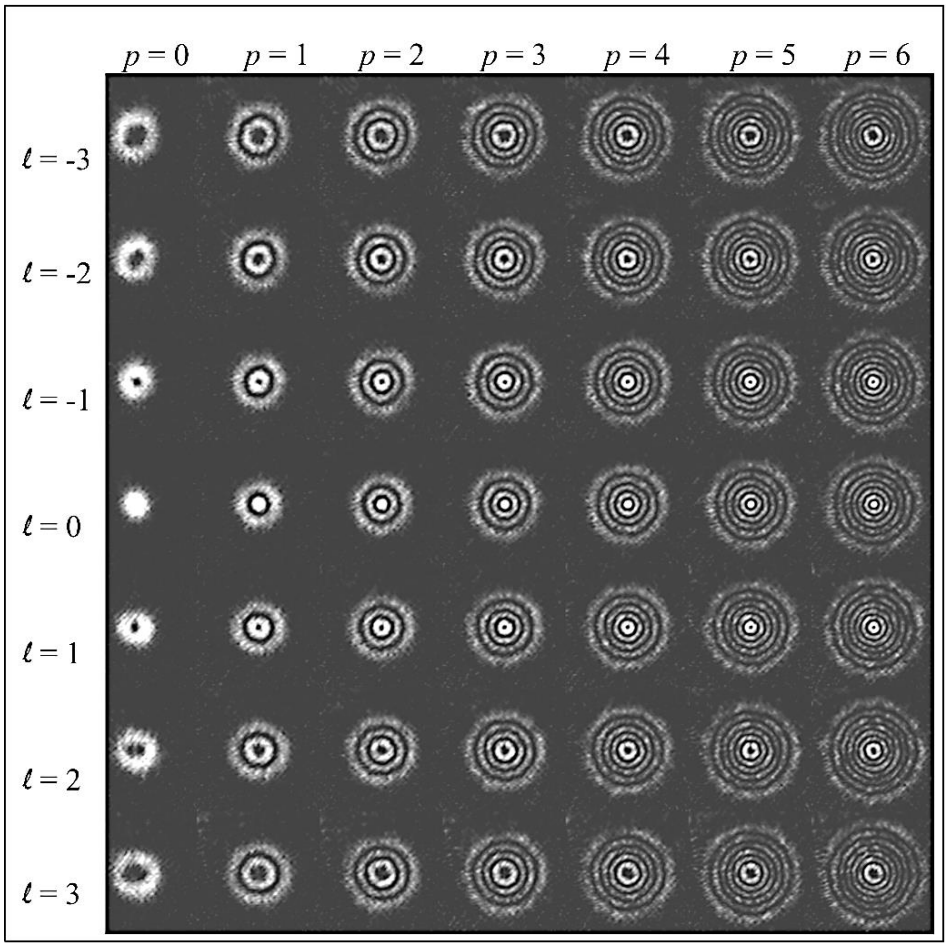

Fig. 5.6. Experimentally observed transverse intensity profiles of the forty-nine considered LG beam modes (ℓ = [-3, 3] and p = [0, 6]). The columns and rows define the azimuthal and radial number, respectively. For visualization purpose higher intensity is represented by a whiter shade.

5.5.2.1 Far-field diffraction of LG beams from a triple concentric triangular slits aperture

To illustrate our approach, we begin with a discussion of the far-field diffraction pattern of a general LG beam from a triple concentric triangular slits aperture (Figure 5.7).

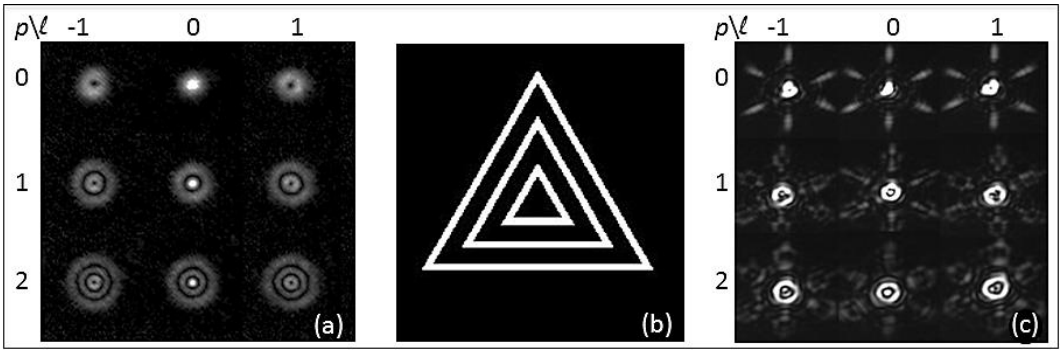

Fig. 5.7. Triple concentric triangular slits aperture experiment. (a) Table showing the nine lowest-order LG beam modes (ℓ = [-1, 1] and p = [0, 2]) and their (c) far-field diffraction intensity pattern of the (b) triple concentric triangular slits aperture.

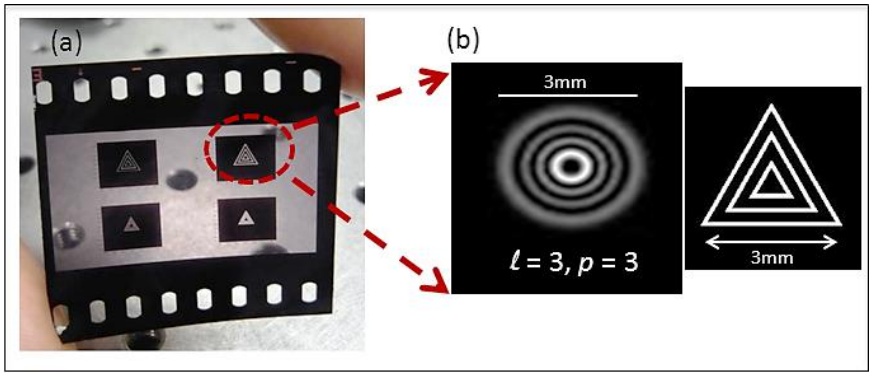

Fig. 5.8. Experimental implementation of the triple concentric triangular slits aperture. (a) A triple concentric triangular slits aperture imprinted onto a photographic film was used, and (b) an adjustment between both the size and the thickness of the aperture to the size of the beam waist of the incident LG beam with mode indices, $\ell = p = 3$ (which is the middle value of the considered data set) was done in order to record distinct images.

For each different LG beam mode, its pattern was recorded for 100 beam samples. The 'training' step is firstly applied, in which the response of the optical diffracting system is measured for every LG beam mode, each with different ℓ and p mode indices. In this manner, a database of all the possible forty-nine LG beams is created. A triple concentric triangular slits aperture imprinted onto a photographic film was used, as is presented in Figure 5.8a. Each side of the printed equilateral

triangular aperture has a thickness of 0.5mm (Figure 5.8b). As previously explained, the PCA algorithm is used in order to create the covariance matrix of all the recorded far-field diffraction patterns (Figure 5.9), by subtraction of the common mean intensity of the recorded intensity patterns (see Figure 5.2), according to the Equations (5.1), (5.2) and (5.3).

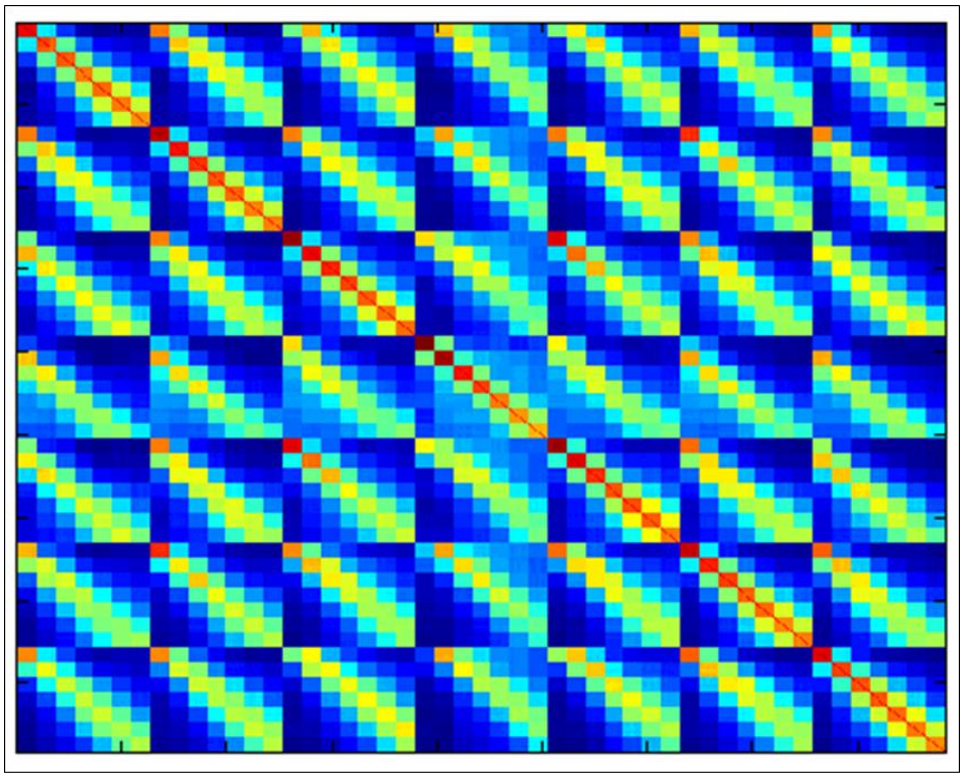

Fig. 5.9. Triple concentric triangular slits aperture PCA experimental analysis. The forty-nine presented covariance matrices were calculated for the 100 examples of the considered LG beam modes (ℓ = [-3, 3] and p = [0, 6]) diffracted by the triple concentric slits aperture (see Figure 5.2).

The covariance matrix captures the variance and linear correlation in multivariate/multidimensional data. As previously stated, each rectangular recorded far-field diffraction intensity pattern, $\boldsymbol{I}_i$, has a size of (W*L), where W, L correspond to the width and length of the rectangular image in pixel number, respectively. Hence, the array containing all the column image vectors, A_{ij}, will have dimensions of (N x W*L) and the new feature vectors, Φ_{ij}, can be defined by subtracting the mean image vector. So next, the covariance matrix, C, can be computed by the tensor product $C_{jk} = \sum_{i=1}^{N} \Phi_{ij} \Phi_{ik}$ and have dimensions of a (W*L x W*L) matrix (see Section 5.4.1. for a step-by-step calculation) (Figure 5.9).

The covariance of two variables, A_i and A_j, can be mathematically represented as:

$$\mathrm{cov}\left(A_i, A_j\right) = \left[\left(A_i - \Psi_i\right)\left(A_j - \Psi_j\right)\right] \tag{5.6}$$

where Ψ_i or Ψ_j, is the mean image vector, calculated by Equation (5.2). This relation can be further generalized to a multivariate situation and for estimated new feature vectors, Φ_{ij}, can be more explicitly represented as:

$$\mathrm{cov}\left(\hat{\Phi}_{ij}\right) = \begin{vmatrix} \mathrm{cov}(\hat{\Phi}_1, \hat{\Phi}_1) & \mathrm{cov}(\hat{\Phi}_1, \hat{\Phi}_2) & \ldots & \mathrm{cov}(\hat{\Phi}_1, \hat{\Phi}_k) \\ \mathrm{cov}(\hat{\Phi}_2, \hat{\Phi}_1) & \mathrm{cov}(\hat{\Phi}_2, \hat{\Phi}_2) & \ldots & \mathrm{cov}(\hat{\Phi}_2, \hat{\Phi}_k) \\ \ldots & \ldots & \ldots & \ldots \\ \mathrm{cov}(\hat{\Phi}_k, \hat{\Phi}_1) & \mathrm{cov}(\hat{\Phi}_k, \hat{\Phi}_2) & \ldots & \mathrm{cov}(\hat{\Phi}_k, \hat{\Phi}_k) \end{vmatrix} \tag{5.7}$$

where the diagonal of this matrix represents the variance of the vector $\hat{\Phi}$ with k elements. Therefore, the matrix can be rewritten as:

$$\mathrm{cov}\left(\hat{\Phi}_{ij}\right) = \begin{vmatrix} \mathrm{var}(\hat{\Phi}_1) & \mathrm{cov}(\hat{\Phi}_1, \hat{\Phi}_2) & \ldots & \mathrm{cov}(\hat{\Phi}_1, \hat{\Phi}_k) \\ \mathrm{cov}(\hat{\Phi}_2, \hat{\Phi}_1) & \mathrm{var}(\hat{\Phi}_2) & \ldots & \mathrm{cov}(\hat{\Phi}_2, \hat{\Phi}_k) \\ \ldots & \ldots & \ldots & \ldots \\ \mathrm{cov}(\hat{\Phi}_k, \hat{\Phi}_1) & \mathrm{cov}(\hat{\Phi}_k, \hat{\Phi}_2) & \ldots & \mathrm{var}(\hat{\Phi}_k) \end{vmatrix} \tag{5.8}$$

This essentially represents the covariance matrix. If the information that the different mode indices provided was different then the covariance matrix between the mode indices should be a diagonal matrix – i.e, the non-zero entries only appear on the diagonal.

So, it turns out that the eigenvectors of the covariance matrix will carry all the information needed to characterize the complicated data set and for data reduction the corresponding eigenvectors and eigenvalues of the covariance matrix are then calculated by solving the eigenvalue equation, see Equation (5.4). The eigenvector with the largest eigenvalue is termed the first ‘eigenface’ or principal component (PC), corresponding to the largest variability of the complicated data set. In the same way, one can introduce the second ‘eigenface’ as the image corresponding to the second largest eigenvalue of the covariance matrix and so on. Thus, a set of the subsequent ‘eigenfaces’ or principal component (PC) representation of the measure is created that represents the most significant features from the data set (Figure 5.10).

Additionally, the plot of the calculated eigenvalues, depicting the corresponding ‘eigenfaces’ or principal components (PCs) of the measure, is presented in the following Figure 5.11. As it is shown, there is little variance after the principal component nine (PC9), so there is no need to keep the rest of the data for the experimental data analysis. Thus, the dimensionality of the data set has been reduced while accounting for as much of the original variation as possible present in the data set by using the PCA algorithm.

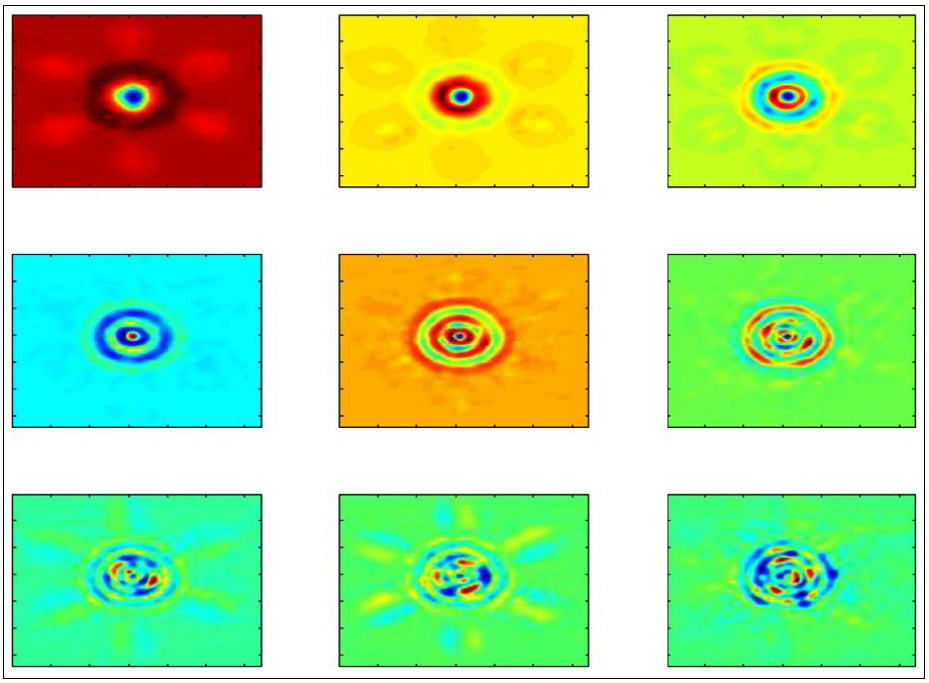

Fig. 5.10. Triple concentric triangular slits aperture PCA experimental analysis. Table showing the first nine principal components (PCs) resulting of the PCA experimental analysis (see covariance matrices in Figure 5.9) of the considered LG beam modes (ℓ = [-3, 3] and p = [0, 6]).

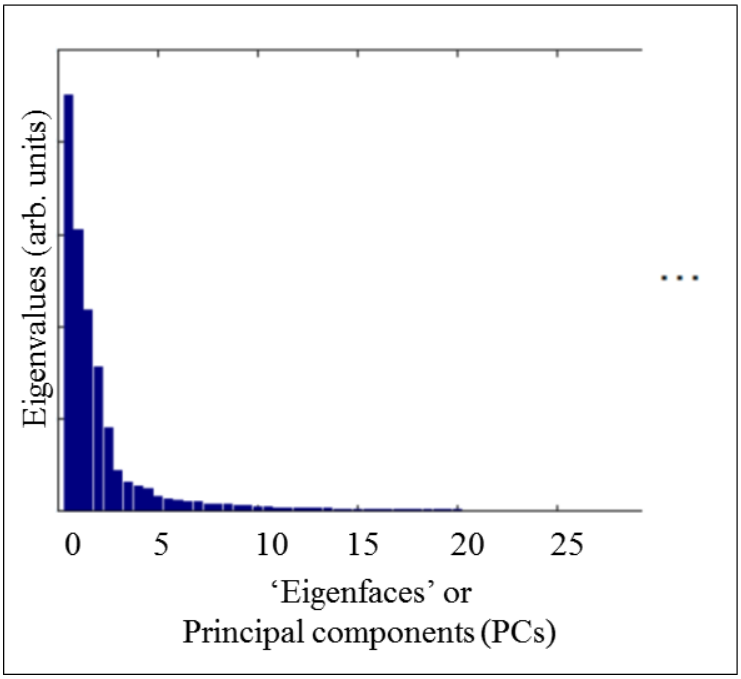

Fig. 5.11. Triple concentric triangular slits aperture PCA experimental analysis. Plot of the calculated eigenvalues, depicting the corresponding 'eigenfaces' or principal components (PCs) of the considered LG beams (ℓ = [-3, 3] and p = [0, 6]).

As is depicted in the following Figure 5.12b, the measured far-field diffraction patterns are then projected onto this subset of PCs, delivering projection coefficients to approximate the incident LG beam. Where each cluster in this representation corresponds to LG beams having the same ℓ and p mode indices (Figure 5.12d). Finally, by representing the far-field diffraction pattern of an 'unknown' beam in the same way, one can use a classification algorithm to determine the membership of beams with 'unknown' mode indices. For simplicity, the nearest neighbour measure was chosen for classification [169]. Figure 5.12c shows the classification results displaying a 100% efficiency, i.e. all unknown beams have been correctly identified. Each axis is representing the forty-nine considered LG beam modes (ℓ = [-3, 3] and p = [0, 6]) and the hue colour chart coded for the efficiency is also highlighted. The PCA 'training step' was done using the first nine PCs of the measure (see Figure 5.10) and the best results were achieved when averaging over the four closest neighbours.

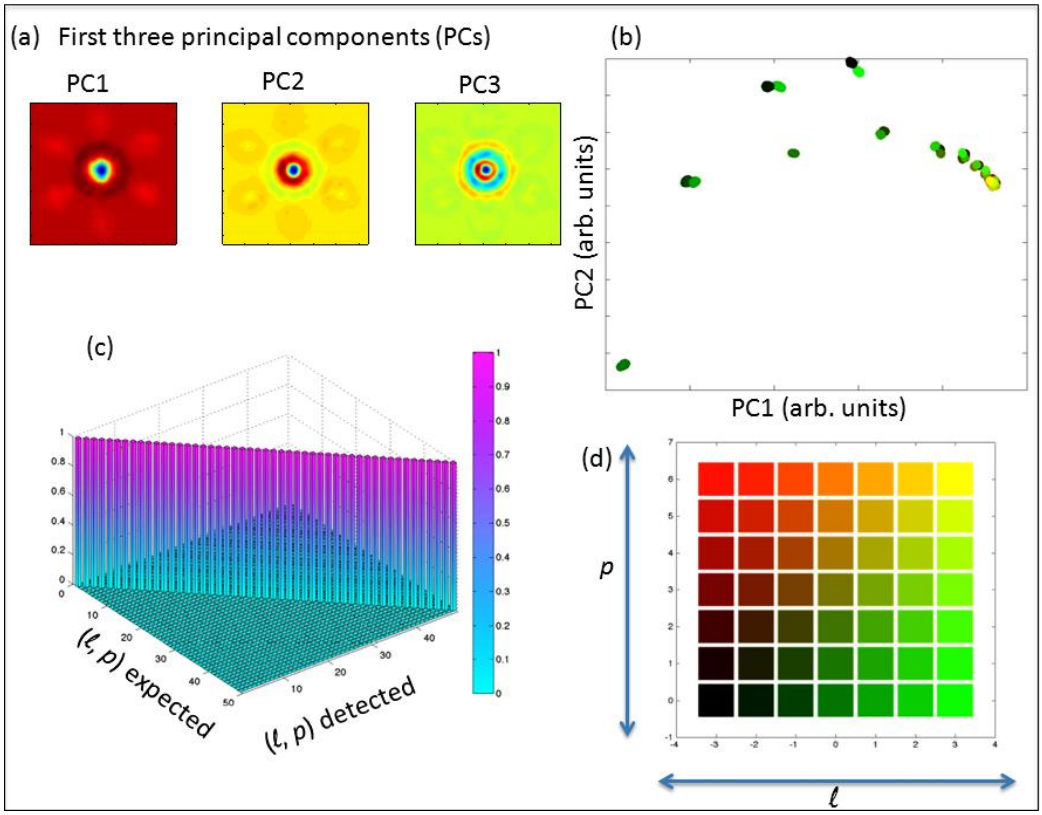

Fig. 5.12. Triple concentric triangular slits aperture PCA experimental analysis. (a) Table showing the first three principal components (PCs) of the considered LG modes (ℓ = [-3, 3] and p = [0, 6]) and their (b) first two PCs analysis and (d) colour coded for the azimuthal and radial mode indices. (c) 3D chart of the confusion matrix linking the expected and detected mode indices.

5.5.2.2 Random scattering mask

It is straight forward to deduce the radial mode index of an LG beam from its intensity profile by simply counting the number of nodal (concentric bright) rings on the beam profile. Unfortunately, the complete characterization of LG beams is more difficult when it has a non-zero azimuthal index and thus possesses a topological vortex. Theoretically, the intensity profile of a beam with ℓ azimuthal index is identical to the $-\ell$ case (see Chapter 2). This makes it impossible to deduce the azimuthal mode index from the intensity profile of the beam. The triangular aperture breaks this symmetry and any mask that is not inversion symmetric would be able to distinguish between the two different signs of the azimuthal mode index, ℓ. More generally, any random mask or aperture can be used to break this symmetry and its diffraction pattern can be used to detect simultaneously both beam mode indices. Figure 5.13a shows that the diffraction patterns do not present any prominent features at all.

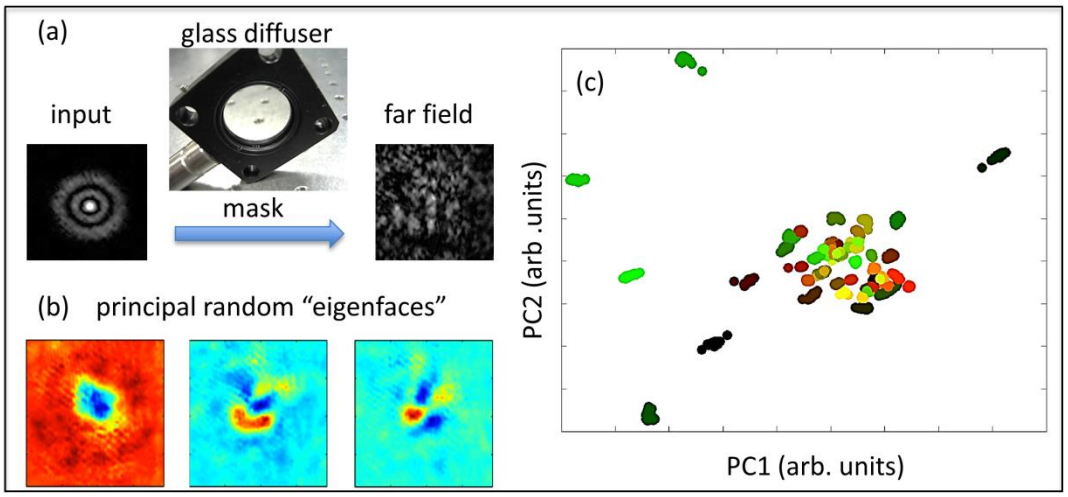

Fig. 5.13. Random aperture PCA experimental analysis. (a) Experimental implementation of the random mask, (b) first three principal components (PCs) or 'eigenfaces', based on the far-field diffraction patterns (ℓ = [-3, 3] and p = [0, 6]) from the random mask, and (c) first two PCs analysis using the same colour coding for the azimuthal and radial mode indices as seen in the following Figure 5.14a [53].

Furthermore, when the random aperture is used, any distinct LG beam results in a different diffraction pattern of similar overall form. Consequently, the variations in the plane of the first two principal components (PCs) are more evenly distributed not privileging any specific radial index as is the previously discussed case for the triple concentric triangular slits aperture. This is due to the uniformity of the random mask over which the beam extends for different radial mode indices.

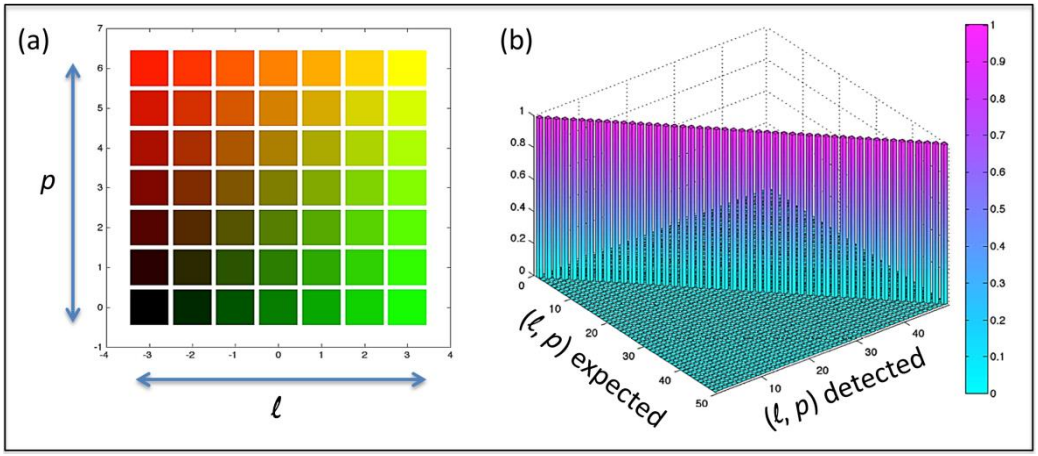

Fig. 5.14. Random aperture PCA experimental analysis. (a) Colour coding for the azimuthal and radial mode indices of the considered LG beams (ℓ = [-3, 3] and p = [0, 6]), and (b) 3D chart of the confusion matrix linking the expected and detected mode indices.

Additionally, it is to be noted that the use of the random mask (glass diffuser) presents an experimental benefit as all diffraction patterns have similar peak intensity enabling the intensity acquisition with similar exposure durations. Using the random mask we achieve, as indeed for the triple concentric triangular slits aperture, a 100% classification efficiency while eliminating the need to match the beam waist and radial index to the size of the triangular apertures used (Figure 5.14b). Finally, the PCA 'training step' was also done using the first nine PCs of the measure and averaging over the four closest neighbours in order to classify the 'unknown' data.

5.5.2.3 Beam parameter fluctuations

The fundamental question of the interdependence between the azimuthal and radial mode indices, beam alignment, and the beam waist is also interesting [31, 172]. Therefore in the present subsection, the influence of the beam waist fluctuation and beam mis-alignment are investigated on the classification ability of our scheme. Using the PCA detection method, outlined above, it is possible to study the effect of the variation of these parameters by controllably changing the amplitude profile of the LG beam generated by the SLM [173]. This study was performed when a triple concentric triangular slits aperture was used.

The first nine PCs for the beam waist fluctuations of 10% relative to the waist and beam position fluctuations of 10% relative to the waist size are depicted in Figure 5.15. While the Figure 5.16 shows the results when considering the effect of these parameter fluctuations.

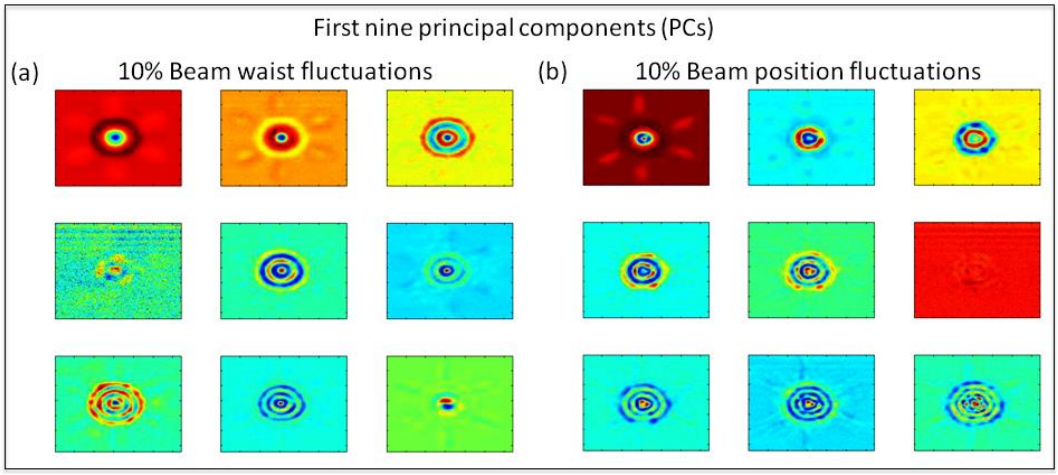

Fig. 5.15. Experimental study of position and beam fluctuations. (a) and (b) first nine principal components (PCs) for (a) the beam waist fluctuations of 10% relative to the waist and (b) beam position fluctuations of 10% relative to the waist size.

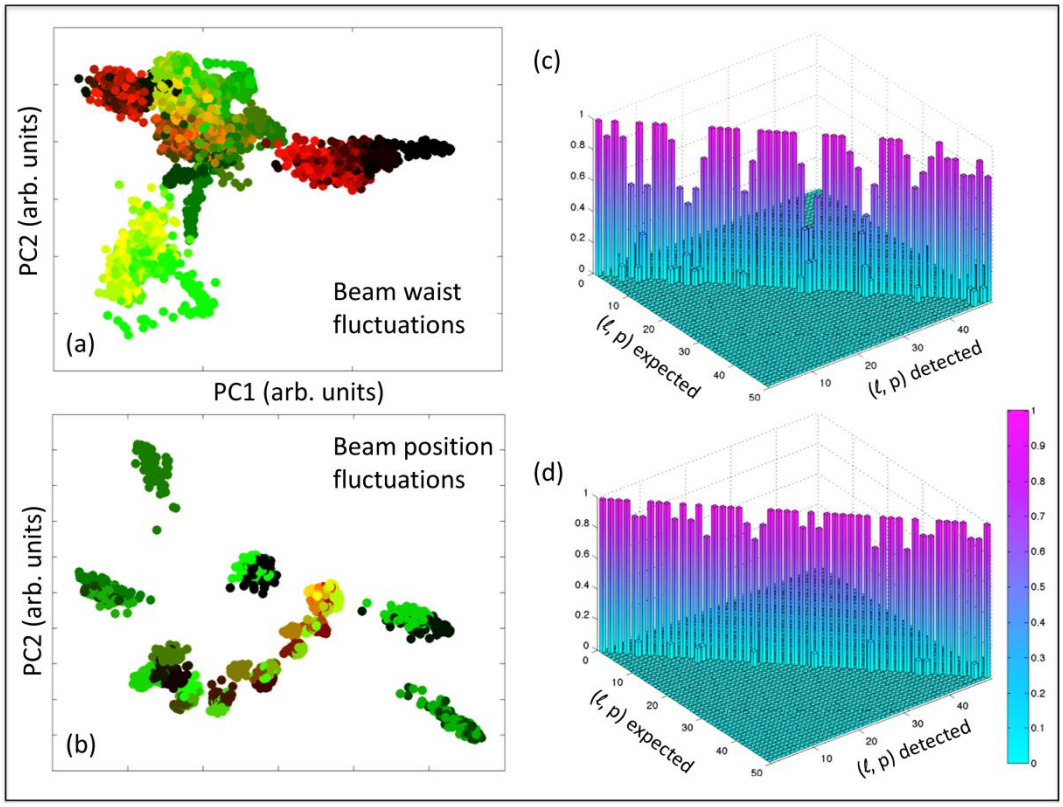

Fig. 5.16. Experimental analysis of position and beam fluctuations. (a) and (b) first two PCs analysis using the same colour coding as in Figure 5.14a for (a) the beam waist fluctuations of 10% relative to the waist and (b) beam position fluctuations of 10% relative to the waist size, (c) and (d) respective confusion matrices for the same cases. An efficiency of (c) 75% and (d) 86% for nine PCs in the studied range was achieved [53].

The first effect is a clear widening of the scattering cluster of each given beam parameter. This is understandable as beam parameter fluctuations naturally induce a certain variability of the intensity beam profile.

Nevertheless, the correct detection can still be achieved provided that either a larger training set is considered and/or a larger dimensionality of the data is allowed by taking more principal components (PCs) into account. This last point is illustrated in Figure 5.17 where the detection efficiency of position fluctuations, defined by the trace of the confusion matrix normalized to the total number of unknown beams considered, is evaluated as a function of the number of principal components (PCs). It should be noted that the beam axis and waist information is actually included in the 'training' set and as such its explicit knowledge is not necessary to correctly identify the azimuthal and radial mode indices.

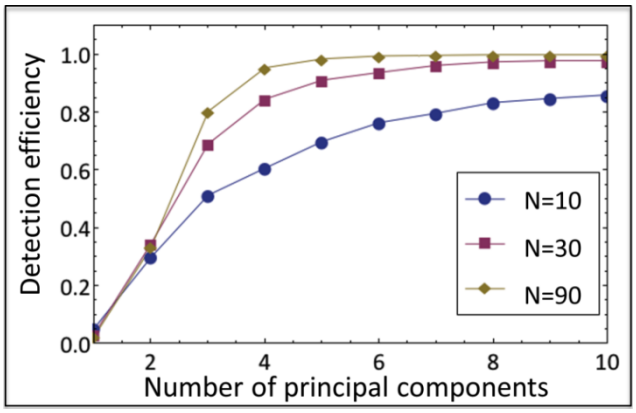

Fig. 5.17. Detection efficiency of position fluctuations. The detection efficiency as a function of the number of PCs used for the beam parameter identification, where N is the number of far-field diffraction images used as a 'training set' for the PCA, is presented.

5.5.2.4 Laguerre-Gaussian beam superposition

In quantum optics, entanglement requires an analysis of superpositions states. Such superpositions may also occur in the classical domain, for example when considering light fields with fractional azimuthal mode index [160]. It is therefore interesting to extend our PCA approach to the more general case of a superposition of multiple LG beams having different relative amplitudes and phases [174]. To that end, the PCA eigenface algorithm is 'trained' on a set of 900 random complex superpositions (keeping the total intensity constant) of four LG beams (ℓ = [0, 1] and p = [0, 1]). A startling observation is that 97% of the whole training set's variability can be accounted for only the first nine PCs (Figure 5.18). Then, the amplitude distribution of an 'unknown' beam can be identified by using nearest neighbour

classification. Experimentally, the best results were achieved when averaging over the six closest neighbours. The relative phase between the constituent beams can be retrieved by using an OEi [155, 156] decomposition (see Appendix C) together with a GS algorithm. The GS algorithm is an iterative algorithm that can retrieve the phase of a pair of light distributions related by the Fourier transform, if their intensities at the respective optical planes are known [165]. More details are discussed in the next subsection. The knowledge of these amplitudes and phases of the individual components makes their representation on a higher-order Poincaré sphere possible [175].

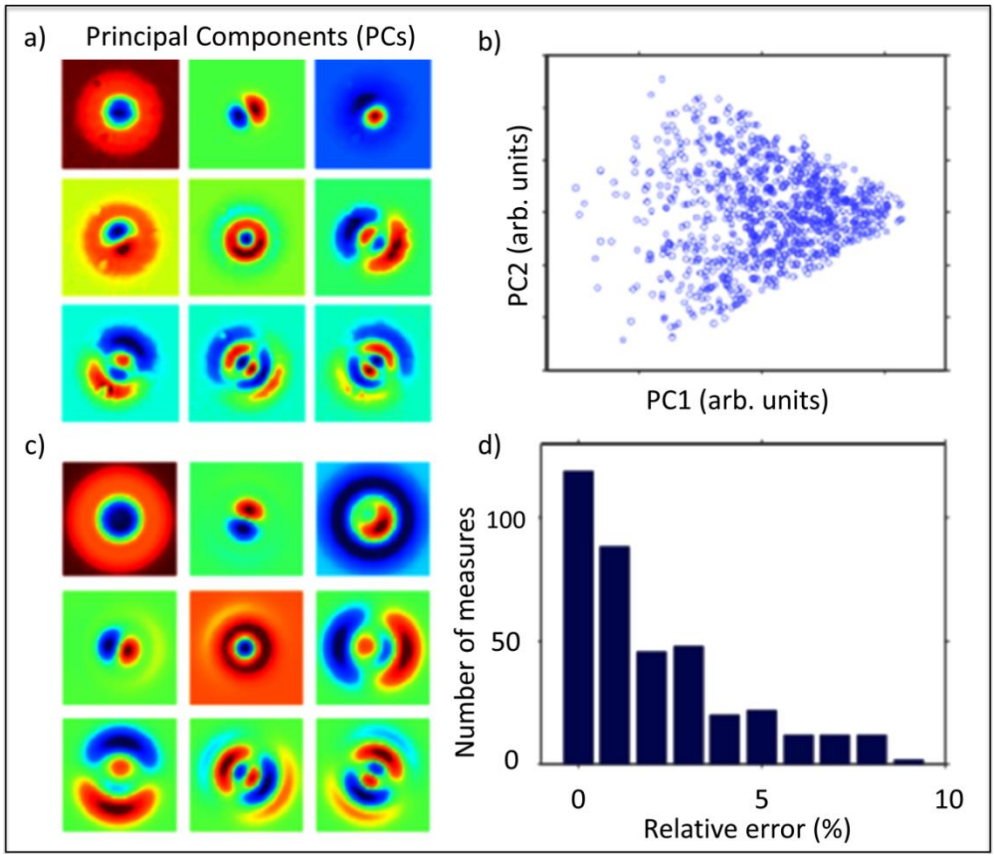

Fig. 5.18. Modal characterization of the LG beam superposition. The first a) experimental and c) theoretical PCs deduced from 900 random LG beam superposition (ℓ = [0, 1] and p = [0, 1]), b) first two PC projections (experimental), d) experimentally measured individual beam detection errors for a different set of 100 random superpositions. The intensity error is defined as $(c_i - m_i)^2$, where c_i and m_i are the encoded and respectively measured real and amplitude superposition coefficients, respectively [61].

5.5.2.4.1 LG beam superposition phase retrieval using optical eigenmode (OEi) Gerchberg-Saxton (GS) algorithm

The PCA method employed in the current chapter is able to retrieve the real amplitude of a superposition of LG beams. To deduce the relative phase between the different LG beam constituents, a method based upon a generalized GS algorithm [165] is used working in tandem with an OEi [155, 156] decomposition. These OEis correspond to a family of electromagnetic fields that in the imaging plane form, by construction, an orthogonal set of fields (see Appendix C).

The OEi can be measured experimentally by probing the optical system with a set of interfering beams created by the SLM (schematically illustrated in Figure 5.19a). Then, the closure relationship of the OEi base corresponds to a projection operator that accounts for the optical degrees of freedom of the system [176].

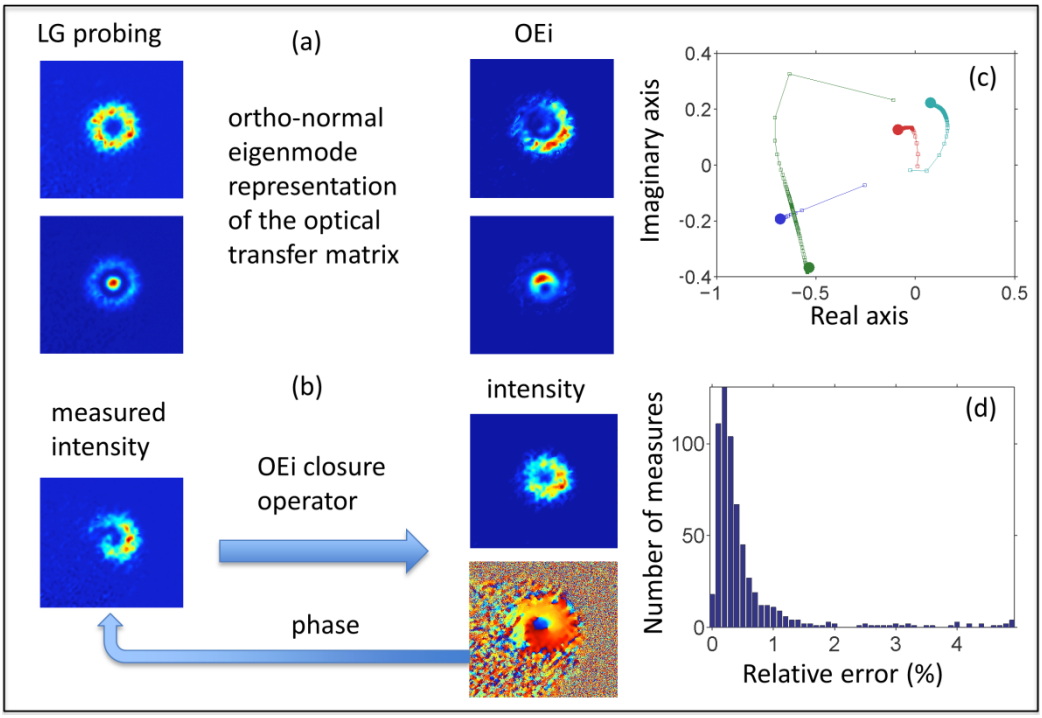

Fig. 5.19. LG beam superposition phase retrieval using optical eigenmode (OEi) Gerchberg-Saxton (GS) algorithm. a) Example LG input beam probing the optical system and resulting OEis, b) schematic representing the generalized GS algorithm based on the closure relation defined by the OEis from part a), c) convergence plot of the GS algorithm in the complex plane representing the amplitude and phases of the LG beam superposition (ℓ = [0, 1] and p = [0, 1]), and d) relative detection error for a set of 100 random superpositions. We observe that 80% of tests are below the 2% relative error mask defined as $(c_i - m_i)^2$, where c_i and m_i are the, encoded and respectively measured real and amplitude superposition coefficients [53].

Here, replacing the Fourier transform in the GS algorithm with this projection operator delivers a constrained iterative GS procedure that can be used to deduce the complex superposition coefficients of the incident LG beams (Figure 5.19b). Figures 5.19c and 5.19d show that this iterative process converges to the correct relative phases in more than 60% of cases. This convergence is helped through the use of the amplitudes measured using the PCA method (discussed in previous subsection) as starting points.

5.6 Discussion and Conclusions

In the present chapter, a triple concentric triangular slits aperture is illuminated by LG beams with non-zero ℓ and p mode indices. This is an extension of the single triangular aperture already considered in Chapter 4, which is presently one of the most powerful techniques for determining the azimuthal mode index ℓ by simply counting the number of interference lobes in the far-field diffraction intensity pattern [48, 49]. Superposing multiple such apertures might appear, at the first glance, an appropriate method to determine both the radial and azimuthal mode indices of an incident vortex field (see Chapter 3). Thus, we explored how the form of the far-field diffraction pattern is altered by the radial index, p, as well as the potential of determining, theoretically and experimentally, both mode indices (ℓ and p) simultaneously in any measurement.

From the current study, one may deduce that the far-field diffraction patterns from the triple concentric triangular slits aperture do not offer any simple way to determine the ℓ and p beam mode indices. However, it should be noted that regardless of the radial index, the pattern orientation does depend on the sign of the azimuthal index. These results are in agreement with the theoretical simulations previously presented in Chapter 3. The far-field intensity diffraction pattern rotates for opposite sign but same magnitude of the azimuthal index ℓ. Although, it cannot be excluded that there exists a specifically designed aperture that would deliver a simple rule for the detection of both ℓ and p mode indices, this is not the case for the triple concentric triangular slits aperture. Importantly, the deduction of a complicated ℓ and p retrieval rule can be replaced by considering a face-recognition algorithm readily employed in biometric identification, the principal component analysis (PCA) algorithm [50].

Consequently, our straight forward approach for the simultaneous determination of both the radial and azimuthal mode indices of LG beams followed. Our detection method is based on the projection of the far-field diffraction pattern onto a set of uncorrelated variables, using the PCA algorithm [51]. This method is robust and can even tolerate a certain degree of beam misalignment and beam waist variations.

Whilst here we focus on the LG family of optical beams, the approach presented in the present chapter can be generalized to other orthogonal mode families, which will be useful for many applications relating the optical technologies, such as the modal decomposition for optical fibers, laser resonators and information processing.

In this study, the values of $|\ell|$ and *p* are limited by our present setup to no more than 7. For example, the annular intensity profile may go out of range of the CCD chip when $|\ell|$ or *p* is larger. Actually, the values of the mode indices can go up to higher values, if for example a larger CCD could be used or a different telescope with a higher magnification. It should be noted that this method preserves a high detectability even in case of strong distortions (e.g. those caused by random aperture), provided that the 'training set' members undergo the same distortions [167]. Here, the PCA 'training set' was done using ten LG beams in the studied range.

Finally, with suitable training, one could envisage the use of this approach to detect low order aberrations that can be described by the family of Zernike polynomials. This mode determination method may be applied beyond the field of electromagnetic waves to sound and matter waves, for example, and electron beams. Our method is generic and may be extended to superpositions of different families of lights fields. Here, the amplitudes of the different LG components in a limited superposition of LG beams were measured.

In future work, the applicability of this method to superposition of a larger number of modes will be tested and its limitations for general beam characterization will be studied. It is important to establish the validity of our method for the other families of light fields to demonstrate its full applicability. In this regard our approach was extended to Hermite-Gaussian (HG) and Bessel beams (BBs) which will be discussed in the following chapter.

A significant portion of this chapter was reprinted with permission from [M. Mazilu et al, Appl. Phys. Lett. ***100****, 231115 (2012)]. Copyright 2012 AIP Publishing LLC. A. Mourka designed the considered triangular apertures and performed the experimental work. Dr. M. Mazilu performed the analysis of the discussed data and Dr. T. Vettenburg assisted with the wavefront correction of the used SLM and the measurements for the superposition study. A. Mourka also contributed to the preparation of the manuscript.*

CHAPTER 6

Modal Characterization of Hermite-Gaussian and Bessel beams using Principal Component Analysis

6.1 Synopsis and Motivation

The modal characterization of various families of beams is a topic of current interest. As previously discussed in Chapter 5, we recently developed a new method for the simultaneous determination of both the azimuthal and radial mode indices for light fields possessing orbital angular momentum (OAM). Our novel method is based upon probing the far-field diffraction pattern from a random aperture and using the recorded data as a 'training set'. Subsequently, one can transform the observed data into uncorrelated variables using the principal component analysis (PCA) algorithm. In this chapter, the generic nature of this approach is presented, for the simultaneous determination of the modal parameters of Hermite-Gaussian (HG) and Bessel beams (BBs). This reinforces the widespread applicability of this method for various applications including information processing, spectroscopy and optical manipulation.

6.2 Introduction

The characterization of the modal decomposition of light remains a key requirement in numerous fields in optics. This includes classical and quantum information processing [177], laser resonator dynamics [178], fiber optics delivery of light [179-181] and the OAM of light [182, 183]. As previously discussed in Chapter 5, we recently developed a new method using multivariate analysis to obtain both the radial and azimuthal mode indices simultaneously for LG beams [53]. This approach is based on 'training' our optical system, with the measured far-field diffraction patterns from known pure incident LG beams, upon a random diffuser and transforming the observed patterns into uncorrelated variables using the principal component analysis (PCA) algorithm.

It is important to establish the validity of our PCA method for the other families of light fields to demonstrate its full applicability. In this regard, HG modes are of major interest in laser resonator output analysis [54] and spectroscopy [55]. As previously presented in Chapter 2, pure HG modes are characterized by nodes in orthogonal directions in a cartesian coordinate space as is well documented [56]. BBs offer new directions in manipulation [57], nanosurgery [58], microscopy [59] and are delineated again by an azimuthal index ℓ and a radial wavevector (k_r), since BBs can have vortices embedded. Both HG and Bessel beams are also of interest for information processing [60]. Recently, entanglement in the Bessel basis has been measured, showing an increased spiral bandwidth [83].

In the present chapter, the application of our multivariate analysis approach for the modal characterization of both HG and Bessel beams is demonstrated [61]. The variations between the different far-field diffraction patterns of both HG and Bessel

beams from a random aperture (glass diffuser) are reported, upon which PCA is performed. The different far-field diffraction patterns contain information for the different mode indices for the considered laser beam modes. Using PCA, the optical system is 'trained' and it is subsequently possible to simultaneously determine the modal characteristics of 'unknown' HG or Bessel beams incident upon our random aperture. Additionally, the role of rotational misalignments upon our method is investigated.

6.3 Theoretical background

In the current section the theoretical background necessary for discussing the experimental results is given. Both light fields, HG and Bessel beams considered here, are presented. Finally, the detection through 'eigenface' classification when applying the PCA algorithm is described.

6.3.1 Hermite-Gaussian (HG) beams

The Hermite-Gaussian (HG) modes are described in part by the product of two-independent Hermite polynomials, for the field distribution in the *x* and *y* directions, respectively [56] (as seen in Chapter 2). The values of *m* and *n* correspond to the number of nodes in the electromagnetic field. The electric field, *E(x, y, z)*, transverse to the direction of propagation for the HG modes is essentially given by the product of a Gaussian function and a Hermite polynomial, apart from the phase term:

$$E_{mn}(x,y,z) = E_0 \frac{w_0}{w(z)} \cdot H_m\left(\sqrt{2}\frac{x}{w(z)}\right)\exp\left(-\frac{x^2}{w(z)^2}\right)\cdot H_n\left(\sqrt{2}\frac{y}{w(z)}\right)\exp\left(-\frac{y^2}{w(z)^2}\right) \cdot\exp\left(-i\left[kz-(1+n+m)\arctan\frac{z}{z_R}+\frac{k\left(x^2+y^2\right)}{2R(z)}\right]\right) \quad (6.1)$$

where the E_0 is the field amplitude, *R(z)* is the radius of curvature, $z_R = \pi w_0^2 / \lambda$ is the Rayleigh range, w_0 is the beam waist in the focal plane, *k* is the wavenumber of the electromagnetic wave, while *x*, *y* and *z* are the cartesian coordinates and *w(z)* is the beam radius. The Hermite polynomials obey the following recursion relation (see Equation 2.8), which is also discussed here for completeness in presentation:

$$H_{n+1}(x) = 2x \cdot H_n(x) - \frac{d}{dx}H_n(x) \quad (6.2)$$

The following Figure 6.1 illustrates the transverse mode patterns for HG beam modes of various orders.

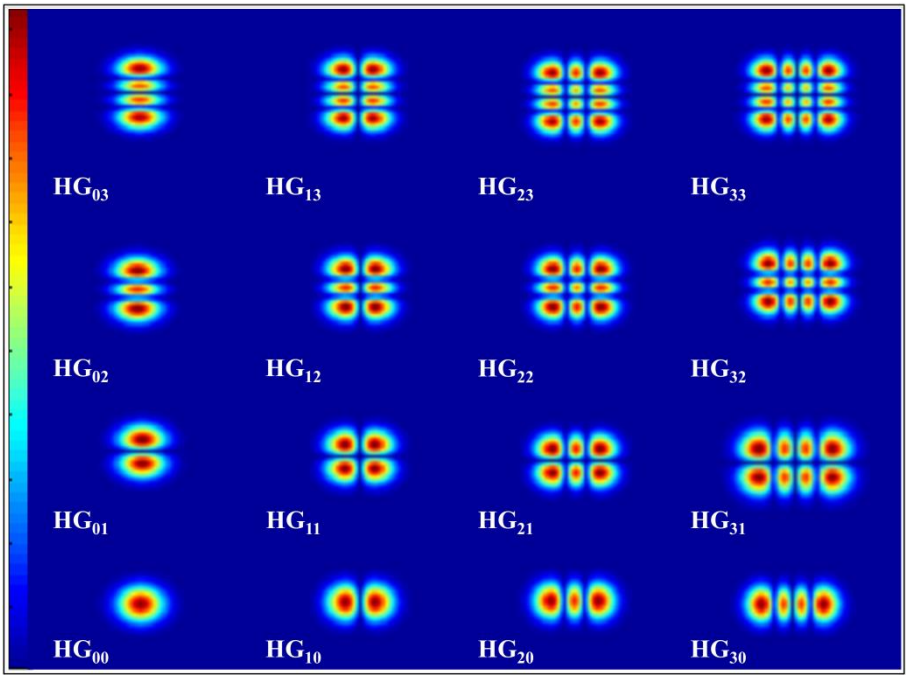

Fig. 6.1. Numerical simulation of the transverse intensity profiles of the lowest-order Hermite-Gaussian beam modes. Starting with HG_{00} (lower left-hand side) and going up to HG_{33} (upper right-hand side). The colour coded for the intensity is highlighted on the left-hand side where the blue and red colours indicate the lower and higher intensity, respectively.

6.3.2 Bessel beams (BBs)

The electric field, $E(r, \varphi, z)$, of the BB is given by (see Equation 2.14) [81]:

$$E(r,\varphi,z) = E_0 \cdot \exp\left(ik_z z\right) \cdot J_\ell\left(k_r r\right) \cdot \exp\left(-i\ell\varphi\right) \tag{6.3}$$

where the E_0 is the field amplitude, k_z and k_r are the longitudinal and radial components wavevectors, with $k = \sqrt{k_z^2 + k_r^2} = 2\pi/\lambda$, J_ℓ is the Bessel function of the ℓ^{th}-order and r, φ and z are the radial, azimuthal and longitudinal cylindrical co-ordinates respectively.

As previously discussed in Chapter 2, a zeroth order BB has a transverse intensity profile with a bright central spot surrounded by concentric rings. For higher order BBs, integer $\ell \neq 0$, the phase singularity on the beam axis results in a transverse intensity profile of concentric rings but with a phase singularity on the beam axis. This results in a 'non-diffracting' dark, rather than bright, core whose radius increases with the azimuthal index ℓ. Due to their intensity profile and reconstructed properties, these beams can find many applications in various fields [184]. The transverse intensity profiles of BBs with different ℓ, k_r values are shown in Figure 6.2 below.

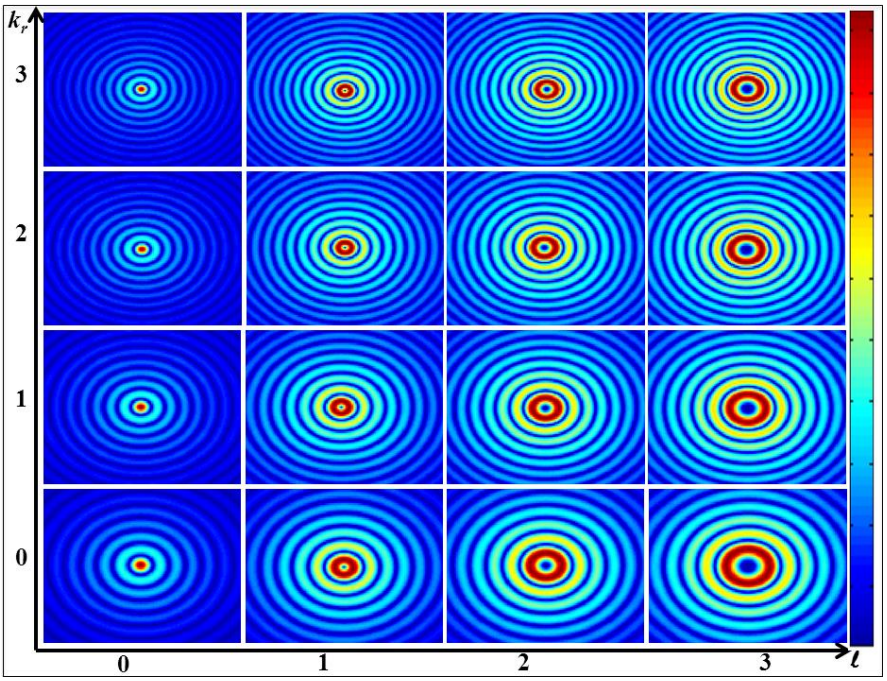

Fig. 6.2. Numerical simulation of the transverse intensity profiles of the sixteen lowest-order BB modes considered. The rows and columns define the radial wavevectors and azimuthal mode indices, respectively. The colour coded for the intensity is also highlighted on the right-hand side where the blue and red colours accordingly indicate the lower and higher intensity.

6.3.3 Detection through 'eigenface' classification

As previously described in Chapter 5, the central aim of the principal component analysis (PCA) algorithm is to reduce the dimensionality of a multivariate data set while accounting for as much of the original variation as possible present in the data set. This aim is achieved by the orthogonal transformation to principal components (PCs) or 'eigenfaces' that are linear combinations of the original variables. The PCs are uncorrelated variables and are ordered so that the first few of them account for most of the variation in all the original data set [53]. Thus, a simpler basis can be provided for the further multivariate analysis of the data.

The first step of applying the PCA algorithm to our study corresponds to creating a database of all possible HG or Bessel beams that we wish to detect. After subtraction of the common mean intensity, the covariance matrix of the recorded intensity patterns is calculated. Then, the resultant eigenvector with the largest eigenvalue is termed the first 'eigenface' which corresponds to the largest variability of the HG or BB modes 'training set'. In the same way, the second 'eigenface' corresponds to the second largest variability of the covariance matrix and so on. Projecting the measured beams onto these 'eigenfaces', we determine the first and

subsequent principal components (PCs) representation of the measure. The HG or BB modes with the same (mode indices) variables form very tight clusters. Finally, a classification algorithm of the nearest neighbour is applied in order to classify the 'unknown' data [169].

6.4 Experiments

Our multivariate analysis approach is applied for the modal characterization of both HG and Bessel beams. The variations between the different far-field diffraction patterns of both HG and BB modes from a random aperture (glass diffuser) are measured, upon which will be performed. The different far-field diffraction patterns contain information for the different mode indices for the considered laser beam modes. Using PCA the optical system is 'trained' and it is subsequently possible to simultaneously determine the modal characteristics of 'unknown' HG or BB modes incident upon our random aperture.

6.4.1 Generation of Hermite-Gaussian and Bessel beams

Nowadays both light fields, considered here, can be holographically generated using a computer controlled device, such as a spatial light modulator (SLM) [84]. The holograms were calculated according to Equations (6.1) and (6.3); additionally the required phase distribution was imprinted onto the incident Gaussian beam which was illuminating the SLM. The optical Fourier transform algorithm of a HG function is always another HG function of the same order. The modulations of the encoded transmission functions, used for creating the four lowest-order HG modes, are depicted in Figure 6.3. In the present study, the forty-nine lowest-order HG modes were created and analyzed.

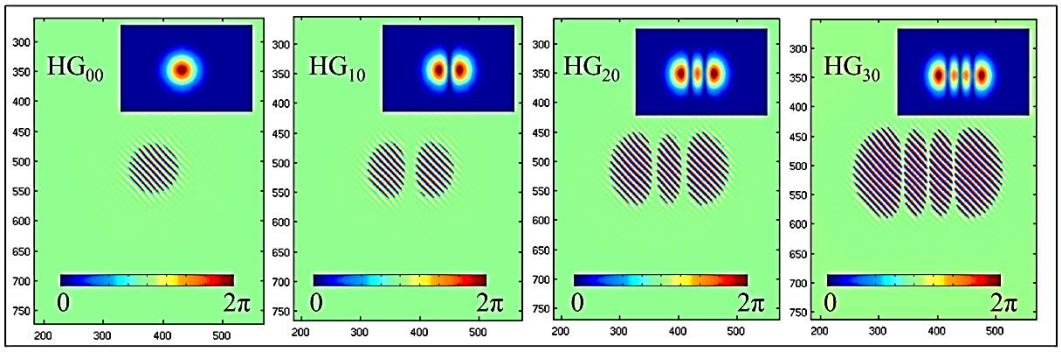

Fig. 6.3. The phase modulations of the encoded phase-only transmission functions used for generating the four lowest-order Hermite-Gaussian beam modes. The HG_{00}, HG_{10}, HG_{20}, and HG_{30} beam modes are depicted exemplarily. Numerical simulated intensity profiles are given as inserts.

For the study of BBs, far-field diffraction patterns of forty-nine different BB modes from a random aperture were also determined. Here, annuli were displayed on the SLM, which when Fourier transformed, created the different BBs considered (Figure 6.4). A wavefront correction to all beams was applied using the OEi decomposition technique (see Appendix C) [155, 156]. Finally, a blazed grating was added in order to select the 1st diffraction order.

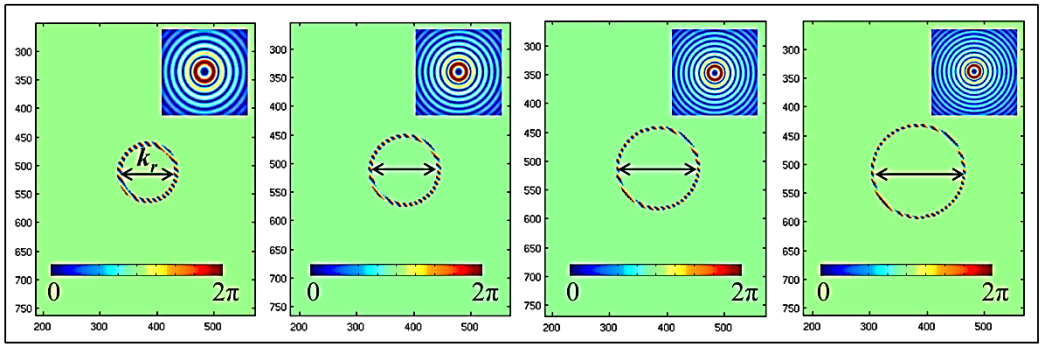

Fig. 6.4. The phase modulations of the encoded phase-only transmission functions used for generating the BB modes. By altering the diameter of the annuli holograms which were displayed on the SLM, different Bessel beams can result with k_r = [0, 3] and ℓ = 3 that are depicted exemplarily. Numerical simulated intensity profiles are given as inserts.

6.4.2 Experimental apparatus

The experimental set-up used is shown in the following Figure 6.5 and is similar to that used in the previous study discussed in Chapter 5 [53]. A laser beam (He-Ne, λ = 633nm, P_{max} = 5mW) with an output Gaussian profile of beam waist w = 5mm, was expanded using a dual lens telescope (L_1 and L_2). A half-waveplate ($\lambda/2$) was used in order to rotate the polarization of the incoming beam to the optimum angle for the SLM (Holoeye, LC-R 2500) so as to maximize the power diffracted into the first-order. The polarization state was verified by the use of a polarized beam-splitter after the half-waveplate. The holograms used to generate the HG and Bessel beams were displayed on the SLM. A lens (L_3) and a pinhole were introduced to the beam path to allow for spatial filtration to block all the unwanted diffraction orders. Then, a lens (L_4) was used to image the different laser beam modes on the random aperture, which in our case was a glass diffuser (Edmund Optics, 0.5^o diffusing angle). Finally, lens L_5 served to create the far-field diffraction patterns in its back focal plane where a CCD camera (pike, Allied Vision Technologies, pixel size: 7.4μm x 7.4μm) was used, in order to record and save the far-field diffraction patterns onto the hard-drive of a computer.

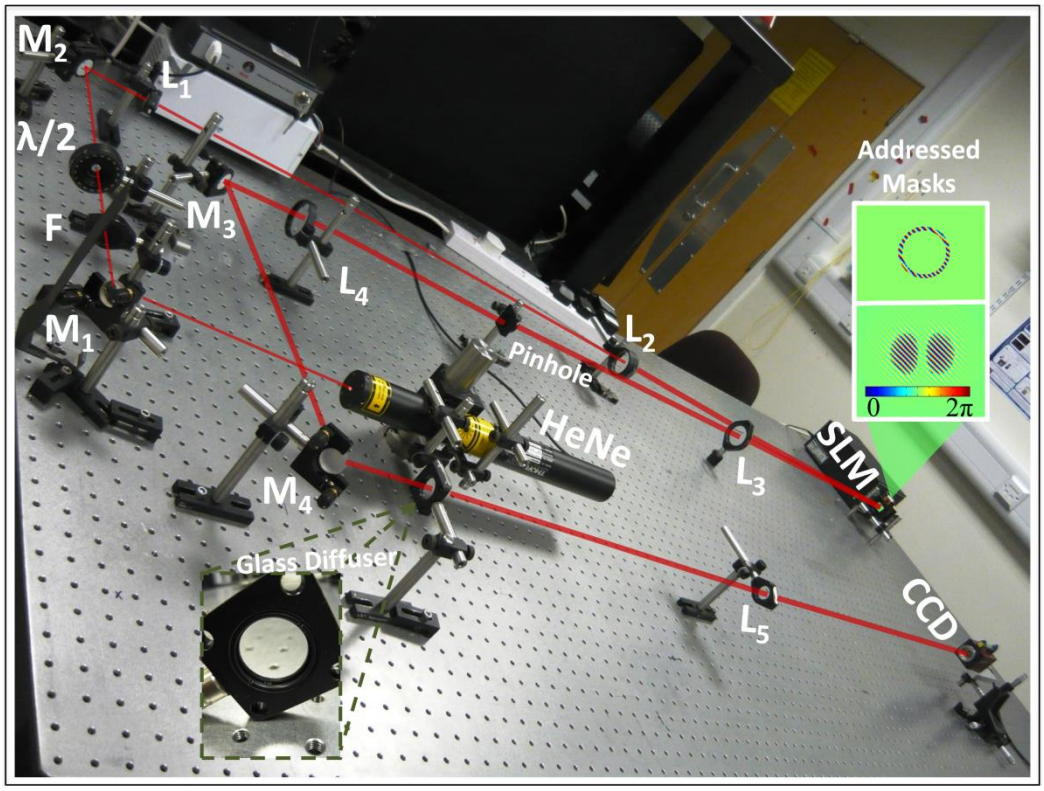

Fig. 6.5. The experimental arrangement for the observation of the far-field diffraction patterns of Hermite-Gaussian and Bessel beams from a glass diffuser. L = lens, SLM = spatial light modulator, M = mirror, CCD = charge couple device camera, F = ND filter. Focal lengths of lenses: f_1 = 150mm, f_2 = 1000mm, f_3 = 680mm, f_4 = 400mm, and f_5 = 800mm [61].

6.4.3 Experimental results

6.4.3.1 Modal characterization of Hermite-Gaussian beams

To illustrate our generic approach, let us begin with a discussion of propagating HG beams. For each different HG beam mode considered, its pattern was recorded for 1000 beam samples. The 'training step' is firstly applied, in which the response of the optical diffracting system is measured for every HG beam mode, each with different *m* and *n* values. The beam mode indices *m* and *n* could vary from 0 to 6, increasing in integer step, yielding seven different values for each. In this manner, a database of all possible forty-nine HG beams is created.

Then, the PCA algorithm is used so as to create the covariance matrix of all the recorded patterns, by subtraction of the common mean intensity of these recorded intensity patterns. The experimentally observed transverse intensity profiles of the slightly rotated ($\approx 3^o$) lowest-order Hermite-Gaussian beam modes are depicted in Figure 6.6; since the effect of the rotation of the HG beams is studied in a later subsection.

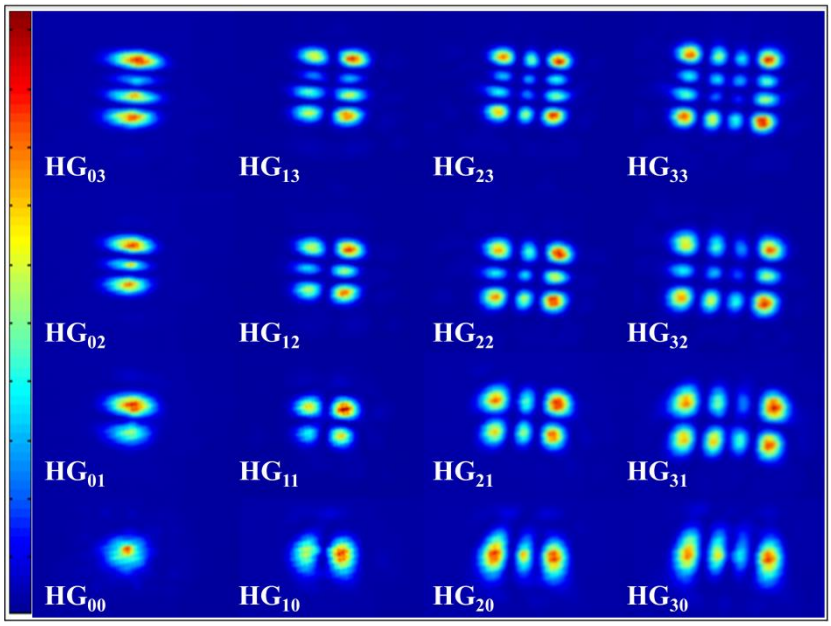

Fig. 6.6. The experimentally observed transverse intensity profiles of the slightly rotated (≈ 3°) lowest-order Hermite-Gaussian beam modes. Starting with HG_{00} (lower left-hand side) and going up to HG_{33} (upper right-hand side). The colour coded for the intensity is highlighted on the left-hand side where the blue and the red colours indicate the lower and higher intensity, respectively.

The subsequent principal components (PCs) of the measure are shown in the Figure 6.7a. The intensity patterns of the 'unknown' beam modes can be represented in the same way, using the method of the nearest neighbour measurement in order to classify them [169]. The colour coded for the different *m* and *n* mode indices of the HG beams (*m* = [0, 6], *n* = [0, 6]) is presented in Figure 6.7d. The first two principal components (PCs) analysis is shown in Figure 6.7b, where HG beams with the same (mode indices) variables form very tight clusters. As seen by 'training' our optical system by using the first nine PCs of the measure and averaging over the four closest neighbours, a 100% classification efficiency for the detection of the 'unknown' propagation HG beams can be achieved. By the same token, all the 'unknown' HG beam modes have been correctly identified as the expected HG beam modes.

6.4.3.1.1 Random scattering mask

Then, the diffraction of HG beams from a glass diffuser was considered. This is an aperture that can break the symmetry of a given HG beam mode and, as might be expected, speckle patterns result (Figure 6.8a). Here, the resulting speckle patterns from the diffraction of HG beams from a glass diffuser can be used to probe the modal characteristics of the HG beams (Figure 6.8b).

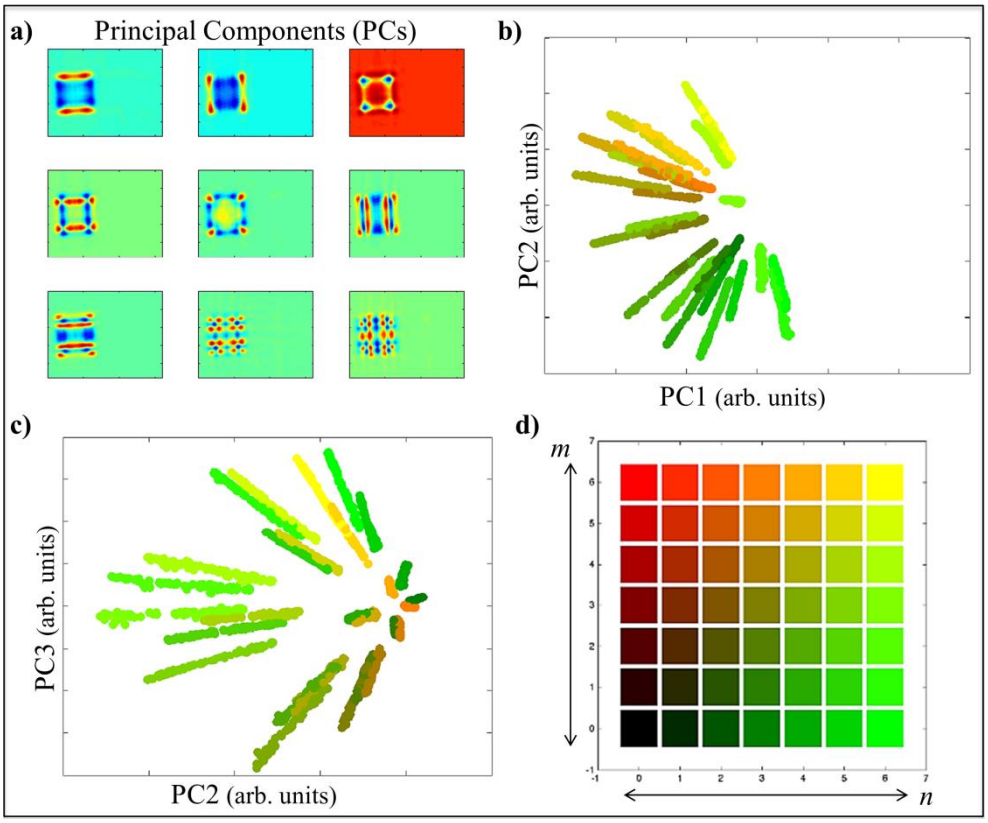

Fig. 6.7. Modal characterization of propagating Hermite-Gaussian (HG) beam modes. a) The first 9 principal components (PCs) of the measure, b) first two PCs analysis, c) second and third PCs analysis, and d) colour coded for the *m* and *n* indices of the HG beam modes (*m* = [0, 6], *n* = [0, 6]) [61].

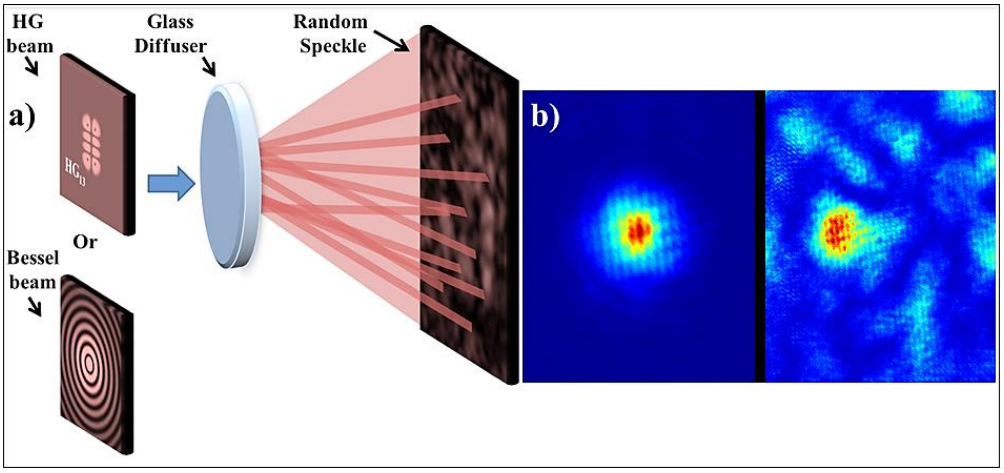

Fig. 6.8. Experimental implementation of the random aperture. a) Design of the experiment where a HG (HG_{13}) or a Bessel ($\ell = 0$, $k_r = 2$) mode is focused on a glass diffuser aperture and a speckle pattern is generated, and b) the figure includes an animation in which the incident HG_{00} beam mode is presented on the left-hand picture while on the right-hand picture the speckle pattern resulting from its diffraction from the glass diffuser is seen. To access the animation, see the published work in Ref. [61].

In Figure 6.9 below, the range of speckle patterns that result from the random perturbation of the glass diffuser and their subsequent analysis is presented. Furthermore, it is to be noted that the use of a random aperture presents an experimental benefit as all diffraction patterns have similar peak intensities enabling acquisition with similar exposure durations. Remarkably, using this 'random' aperture we achieve a 100% classification efficiency, by 'training' our optical system using the first nine PCs of the measure and averaging over the four closest neighbours, as indeed for the propagating beams (Figure 6.9d).

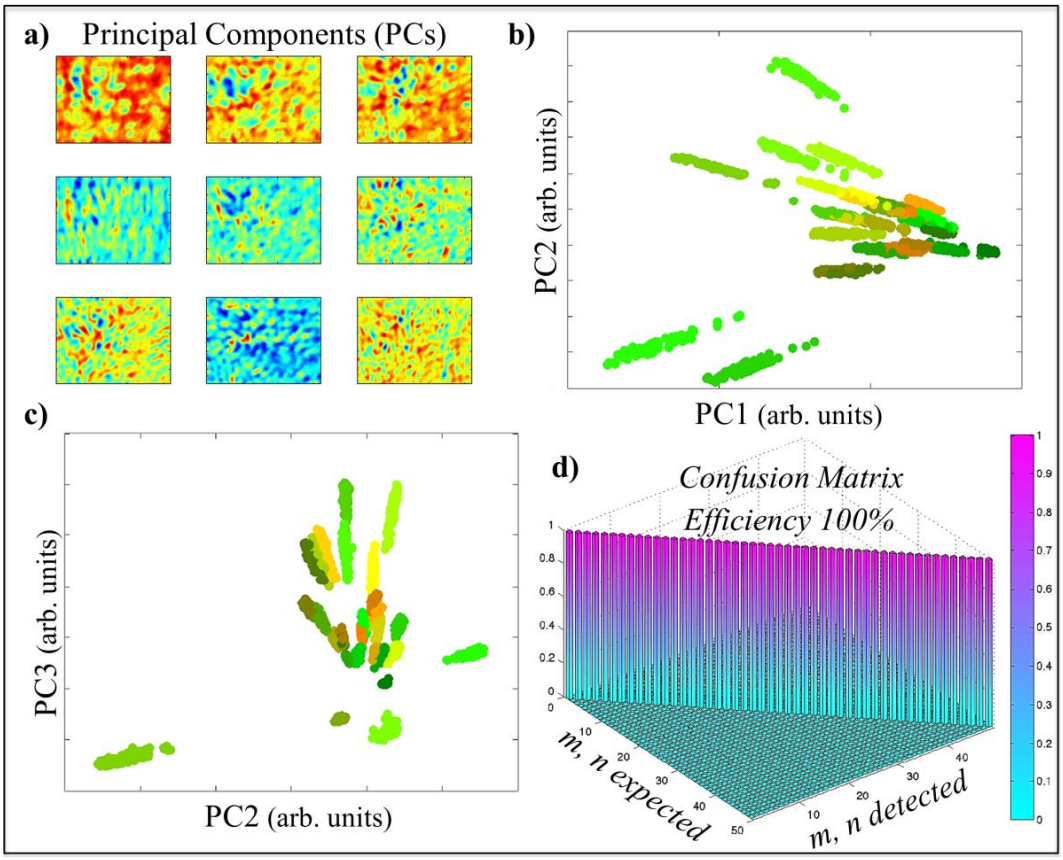

Fig. 6.9. Modal characterization of the diffracted Hermite-Gaussian (HG) beams from a random aperture. a) The first 9 principal components (PCs) of the measure, b) analysis for the first two PCs, c) analysis for the second and third PCs, d) the 3D chart of the confusion matrix linking the expected and detected indices of the HG beam modes and the colour coded for the *m* and *n* indices of the HG beam modes (*m* = [0, 6], *n* = [0, 6]) is the same as in Figure 6.7d [61].

6.4.3.1.2 Beam parameters fluctuations

The fundamental question of beam misalignment in the optical system and the impact upon the detection efficiency is also very interesting. Therefore in this subsection, the influence of the beam rotation around its central optical axis on the

classification ability of our method is investigated. This can be done by controllably rotating the SLM mask used to generate the considered beams.

Here, the effect of rotation angles from -7π/32 to -7π/32 is studied. By 'training' our optical system using the first nine PCs of the measure and averaging over the four closest neighbours, we observed 99% classification efficiency for correctly identifying the 'unknown' HG beam mode even in presence of rotation (Figure 6.10). This may prove very useful for applications such as beam converters and laser resonators, where the beam alignment is crucial [185, 186].

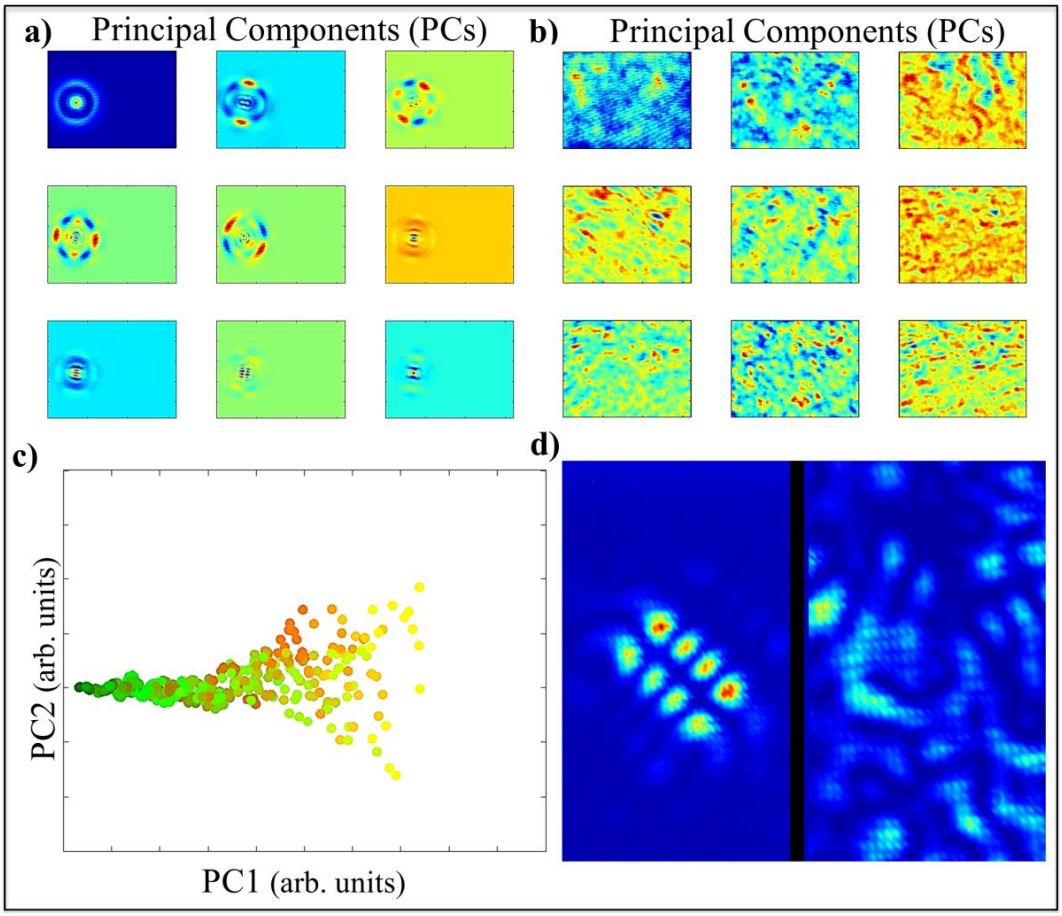

Fig. 6.10. Modal characterization of the rotated Hermite-Gaussian (HG) beams which were diffracted from a random aperture. a) The first 9 principal components (PCs) of the rotated HG beam modes, b) the first 9 PCs of the diffracted HG beam modes from a random aperture, and their c) first and second PCs analysis. d) The figure includes an animation in which the incident HG_{13} beam mode is presented on the left-hand picture while on the right-hand picture the speckle pattern resulting from its diffraction from the glass diffuser is seen. The colour coded for the *m* and *n* indices of the HG beam modes is the same as in Figure 6.7d. To access the animation, see the published work in Ref. [61].

Rotating the HG beam introduces additional degrees of freedom in the beam profile. This is clearly a different behaviour as in the case of pure LG beams for which a rotation would not induce any change of the beam profile. Training and detecting without the ground glass also work provided that the CCD camera measures the full HG beam profile.

However, partially probed beams are more challenging and here the random mask helps in delivering a more adequate sample. Furthermore, as already stated, the use of a random aperture presents an experimental benefit as all diffraction patterns have similar peak intensities enabling acquisition with similar exposure durations. As previously discussed in Chapter 5, this detection method can accommodate a certain degree of misalignment or variations in the optical system [53]. Since the correct detection can still be achieved, provided that either a larger 'training set' is considered and/or a larger dimensionality of the data is allowed by taking more PCs into account. Our PCA detection method is limited by the number of detectable degrees of freedom of the far-field diffraction patterns [176]. Indeed, low resolution cameras would greatly decrease the distinguishability between the different beams. It should be noted that very specific misalignments, such as a rotation by $\pi/2$ for example, would make some HG modes indistinguishable. We can deduce from this statement that the PCA method is also limited by specific beam dependence misalignments. The precise limitation can be assessed by considering the optical degrees of freedom (see section on Laguerre-Gaussian beam superposition in Chapter 5).

6.4.3.2 Modal characterization of Bessel beams

Our PCA detection method was then applied to BBs. Forty-nine different BB modes were considered. We explored beams where the azimuthal index ℓ, varied from -3 to 3 increasing in integer step sizes, and for seven different values of the radial wavevector, k_r. This maintains the same dimensionality used before for the analysis of HG beams.

The experimentally observed transverse intensity profiles of the lowest-order BB modes are depicted in the following Figure 6.11. The recorded image is not centred on the CCD display because we wanted to avoid an area with damaged pixels close to that region. The values of the BB mode indices $|\ell|$ and k_r are limited by our present setup to no more than 6. For example, the rings in the intensity profile may go out of range of the CCD chip when $|\ell|$ is larger. Actually, both mode indices can go up to higher values if for example a larger CCD could be used or a different telescope with a higher magnification.

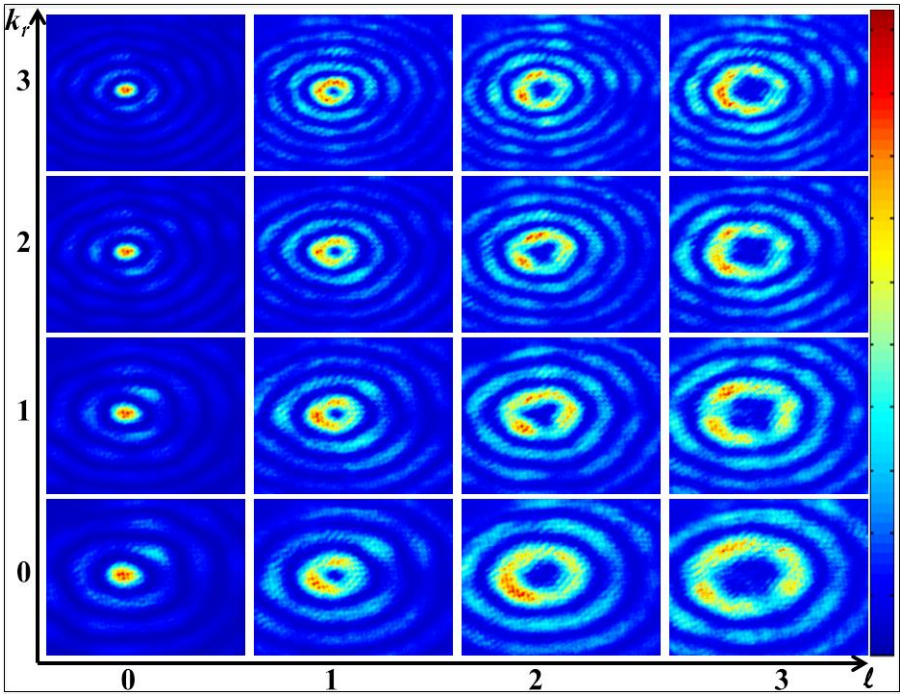

Fig. 6.11. The experimentally observed transverse intensity profiles of the lowest-order BB modes considered. The rows and columns define the radial wavevectors and azimuthal mode indices, respectively. The colour coded for the intensity is highlighted on the right-hand side where the blue and red colours accordingly indicate the lower and higher intensity.

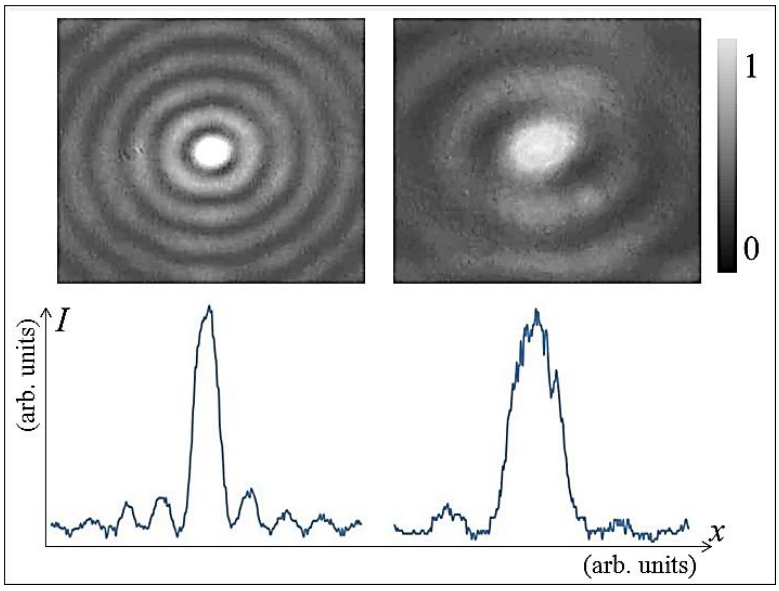

Fig. 6.12. The experimentally observed images and transverse intensity profiles of the BB modes considered. (Top row) The BB mode with k_r = 6, ℓ = 0 results in a central spot width equal to 0.3mm in the detector plane, going up to 0.5mm when a k_r = 0, ℓ = 0 is considered (in the left hand-side). (Bottom row) The intensity profiles are shown, respectively.

After the 'training step' and the application of the classification algorithm, as depicted in Figure 6.13d below, a 100% classification efficiency was achieved i.e. all the 'unknown' BBs have been correctly identified. The PCA 'training step' was also done using the first nine PCs of the measure and the classification by averaging over the four closest neighbours.

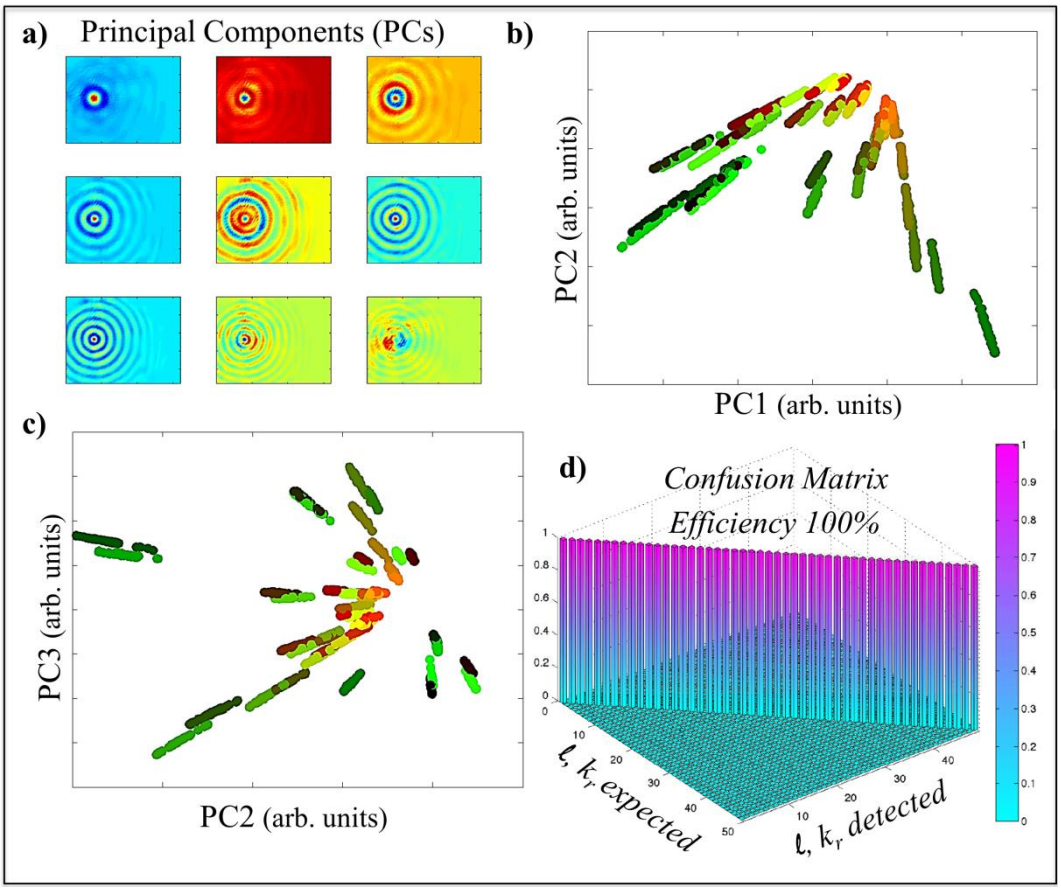

Fig. 6.13. Modal characterization of propagating Bessel beams. a) The first 9 principal components (PCs) of the measure, b) analysis for the first two PCs using the same colour coding as in the following Figure 6.14d, c) analysis for the second and third PCs, and d) the 3D chart of the confusion matrix linking the expected and detected mode indices of the Bessel beams.

It should be noted that recently it has been demonstrated that the mode sorter [136, 137], which was comprising two free-form refractive optical elements that can be used to transform OAM states into transverse momentum states, was also applied to extract the information in both the azimuthal and radial components of BBs [187]. The two free-form optical elements are used to map a position (x, y) in an input plane to a position (v, u) in the output plane by a conformal mapping. In this arrangement, an annular ring of light (Fourier transform of the BB) is mapped to a horizontal line of fixed width and any azimuthal phase variation into a tilt of the

phase front. Thus, a focused spot is produced at an ℓ-dependent horizontal position. An optical system with three cylindrical lenses can be implemented and care should be taken during the alignment in order to avoid any distortion. Finally, an example of a BB superposition is also discussed in Ref. [187].

6.4.3.2.1 Random scattering mask

In the present subsection, the study of the far-field diffraction patterns of the diffracted BBs from a random (glass diffuser) aperture is presented (Figure 6.14).

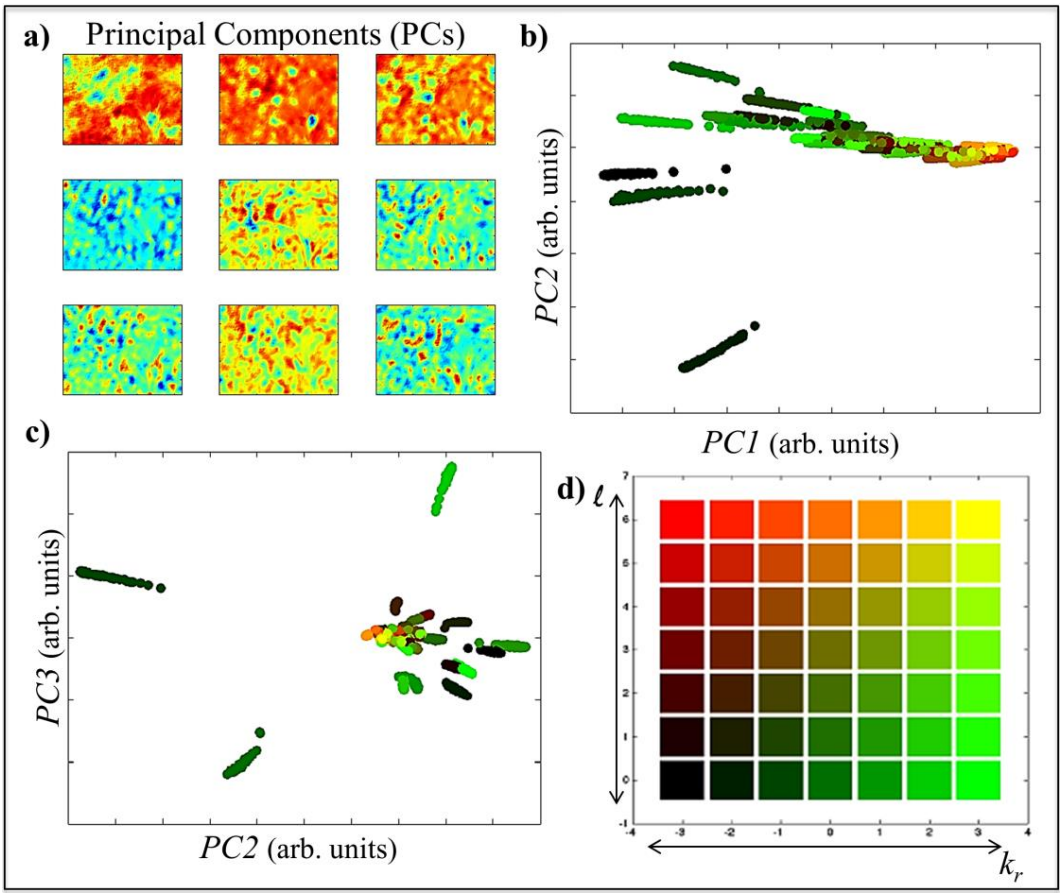

Fig. 6.14. Modal characterization of the diffracted Bessel beams from a random aperture. a) The first 9 principal components (PCs) of the measure, b) first two PCs analysis, c) second and third PCs analysis, and d) colour coded for the azimuthal index ℓ and the radial index k_r of the BBs considered [61].

First the 'training step' is applied in which the response of the optical diffracting system is measured for every single BB considered. Then the second step followed, where we used the classification algorithm which corresponds to the actual identification or measurement of an 'unknown' BB, delivering simultaneously the mode indices which characterize this beam. Finally, the classification results again

displaying a 100% efficiency i.e. all the 'unknown' BBs have been correctly identified, by using the first nine PCs in the 'training' step and averaging over the four closest neighbours.

6.5 Discussion and Conclusions

The present chapter presents a powerful method by which the mode indices of both Hermite-Gaussian and Bessel beams can be determined [61]. In addition to standard methods used to characterize higher-order beam modes, it is shown how a PCA analysis algorithm can be used to characterize diffracted light modes. Our method is based on the measurement of correlations between the probed far-field diffraction pattern and the 'training set' of preliminary recorded far-field diffraction patterns of standard HG and BBs. The principal component analysis (PCA) algorithm calculates a projection of the 'unknown' beam onto the term of the mode composition.

The experimental data show that the methodology preserves a high detectability in case of strong beam distortions (e.g. ground glass), provided that the 'training set' members undergo the same distortions. Since the correct detection can still be achieved, provided that either a larger 'training set' is considered and/or a larger dimensionality of the data is allowed by taking more PCs into account. Here, the PCA 'training set' was done using ten HG or BB modes in the studied range

The influence of the HG beam rotation around its central optical axis on the classification ability of our method is also investigated. This can be done by controllably rotating the SLM mask used to generate the considered beams. Here, the effect of rotation angles from $-7\pi/32$ to $7\pi/32$ is studied. By using the first nine PCs in the 'training set', we observed a 99% classification efficiency for correctly identifying the 'unknown' HG beam mode even in presence of rotation. This may prove very useful for applications such as beam converters and laser resonators, where the beam alignment is crucial [185, 186].

Furthermore, partially probed beams are more challenging and here the random mask helps in delivering a more adequate sample. Moreover, as previously stated in Chapter 5, the use of a random aperture presents an experimental benefit as all diffraction patterns have similar peak intensities enabling acquisition with similar exposure durations, while eliminating the need to design a clever aperture and match the beam waist of the incident beam to the size of the used aperture.

Finally, very specific misalignments, such as a rotation by $\pi/2$ for example, would make some HG modes indistinguishable. We can deduce from this statement that the PCA method is also limited by specific beam dependence misalignments. The precise limitation can be assessed by considering the optical degrees of freedom (see section on Laguerre-Gaussian beam superposition in Chapter 5).

It should be also noted that in this study, the values of the HG and Bessel beams mode indices are limited by our present setup to no more than 6. Actually, both mode indices can go up to higher values if for example a larger CCD could be used or a different telescope with a higher magnification.

In future work, we will expand our PCA detection method to explore complex superpositions of BBs, enabling the encoding, decoding and manipulation of both the radial and azimuthal degrees of freedom.

---

*A significant portion of this chapter was reprinted with permission from [A. Mourka et al, Sci. Rep. **3**, 1422 (2013)]. Copyright 2013 Nature Publishing Group.*

A. Mourka set up the optical system and performed the experimental work. Dr. M. Mazilu assisted with the analysis of the discussed data. A. Mourka also contributed to the writing of the manuscript.

CHAPTER 7

Dependency of the cross-correlation function upon the azimuthal and radial mode indices of a partially coherent vortex field

7.1 Synopsis and Motivation

All of the previously presented studies have assumed that the optical field is fully spatially coherent, however here the dependency of the far-field cross-correlation function (CCF) on both the radial and azimuthal mode indices (p and ℓ) of a partially coherent vortex field is demonstrated through an observation of the dislocation rings in the far-field CCF. The number of the dislocations rings (dark zones), N_d, of the far-field CCF is theoretically shown to be equal to $N_d = 2p + |\ell|$ and this is verified experimentally. Our results are consistent with earlier experimental results for the limiting case where: $p = 0$, $\ell = 1$ [188]. Thus, the dependency of the far-field CCF on both the radial and azimuthal degrees of freedom (p, ℓ) in a partially coherent light field through an observation of the phase correlation singularities is demonstrated. This offers a powerful method for the measurement of partially coherent fields with embedded vortices.

7.2 Introduction

To begin with, a brief introduction into the optical coherence will take place. The concept of coherence is related to the stability, or predictability, of phase. Spatial coherence describes the correlation between waves at different points in space. Temporal coherence describes the correlation, or predictable relationship, between waves observed at different moments in time [189].

All functions of time can be expressed as a linear combination of pure sine waves of various frequencies. When the temporal coherence is high, the range of frequencies is very small, i.e. the wave is nearly monochromatic. Thus, if one knows the phase of a wave under study at time t, how well can the phase of the wave at a later time, Δt, i.e. $t + \Delta t$, be predicted? The delay over which the phase changes by a significant amount is defined as the coherence time. Temporal coherence gives the ability to observe good interference patterns between the wave and the time-delayed version of itself, for example in a Michelson interferometer [66].

Spatial coherence is exactly the same thing except that wavevectors are considered (i.e. vector spatial frequencies; cycles per unit length in 3D) instead of temporal frequencies [66]. Hence, the lateral coherence length is determined, which is a measure of how far apart two points in a wavefront can be, such that knowing the phase at one point still let us confidently predict the phase at the other point. Spatial coherence relates to the ability to focus a beam down to a diffraction-limited spot. It also relates to the ability to perform experiments in areas such as holography, which rely on building up an interference pattern by illuminating a large area [190].

Spatial coherence can be improved with lenses and apertures and is taking into account in the current study.

The partially coherent fields have found many applications, such as optical coherence tomography (OCT), optical communication, and imaging science [66]. Moreover, the interest for OAM of light in astronomy and astrophysics has grown [67, 79]. OVs generated from starlight beams have been observed at the Asiago telescope [67], and the light coming from a distant star is certainly partially coherent. The properties of OVs have found interesting applications in astronomical coronagraphy [79]. The preservation of the vortex structure during propagation makes partially coherent beams good candidates for various applications; accordingly, a better understanding of the spatial coherence properties is of fundamental importance.

Recently, the coherence of OVs or the phase singularities of a partially coherent field have been studied by optical coherence theory [68, 69], and the cross-correlation function (CCF) of a partially coherent beam has been studied theoretically and experimentally [70-73]. It has been shown that spatial correlation functions have interesting topological properties associated with their phase singularities, and there exist correlation singularities (denoting nulls of the cross-spectral density function) in the regions where the phase is ill-defined.

On the other hand, determining the radial and azimuthal mode indices, p and ℓ, of an OV remains an intriguing problem in both the quantum and classical domain [77]. For partially coherent vortex light fields, the mutual coherent function (MCF) may denote the spatial coherence properties of the field in question [191]. From an experimental viewpoint, it has been noted that the projections of the four-variable MCF, as the CCF, may yield information with regard to the field [192]. In particular, one may observe phase correlation singularities denoting nulls of the cross-spectral function [66, 71, 188, 192, 193] which they have recently been shown to be linked to the azimuthal mode index of the partially coherent OV field [71]. Applications of these approaches have shown that a partially coherent beam, with no overall OAM, may be described as a statistical sum of completely coherent beams with a well-defined OAM [194]. As previously mentioned in Chapter 3, a recent study has shown that the low degree of coherence may invalidate the method of detecting a vortex based on the Fourier transform of its intensity distribution and the complex degree of coherence should be considered [141]. However, a generic understanding of how both the radial and azimuthal degrees of freedom influence the form of the CCF has never been presented.

Additionally, the radial degree of freedom is usually neglected but is crucial facet for the correct description of the transversal state of a light field and thus it is

important to understand this in relation to the CCF. In the present chapter, the form of the CCF for a partially coherent light field including both the azimuthal and radial mode indices is theoretically and experimentally delineate. The results show the definitive linkage between both the radial and azimuthal mode indices of partially coherent OVs to the number of dislocation rings in the CCF.

7.3 Theoretical background

In the cylindrical coordinate system, a fully coherent OV field with topological charge, ℓ, at the source plane $z = 0$ has complex amplitude that is given by Equation (2.1). By propagating a fully coherent LG beam through an optical diffuser, a partially coherent LG beam can be rendered with a random phase that has a Schell-model correlator [195, 196]:

$$\mu\left(\vec{r}_1', \vec{r}_2'\right) = \exp\left(-\frac{\left|\vec{r}_1' - \vec{r}_2'\right|^2}{{L_c}^2}\right) \tag{7.1}$$

where *Lc* is the transverse coherence length. One can write the mutual coherence function (MCF) of such a partially coherent LG beam at the source plane $z = 0$ in the cylindrical coordinate system as [188]:

$$\Gamma'\left(\vec{r}_1', \vec{r}_2', 0\right) \propto \left(\vec{r}_1' \cdot \vec{r}_2'\right)^{|\ell|} \exp\left(-\frac{\left|\vec{r}_1' - \vec{r}_2'\right|^2}{{L_c}^2}\right) L_p^{\ell}\left(\frac{2\vec{r}_1'^2}{{w_0}^2}\right) L_p^{\ell}\left(\frac{2\vec{r}_2'^2}{{w_0}^2}\right)$$
$$\times \exp\left(-\left(\vec{r}_1'^2 + \vec{r}_2'^2\right)/{w_0}^2\right) \exp\left[-i\ell\left(\phi_2' - \phi_1'\right)\right] \tag{7.2}$$

Therefore, the far-field MCF in the detection plane after the beam has propagated a distance *z*, may be expressed as:

$$\Gamma\left(\vec{r}_1, \vec{r}_2, z\right) = \left(1/\lambda z\right)^2 \iint\iint \Gamma'\left(\vec{r}_1', \vec{r}_2', 0\right) \exp\left[-\frac{i2\pi}{\lambda z}\left(\vec{r}_1' \cdot \vec{r}_1 - \vec{r}_2' \cdot \vec{r}_2\right)\right] \mathrm{d}\vec{r}_1' \mathrm{d}\vec{r}_2' \tag{7.3}$$

where λ is the wavelength.

7.3.1 The cross-correlation function (CCF) of a partially coherent vortex beam in far-field

From the far-field MCF in Equation (7.3), one may determine the far-field cross-correlation function (CCF) such as:

$$\chi_c\left(\vec{r}\right) = \Gamma\left(\vec{r}, -\vec{r}\right) \tag{7.4}$$

which is a more robust pattern than the intensity in a partially coherent beam. Importantly, dark dislocation rings emerge where the two-point correlation vanishes due to the absence of coherence. Spatial correlation singularities may exist even in a

non-vortex beam when $\ell = 0$. Numerically calculated far-field CCF of partially coherent OVs with different radial and azimuthal mode indices, as seen in Figure 7.1, give a definitive general relationship between the number of dislocation rings and the radial and azimuthal mode indices of partially coherent OVs as:

$$N_d = 2p + |\ell| \tag{7.5}$$

The examples shown in the following Figure 7.1 are numerical evaluations that have been calculated based on Equations (7.4) and (7.5).

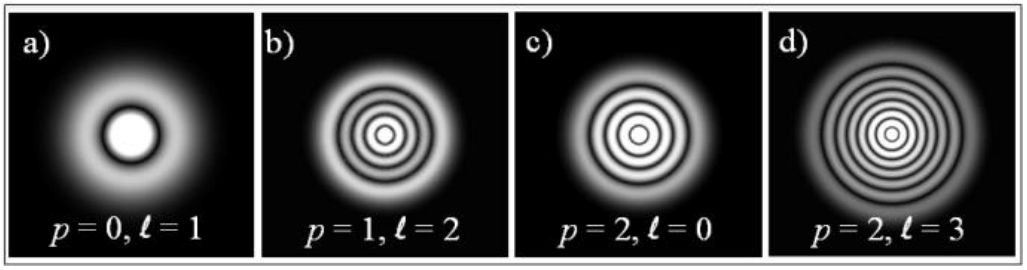

Fig. 7.1. Numerical simulation of the far-field CCFs of partially coherent LG beams. The beam mode indices are given as inserts.

To explore the relationship between the number of dislocation rings (N_d) in the far-field CCF and the radial and azimuthal mode indices of a partially coherent OV, more examples are given in Table 7.1.

N_d : p \ ℓ	0	1	2	3	4
0	0	1	2	3	4
1	2	3	4	5	6
2	4	5	6	7	8
3	6	7	8	9	10
4	8	9	10	11	12

Table 7.1. Number of dark ring dislocations (N_d) in the far-field CCF versus different radial and azimuthal mode indices of a partially coherent OV.

It should be also noted that the relationship established in Equation (7.5) is consistent with the earlier experimental results for the limiting case of $p = 0$, $\ell = 1$, namely, there is one dark dislocation ring in the far-field CCF [188]. When $p = 0$, Equation (7.5) is rewritten by $N_d = |\ell|$, which is consistent with the earlier

theoretical study in [71]. Equation (7.5) can be understood by considering the different steps involved in measuring the CCF of a partially coherent LG beam.

The following Figure 7.2 shows how the CCF cross-correlates two regions of the beam diametrically opposite to each other (highlighted using the yellow circles in parts a), d) and g)). The size of these regions is determined by the transverse coherence length, L_c. The product of the two fields in these two regions, corresponding to the integrand of the CCF is represented in parts c), f) and i) of Figure 7.2. It is observed that this product function has multiple features.

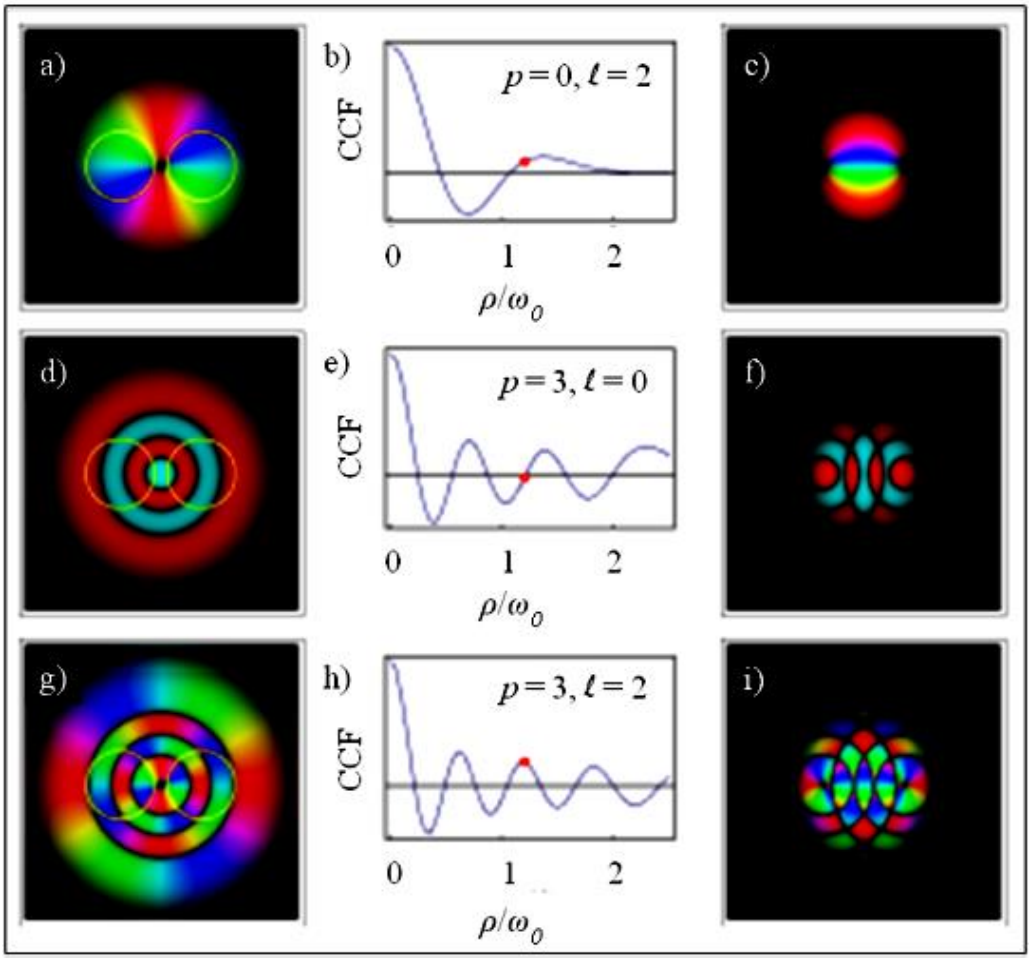

Fig. 7.2. Step by step numerical simulation of the far-field CCF pattern for different mode indices of a partially coherent OV beam: (a - c) p = 0, ℓ = 2; (d - f) p = 3, ℓ = 0; (g - i) p = 3, ℓ = 2. The phase is represented by the hue and the amplitude by the luminosity. Parts (a, d, g) correspond to the beam profile superimposed by the two regions that are used for each CCF point. Parts (c, f, i) correspond to the CCF integrand and parts (b, e, h) to the CCF as a function of the radial distance.

In the 'horizontal' direction, it is shown that the p dark dislocation rings originating from the $p \neq 0$ beam appear doubled up, one for each region. In the 'vertical'

direction, it is shown that the phase changes due to the ℓ vortex charge. As the distance between the two regions increases, a number of destructive interferences appear, each corresponding to a dark dislocation ring in the far-field CCF (Figure 7.2). The number of destructive interferences is given by $2p + |\ell|$ originating from the doubling up of the rings due to the three regions and ℓ originating from the $2\pi\ell$ phase changes in the 'vertical' direction. Therefore, a relationship between the number of dark dislocation rings in the far-field CCF and the radial and azimuthal mode indices of a partially coherent LG beam, can be established as: $N_d = 2p + |\ell|$.

7.3.2 Calculation of the spatial coherence

According to the van Cittert-Zernike theorem, the effective coherence length, L_c, after the use of a rotating diffuser may be written as [195]:

$$R = \frac{L_c^{(@f)}}{w_f} \approx \frac{3.2787 w_i w_s}{\lambda f} \tag{7.6}$$

where, w_i is the initial beam radius after the ISLM, f = 1m is the focal length of the lens after the ISLM, w_s is the aperture radius on the PSLM and w_f is the focal spot radius on the focal plane after PSLM, where the SLM pixel size is 8μm. This relationship can be visualized to the following graph (Figure 7.3). The ratio between L_c and w_f decreases dramatically with the increasing coherence.

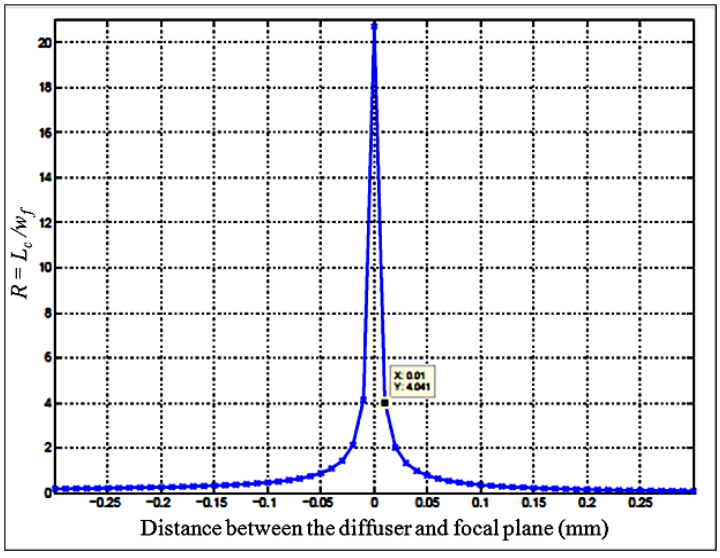

Fig. 7.3. Relationship between the ratio $R = L_c/w_f$ and the diffuser location (step by step numerical calculation for different distances based on Equation 7.6). One can see that the ratio decreases gradually with the increasing coherence.

7.4 Experiments

In this section, the general relationship between the dislocation rings of the far-field CCF and the radial and azimuthal mode indices of partially coherent OVs is experimentally verified. It is demonstrated that the number of dark dislocation rings (N_d) in the far-field CCF have a clear relation with the radial and azimuthal mode indices as shown in Equation (7.5), i. e. $N_d = 2p + |\ell|$. Our experimental data verify that the number of dislocation rings in the far-field CCF of a partially coherent vortex beam is exactly equal to the azimuthal index $|\ell|$ when $p = 0$, which is in agreement with the recent theoretical work [71]. Thus, this study shows one may determine both the radial and azimuthal mode indices of a partially spatially coherent vortex field by observing the CCF in the far-field.

7.4.1 Experimental setup

Here, the CCF of a partially coherent vortex beam was measured with the aid of a wavefront folding (WFF) interferometer [188]. A schematic overview of the experimental setup is shown in Figure 7.4. A partially coherent optical field is generated by focusing a He-Ne laser beam (λ = 633nm, P_{max} = 5mW) onto a rotating holographic diffuser (Edmund Optics, 0.5^o diffusing angle). The spatial coherence of the optical field is controlled by changing the position of the holographic diffuser along the optical axis, as previously seen in 7.3.2 [195, 196].

The beam is re-collimated onto a dual display liquid crystal spatial light modulator (SLM) system (Holoeye, HEO1080P). The first SLM display ISLM in conjunction with two crossed polarisers P_1 and P_2 performs intensity modulation of the beam and the second display PSLM modulates the phase. For this, the linearly polarized laser beam is expanded with a telescope (L_1 and L_2) such that it visually fills the active area of the ISLM with homogeneous intensity. The polarizer P_1 makes sure the polarization is correct. Depending on the encoded 8-bit value the ISLM turns the polarization of the light such that the intensity is spatially modulated by the polariser P_2. Via a 1 : 1 telescope consisting of lenses L_3 and L_4, the ISLM is imaged onto the PSLM and the half-waveplate ($\lambda/2$) turns the polarization as it is required for phase modulation by the PSLM, where an intensity-coded phase function [197] is imprinted in order to generate LG beams with different radial and azimuthal mode indices. By selecting the first diffraction order with a pinhole ($Pinhole_1$), we realise a partially coherent vortex beam results at the back focal plane of lens (L_5) with a designated radial and azimuthal mode indices (p, ℓ). This partially coherent vortex field is then imaged onto a CCD camera (Basler pilot piA640-

210gm, 648 × 488 pixel resolution, 7:4μm pixel pitch) by a 2× telescope (L_6 and L_7).

The spatial distribution of the far-field CCF can be obtained by the WFF interferometer. The WFF interferometer was created by placing two Dove prisms, DP_1 and DP_2, in each arm of the Mach-Zehnder interferometer. These prisms inverted the beam in one arm across the x-axis $\left[E_1(x',y')=E(-x',y')\right]$ and the other arm across the y-axis $\left[E_2(x',y')=E(x',-y')\right]$. When both optical arms in the WFF interferometer are unblocked, the recorded interference intensity patterns can reveal the locations of dislocation rings in the CCF which are sued to determine the original radial and azimuthal mode indices. The aberrations due to unevenness of the display surfaces were corrected by a wavefront correction using the OEi technique (see Appendix C) [155, 156].

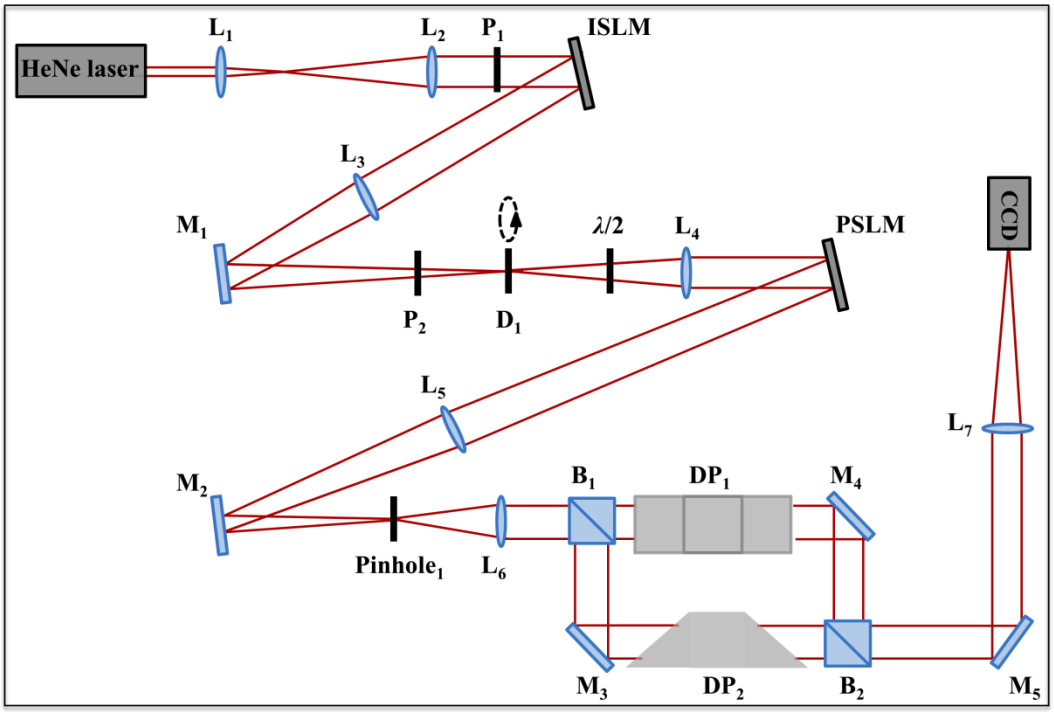

Fig. 7.4. Schematic of the experimental apparatus used for measuring the dislocation rings of CCF in a partially coherent vortex field. D = rotating glass diffuser, L = lens, P = polariser, SLM = spatial light modulator, M = mirror, CCD = charge coupled camera, B = beam splitter cube and DP = dove prism. Focal widths of lenses: f_1 = 50mm, f_2 = 250mm, f_3 = f_4 = 400mm, f_5 = 1000mm, f_6 = 200mm, and f_7 = 400mm.

A circular aperture (Ap_1) was displayed onto the ISLM of 500 pixels in diameter (the pixel bitch is 8μm). The spatial coherence of the source was controlled by varying the position of the rotating diffuser in the focal plane of the circular aperture

(Ap_1). During the experiment the rotating diffuser was mounted onto a translation stage with a precision of ±0.005mm. The dislocation rings may be observed at a very high contrast in the raw interference patterns without any post processing if we set the coherent length and the beam waist properly. At the largest transverse coherence length, the predicted ring dislocation was barely detectable.

7.4.2 Experimental measurement of the degree of coherence

Since the fundamental paper on partial coherence in 1938 of Zernike's [198], the measurement of the maximum visibility of the interferences obtainable from two points in a wave field is defined as their degree of coherence, γ_{12} [195, 199, 200]. Here, double slits were displayed onto the PSLM of 300 pixels in length and 150 pixels in width (the pixel bitch is 8μm). Let I_{max} be the maximum intensity and I_{min} be an adjacent minimum; then the visibility of the fringes υ, is given by:

$$\upsilon = \frac{I_{\max} - I_{\min}}{I_{\max} + I_{\min}} \tag{7.17}$$

Hence, when $I_{max} = I_{min}$, $\upsilon = 0$ and $|\gamma_{12}| = 0$. This is the incoherent limit. When $I_{min} = 0$ (very sharp fringes), $\upsilon = 1$ and $|\gamma_{12}| = 1$. This is the coherent limit. Here, the degree of coherence was investigated over a range of different positions of the rotating glass diffuser. The two beams selected by the two slits (displayed in PSLM) were then allowed to interfere and the resulting fringes were investigated. In the quasi-monochromatic approximation the function γ_{12} is given by:

$$\gamma_{12} = 2J_1(x)/x \tag{7.18}$$

where $J_1(x)$ is a Bessel function of the first kind and x is a function of the separation of the two points, α, and the angle subtended by the diameter of the source at the mid-point of the line joining the two points, φ, and it is given by:

$$x = \frac{2\pi}{\lambda}\alpha \sin\varphi \tag{7.19}$$

The degree of coherence γ_{12} may be split up into its magnitude, g_{12}, and its relative phase, β_{12}, which may have a value of either 0 or π. The following Figures 7.5 – 7.7 show the variation in the degree of coherence for each position, P, of the rotating glass diffuser at the focal plane of lens L_3. The observed fringe systems and the calculated intensity distributions are shown. The chain lines represent the maximum and minimum of intensity and the fall-off is due to the diffraction envelope associated with the individual slits. Thus, this well-known double slits method can provide information about the degree of coherence in our optical system.

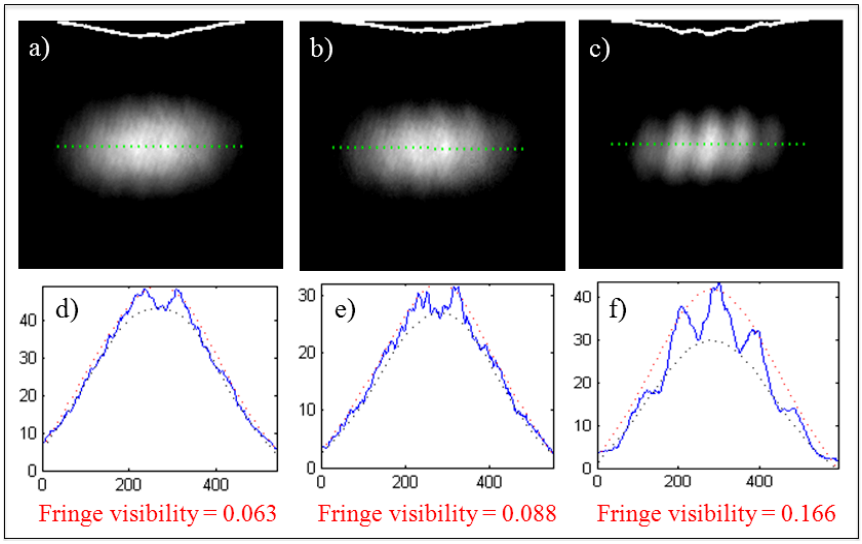

Fig. 7.5. Two-beam interference with partially coherent light, showing the change of phase. a) – c) Observed interference patterns and, d) – f) observed intensity curves, respectively. The chain lines represent the curves I_{max} and I_{min}. d) g_{12} = 0.063, $\beta_{12} = \pi$ at position P_1 = 0mm; e) g_{12} = 0.088, $\beta_{12} = \pi$ at P_2 = 5mm, and f) g_{12} = 0.166, $\beta_{12} = 0$ at P_3 = 10mm.

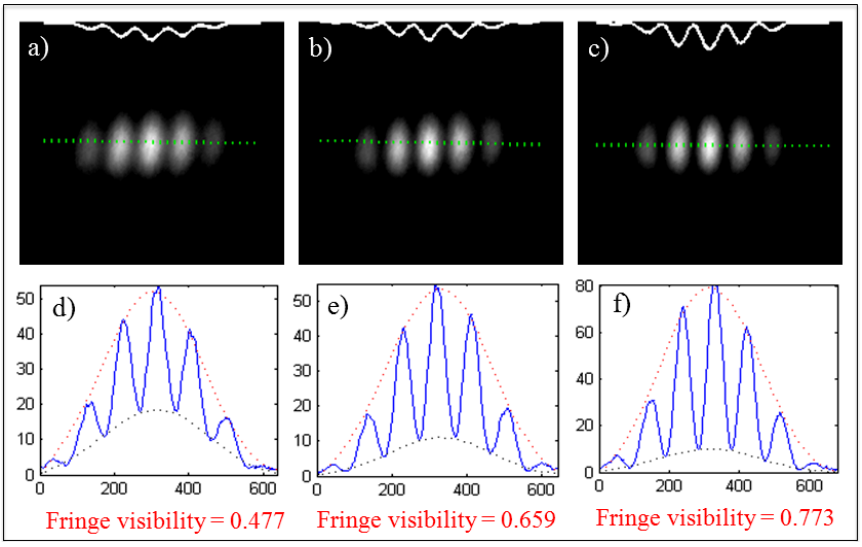

Fig. 7.6. Two-beam interference with partially coherent light, showing the change of phase. a) – c) Observed interference patterns and, d) – f) observed intensity curves, respectively. The chain lines represent the curves I_{max} and I_{min}. d) g_{12} = 0.477, $\beta_{12} = 0$ at P_4 = 15mm; e) g_{12} = 0.659, $\beta_{12} = 0$ at P_5 = 17.5mm, and f) g_{12} = 0.773, $\beta_{12} = 0$ at P_6 = 20mm.

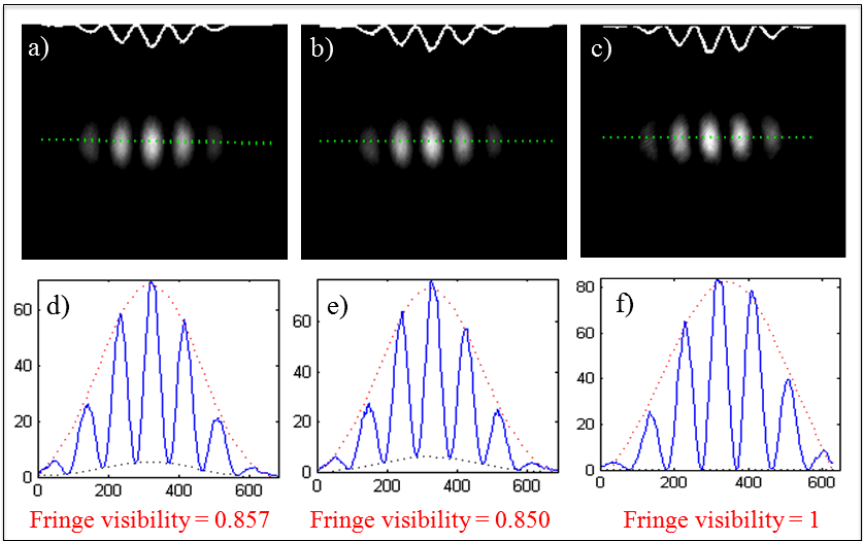

Fig. 7.7. Two-beam interference with partially coherent light, showing the change of phase. a) – c) Observed interference patterns and, d) – f) observed intensity curves, respectively; d) $g_{12} = 0.857$, $\beta_{12} = 0$ at $P_7 = 22.5$mm; e) $g_{12} = 0.850$, $\beta_{12} = 0$ at $P_8 = 25$mm, and f) $g_{12} = 1$, $\beta_{12} = 0$ at $P_1 = 0$mm for an incident coherent Gaussian beam.

7.4.3 Dependency of the far-field CCF upon the mode indices of a partially coherent vortex field

In the present study, partially coherent LG beams with both radial and azimuthal mode indices ranging each from 1 to 4, increasing in integer step, were considered. The experimentally observed interference patterns when $\ell = 1$ to 4, increasing in integer step, and $p = 1, 2$ are presented in the following Figures 7.8 and 7.9.

As it can be predicted, the phase dislocation ring is located at the π phase shift which is indicated by the fringe shift (from bright to dark) in the recorded interference patterns. A clear relationship between the number of dislocation rings (N_d) in the CCF and the mode indices (p and ℓ) can be established as $N_d = 2p + |\ell|$, which is in agreement with the theoretical prediction described in the previous section. Then, the far-field CCF of the different partially coherent LG beams with azimuthal indices $\ell = 1$ to 4, increasing in integer step and radial indices $p = 3, 4$ were experimentally observed and are presented in the following Figures 7.10 and 7.11.

In Figure 7.8, the dislocation rings are experimentally observed and visualized by dashed-line black concentric circles for clarity. It should be noted that the ring size is dictated by the coherence length and the beam waist size. In this study, the dislocation rings may be observed at a very high contrast in the raw interference

patterns in the absence of any post processing if the coherence length and the beam waist are properly adjusted. From the experimental results presented in the present subsection, a clear relationship between the number of dislocation rings in the CCF, which is represented by the dislocation rings in the Figures 7.8 – 7.11, and the mode indices (p, ℓ) of a partially coherent OV, as in Equation (7.5), can be established. These experimental results verify our theoretical and numerical predictions described in the previous section.

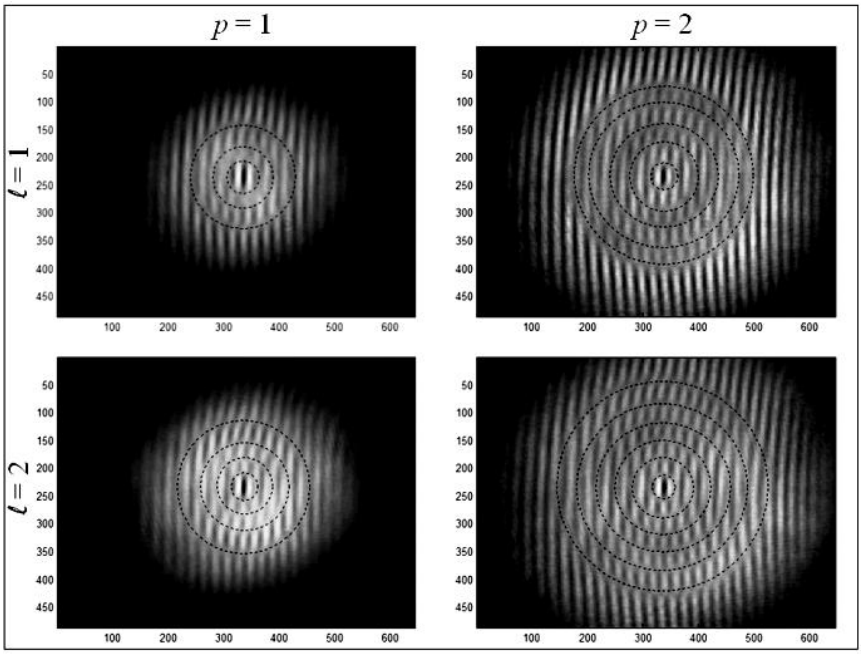

Fig. 7.8. Far-field CCFs of partially coherent LG beams (ℓ = 1, 2 and p = 1, 2). The beam waist on the CCD, w, is given by: w = 2.7mm. Degree of coherence is measured as 0.05 by the previously described double-slit method at position P_1 = 0mm. Dashed-line black concentric circles are drawn purposely to visualize phase dislocation rings. The light intensity increases from black to white.

In the current study, the values of $|\ell|$ and p are limited by our present setup to no more than 5. For example, rings may go out of range of the CCD chip when p is larger. The method presented here is also limited by the number of detectable optical degrees of freedom of the far-field CCF [176]. Indeed, low resolution cameras would greatly decrease the distinguishability between the different partially coherent beams and decrease the number of modes that can be detected.

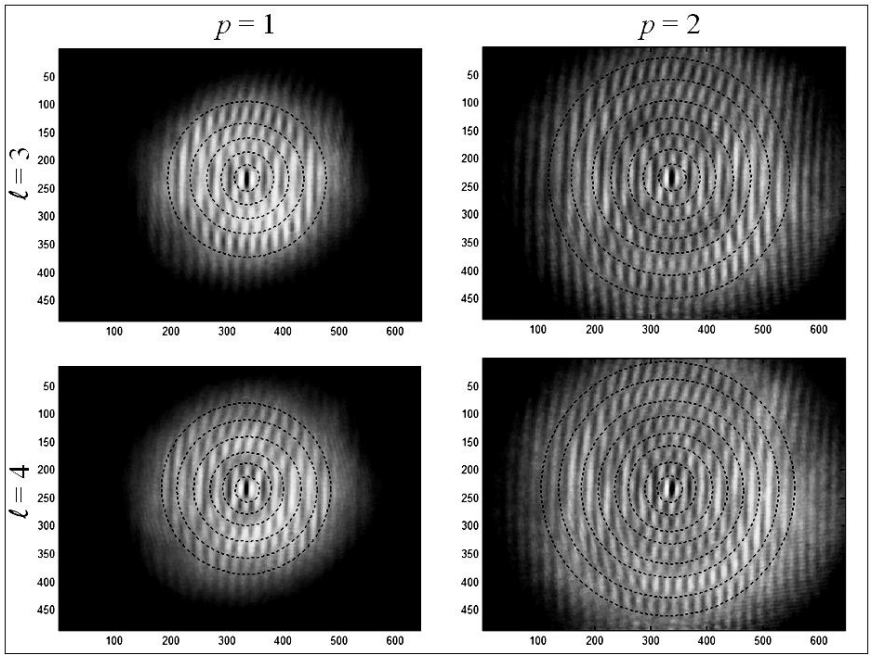

Fig. 7.9. Far-field CCFs of partially coherent LG beams (ℓ = 3, 4 and p = 1, 2). w = 2.7mm for LG_{31} and LG_{32} beam modes, and w = 3.2mm for LG_{41} and LG_{42} beam modes (w is the beam waist on the CCD). Degree of coherence is measured as 0.05 at position P_1 = 0mm. Dashed-line black concentric circles are drawn purposely to visualize phase dislocation rings.

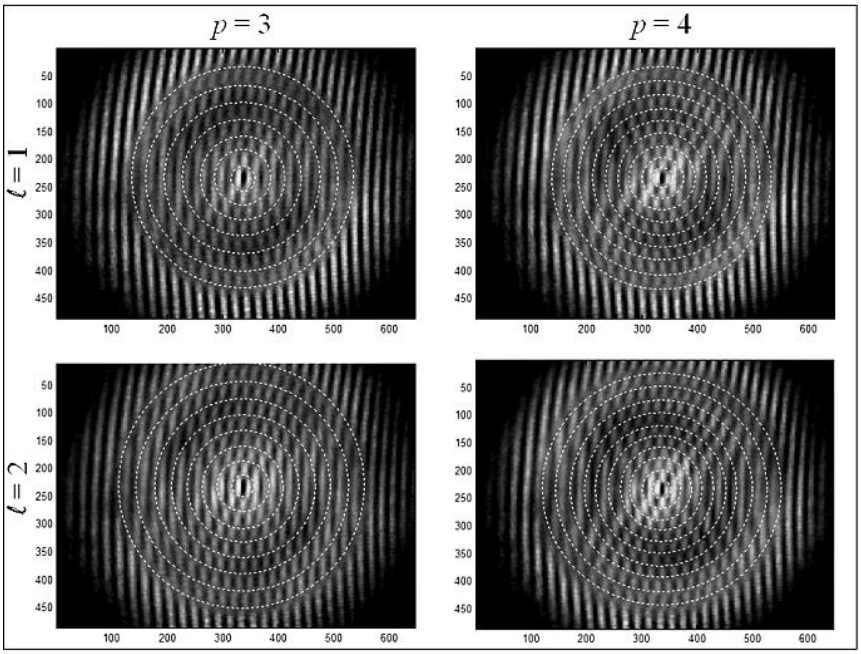

Fig. 7.10. Far-field CCFs of partially coherent LG beams (ℓ = 1, 2 and p = 3, 4). w = 2.7mm, which is the beam waist on the CCD. Degree of coherence is measured as 0.05 at position P_1 = 0mm. Dashed-line white concentric circles are drawn purposely to visualize phase dislocation rings. The light intensity increases from black to white.

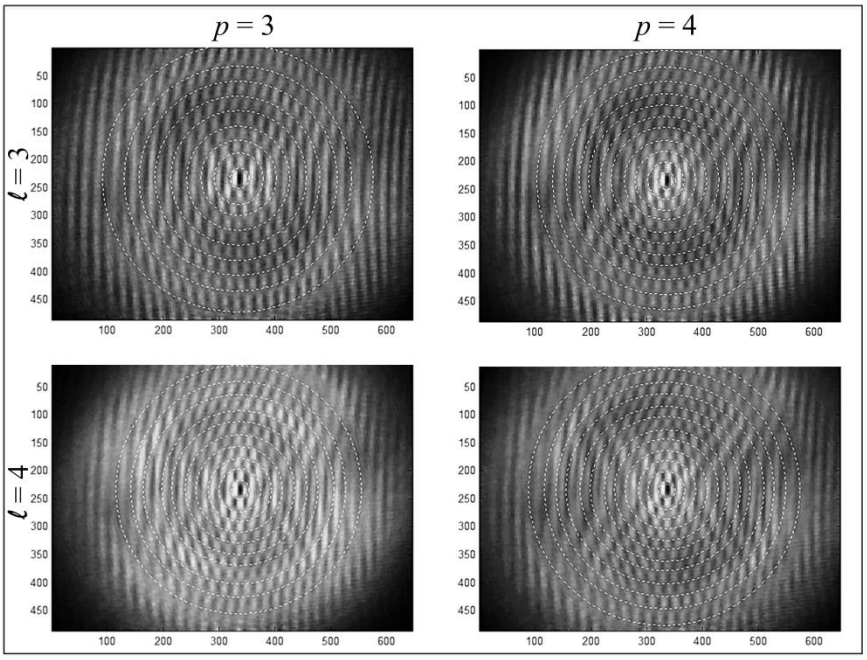

Fig. 7.11. Far-field CCFs of partially coherent LG beams (ℓ = 3, 4 and p = 3, 4). w = 2.7mm for LG_{33}, and w = 3.2mm for LG_{34}, LG_{43} and LG_{44} beam modes (w is the beam waist on the CCD). Degree of coherence is measured as 0.05 at position P_1 = 0mm.

In the case of a partially coherent LG beam with both mode indices equal to five, $\ell = p = 5$, the contrast in the interference pattern is too low to precisely locate the dislocation rings. Actually, both ℓ and p mode indices can go up to higher values while one can still have the established relationship if for example a larger CCD could be used, a different telescope with a higher magnification, a lower coherent field or a more powerful laser source.

For the partially coherent beams with no embedded vortices (ℓ = 0), two experiments were performed for the different cases of p = 1, 2 (Figure 7.12). The number of dislocation rings in the recorded far-field CCFs is equal to $2p$, which obeys the relation in Equation (7.5). Due to the limited purity of generated LG beams with our method, the central spot when ℓ = 0 has very high intensity and makes the other outer rings very dim. As a result, the data showed very low contrast in the far-field CCFs when $p > 2$ and $\ell = 0$.

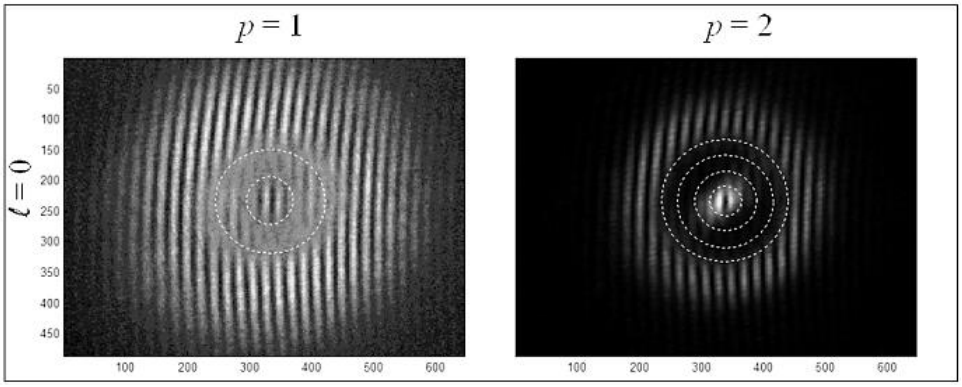

Fig. 7.12. Far-field CCFs of partially coherent LG beams with p = 1, 2 and ℓ = 0. w = 2.2mm, which is the beam waist on the CCD. Degree of coherence is measured as 0.05 at position P_1 = 0mm. Dashed-line white concentric circles are drawn purposely to visualize phase dislocation rings. The light intensity increases from black to white and the exposure time was altered in order to highlight the characteristics of the interference patterns.

7.4.4 Measuring the topological charge of partially coherent OVs through correlation singularities in their far-field CCFs

It is straight forward to deduce the topological charge of a partially coherent LG beam from its far-field CCF by simply counting the number of dislocation rings in the far-field CCF images, when $p = 0$ while $\ell \neq 0$. Our experimental data verify that the number of dislocation rings in the far-field CCF of such a partially coherent vortex beam is exactly equal to the azimuthal index (topological charge) $|\ell|$, which is in agreement with the recent theoretical work [71]. Let us start by generating the coherent LG beams with different azimuthal indices, ℓ ranging from 0 to 3 increasing in integer step, while the radial index was kept zero, $p = 0$.

The following Figures 7.13 and 7.14 show the far-field intensity profile and cross-correlation functions (CCFs) for coherent LG beams; the rotating diffuser has not been used in this case. As expected, the coherent vortex fields have a well define dark core in the far-field intensity profile and CCF images. Then, the far-field intensity profile and CCFs for partially coherent OVs for different positions of the rotating diffuser, which result in different coherence lengths, were considered. The dark vortex core fills with diffuse light as the coherence decreases, a feature well established in the literature [188].

Furthermore, interestingly dislocation rings appear in the dark core of the vortex fields in the far-field CCF images as the degree of coherence decreases (Figures 7.15 and 7.17). Although, the dislocation rings in the far-field CCF are still not distinguishable for a higher-order vortex field, in this case, when $\ell = 3$.

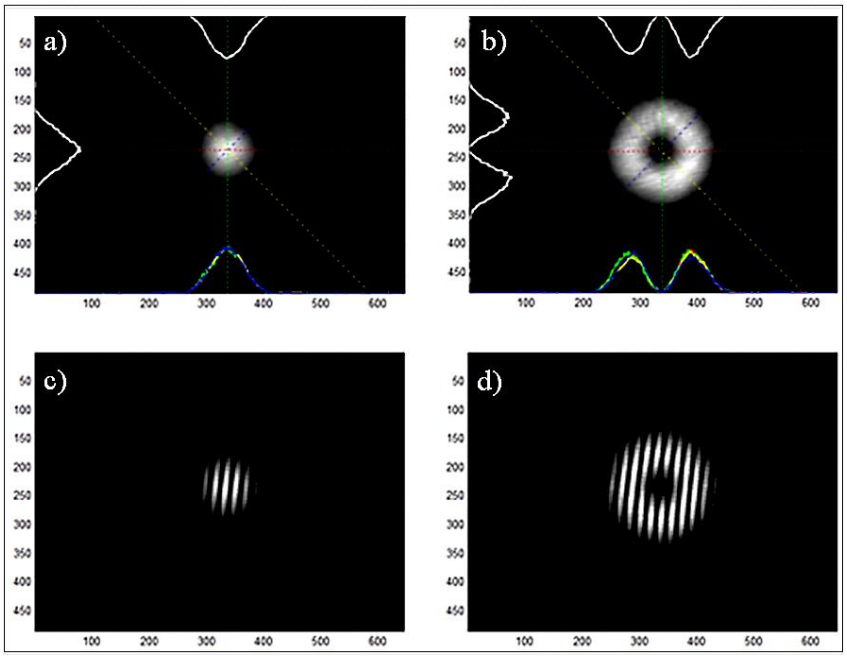

Fig. 7.13. Experimentally observed far-field intensity profile and CCF. Coherent LG beams with a) $\ell = 0$ to b) $\ell = 1$ were generated and their CCFs are presented in c) and d), respectively. The light intensity increases from black to white.

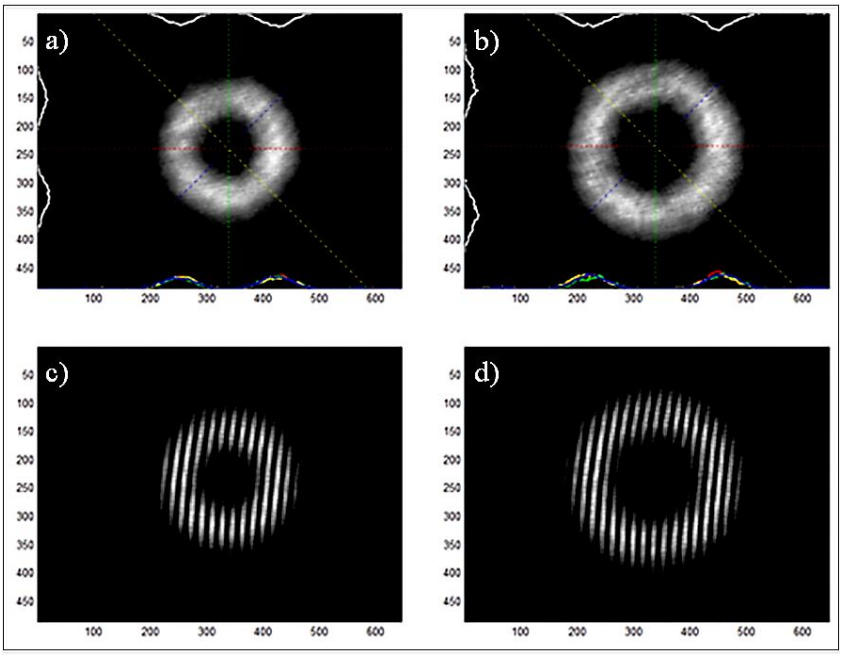

Fig. 7.14. Experimentally observed far-field intensity profile and CCF. Coherent LG beams with a) $\ell = 2$ to b) $\ell = 3$ were generated and their CCFs are presented in c) and d), respectively.

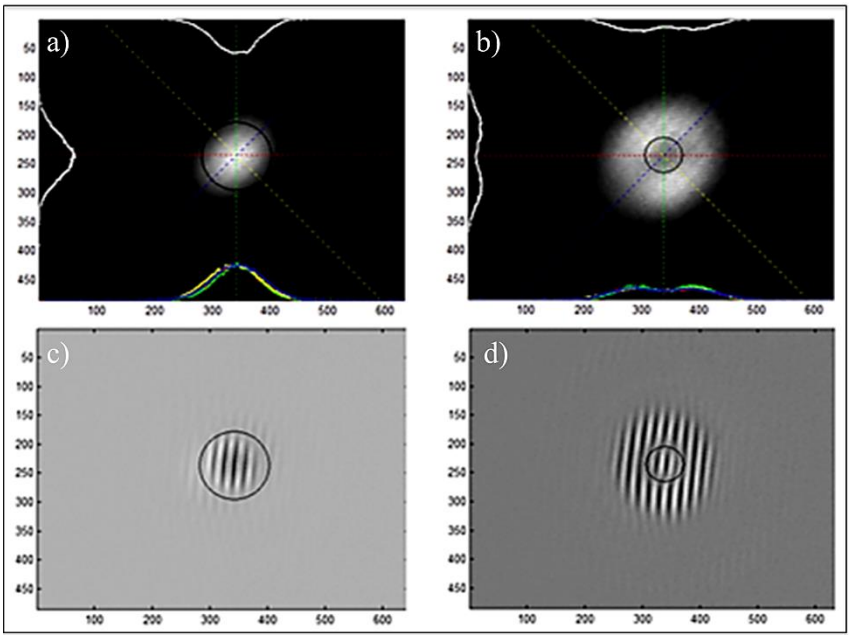

Fig. 7.15. Experimentally observed far-field intensity profile and CCF. Partially coherent OVs with a) $\ell = 0$ to b) $\ell = 1$ were generated and their far-field CCFs are presented in c) and d), respectively. Degree of coherence is measured as 0.849 at position P_7 = 22.5mm. The region of the dislocation rings is indicated by the black circles.

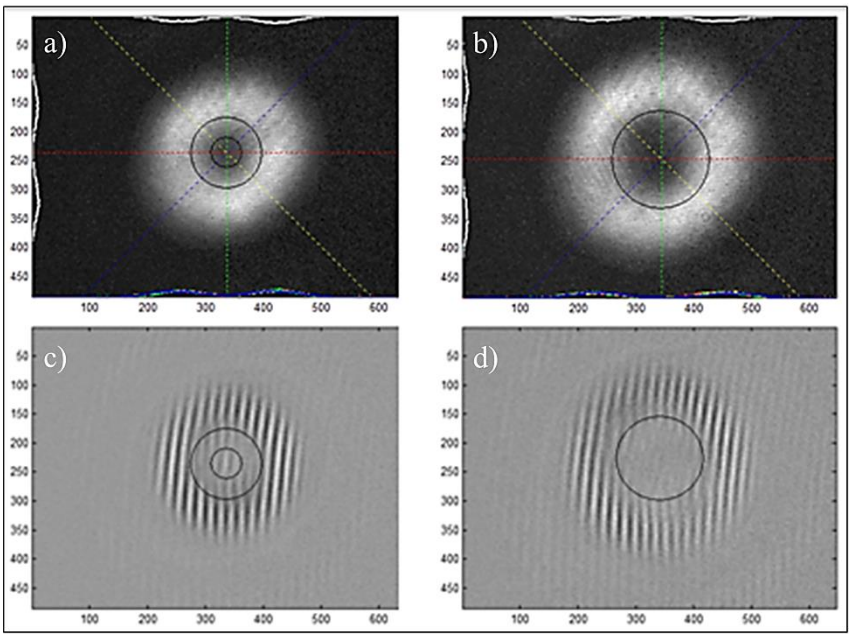

Fig. 7.16. Experimentally observed far-field intensity profile and CCF. Partially coherent OVs with a) $\ell = 2$ to b) $\ell = 3$ were generated and their far-field CCFs are presented in c) and d), respectively. Degree of coherence is measured as 0.849 at position P_7 = 22.5mm.

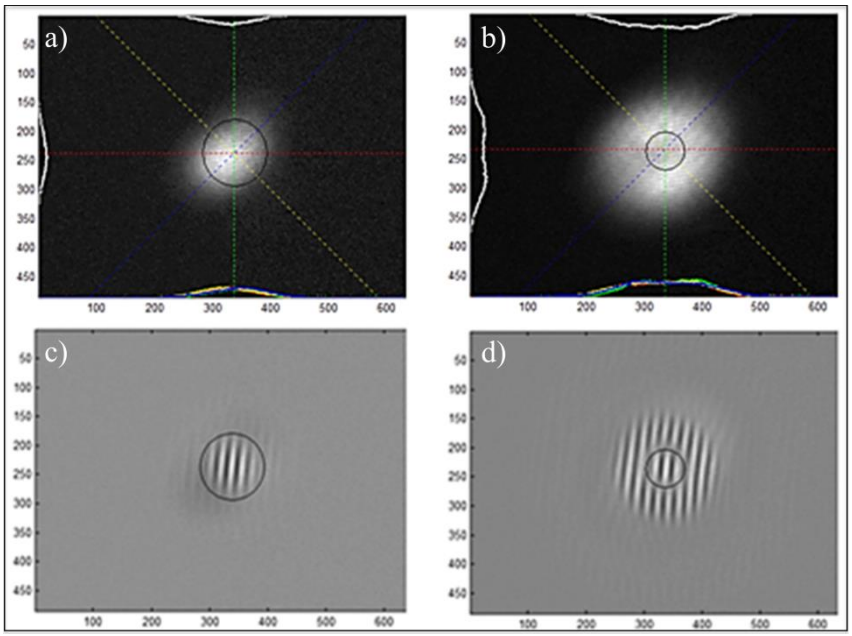

Fig. 7.17. Experimentally observed far-field intensity profile and CCF. Partially coherent OVs with a) $\ell = 0$ to $\ell = 1$ were generated and their far-field CCFs are presented in c) and d), respectively. Degree of coherence is measured as 0.464 at position P_4 = 15mm. The region of the dislocation rings is indicated by the black circles.

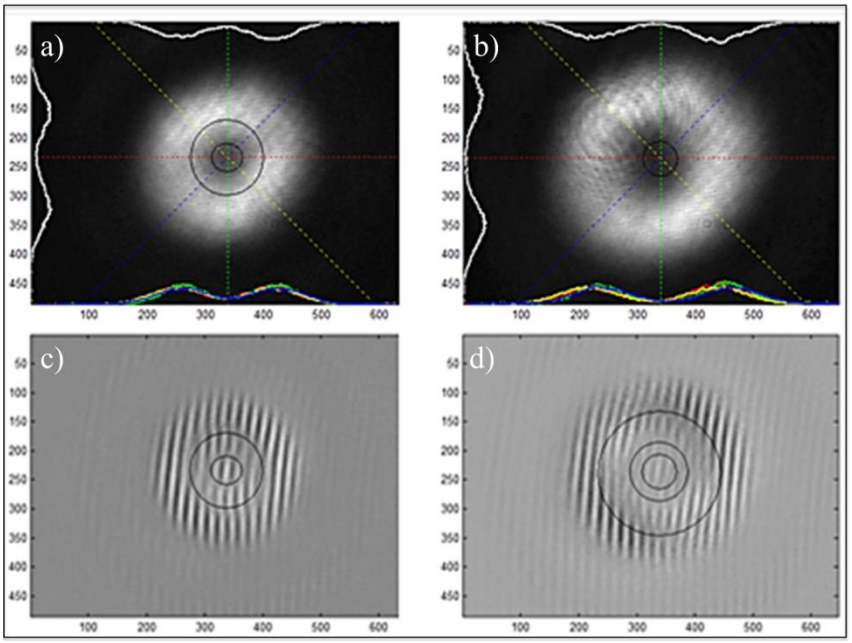

Fig. 7.18. Experimentally observed far-field intensity profile and CCF. Partially coherent OVs with a) $\ell = 2$ to b) $\ell = 3$ were generated and their far-field CCFs are presented in c) and d), respectively. Degree of coherence is measured as 0.464 at position P_4 = 15mm.

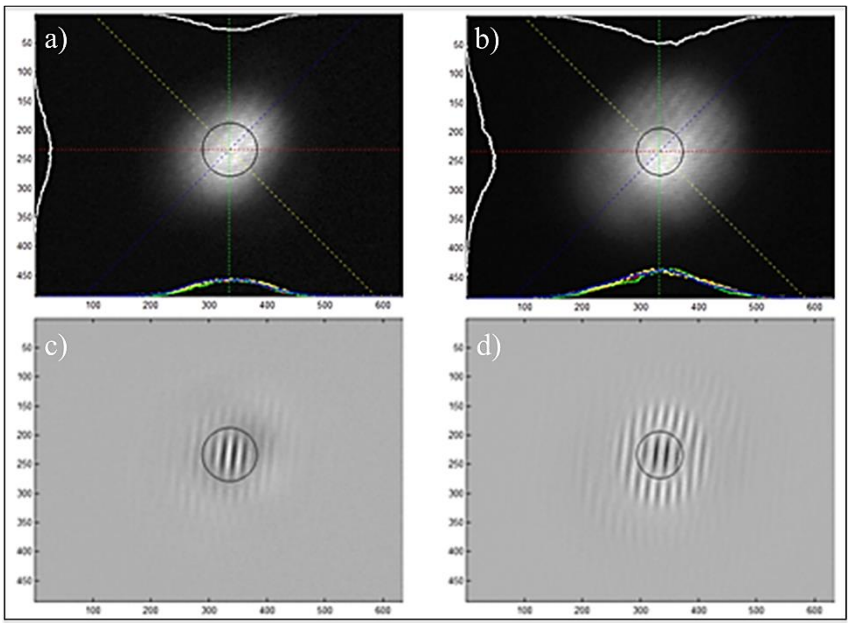

Fig. 7.19. Experimentally observed far-field intensity profile and CCF. Partially coherent OVs with a) $\ell = 0$ to b) $\ell = 1$ were generated and their far-field CCFs are presented in c) and d), respectively. Degree of coherence is measured as 0.078 at position P_2 = 5mm. The region of the dislocation rings is indicated by the black circles.

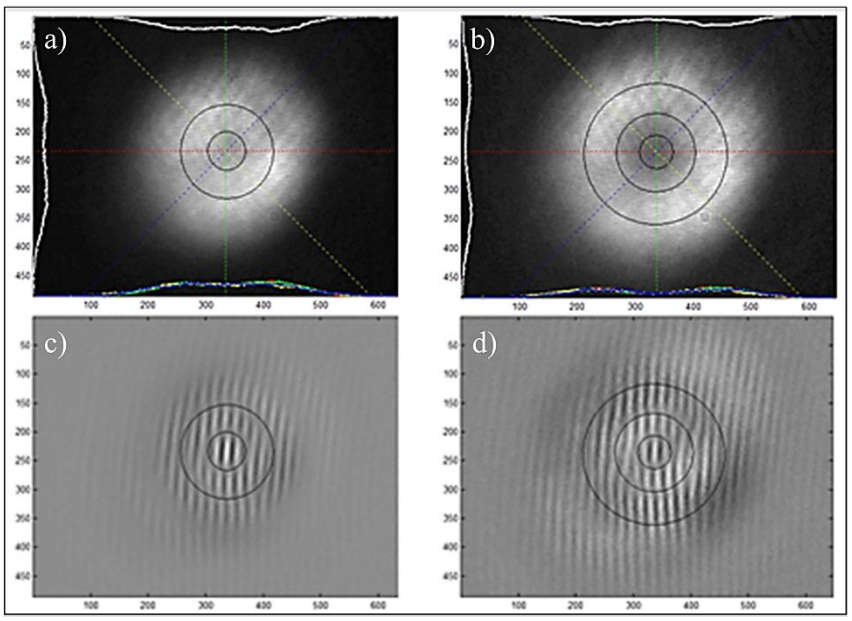

Fig. 7.20. Experimentally observed far-field intensity profile and CCF. Partially coherent OVs with a) $\ell = 2$ to b) $\ell = 3$ were generated and their far-field CCFs are presented in c) and d), respectively. Degree of coherence is measured as 0.078 at position P_2 = 5mm.

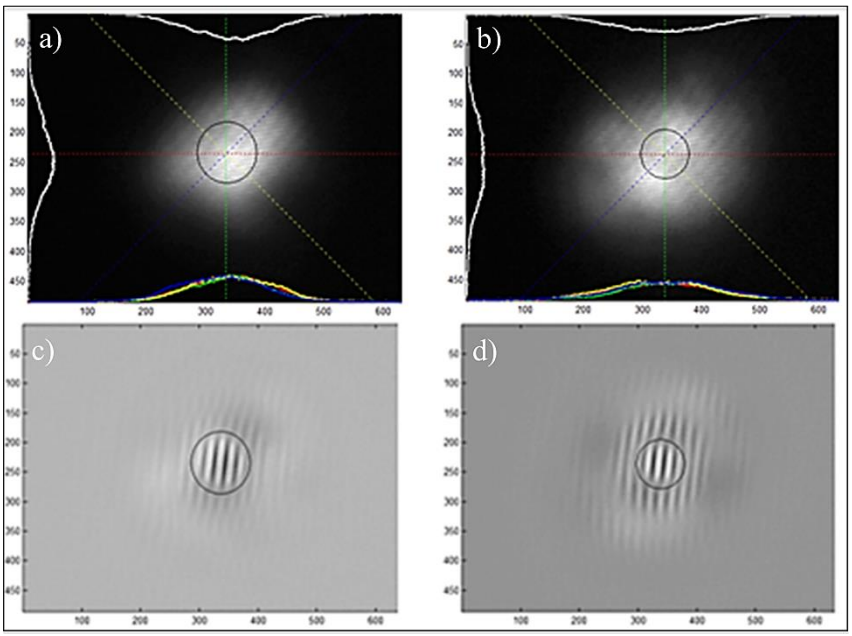

Fig. 7.21. Experimentally observed far-field intensity profile and CCF. Partially coherent OVs with a) $\ell = 0$ to b) $\ell = 1$ were generated and their far-field CCFs are presented in c) and d), respectively. Degree of coherence is measured as 0.05 at position $P_1 = 0$mm.

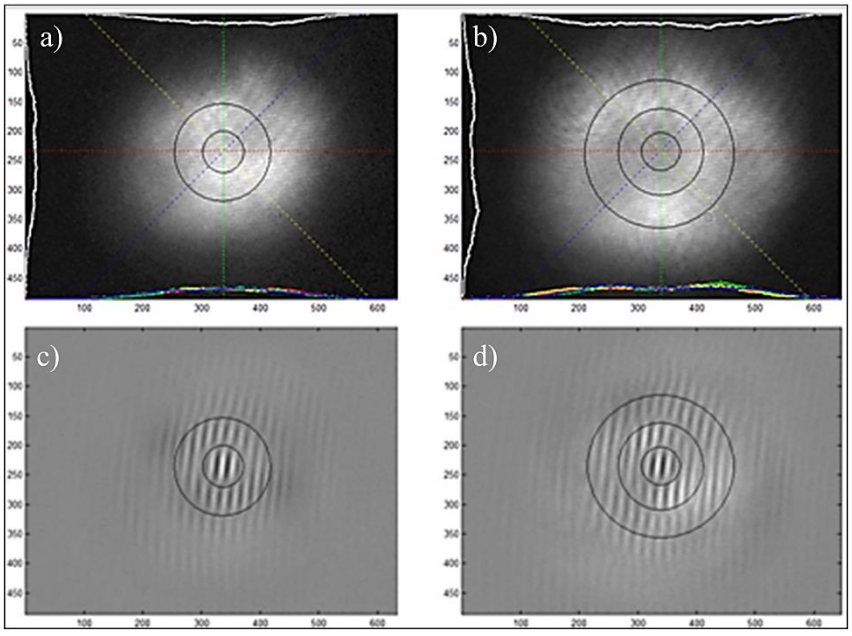

Fig. 7.22. Experimentally observed far-field intensity profile and CCF. Partially coherent OVs with a) $\ell = 2$ to b) $\ell = 3$ were generated and their far-field CCFs are presented in c) and d), respectively. Degree of coherence is measured as 0.05 at position $P_1 = 0$mm.

As the degree of coherence decreases to 0.464 at position P_4 = 15mm, the dislocation rings in the far-field CCF become visible even for the higher-order partially coherent vortex field, in this case, ℓ = 3 (Figure 7.18). These results are in agreement with the recently published theoretical prediction [71]. The various far-field CCFs with different topological charges for the partial and low-coherence cases of OVs are seen in the Figures 7.19 to 7.22 above.

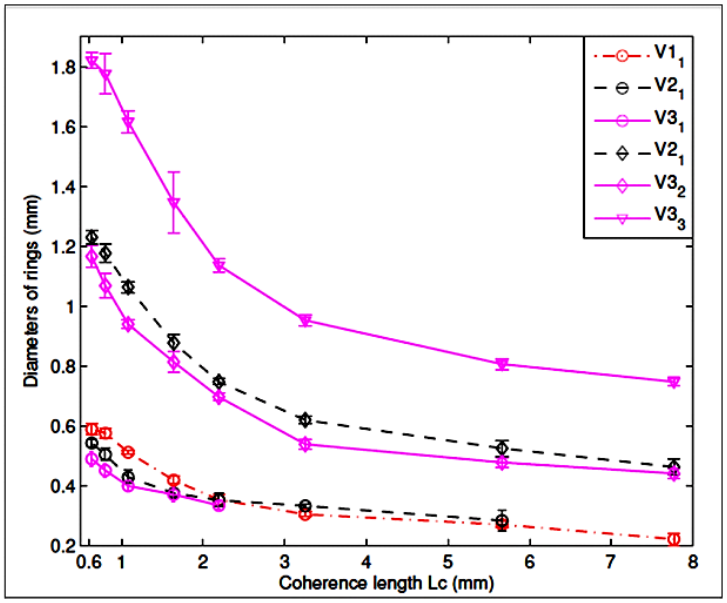

Fig. 7.23. Experimentally measured diameters of dislocation rings of the far-field CCFs as a function of the coherence length in partially coherence vortex beam when *p* = 0. The dislocation rings are presented with red dashed lines for ℓ = 1, with black dashed lines for ℓ = 2, and pink solid lines for ℓ = 3. Subscripts denote the mode indices of the dislocation rings. Each point is an average of five experimental measurements. The coherent length was estimated using the theoretical calculation described in section 7.3.2.

In the current subsection, the experimental verification of the recently published theoretical prediction for the measurement of the orbital angular momentum of partially coherent OVs through singularities in their cross-spectral density functions is presented [71]. Therefore, one can measure the topological charge of a partially coherent OV through the analysis of the CCF.

The relationship between the measured diameters of dislocation rings of the far-field CCFs and the coherence length of the partially coherent vortex beam is also plotted as presented in Figure 7.23. The diameter of dislocation rings decrease when the coherence length of the partially coherent vortex field becomes larger. In a highly coherent vortex field, the dislocation rings of the far-field CCFs vanish as recently theoretically described [71].

Finally, it should be noted that the measured interference patterns in subsection 7.4.3 are raw data without any post processing. However in subsection 7.4.4 the far-field CCFs were obtained by the measured interference patterns and subtracting the single intensities, which were obtained by blocking either arm of the interferometer.

7.5 Discussion and Conclusions

In conclusion, the dependency of the far-field cross-correlation function (CCF) on both the radial and azimuthal mode indices (p and ℓ) of a partially coherent optical vortex (OV) is demonstrated through an observation of the dislocation rings in the far-field cross-correlation function (CCF). A well-defined relationship between the number of the dislocations rings (dark zones), N_d of the far-field CCF and both the radial and azimuthal mode indices in the partially coherent OV can be established, as presented in Equation (7.5), i.e. $N_d = 2p + |\ell|$ and it is verified experimentally. These results are consistent with earlier experimental results for the limiting case of: $p = 0$, $\ell = 1$ [188].

In this study, the values of $|\ell|$ and p are limited by our present setup to no more than 4. Actually, both mode indices can go up to higher values while one can still have the established relationship if for example a larger CCD could be used, a different telescope with a higher magnification, a lower coherent field or a more powerful laser source.

Thus, the dependency of the far-field cross-correlation function (CCF) on both the radial and azimuthal degrees of freedom (p, ℓ) in a partially coherent light field through an observation of the phase correlation singularities is demonstrated. These results may contribute to a better understanding of the connection between the correlation vortices of a partially coherent field and the OVs of the corresponding fully coherent field. The dependency of the CCF upon both the radial and azimuthal mode indices of a partially coherent OV may create new ways to study other topological phenomena for the complex coherence function.

A. Mourka and Dr. M. Chen set up the optical system and performed the experimental work. Dr. Y. Yang and Dr. M. Mazilu assisted with the theoretical study. A. Mourka also contributed to the preparation of the manuscript. Manuscript accepted for publication in New J. Phys. (2013).

CHAPTER 8

Conclusions & Future work

8.1 Summary of the thesis

The study of light beams carrying angular momentum started with the realization by Poynting that circularly polarized light could exert torque on a cascaded array of quarter-waveplates [3]. Several experiments have been carried out to measure this quantity, including an elegant one proposed by Beth, where he used a birefringent half-waveplate hanging from a filament (see Figure 1.2) [5]. The mechanical torque measured in all these experiments relays on the polarization of the incident light and it is due to what is usually refer to as the spin angular momentum (SAM) of photons. Additionally, in early 1930s, Sir C. G. Darwin (the grandson of Charles Darwin) in his '*Notes on the Theory of Radiation*' made the first assumption that linear momentum at a radius exerts a torque [4]. Moreover, providing the lever is long enough, a fixed linear momentum can exert an arbitrary high torque. Several years later in 1992, a new form of angular momentum of light arising from the spatial mode of a light beam was realized by Allen et al. [1]. This form of angular momentum, called orbital angular momentum (OAM), has started new lines of research and found numerous applications, but is still at its early days [36, 37, 201]. The OAM of light is fundamentally associated with the phase properties of the light field. This contrast with the SAM associated to the polarization of the light field. Furthermore, the OAM of light is associated to screw dislocations embedded in the phase of the electromagnetic field and a quantized OAM of $l\hbar$ can be associated to this helically phased light beams, where l is the azimuthal mode index (sometimes it is denoted as the topological charge or winding number) indicating the number of multiples of 2π of phase change around one circumference of the optical axis (see Figure 1.1). Reference [90] gathers several published papers on both theoretical and experimental results in which the concept of OAM plays a crucial role.

An introduction to the present thesis and the light beams carrying OAM was presented in Chapter 1. This was followed, in Chapter 2, by a detailed discussion on the optical phase dislocations. The existing methods to produce the considered beam shapes were discussed, where the relevancy of technology in spatial light modulators (SLMs) to produce these beam shapes in an easy manner was also pointed out. Then, Chapter 3 described previous studies investigating diffraction of OVs past a variety of apertures and obstacles that can reveal interesting structural phase properties of the wavefronts of the considered LG beams and can be employed to measure the azimuthal mode index, ℓ, of an unknown vortex beam. In Chapter 4, an investigation into the far-field diffraction of LG beams with various azimuthal mode indices from a triangular aperture was explored. The behaviour of the far-field diffraction intensity pattern was shown to be dependent upon the Gouy phase of the light field

for the first time [49]. The evolution and form of the far-field diffraction intensity pattern from the triangular aperture for incident fields of fractional values of the azimuthal index has also been explored. The experimental data showed that the methodology is applicable to both monochromatic and broadband light sources and results in an intensity lattice forming a triangle. The magnitude of the azimuthal index, ℓ, is directly related to the external points (interference lobes) of the lattice. The total charge is given by $|\ell| = N - 1$, where N is the number of points on any side of the triangle. The far-field diffraction pattern will be rotated by 180^{o} in relation to the former when opposite signed value of the azimuthal index will be used. Therefore, this method is a direct way to determine the magnitude and the sign of the topological charge of the LG beam. This method allowed photons to be tested for one particular OAM state, but recently it was used for the measurement of the OAM at photon level via the spatial probability distribution, where it was also shown that by changing the aperture size it is possible to discriminate OAM state superpositions [162].

In this study, the values of ℓ are limited by our present setup to no more than 7 or less than -7. For example, the annular intensity profile may go out of range of the CCD chip when $|\ell|$ is larger. Actually, the values of the azimuthal mode indices, ℓ, can go up to higher values while one can still determine the azimuthal mode index by simply counting the number of interference lobes in the far-field diffraction intensity pattern, if for example a larger CCD could be used or a different telescope with a higher magnification. It should be also noted that the size of the triangular aperture should be chosen to be of the order of the waist size of the incident LG beam in order to collect maximum intensity from the annular shaped intensity profile of the LG beam under study. Finally, in Chapter 4, this method has only been considered for LG beams of zero radial index p, so next in Chapter 5 the far-field diffraction intensity pattern for LG beams of various both mode indices ℓ and p was numerically and experimentally explored to ascertain the performance of a triangular aperture.

Consequently, in Chapter 5, it was shown that the inclusion of the radial mode index, p, makes a dramatic difference to the form of the far-field diffraction pattern and is an important consideration in using a triangular aperture for measuring the azimuthal index, ℓ, but no clear rules could be established for determining both mode indices directly from the complex far-field diffraction patterns. Therefore, a new straight forward approach for the simultaneous determination of both the radial and azimuthal mode indices of LG beams using the method of the principal component analysis (PCA) was developed [53]. Our PCA detection method is based upon probing the far-field diffraction pattern from a random aperture and using the

recorded data as a 'training' set. Subsequently, we can transform the observed data into uncorrelated variables (principal components) using the PCA algorithm. Our PCA detection method is very simple to implement and uses a straightforward optical system (e.g. works with ground glass). It is based on the measurement of correlations between the probed far-field diffraction patterns and the 'training set' of preliminary recorded far-field diffraction patterns of the considered LG and superposed beams. The PCA calculates a projection of the 'unknown' beam onto the term of the mode composition. The experimental data show that the methodology preserves a high detectability in case of strong beam distortions (e.g. those caused by a random aperture), provided that the 'training set' members undergo the same distortions. Thus, it is tolerant to misalignment, beam fluctuations, rotation, focusing and defocusing provided it has been 'trained' for these fluctuations. Furthermore, the used mask does not need any clever design or complicated mathematical framework. The shape of the diffracting mask used to measure the mode indices is of little importance. The crucial step is 'training' any diffracting optical system. This allows the transformation of the observed far-field diffraction pattern into uncorrelated variables ('eigenfaces' or principal components) that can be mapped onto transversal mode profile index. Our method presented here is limited by the number of detectable optical degrees of freedom of the far-field diffraction pattern [176]. Since the correct detection can still be achieved, provided that either a larger 'training set' is considered and/or a larger dimensionality of the data is allowed by taking more PCs into account. In the current study, the values of $|\ell|$ and p are limited by our present setup to no more than 7.

Importantly, beam superpositions can be experimentally decomposed delivering the intensity of each mode and their relative phase. Here, our approach was extended to the more general case of a superposition of multiple Laguerre-Gaussian (LG) beams having different relative amplitudes and phases. To that end, we trained the PCA algorithm on a set of 900 random complex superpositions (keeping the total intensity constant) of four LG beams (ℓ = [0, 1] and p = [0, 1]). These results demonstrate the complete characterization of LG beams including both radial and azimuthal mode indices.

Our PCA approach is generic and was further extended to other families of light fields such as Hermite-Gaussian (HG) and Bessel beams (BBs) as it was next discussed in Chapter 6 [61]. It is important to establish the validity of our method to the other families of light fields to demonstrate its full applicability for various applications including information processing, spectroscopy and manipulation. Additionally, the role of rotational misalignments upon our method was investigated. This further degree of freedom is particularly important when

considering HG beams, which compared to LG or Bessel beams do not possess a cylindrical symmetry. Rotating the HG beam introduces additional degrees of freedom in the beam profile. This is clearly a different behaviour as in the case of pure LG beams for which a rotation would not induce any change of the beam profile. Furthermore, partially probed beams are more challenging and here the random mask helps in delivering a more adequate sample. Moreover, the use of a random aperture presents an experimental benefit as all diffraction patterns have similar peak intensities enabling acquisition with similar exposure durations. It should be noted that very specific misalignments, such as a rotation by $\pi/2$ for example, would make some HG modes indistinguishable. We can deduce from this statement that the PCA method is also limited by specific beam dependence misalignments. It should be also noted that in this study, the values of the HG or BB mode indices are limited by our present setup to no more than 6. The precise limitation can be assessed by considering the optical degrees of freedom (see section on Laguerre-Gaussian beam superposition in Chapter 5). Thus, our PCA detection approach is a powerful method for characterizing the optical multi-dimensional Hilbert space.

Whilst success has been seen for determining the azimuthal phase term of LG beams, the more typical and demanding case of partially coherent light fields has lagged behind its fully coherent counterpart in this respect. All of the previously presented studies have assumed that the optical field is fully coherent; however in Chapter 7, a study upon the dependency of the far-field cross-correlation function (CCF) on both the radial and azimuthal mode indices (ℓ and p) of a partially coherent OV is presented. For the case of partially coherent vortex light fields, the spatial correlation function shows interesting behaviour. Furthermore, the spatial correlation function may possess phase correlation singularities denoting nulls of the cross-spectral density function. In Chapter 7, this concept was both theoretically and experimentally generalized to show that looking for the dislocation rings in the cross-correlation function (CCF) can directly lead to a determination of both the azimuthal and radial mode indices of a partially coherent light field possessing OAM. Both the radial and azimuthal degrees of freedom need to be considered in tandem as both are needed to describe the full transversal state of the partially coherent light field. In this study, partially coherent LG beams with both radial and azimuthal mode indices ranging from 0 to 5, increasing in integer steps, were considered. As it can be predicted, the phase dislocation ring in the far-field cross-correlation function (CCF) is located at the π phase shift which is indicated by the one fringe shift in the recorded interference fringes. Our experimental results verify that the dislocation rings may be observed at a very high contrast in the raw interference patterns without any post processing if the coherence length and beam

waist are properly adjusted. The detectable values of $|\ell|$ and p are limited by our present setup to no more than 4. Without considering this limitation, a clear relationship between the number of dislocation rings in the CCFs and the mode indices (p, ℓ) of a partially coherent OV can be established as $N_d = 2p + |\ell|$. The dependency of the CCF upon both the radial and azimuthal mode indices of a partially coherent OV may create new ways to study other topological phenomena for the complex coherence function. On a final note, Jesus-Silva et. al. recently showed that a distributed triangular aperture can be used to study strong correlations between incoherent OVs using numerical intensity correlation [202].

Lastly, the present chapter summarizes the thesis and in the next section future work and applications will be suggested.

8.2 Future outlook

This thesis describes an investigation into the parameters that can delineate the properties of novel beam shapes, such as Laguerre-Gaussian (LG), Hermite-Gaussian (HG) and Bessel beams (BBs). Quantitative measurement of these parameters is essential for the studies and potential ground-breaking applications that these beams have found over the last few decades. Consequently, the advantages and challenges of the considered methods were highlighted and future directions have been pointed out.

One of the most promising applications of an OAM mode is found in quantum cryptography, where it can be used to code cryptographic keys with increased security in distribution having important consequences for new quantum information protocols [25]. Thus, in recent years, a lot of research has been devoted to study the more general case of a superposition of multiple light beams carrying OAM [174].

Our PCA detection method (that was discussed in Chapters 5 and 6) was applicable to a limited superposition of LG beams, and the intensity of each mode and their relative phase were measured. Our method is generic and may be extended to superpositions of different families of light fields. In future work, the applicability of the method to superposition of larger number of modes will be tested and its limitations for general beam characterization will be also studied.

We firmly believe that the modal characterization of novel beam shapes holds promise for a vibrant future full of exciting applications. For example, one could envisage the use of our PCA approach to detect low order aberrations that can be described by the family of Zernike polynomials. Additionally, this mode determination method may be applied beyond the field of electromagnetic to sound and matter waves, for example, and electron beams.

As seen in Chapter 6, our PCA method was successfully extended to HG and Bessel beams; thus it represents a powerful method for characterizing the optical multi-dimensional Hilbert space, which will be useful for many applications relating the optical technologies, such as the modal decomposition for optical fibers, laser resonators and information processing. Furthermore, our PCA approach could be also applied to optical manipulation so as to study the trap dynamics, like detecting the position and correlations in trapped particles motion.

Our PCA method is applicable for classical light fields and in the presented studies a laser beam (P = 5mW, HeNe) was used leading to a flux of 10^{20} photons/sec though lower light levels will suffice. Further, any method that measures a single photon is at the same time probing the transversal profile of this single photon. This profile is determined by the optical system that the photon propagates through prior to detection. This optical path can also include lenses to determine the plane wave component or holographic masks that achieve mode transformation mapping a circle into a line that is further focused onto a point [134-137]. Our PCA approach is a measure of multiple photons detected in the same OAM state and it cannot be translated to the single photon level detection because at the single photon level detection would only occur in a single pixel of the CCD. This will not deliver enough information for correct detection of the OAM state using the PCA approach.

To conclude, in the studies of partially coherent vortex beams, interesting questions are raised, such as: whether the OV is really there and when it evolves. Therefore, our PCA method may be combined with our study on the dependency of the far-field CCF on both the radial and azimuthal mode indices of a partially coherent LG beam in order to study the properties of a partially coherent vortex beam. This might be a major benefit that can contribute to a better understanding of the connection between the correlation vortices of a partially coherent field and the OVs of the corresponding fully coherent field. As a final remark, this approach could be employed in astronomy, where the interest for OAM has grown.

Bibliography

1. L. Allen, M. W. Beijersbergen, R. J. C. Spreeuw, and J. P. Woerdman, "Orbital angular momentum of light and the transformation of Laguerre-Gaussian laser modes," Phys. Rev. A **45**, 8185-8189 (1992).
2. M. Padgett, "Optics: Droplets set light in a spin," Nature **461**, 600-601 (2009).
3. J. H. Poynting, "The wave motion of a revolving shaft, and a suggestion as to the angular momentum in a beam of circularly polarized light." Proc. R. Soc. Lond. A **82,** 560 (1909).
4. C. G. Darwin, "Notes on the Theory of Radiation." Proc. R. Soc. Lond. A **136** (829), 36-52 (1932).
5. R. A. Beth, "Mechanical Detection and Measurement of the Angular Momentum of Light," Phys. Rev. **50**, 115-125 (1936).
6. M . P. Lee and M. J. Padgett, "Optical tweezers: a light touch," J. Microsc. **248**, 219-222 (2012).
7. A. Ashkin, "Acceleration and Trapping of Particles by Radiation Pressure," Phys. Rev. Lett. **24**, 156 (1970).
8. A. Ashkin, J. M. Dziedzic, J. E. Bjorkholm and S. Chu, "Observation of a single-beam gradient force optical trap for dielectric particles," Opt. Lett. **11**, 288-290 (1986).
9. H. He, M. E. J. Friese, N. R. Heckenberg, and H. Rubinsztein-Dunlop, "Direct Observation of Transfer of Angular Momentum to Absorptive Particles from a Laser Beam with a Phase Singularity," Phys. Rev. Lett. **75**, 826-829 (1995).
10. N. B. Simpson, K. Dholakia, L. Allen, and M. J. Padgett, "Mechanical equivalence of spin and orbital angular momentum of light: an optical spanner," Opt. Lett. **22**, 52-54 (1997).
11. M. E. J. Friese, T. A. Nieminen, N. R. Heckenberg, and H. Rubinsztein-Dunlop, "Optical alignment and spinning of laser-trapped microscopic particles," Nature **394**, 348-350 (1998).
12. V. Garcés-Chávez, K. Volke-Sepulveda, S. Chávez-Cerda, W. Sibbett, and K. Dholakia, "Transfer of orbital angular momentum to an optically trapped low-index particle," Phys. Rev. A **66**, 063402 (2002).

13. J. E. Curtis, and D. G. Grier, "Modulated optical vortices," Opt. Lett. **28**, 872-874 (2003).
14. R. Dasgupta, S. Ahlawat, R. S. Verma, and P. K. Gupta, "Optical orientation and rotation of trapped red blood cells with Laguerre-Gaussian mode," Opt. Express **19**, 7680-7688 (2011).
15. S. Mohanty, A. Uppal, and P. Gupta, "Self-rotation of red blood cells in optical tweezers: prospects for high throughput malaria diagnosis," Biotechnol. Lett. **26**, 971-974 (2004).
16. P. Galajda, and P. Ormos, "Complex micromachines produced and driven by light," Appl. Phys. Lett. **78**, 249-251 (2001).
17. M. E. J. Friese, H. Rubinsztein-Dunlop, J. Gold, P. Hagberg, and D. Hanstorp, "Optically driven micromachine elements," Appl. Phys. Lett. **78**, 547-549 (2001).
18. L. Paterson, M. P. MacDonald, J. Arlt, W. Sibbett, P. E. Bryant, and K. Dholakia, "Controlled Rotation of Optically Trapped Microscopic Particles," Science **292**, 912-914 (2001).
19. M. Padgett, and R. Bowman, "Tweezers with a twist," Nat. Photon. **5**, 343-348 (2011).
20. V. Bingelyte, J. Leach, J. Courtial, and M. J. Padgett, "Optically controlled three-dimensional rotation of microscopic objects," Appl. Phys. Lett. **82**, 829-831 (2003).
21. A. T. O'Neil, I. MacVicar, L. Allen, and M. J. Padgett, "Intrinsic and Extrinsic Nature of the Orbital Angular Momentum of a Light Beam," Phys. Rev. Lett. **88**, 053601 (2002).
22. V. Garcés-Chávez, D. McGloin, M. J. Padgett, W. Dultz, H. Schmitzer, and K. Dholakia, "Observation of the Transfer of the Local Angular Momentum Density of a Multiringed Light Beam to an Optically Trapped Particle," Phys. Rev. Lett. **91**, 093602 (2003).
23. M. B. Stephen, "Optical angular-momentum flux," J. Opt. B - Quantum S. O. **4**, S7 (2002).
24. S. Fürhapter, A. Jesacher, S. Bernet, and M. Ritsch-Marte, "Spiral interferometry," Opt. Lett. **30**, 1953-1955 (2005).
25. A. Mair, A. Vaziri, G. Weihs, and A. Zeilinger, "Entanglement of the orbital angular momentum states of photons," Nature **412**, 313-316 (2001).

26. B. Thidé, H. Then, J. Sjöholm, K. Palmer, J. Bergman, T. D. Carozzi, Y. N. Istomin, N. H. Ibragimov, and R. Khamitova, "Utilization of Photon Orbital Angular Momentum in the Low-Frequency Radio Domain," Phys. Rev. Lett. **99**, 087701 (2007).
27. Z. Bouchal, and R. Celechovský ,"Mixed vortex states of light as information carriers," New J. Phys. **6**, 131 (2004).
28. G. Molina-Terriza, J. P. Torres, and L. Torner, "Management of the angular momentum of light: preparation of photons in multidimensional vector states of angular momentum," Phys. Rev. Lett. **88**, 013601 (2002).
29. J. Wang, J.-Y. Yang, I. M. Fazal, N. Ahmed, Y. Yan, H. Huang, Y. Ren, Y. Yue, S. Dolinar, M. Tur, and A. E. Willner, "Terabit free-space data transmission employing orbital angular momentum multiplexing," Nat. Photon. **6**, 488-496 (2012).
30. F. Tamburini, E. Mari, A. Sponselli, B. Thidé, A. Bianchini, and F. Romanato, "Encoding many channels on the same frequency through radio vorticity: first experimental test," New J. Phys. **14**, 033001 (2012).
31. G. Gibson, J. Courtial, M. Padgett, M. Vasnetsov, V. Pas'ko, S. Barnett, and S. Franke-Arnold, "Free-space information transfer using light beams carrying orbital angular momentum," Opt. Express **12**, 5448-5456 (2004).
32. Y.-D. Liu, C. Gao, X. Qi, and H. Weber, "Orbital angular momentum (OAM) spectrum correction in free space optical communication," Opt. Express **16**, 7091-7101 (2008).
33. G. C. G. Berkhout, and M. W. Beijersbergen, "Measuring optical vortices in a speckle pattern using a multi-pinhole interferometer," Opt. Express **18**, 13836-13841 (2010).
34. F. Tamburini, B. Thide, G. Molina-Terriza, and G. Anzolin, "Twisting of light around rotating black holes," Nat. Phys. **7**, 195-197 (2011).
35. M. Merano, N. Hermosa, J. P. Woerdman, and A. Aiello, “How orbital angular momentum affects beam shifts in optical reflection,” Phys. Rev. A **82**, 023817 (2010).
36. S. Franke-Arnold, L. Allen, and M. Padgett, "Advances in optical angular momentum," Laser Photonics Rev. **2**, 299-313 (2008).
37. A. M. Yao, and M. J. Padgett, "Orbital angular momentum: origins, behavior and applications," Adv. Opt. Photon. **3**, 161-204 (2011).

38. M. W. Beijersbergen, L. Allen, H. E. L. O. van der Veen, and J. P. Woerdman, "Astigmatic laser mode converters and transfer of orbital angular momentum," Opt. Commun. **96**, 123-132 (1993).
39. M. W. Beijersbergen, R. P. C. Coerwinkel, M. Kristensen, and J. P. Woerdman, "Helical-wavefront laser beams produced with a spiral phaseplate," Opt. Commun. **112**, 321–327 (1994).
40. N. R. Heckenberg, R. McDuff, C. P. Smith, and A. G. White, "Generation of optical phase singularities by computer-generated holograms," Opt. Lett. **17**, 221-223 (1992).
41. S. N. Khonina, V. V. Kotlyar, R. V. Skidanov, V. A. Soifer, P. Laakkonen, and J. Turunen, "Gauss–Laguerre modes with different indices in prescribed diffraction orders of a diffractive phase element," Opt. Commun. **175**, 301-308 (2000).
42. R. K. Tyson, M. Scipioni, and J. Viegas, "Generation of an optical vortex with a segmented deformable mirror," Appl. Opt. **47**, 6300-6306 (2008).
43. L. Marrucci, C. Manzo, and D. Paparo, "Optical spin-to-orbital angular momentum conversion in inhomogeneous anisotropic media," Phys. Rev. Lett. **96**, 163905 (2006).
44. M. Harris, C. A. Hill, P. R. Tapster, and J. M. Vaughan, "Laser modes with helical wave fronts," Phys. Rev. A **49**, 3119-3122 (1994).
45. M. Padgett, J. Arlt, N. Simpson, and L. Allen, "An experiment to observe the intensity and phase structure of Laguerre-Gaussian laser modes," Am. J. Phys. **64**, 77-82 (1996).
46. S. Franke-Arnold, S. M. Barnett, M. J. Padgett, and L. Allen, "Two-photon entanglement of orbital angular momentum states," Phys. Rev. A **65**, 033823 (2002).
47. J. Leach, J. Courtial, K. Skeldon, S. M. Barnett, S. Franke-Arnold, and M. J. Padgett, "Interferometric Methods to Measure Orbital and Spin, or the Total Angular Momentum of a Single Photon," Phys. Rev. Lett. **92**, 013601 (2004).
48. J. M. Hickmann, E. J. S. Fonseca, W. C. Soares, and S. Chávez-Cerda, "Unveiling a Truncated Optical Lattice Associated with a Triangular Aperture Using Light's Orbital Angular Momentum," Phys. Rev. Lett. **105**, 053904 (2010).

49. A. Mourka, J. Baumgartl, C. Shanor, K. Dholakia, and E. M. Wright, "Visualization of the birth of an optical vortex using diffraction from a triangular aperture," Opt. Express **19**, 5760-5771 (2011).
50. K. Pearson, "LIII. On lines and planes of closest fit to systems of points in space," Philos. Mag. **2**, 559-572 (1901).
51. M. Turk, and A. Pentland, "Eigenfaces for Recognition," J. Cogn. Neurosci. **3**, 71-86 (1991).
52. M. Meyer, and J. Anderson, "Key Point Subspace Acceleration and soft caching," ACM Trans. Graph. **26**, 74 (2007).
53. M. Mazilu, A. Mourka, T. Vettenburg, E. M. Wright, and K. Dholakia, "Simultaneous determination of the constituent azimuthal and radial mode indices for light fields possessing orbital angular momentum," Appl. Phys. Lett. **100**, 231114 (2012).
54. H. Kogelnik, and T. Li, "Laser Beams and Resonators," Appl. Opt. **5**, 1550-1567 (1966).
55. L. Novotny, E. J. Sánchez, and X. Sunney Xie, "Near-field optical imaging using metal tips illuminated by higher-order Hermite–Gaussian beams," Ultramicroscopy **71**, 21-29 (1998).
56. A. E. Siegman, *Lasers* (University Science, 2004).
57. V. Garces-Chavez, D. McGloin, H. Melville, W. Sibbett, and K. Dholakia, "Simultaneous micromanipulation in multiple planes using a self-reconstructing light beam," Nature **419**, 145-147 (2002).
58. X. Tsampoula, V. Garces-Chavez, M. Comrie, D. J. Stevenson, B. Agate, C. T. A. Brown, F. Gunn-Moore, and K. Dholakia, "Femtosecond cellular transfection using a nondiffracting light beam," Appl. Phys. Lett. **91**, 053902 (2007).
59. F. O. Fahrbach, P. Simon, and A. Rohrbach, "Microscopy with self-reconstructing beams," Nat. Photon. **4**, 780-785 (2010).
60. C. H. Bennett, and D. P. DiVincenzo, "Quantum information and computation," Nature **404**, 247-255 (2000).
61. A. Mourka, M. Mazilu, E. M. Wright, and K. Dholakia, "Modal Characterization using Principal Component Analysis: application to Bessel, higher-order Gaussian beams and their superposition," Sci. Rep. **3**, 1422 (2013).

62. J. Arlt, V. Garces-Chavez, W. Sibbett, and K. Dholakia, "Optical micromanipulation using a Bessel light beam," Opt. Commun. **197**, 239-245 (2001).
63. S. Vyas, Y. Kozawa, and S. Sato, "Self-healing of tightly focused scalar and vector Bessel-Gauss beams at the focal plane," J. Opt. Soc. Am. A **28**, 837-843 (2011).
64. L. Paterson, E. Papagiakoumou, G. Milne, V. Garcés-Chávez, T. Briscoe, W. Sibbett, K. Dholakia, and A. C. Riches, "Passive optical separation within a 'nondiffracting' light beam," J. Biomed. Opt. **12**, 054017 (2007).
65. L. Paterson, E. Papagiakoumou, G. Milne, V. Garces-Chavez, S. A. Tatarkova, W. Sibbett, F. J. Gunn-Moore, P. E. Bryant, A. C. Riches, and K. Dholakia, "Light-induced cell separation in a tailored optical landscape," Appl. Phys. Lett. **87**, 123901 (2005).
66. G. Gbur, and. T. D. Visser, "The Structure of Partially Coherent Fields," in E. Wolf (Ed.) Prog. in Optics, **55**, 285 (Elsevier, Amsterdam, 2010).
67. G. Anzolin, F. Tamburini, A. Bianchini, G. Umbriaco, and C. Barbieri, "Optical vortices with starlight," Astrono. & Astrophy. **488**, 1159-1165 (2008).
68. H. F. Schouten, G. Gbur, T. D. Visser, and E. Wolf, "Phase singularities of the coherence functions in Young's interference pattern," Opt. Lett. **28**, 968-970 (2003).
69. G. Gbur, and T. D. Visser, "Coherence vortices in partially coherent beams," Opt. Commun. **222**, 117-125 (2003).
70. Y. Zhao, Z. Wang, H. Yu, S. Zhuang, H. Zhang, X. Xu, J. Xu, X. Xu, and J. Wang, "Direct generation of optical vortex pulses," Appl. Phys. Lett. **101**, 031113 (2012).
71. Y. Yang, M. Mazilu, and K. Dholakia, "Measuring the orbital angular momentum of partially coherent optical vortices through singularities in their cross-spectral density functions," Opt. Lett. **37**, 4949-4951 (2012).
72. G. A. Swartzlander, Jr., and R. I. Hernandez-Aranda, "Optical Rankine Vortex and Anomalous Circulation of Light," Phys. Rev. Lett. **99**, 163901 (2007).
73. W. Wang, Z. Duan, S. G. Hanson, Y. Miyamoto, and M. Takeda, "Experimental Study of Coherence Vortices: Local Properties of Phase Singularities in a Spatial Coherence Function," Phys. Rev. Lett. **96**, 073902 (2006).

74. M. V. Berry, "Optical vortices evolving from helicoidal integer and fractional phase steps," J. Opt. A, Pure Appl. Opt. **6**, 259 (2004).
75. J. F. Nye, and M. V. Berry, "Dislocations in Wave Trains," Proc. R. Soc. Lond. A. **336**, 165-190 (1974).
76. K. Volke-Sepúlveda, A. O. Santillán, and R. R. Boullosa, "Transfer of Angular Momentum to Matter from Acoustical Vortices in Free Space," Phys. Rev. Lett. **100**, 024302 (2008).
77. J. Verbeeck, H. Tian, and P. Schattschneider, "Production and application of electron vortex beams," Nature **467**, 301-304 (2010).
78. M. Berry, "Making waves in physics," Nature **403**, 21-21 (2000).
79. C. Barbieri, F. Tamburini, G. Anzolin, A. Bianchini, E. Mari, A. Sponselli, G. Umbriaco, M. Prasciolu, F. Romanato, and P. Villoresi, "Light's Orbital Angular Momentum and Optical Vortices for Astronomical Coronagraphy from Ground and Space Telescopes," Earth Moon Planets **105**, 283-288 (2009).
80. J. G. A. Swartzlander, E. L. Ford, R. S. Abdul-Malik, L. M. Close, M. A. Peters, D. M. Palacios, and D. W. Wilson, "Astronomical demonstration of anoptical vortex coronagraph," Opt. Express **16**, 10200-10207 (2008).
81. J. Durnin, "Exact solutions for nondiffracting beams. I. The scalar theory," J. Opt. Soc. Am. A **4**, 651-654 (1987).
82. J. Durnin, J. J. Miceli, Jr., and J. H. Eberly, "Diffraction-free beams," Phys. Rev. Lett. **58**, 1499-1501 (1987).
83. M. McLaren, M. Agnew, J. Leach, F. S. Roux, M. J. Padgett, R. W. Boyd, and A. Forbes, "Entangled Bessel-Gaussian beams," Opt. Express **20**, 23589-23597 (2012).
84. K. Dholakia, and T. Cizmar, "Shaping the future of manipulation," Nat. Photon. **5**, 335-342 (2011).
85. M. R. Dennis, R. P. King, B. Jack, K. O'Holleran, and M. J. Padgett, "Isolated optical vortex knots," Nat. Phys. **6**, 118-121 (2010).
86. M. M. Salomaa, and G. E. Volovik, "Quantized vortices in superfluid ^{3}He," Rev. Mod. Phys. **59**, 533-613 (1987).
87. R. S. Scorer, and L. J. Davenport, "Contrails and aircraft downwash," J. Fluid. Mech. **43**, 451-464 (1970).
88. E. W. McCaul, "Buoyancy and Shear Characteristics of Hurricane-Tornado Environments," Mon. Weather Rev. **119**, 1954-1978 (1991).

89. K. Shariff, and A. Leonard, "Vortex Rings," Annu. Rev. Fluid Mech. **24**, 235-279 (1992).
90. L. Allen, M. J. Padgett, and M. Babiker, "IV The Orbital Angular Momentum of Light," in *Progress in Optics*, E. Wolf, ed. (Elsevier, 1999), pp. 291-372.
91. J. Arlt, K. Dholakia, L. Allen, and M. J. Padgett, "The production of multiringed Laguerre–Gaussian modes by computer-generated holograms" J. Mod. Opt. **45**, 1231-1237 (1998)
92. B. Spain, M.G. Smith, *Functions of mathematical physics*, Van Nostrand Reinhold Company, London, (1970). Chapter 10 deals with Laguerre polynomials.
93. M. J. Padgett, and L. Allen, "The Poynting vector in Laguerre-Gaussian laser modes," Opt. Commun. **121**, 36-40 (1995).
94. J. C. Gutiérrez-Vega, M. D. Iturbe-Castillo, and S. Chávez-Cerda, "Alternative formulation for invariant optical fields: Mathieu beams," Opt. Lett. **25**, 1493-1495 (2000).
95. S. Franke-Arnold, J. Leach, M. J. Padgett, V. E. Lembessis, D. Ellinas, A. J. Wright, J. M. Girkin, P. Ohberg, and A. S. Arnold, "Optical ferris wheel for ultracold atoms," Opt. Express **15**, 8619-8625 (2007).
96. E. Zauderer, "Complex argument Hermite-Gaussian and Laguerre-Gaussian beams," J. Opt. Soc. Am. A **3**, 465-469 (1986).
97. C. Tamm, and C. O. Weiss, "Bistability and optical switching of spatial patterns in a laser," J. Opt. Soc. Am. B **7**, 1034-1038 (1990).
98. A. A. Ishaaya, N. Davidson, G. Machavariani, E. Hasman, and A. A. Friesem, "Efficient selection of high-order Laguerre-Gaussian modes in a Q-switched Nd:YAG laser," Quantum Electron. **39**, 74-82 (2003).
99. M. Okida, T. Omatsu, M. Itoh, and T. Yatagai, "Direct generation of high power Laguerre-Gaussian output from a diode-pumped Nd:YVO4 1.3-μm bounce laser," Opt. Express **15**, 7616-7622 (2007).
100. L. Allen, J. Courtial, and M. J. Padgett, "Matrix formulation for the propagation of light beams with orbital and spin angular momenta," Phys. Rev. E **60**, 7497-7503 (1999).
101. A. T. O'Neil, and J. Courtial, "Mode transformations in terms of the constituent Hermite–Gaussian or Laguerre–Gaussian modes and the variable-phase mode converter," Opt. Commun. **181**, 35-45 (2000).

102. J. Courtial, and M. J. Padgett, "Performance of a cylindrical lens mode converter for producing Laguerre–Gaussian laser modes," Opt. Commun. **159**, 13-18 (1999).
103. I. V. Basistiy, M. S. Soskin, and M. V. Vasnetsov, "Optical wavefront dislocations and their properties," Opt. Commun. **119**, 604-612 (1995).
104. F. Ricci, W. Löffler, and M. P. van Exter, "Instability of higher-order optical vortices analyzed with a multi-pinhole interferometer," Opt. Express **20**, 22961-22975 (2012).
105. M. J. Padgett, and J. Courtial, "Poincaré-sphere equivalent for light beams containing orbital angular momentum," Opt. Lett. **24**, 430-432 (1999).
106. V. V. Kotlyar, A. A. Almazov, S. N. Khonina, V. A. Soifer, H. Elfstrom, and J. Turunen, "Generation of phase singularity through diffracting a plane or Gaussian beam by a spiral phase plate," J. Opt. Soc. Am. A **22**, 849-861 (2005).
107. J. Leach, E. Yao, and M. J. Padgett, "Observation of the vortex structure of a non-integer vortex beam," New J. Phys. **6**, 71 (2004).
108. S. S. R. Oemrawsingh, X. Ma, D. Voigt, A. Aiello, E. R. Eliel, G. W. 't Hooft, and J. P. Woerdman, "Experimental Demonstration of Fractional Orbital Angular Momentum Entanglement of Two Photons," Phys. Rev. Lett. **95**, 240501 (2005).
109. H.-Y. Tsai, H. I. Smith, and R. Menon, "Fabrication of spiral-phase diffractive elements using scanning-electron-beam lithography," J. Vac. Sci. Technol. B **25**, 2068 (2007).
110. J. G. A. Swartzlander, "Achromatic optical vortex lens," Opt. Lett. **31**, 2042-2044 (2006).
111. C. Rotschild, S. Zommer, S. Moed, O. Hershcovitz, and S. G. Lipson, "Adjustable Spiral Phase Plate," Appl. Opt. **43**, 2397-2399 (2004).
112. V. Y. Bazhenov, M. S. Soskin, and M. V. Vasnetsov, "Screw Dislocations in Light Wavefronts," J. Mod. Opt. **39**, 985-990 (1992).
113. S. A. Kennedy, M. J. Szabo, H. Teslow, J. Z. Porterfield, and E. R. I. Abraham, "Creation of Laguerre-Gaussian laser modes using diffractive optics," Phys. Rev. A **66**, 043801 (2002).
114. D. Pal Ghai, P. Senthilkumaran, and R. S. Sirohi, "Adaptive helical mirror for generation of optical phase singularity," Appl. Opt. 47, 1378-1383 (2008).

115. D. McGloin, and K. Dholakia, "Bessel beams: Diffraction in a new light," Contemp. Phys. **46**, 15-28 (2005).
116. R. P. MacDonald, S. A. Boothroyd, T. Okamoto, J. Chrostowski, and B. A. Syrett, "Interboard optical data distribution by Bessel beam shadowing," Opt. Commun. **122**, 169-177 (1996).
117. Z. Bouchal, J. Wagner, and M. Chlup, "Self-reconstruction of a distorted nondiffracting beam," Opt. Commun. **151**, 207-211 (1998).
118. J. H. McLeod, "The Axicon: A New Type of Optical Element," J. Opt. Soc. Am. **44**, 592-592 (1954).
119. J. Arlt, and K. Dholakia, "Generation of high-order Bessel beams by use of an axicon," Opt. Commun. **177**, 297-301 (2000).
120. B. P. S. Ahluwalia, X. C. Yuan, S. H. Tao, J. Bu, H. Wang, X. Peng, and H. B. Niu, "Microfabricated-composite-hologram-enabled multiple channel longitudinal optical guiding of microparticles in nondiffracting core of a Bessel beam array," Appl. Phys. Lett. **87**, 084103 (2005).
121. J. Turunen, A. Vasara, and A. T. Friberg, "Holographic generation of diffraction-free beams," Appl. Opt. **27**, 3959-3962 (1988).
122. A. Vasara, J. Turunen, and A. T. Friberg, "Realization of general nondiffracting beams with computer-generated holograms," J. Opt. Soc. Am. A **6**, 1748-1754 (1989).
123. http://www.hamamatsu.com/jp/en/technology/innovation/lcos-slm/index.html
124. N. B. Baranova, B. Ya. Zel'dovich, A. V. Mmaev, N. F. Pilipetskii, and V. V. Shkunov, "Dislocation density on wavefront of a speckle-structure light field," Sov. Phys. JETP **56**, 983-988 (1982).
125. T. Young, "An Account of Some Cases of the Production of Colours, not Hitherto Described," Philos. T. Roy. Soc. Lond. **92**, 387-397 (1802).
126. Robert P. Crease, "The most beautiful experiment," http://physicsworld.com/cws/article/print/9746.
127. H. I. Sztul, and R. R. Alfano, "Double-slit interference with Laguerre-Gaussian beams," Opt. Lett. **31**, 999-1001 (2006).
128. P. Fischer, S. E. Skelton, C. G. Leburn, C. T. Streuber, E. M. Wright, and K. Dholakia, "Propagation and diffraction of optical vortices," Physica C **468**, 514-517 (2008).

129. G. C. G. Berkhout, and M. W. Beijersbergen, "Method for Probing the Orbital Angular Momentum of Optical Vortices in Electromagnetic Waves from Astronomical Objects," Phys. Rev. Lett. **101**, 100801 (2008).
130. G. C. G. Berkhout, and M. W. Beijersbergen, "Using a multipoint interferometer to measure the orbital angular momentum of light in astrophysics," J. Opt. A: Pure Appl. Opt. **11**, 094021 (2009).
131. C.-S. Guo, S.-J. Yue, and G.-X. Wei, "Measuring the orbital angular momentum of optical vortices using a multipinhole plate," Appl. Phys. Lett. **94**, 231103 (2009).
132. Y. Liu, J. Pu, and B. Lü, "Method for exploring the orbital angular momentum of an optical vortex beam with a triangular multipoint plate," Appl. Opt. **50**, 4844-4847 (2011).
133. L. Shi, L. Tian, and X. Chen, "Characterizing topological charge of optical vortex using non-uniformly distributed multi-pinhole plate," COL **10** (12), 120501 (2012).
134. G. C. G. Berkhout, M. P. J. Lavery, J. Courtial, M. W. Beijersbergen, and M. J. Padgett, "Efficient Sorting of Orbital Angular Momentum States of Light," Phys. Rev. Lett. **105**, 153601 (2010).
135. G. C. G. Berkhout, M. P. J. Lavery, M. J. Padgett, and M. W. Beijersbergen, "Measuring orbital angular momentum superpositions of light by mode transformation," Opt. Lett. **36**, 1863-1865 (2011).
136. M. P. J. Lavery, D. J. Robertson, G. C. G. Berkhout, G. D. Love, M. J. Padgett, and J. Courtial, "Refractive elements for the measurement of the orbital angular momentum of a single photon," Opt. Express **20**, 2110-2115 (2012).
137. M. P. J. Lavery, D. J. Robertson, A. Sponselli, J. Courtial, N. K. Steinhoff, G. A. Tyler, A. E. Wilner, and M. J. Padgett, "Efficient measurement of an optical orbital-angular-momentum spectrum comprising more than 50 states," New J. Phys. **15**, 013024 (2013).
138. I. Moreno, J. A. Davis, B. M. L. Pascoguin, M. J. Mitry, and D. M. Cottrell, "Vortex sensing diffraction gratings," Opt. Lett. **34**, 2927-2929 (2009).
139. N. Zhang, Jeffrey A. Davis, I. Moreno, J. Lin, K.-J. Moh, Don M. Cottrell, and X. Yuan, "Analysis of fractional vortex beams using a vortex grating spectrum analyzer," Appl. Opt. **49**, 2456-2462 (2010).

140. S. Prabhakar, A. Kumar, J. Banerji, and R. P. Singh, "Revealing the order of a vortex through its intensity record," Opt. Lett. **36**, 4398-4400 (2011).
141. C. Zhao, F. Wang, Y. Dong, Y. Han, and Y. Cai, "Effect of spatial coherence on determining the topological charge of a vortex beam," Appl. Phys. Lett. **101**, 261104 (2012).
142. Y. Liu, and J. Pu, "Measuring the orbital angular momentum of elliptical vortex beams by using a slit hexagon aperture," Opt. Commun. **284**, 2424-2429 (2011).
143. H. Tao, Y. Liu, Z. Chen, and J. Pu, "Measuring the topological charge of vortex beams by using an annular ellipse aperture," Appl. Phys. B **106**, 927-932 (2012).
144. C.-S. Guo, L.-L. Lu, and H.-T. Wang, "Characterizing topological charge of optical vortices by using an annular aperture," Opt. Lett. **34**, 3686-3688 (2009).
145. Y. Liu, S. Sun, J. Pu, and B. Lü, "Propagation of an optical vortex beam through a diamond-shaped aperture," Opt. Laser Technol. **45**, 473-479 (2013).
146. Q. S. Ferreira, A. J. Jesus-Silva, E. J. S. Fonseca, and J. M. Hickmann, "Fraunhofer diffraction of light with orbital angular momentum by a slit," Opt. Lett. **36**, 3106-3108 (2011).
147. P. H. F. Mesquita, A. J. Jesus-Silva, E. J. S. Fonseca, and J. M. Hickmann, "Engineering a square truncated lattice with light's orbital angular momentum," Opt. Express **19**, 20616-20621 (2011).
148. L. E. E. de Araujo, and M. E. Anderson, "Measuring vortex charge with a triangular aperture," Opt. Lett. **36**, 787-789 (2011).
149. L. Yongxin, T. Hua, P. Jixiong, and L. Baida, "Detecting the topological charge of vortex beams using an annular triangle aperture," Opt. Laser Technol. **43**, 1233-1236 (2011).
150. I. V. Basistiy, V. A. Pas'ko, V. V. Slyusar, M. S. Soskin, and M. V. Vasnetsov, "Synthesis and analysis of optical vortices with fractional topological charges," J. Opt. A: Pure Appl. Opt. **6**, S166 (2004).
151. W. M. Lee, X. C. Yuan, and K. Dholakia, "Experimental observation of optical vortex evolution in a Gaussian beam with an embedded fractional phase step," Opt. Commun. **239**, 129-135 (2004).
152. R. C. Smith, and J. S. Marsh, "Diffraction patterns of simple apertures," J. Opt. Soc. Am. **64**, 798-803 (1974).

153. J. Arlt, "Handedness and azimuthal energy flow of optical vortex beams," J. Mod. Opt. **50**, 1573-1580 (2003).
154. A. J. Jesus-Silva, E. J. S. Fonseca, and J. M. Hickmann, "Study of the birth of a vortex at Fraunhofer zone," Opt. Lett. **37**, 4552-4554 (2012).
155. A. C. De Luca, S. Kosmeier, K. Dholakia, and M. Mazilu, "Optical eigenmode imaging," Phys. Rev. A **84**, 021803 (2011).
156. M. Mazilu, J. Baumgartl, S. Kosmeier, and K. Dholakia, "Optical Eigenmodes; exploiting the quadratic nature of the energy flux and of scattering interactions," Opt. Express **19**, 933-945 (2011).
157. J. Leach, and M. J. Padgett, "Observation of chromatic effects near a white-light vortex," New J. Phys. **5**, 154 (2003).
158. J. E. Curtis, and D. G. Grier, "Structure of Optical Vortices," Phys. Rev. Lett. **90**, 133901 (2003).
159. J. W. Goodman, *Introduction to Fourier Optics* (McGraw-Hill Inc., 1968).
160. J. B. Götte, K. O'Holleran, D. Preece, F. Flossmann, S. Franke-Arnold, S. M. Barnett, and M. J. Padgett, "Light beams with fractional orbital angular momentum and their vortex structure," Opt. Express **16**, 993-1006 (2008).
161. M. E. Anderson, H. Bigman, L. E. de Araujo, and J. L. Chaloupka, "Measuring the topological charge of ultra-broadband, optical-vortex beams with a triangular aperture," J. Opt. Soc. Am. B **29**, 1968-1976 (2012).
162. A. J. Jesus-Silva, E. J. S. Fonseca, and J. M. Hickmann, "Measurement of the orbital angular momentum at photon level via the spatial probability distribution," J. Mod. Optic **59**, 1194-1198 (2012).
163. A. Alexandrescu, D. Cojoc, and E. D. Fabrizio, "Mechanism of Angular Momentum Exchange between Molecules and Laguerre-Gaussian Beams," Phys. Rev. Lett. **96**, 243001 (2006).
164. A. F. Abouraddy, T. M. Yarnall, and B. E. A. Saleh, "Angular and radial mode analyzer for optical beams," Opt. Lett. **36**, 4683-4685 (2011).
165. R. Gerchberg, and W. Saxton, "A practical algorithm for the determination of the phase from image and diffraction plane pictures," Optik **35**, 237-246 (1972).
166. B. Everitt, and T. Hothorn, in *An Introduction to Applied Multivariate Analysis with R*, Chapt. 3,pp. 61-103, (Springer New York, 2011).

167. P. N. Belhumeur, J. P. Hespanha, and D. J. Kriegman, "Eigenfaces vs. Fisherfaces: recognition using class specific linear projection," IEEE T. Pattern Anal. **19**, 711-720 (1997).
168. L. J. van 't Veer, H. Dai, M. J. van de Vijver, Y. D. He, A. A. M. Hart, M. Mao, H. L. Peterse, K. van der Kooy, M. J. Marton, A. T. Witteveen, G. J. Schreiber, R. M. Kerkhoven, C. Roberts, P. S. Linsley, R. Bernards, and S. H. Friend, "Gene expression profiling predicts clinical outcome of breast cancer," Nature **415**, 530-536 (2002).
169. T. Cover, and P. Hart, "Nearest neighbor pattern classification," IEEE Trans. Inf. Theory **13**, 21-27 (1967).
170. B. A. Draper, K. Baek, M. S. Bartlett, and J. R. Beveridge, "Recognizing faces with PCA and ICA," Comput. Vis. Image Underst. **91**, 115-137 (2003).
171. V. Arrizón, U. Ruiz, R. Carrada, and L. A. González, "Pixelated phase computer holograms for the accurate encoding of scalar complex fields," J. Opt. Soc. Am. A **24**, 3500-3507 (2007).
172. M. V. Vasnetsov, V. A. Pas'ko, and M. S. Soskin, "Analysis of orbital angular momentum of a misaligned optical beam," New J. Phys. **7**, 46 (2005).
173. M. P. J. Lavery, G. C. G. Berkhout, J. Courtial, and M. J. Padgett, "Measurement of the light orbital angular momentum spectrum using an optical geometric transformation," J. Opt. **13**, 064006 (2011).
174. A. Vaziri, G. Weihs, and A. Zeilinger, "Superpositions of the orbital angular momentum for applications in quantum experiments," J. Opt. B: Quantum Semiclass. Opt. **4**, S47-S51 (2002).
175. G. Milione, H. I. Sztul, D. A. Nolan, and R. R. Alfano, "Higher-order Pointcaré Sphere, Stokes Parameters, and the Angular Momentum of Light," Phys. Rev. Lett. **107**, 053601 (2011).
176. R. Piestun, and D. A. B. Miller, "Electromagnetic degrees of freedom of an optical system," J. Opt. Soc. Am. A **17**, 892-902 (2000).
177. W. H. Zurek, "Reversibility and Stability of Information Processing Systems," Phys. Rev. Lett. **53**, 391-394 (1984).
178. A. E. Siegman, "Hermite-gaussian functions of complex argument as optical-beam eigenfunctions," J. Opt. Soc. Am. **63**, 1093-1094 (1973).

179. O. Shapira, A. F. Abouraddy, J. D. Joannopoulos, and Y. Fink, "Complete Modal Decomposition for Optical Waveguides," Phys. Rev. Lett. **94**, 143902 (2005).
180. D. N. Schimpf, and S. Ramachandran, "Polarization-resolved imaging of an ensemble of waveguide modes," Opt. Lett. **37**, 3069-3071 (2012).
181. D. Beom Soo Soh, J. Nilsson, S. Baek, C. Codemard, Y. Jeong, and V. Philippov, "Modal power decomposition of beam intensity profiles into linearly polarized modes of multimode optical fibers," J. Opt. Soc. Am. A **21**, 1241-1250 (2004).
182. A. Y. Bekshaev, M. S. Soskin, and M. V. Vasnetsov, "Optical vortex symmetry breakdown and decomposition of the orbital angular momentum of light beams," J. Opt. Soc. Am. A **20**, 1635-1643 (2003).
183. G. Molina-Terriza, A. Vaziri, J. Řeháček, Z. Hradil, and A. Zeilinger, "Triggered Qutrits for Quantum Communication Protocols," Phys. Rev. Lett. **92**, 167903 (2004).
184. M. Mazilu, D. J. Stevenson, F. Gunn-Moore, and K. Dholakia, "Light beats the spread: “non-diffracting” beams," Laser Photon. Rev. **4**, 529-547 (2010).
185. E. Abramochkin, and V. Volostnikov, "Beam transformations and nontransformed beams," Opt. Commun. **83**, 123-135 (1991).
186. S. J. M. Habraken, and G. Nienhuis, "Modes of a rotating astigmatic optical cavity," Phys. Rev. A **77**, 053803 (2008).
187. A. Dudley, T. Mhlanga, M. Lavery, A. McDonald, F. S. Roux, M. J. Padgett, and A. Forbes, "Efficient sorting of Bessel beams," Opt. Express **21**, 165-171 (2013).
188. D. M. Palacios, I. D. Maleev, A. S. Marathay, and G. A. Swartzlander, Jr., "Spatial Correlation Singularity of a Vortex Field," Phys. Rev. Lett. **92**, 143905 (2004).
189. M. J. Beran, and G. B. Parrent, *Theory of Partial Coherence*, (Englewood Cliffs, N.J., Prentice-Hall, 1964).
190. P. Günter, "Holography, coherent light amplification and optical phase conjugation with photorefractive materials," Phys. Rep. **93**, 199-299 (1982).
191. I. D. Maleev, D. M. Palacios, A. S. Marathay, and J. G. A. Swartzlander, "Spatial correlation vortices in partially coherent light: theory," J. Opt. Soc. Am. B **21**, 1895-1900 (2004).

192. G. Gbur, and J. G. A. Swartzlander, "Complete transverse representation of a correlation singularity of a partially coherent field," J. Opt. Soc. Am. B **25**, 1422-1429 (2008).
193. H. D. L. Pires, J. Woudenberg, and M. P. van Exter, "Measurements of spatial coherence of partially coherent light with and without orbital angular momentum," J. Opt. Soc. Am. A **27**, 2630-2637 (2010).
194. H. Di Lorenzo Pires, J. Woudenberg, and M. P. van Exter, "Measurement of the orbital angular momentum spectrum of partially coherent beams," Opt. Lett. **35**, 889-891 (2010).
195. G. B. Parrent, "Basic theory of partial coherence," in *Proceedings of the April 26-28, 1966, Spring joint computer conference* (ACM, Boston, Massachusetts, 1966), pp. 17-24.
196. T. Shirai, and E. Wolf, "Coherence and polarization of electromagnetic beams modulated by random phase screens and their changes on propagation in free space," J. Opt. Soc. Am. A **21**, 1907-1916 (2004).
197. J. Leach, M. R. Dennis, J. Courtial, and M. J. Padgett, "Vortex knots in light," New J. Phys. **7**, 55 (2005).
198. F. Zernike, "The concept of degree of coherence and its application to optical problems," Physica **5**, 785 (1938).
199. B. J. Thompson, and E. Wolf, "Two-beam interference with partially coherent light," J. Opt. Soc. Am. **47**, 895 (1957).
200. B. J. Thompson, "Illustration of the Phase Change in Two-Beam Interference with Partially Coherent Light," J. Opt. Soc. Am. **48**, 95-96 (1958).
201. L. Allen, "Introduction to the atoms and angular momentum of light special issue," J. Opt. B-Quantum S. O. **4**, S1 (2002).
202. A. J. Jesus-Silva, J. M. Hickmann, and E. J. S. Fonseca, "Strong correlations between incoherent vortices," Opt. Express **20**, 19708-19713 (2012).

Appendix A

Programming Code for Far-field Diffraction of an OV from different types of apertures

For the numerical implementation of the far-field diffraction patterns, the scalar field of each incident LG beam is discretized over a square grid and apertured by the used aperture. The Matlab programming code that was used to the numerical simulations presented in Chapter 3 is the following:

```
% Vortex propagation through different types of apertures
% Areti Mourka - am2547@st-andrews.ac.uk

clc
clear all
close all hidden

%   Setup Grid
xmax = 250.00;              % x grid size in microns
ymax = xmax;                % y grid size in microns
N  = 2*1024+1;              % number of x & y grid points
v = 0:1:(N-1);              % integer vector from 0 to N-1
dx = xmax/(N-1);            % spacing in x
dy = ymax/(N-1);            % spacing in y
[x,y] = meshgrid(v,v);      % meshgrid containing NxN points (integer values)
x = -xmax/2 + x*dx;         % shifts mesh to cover +/- xmax/2, 2D-grid
y = -ymax/2 + y*dy;         % shifts mesh to cover +/- ymax/2, 2D-grid
xar = -xmax/2 + v*dx;       % cross section to cover +/- xmax/2, 1D
yar = -ymax/2 + v*dy;       % cross section to cover +/- ymax/2, 1D
dkx = 2*pi/xmax;            % spacing in kx (inverse microns)
dky = 2*pi/ymax;            % spacing in ky (inverse microns)
kxmax = 2*pi/dx;            % grid size in microns (from kx1 to kxN)
kymax = 2*pi/dy;            % grid size in microns (from ky1 to kyN)
[kx,ky] = meshgrid(v,v);    % meshgrid containing NxN points (integer values)
kx = -kxmax/2 + kx*dkx;     % shifts mesh to cover +/- kxmax/2, 2D-grid
ky = -kymax/2 + ky*dky;     % shifts mesh to cover +/- kymax/2, 2D-grid
kxar = -kxmax/2 + v*dkx;    % cross section to cover +/- kxmax/2, 1D
kyar = -kymax/2 + v*dky;    % cross section to cover +/- kymax/2, 1D
%   System Properties
wx = 15;            % field width in x in microns
wy = wx;            % field width in y in microns
E0 = 1;             % peak field strength (arbitrary units)
lambda = 1;         % wavelength in microns
L = 1.00e4;         % distance to observation screen in microns
```

```
l = 6;                  % azimuthal mode index
                        % convert to polar coordinates
[theta,rho]=cart2pol(x,y);
%   Generate aperture
E = zeros(N);           % 0 matrix to setup aperture & propagate
aperture = 5;
switch aperture
case 1
% Triangular aperture
deg = 30*pi/180;        % angle of equilateral triangle in radians
h = find (y>(x./(tan(deg))-(wx)*2/3)&y>-x./tan(deg)-(wx)*2/3&y<((wx)*1/3));
case 2
% Square Aperture
Squareaperture = (abs(x)>=0 &abs(x)<wx).*(abs(y)>0 &abs(y)<=wy);
h = find (Squareaperture);
case 3
% Circular Aperture
R = 20;
Circularaperture = sqrt(abs(x).^2 + abs(y).^2) < R ;
h = find(Circularaperture);
case 4
% Annular Triangle with Radial spokes Aperture
wxInner=wx;
wx1=wx;
dw1=2;
deg = 30*pi/180;        % angle of equilateral triangle in radians
h1= find (y>(x/tan(deg)-(wx1+dw1)*2/3)&y>-x/tan(deg)
(wx1+dw1)*2/3&y<((wx1+dw1)*1/3)&...
~(y>(x/tan(deg)-(wx1-dw1)*2/3)&y>-x/tan(deg)-(wx1-dw1)*2/3&y<((wx1
-dw1)*1/3)));
% Create cross
lineLength=10;          %microns
lineThickness=0.1*lineLength;
apAngle=pi/6;
h2=find((rho.*cos(theta-apAngle)>=0 & rho.*cos(theta-apAngle)<=lineLength &
abs(rho.*sin(theta-apAngle))<=lineThickness/2) |...
```

```
(rho.*cos(theta+2*pi/3-apAngle)>=0 & rho.*cos(theta+2*pi/3-
apAngle)<=lineLength & abs(rho.*sin(theta+2*pi/3-apAngle))<=lineThickness/2)
|...
(rho.*cos(theta-2*pi/3-apAngle)>=0 & rho.*cos(theta-2*pi/3-
apAngle)<=lineLength & abs(rho.*sin(theta-2*pi/3-apAngle))
<=lineThickness/2);
h=union(h1,h2);
case 5
% Multi Annular Triangle Aperture
% First Annular Triangle Aperture
wx1=wx;
dw1=2;
deg = 30*pi/180;        % angle of equilateral triangle in radians
h1 = find (y>(x/tan(deg)-(wx1+dw1)*2/3)&y>-x/tan(deg)-
(wx1+dw1)*2/3&y<((wx1+dw1)*1/3)&...
~(y>(x/tan(deg)-(wx1-dw1)*2/3)&y>-x/tan(deg)-(wx1-dw1)*2/3&y<((wx1-
dw1)*1/3)));
% Second Annular Triangle Aperture
wx2=2*wx1;
dw1=2;
h2 = find (y>(x/tan(deg)-(wx2+dw1)*2/3)&y>-x/tan(deg)-
(wx2+dw1)*2/3&y<((wx2+dw1)*1/3)&...
~(y>(x/tan(deg)-(wx2-dw1)*2/3)&y>-x/tan(deg)-(wx2-dw1)*2/3&y<((wx2-
dw1)*1/3)));
h = union(h1,h2);
end
% find martix elements inside used aperture
E(h) = 1;               % set aperture values to 1
Eaperture = E;          % store aperture
%   Generate Fraunhofer propagation pattern
w0 = 7;
p = 5;                  % radial mode index
T = theta(h);
R = rho(h);
Z=[];
beamWaist=w0;           % beam waist
pValue = p;             % radial index value
lValue = l;             % azimuthal index value
```

```
fieldValues(h)=laguerreGaussian(R,T,Z,pValue,lValue,lambda,beamWaist);
                                % calculate the generalized LG beams
E(h) = fieldValues(h);          % electric field envelope
k0 = 2*pi/lambda;               % propagation vector prefactor
X = kx*lambda*L/2/pi;           % propagated X grid, 2D
Y = ky*lambda*L/2/pi;           % propagated Y grid, 2D
Xar = kxar*lambda*L/2/pi;       % cross section of X Grid, 1D
dX = dkx*lambda*L/2/pi;         % propagated dX spacing
dY = dky*lambda*L/2/pi;         % propagated dY spacing
Ek1 = dx*dy*fftshift(fft2(E));      % FT of pattern
EX1 = (1/sqrt(-1)/L/lambda)*exp(sqrt(-1)*k0*L)...
   *exp(sqrt(-1)*k0*(X.^2+Y.^2)/2/L).*Ek1;
                                % Full Fraunhofer propagation
% Plot
% scrsz = get(0,'ScreenSize');   % gets screen size
% figure('OuterPosition',[1 .05*scrsz(4) scrsz(3)/1 .95*scrsz(4)])

figure;
subplot(1,2,1);
imagesc(abs(E));
axis square;
title('amp');
subplot(1,2,2);
imagesc(angle(E));
title('phase');
axis square;

imagesc(Xar,Xar,abs(EX1).^2);
axis equal
set(gca,'FontSize',15);
set(gca,'color',[0 0 0]);
title(['m = ', num2str(m)])
xlim([-1.5*L 1.5*L]);
ylim([-1.5*L 1.5*L]);
```

The generalized LG beams were calculated based on the following Matlab function:

```
% fieldValues=laguerreGaussian(R,T,Z,pValue,lValue,lambda,beamWaist)
%
% Input:
%     R: radial coordinate grid [m]
%     T: azimutal coordinate grid [rad]
%     Z: axial coordinate grid [m]
%     pValue: the p value of the beam (radial)
%     lValue: the l value of the beam (azimutal phase index, must be integer)
%     lambda: the wavelength to simulate [m]
%     beamWaist: the beam waist [m]
%
% Example:
%         xRange=[-4e-6:.05e-6:4e-6];
%         [X,Y]=meshgrid(xRange,xRange);
%         [T,R]=cart2pol(X,Y);
%         Z=[];
%         lambda=500e-9;
%         beamWaist=2*lambda;
%         pValue=3;
%         lValue=0;
%         fieldValues=laguerreGaussian(R,T,Z,pValue,lValue,lambda,beamWaist);
%         imagesc(abs(fieldValues).^2)
%
function fieldValues=laguerreGaussian(R,T,Z,pValue,lValue,lambda,beamWaist)
   if (nargin<1),
      xRange = [-768/2:1:768/2];
      [X,Y] = meshgrid(xRange,xRange);
      [T,R] = cart2pol(X,Y);
      Z = [];
      pValue = 4;
      lValue = 3;
   end

   if (nargin<6)
      lambda = 500e-9;
end
   if (nargin<7)
```

```
beamWaist = 100;
    end
    if (isempty(Z)),
        Z = zeros(size(R));
    end

    rayleighRange = pi*beamWaist^2/lambda;
    W = beamWaist*sqrt(1+(Z./rayleighRange).^2);
    radiusOfCurvature = (Z+(Z==0)).*(1+(rayleighRange./Z).^2);
    gouyPhase = atan2(Z,rayleighRange);
    fieldValues = (1./W).*(R.*sqrt(2)./W).^abs(lValue).*exp(-R.^2./W.^2)...
.*L(abs(lValue),pValue,2*R.^2./W.^2).*exp(1i.*(2*pi/lambda).*R.^2./(2*radiusof
Curvature))...
 .*exp(1i*lValue.*T).*exp(-1i*(2*pValue+abs(lValue)+1).*gouyPhase);

    %Normalize
    fieldValues=fieldValues./sqrt(sum(abs(fieldValues(:)).^2));
    if (nargout==0)
        figure;
        colormap gray;
        imagesc(abs(fieldValues).^2);
        clear fieldValues;
    end
end
```

Appendix B

Theoretical study on the Diffraction of an Optical Vortex from a triangular aperture

1. Basic equations

For the specific case studied here and explored in Chapter 4, *t(x, y)* describes an equilateral triangular aperture which has unity transmission inside the aperture and zero outside the aperture, and over the spatial extent of the aperture the slowly varying electric field envelope of the incident optical vortex at $z = 0$ is written as:

$$E^{(\ell)}(x,y,0) = A\cdot(x+i\cdot\mathrm{sgn}(\ell)y)^{|\ell|} \equiv E^{(\ell)}(\rho,\theta,0) = A\cdot\rho^{|\ell|}\cdot e^{i\ell\theta} \tag{B.1}$$

where A measures the field strength, and we hereafter set $A = 1$. Denoting the transverse coordinates on the aperture plane as $(x, y) = (\rho, \theta)$ in either cartesian or cylindrical polar coordinates, the aperture transmission function is written as $t(x, y) = t(\rho, \theta)$. In this study, the far-field diffraction patterns were created using a standard $2f$ Fourier transforming optical system based on a lens of focal length f, and the transverse Cartesian coordinates were denoted in the focal plane as (ξ, η).

The diffracted field at the distance $z = 2f$ past the aperture is then proportional to the Fourier transform of the product of the optical vortex times the aperture transmission function yielding the following result [56, 152]:

$$E^{(\ell)}(X,Y,z) \propto \int_{-\infty}^{\infty} dx \int_{-\infty}^{\infty} dy t(x,y)(x+i\cdot\mathrm{sgn}(\ell)y)^{|\ell|} e^{-i(Xx+Yy)} \tag{B.2}$$

where $X = 2\pi\xi/\lambda f$ and $Y = 2\pi\eta/\lambda f$ are scaled transverse coordinates in the observation plane. The Equation (B.2) was numerically solved using the discrete Fourier transform algorithm for the case of a triangular aperture and for a variety of input azimuthal indices ℓ, both integer and fractional (non-integer) values. The numerical code was checked against the known analytical solution for the uniformly triangular aperture [152]. In the following section, the numerical simulations of the far-field intensity profile $|E(X,Y,z)|^2$ are presented for a variety of conditions.

2. Far-field diffraction intensity profile for integer azimuthal indices

To begin with, a simpler free-space version of the model introduced in the previous section is used; both models yielding the Fourier transform of the field at the aperture. In the style of Equations (B.1) and (B.2), let's start with the electric field just beyond the aperture at $z = 0$:

$$E^{(\ell)}(\rho,\theta,z=0) = t(x,y)(x+i\cdot\mathrm{sgn}(\ell)y)^{|\ell|} = t(\rho,\theta)\rho^{|\ell|}e^{i\ell\theta} \tag{B.3}$$

In writing this, it is explicitly assumed that the vortex core of the form $\rho^{|\ell|}e^{i\ell\theta}$ is isolated by the aperture.

To proceed, the field beyond the triangular aperture is expanded in terms of the complete orthonormal set of LG modes:

$$U_{p,m}(\rho,\theta,z) = u_{p,|m|}(\rho,z)e^{ik\rho^2/2R(z)}e^{im\theta}e^{i(2p+|m|+1)\Phi(z)} \tag{B.4}$$

where the real functions $u_{p,|m|}(\rho,z)$ are given by [56]:

$$u_{p,|m|}(\rho,z)=\left(\frac{2p!}{(1+\delta_{0,|m|})\pi(|m|+p)!}\right)\frac{1}{w(z)}\left(\frac{\sqrt{2}\rho}{w(z)}\right)^{|m|}L_p^{|m|}\left(\frac{2\rho^2}{w^2(z)}\right)e^{-\rho^2/w^2(z)} \quad \text{(B.5)}$$

where $k = \omega / c$, $w(z)$ and $R(z)$ are the Gaussian spot size and radius of curvature of the propagating modes, $w(0) = w_0$ and $1 / R(0) = 0$. The Gouy phase-shift of the propagating modes is $\Phi(z)$, with $\Phi(0) = 0$ and $\Phi(z \to \infty) = \pi / 2$. Then, we may write the field beyond the aperture as an expansion of LG modes:

$$E^{(\ell)}(\rho,\theta,z)=\sum_{p=0}^{\infty}\sum_{m=-\infty}^{\infty}C_{p,m}^{(\ell)}u_{p,|m|}(\rho,z)e^{ik\rho^2/2R(z)}e^{im\theta}e^{i(2p+|m|+1)\Phi(z)} \quad \text{(B.6)}$$

where the expansion coefficients $C_{p,m}^{(\ell)}$ are evaluated at $z = 0$ are given by:

$$C_{p,m}^{(\ell)}=\int_0^{\infty}\rho d\rho\int_0^{2\pi}d\theta E^{(\ell)}(\rho,\theta,0)U_{p,m}^{*}(\rho,\theta,0) \quad \text{(B.7)}$$

$$=\int_0^{\infty}\rho d\rho\int_0^{2\pi}d\theta t(\rho,\theta)\rho^{|\ell|}e^{i\theta(\ell-m)}u_{p,|m|}(\rho,0) \quad \text{(B.8)}$$

Based on this definition, the following symmetry will be used later:

$$C_{p,m}^{(\ell)}=(C_{p,-m}^{(-\ell)})^{*} \quad \text{(B.9)}$$

and that this symmetry holds independent of the choice of LG spot size w_0. The next step is to specifically consider the far-field for which the Gouy phase-shift is $\Phi(z) \to \pi/2$ [152], in which case the diffracted field becomes:

$$E^{(\ell)}(\rho,\theta,z)=e^{ik\rho^2/2R(z)}\sum_{p=0}^{\infty}i(-1)^p\sum_{m=-\infty}^{\infty}C_{p,m}^{(\ell)}u_{p,|m|}(\rho,z)e^{i(m\theta+|m|\pi/2)} \quad \text{(B.10)}$$

$$=e^{ik\rho^2/2R(z)}F^{(\ell)}(\rho,\theta,z) \quad \text{(B.11)}$$

where:
$$F^{(\ell)}(\rho,\theta,z)=\sum_{p=0}^{\infty}i(-1)^p\sum_{m=-\infty}^{\infty}C_{p,m}^{(\ell)}u_{p,|m|}(\rho,z)e^{i(m\theta+|m|\pi/2)} \quad \text{(B.12)}$$

The far-field intensity is therefore:

$$I^{(\ell)}(\rho,\theta,z)=\left|E^{(\ell)}(\rho,\theta,z)\right|^2=\left|F^{(\ell)}(\rho,\theta,z)\right|^2 \quad \text{(B.13)}$$

Next the same procedure is followed for an incident field with azimuthal index $-\ell$, giving the far-field profile:

$$E^{(-\ell)}(\rho,\theta,z)=e^{ik\rho^2/2R(z)}\sum_{p=0}^{\infty}i(-1)^p\sum_{m=-\infty}^{\infty}C_{p,m}^{(-\ell)}u_{p,|m|}(\rho,z)e^{i(m\theta+|m|\pi/2)} \quad \text{(B.14)}$$

$$=e^{ik\rho^2/2R(z)}\sum_{p=0}^{\infty}i(-1)^p\sum_{m=-\infty}^{\infty}C_{p,-m}^{(-\ell)}u_{p,|m|}(\rho,z)e^{i(-m\theta+|m|\pi/2)} \quad \text{(B.15)}$$

$$=e^{ik\rho^2/2R(z)}\sum_{p=0}^{\infty}i(-1)^p\sum_{m=-\infty}^{\infty}(C_{p,-m}^{(\ell)})^{*}u_{p,|m|}(\rho,z)e^{i(-m\theta+|m|\pi/2)}e^{im\pi} \quad \text{(B.16)}$$

$$=e^{ik\rho^2/2R(z)}\sum_{p=0}^{\infty}i(-1)^p\sum_{m=-\infty}^{\infty}(C_{p,-m}^{(\ell)})^{*}u_{p,|m|}(\rho,z)e^{-i(m\theta+|m|\pi/2)}e^{im\pi} \quad \text{(B.17)}$$

$$= e^{ik\rho^2/2R(z)} \sum_{p=0}^{\infty} i(-1)^p \sum_{m=-\infty}^{\infty} (C_{p,-m}^{(\ell)})^* u_{p,|m|}(\rho, z) e^{-i(m(\theta-m)+|m|\pi/2)} \quad \text{(B.18)}$$

$$= e^{ik\rho^2/2R(z)} \left[F^{(m)}(\rho, \theta-\pi, z) \right]^* \quad \text{(B.19)}$$

where in the second line, *m* switched to –*m*, in the third line the symmetry (Equation B.8) was used, and in the fourth line $e^{i|m|\pi} = e^{im\pi}$. By comparing with Equation (B.11), one therefore can see that the far-field intensity pattern is given by:

$$I^{(-\ell)}(\rho, \theta, z) = \left| F^{(\ell)}(\rho, \theta-\pi, z) \right|^2 = I^{(\ell)}(\rho, \theta-\pi, z) \quad \text{(B.20)}$$

Thus the far-field intensity patterns for $\ell = \pm|\ell|$ have the structure given by:

$$\left| F^{(\ell)}(\rho, \theta, z) \right|^2 \quad \text{(B.21)}$$

but are rotated by 180^o with respect to each other around the vortex center. It should be noted that if one artificially sets the Gouy phase-shift to zero $\Phi(z) = 0$ in the far-field in place of the correct value $\Phi(z) = \pi/2$, then the intensity pattern would not be rotated upon reversing the sign of ℓ, meaning that the rotation has its origin in the Gouy phase-shift. This is the main result of this analysis, and it explains the fact that the diffraction of an optical vortex core from a polygonal aperture in general depends upon the sign of the azimuthal index, and furthermore exposes that this dependence stems from the Gouy phase-shift, giving new physical insight into this problem, compared to previous studies [48].

In conclusion, for example the far-field diffraction intensity pattern produced by a circular aperture is also rotated but this is clearly not observable, and the triangular aperture is likely the simplest aperture that can act as a detector of the magnitude and sign of the azimuthal index.

Appendix C

Calibration of the SLM & Wavefront correction using Optical Eigenmodes (OEi)

1. Calibrating the SLM system

The SLM system must be optimized for a single wavelength. Clearly, with 256 phase levels, represented by 256 grayscale values, an individual pixel can change the phase by $2\pi/256$ or for 633nm light beam a distance of 633nm/256 ≈ 2.5nm. The voltage that would give rise to these increments in retardation over the full 2π range needs to be determined. Thus, the phase modulation that can be achieved with a SLM for a coherent light source will be measured here by using a two beam interference apparatus (Figure C.1).

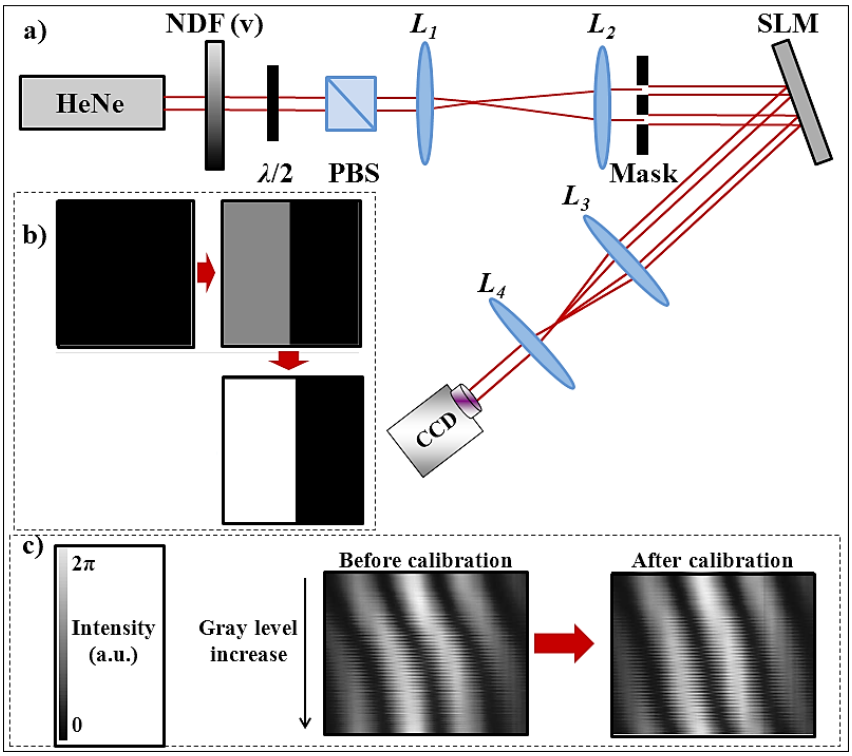

Fig. C.1. Calibration of the SLM system. a) Experimental apparatus used for a reflective SLM (Holoeye LC-R 2500) with LCoS display area ≈ 1.5cm. HeNe = helium neon laser, NDF (v) = variable neutral density filter, PBS = polarizing beam splitter, L = lens, SLM = spatial light modulator, CCD = charged coupled device. b) Three examples of addressed gray level pattern for each display half on the SLM, and c) observed interference pattern shift for increasing phase delays. Swift with default gamma curve (left) and optimized gamma curve (right). With the new gamma curve a linear relationship between the SLM input and the associated retardance is obtained. Focal widths of lenses: f_1 = 10cm, f_2 = 30cm, f_3 = 50 cm and f_4 = 100cm.

The display is illuminated by two coherent and collimated laser beams by using a double hole mask. Both beams are separately guided to an appropriate display half. The right one will be addressed with a constant gray level whereas the other half will be addressed with changing gray levels from 0 to 255 (Figure C.1b). A telescope

behind the display let both reflected beams interfere with each other and also expands the interference pattern onto a CCD camera. A phase shift as a function of the addressed gray level will appear as a shift in the interference pattern and will be evaluated by the supplied software from the manufacturer.

The experimental apparatus used for measuring the phase shift of the considered reflective SLM is shown above in Figure C.1a. The laser beam is guided through a variable neutral density filter to adjust the intensity detected by the CCD camera. A telescope (L_1 and L_2) is then used in order to expand the beam that illuminates the whole display aperture of the reflective SLM (Holoeye LC-R 2500). A half-waveplate ($\lambda/2$) was used in order to rotate the polarization of the incoming beam to the optimum angle for the SLM. The polarization state was verified by the use of a polarizing beam-splitter (PBS) after the $\lambda/2$ plate. A double hole mask (hole diametre ≈ 2mm, distance ≈ 7mm) creates two incident beams, one for each display half on the SLM. The interference pattern of the two reflected beams will then be imaged onto the CCD camera. Thereby an intensity minimum of the interference pattern is the starting point of the measurement. This minimum will be detected by the software (provided by the manufacturer) and its movement as a function of the addressed gray level, is a measure for the phase shift. Hence, extracting a single line from the same place in each interference pattern and stacking them vertically results in Figure C.1c.

The manufacturer of the SLM system provides software in order to modify the gamma curves stored on the controller. The gamma curve is the internal look up table (LUT) which converts the input of the user to the appropriate voltage for the LC display (transferred via parallel port). Ideally, a linear increase in SLM input leads to a linear increase in phase delay.

Adjusting the gamma curve based on the calibration experiments explained above; allow us to obtain a linear input-phase relation. The gamma curve translates 8-bit values sent to the controller into a voltage that is applied to the LC pixel, thus translating a gray scale value into a phase shift. The measured points of the recorded interference pattern have been translated into the gamma curve as depicted in the Figure C.2 and finally the gamma curve was modified such that for the linear gray scale range from 0 to 255 the SLM delivers a linear phase shift as shown in the following Figure C.3.

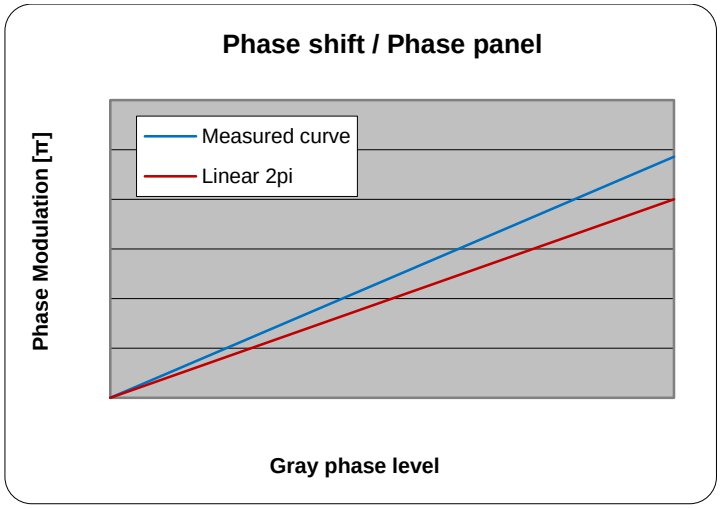

Fig. C.2. Phase modulation after the calibration. The new calculated linear phase shift, where the 0 gray level corresponds to 0π and the 255 gray level corresponds to 2,33π.

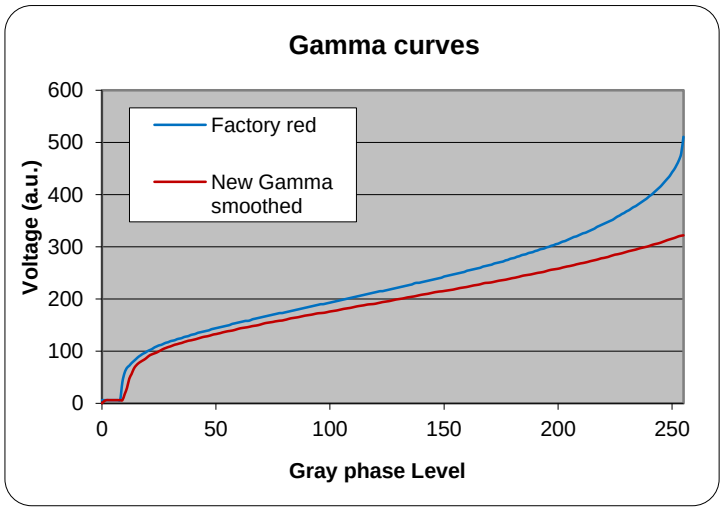

Fig. C.3. Gamma curves. New calculated gamma curve compared with the one provided by the factory when a red wavelength used. Correction to the voltage versus gray scale should be placed on the SLM hardware to act as the LUT.

The amplitude modulation for a certain phase modulation can be achieved by a slightly modified experimental apparatus. One beam is blocked and the CCD camera has to be replaced by a photo detector. The software has to be driven in amplitude mode and the whole display should be addressed with homogeneous gray level. Here, the amplitude SLM (used in studies presented in Chapter 7) was already calibrated and no further steps were required.

2. Optical Eigenmode (OEi) decomposition

The optical eigenmode (OEi) decomposition is based on the definition of the total intensity measured in a given region of interest (ROI). In these studies, superpositions of LG beams were considered and described by $E = \sum_{j=1}^{N_1} a_j E_j$ with $E_j = u_2(\ell_j, p_j)$. The total intensity, *I*, incident in the region of interest is given by:

$$I = \int_{ROI} E \cdot E^* dxdy = \sum_{j,k} a_k^* M_{kj}^{(0)} a_j \qquad \text{(C.1)}$$

where $M_{kj}^{(0)} = \int_{ROI} E_j \cdot E_j^* dxdy$. Matrix $M_{kj}^{(0)}$ can be decomposed into a set of eigenvectors delivering an orthonormal set of optical eigenmodes defined as:

$$E_q = \frac{1}{\sqrt{\lambda^q}} \sum_j \upsilon_{qj} E_j \qquad \text{(C.2)}$$

with $\sum_j M_{jk} \upsilon_{qj} = \lambda^q \upsilon_{qk}$ and where λ^q is an eigenvalue and υ_{qk} the associated eigenvector.

2.1. Wavefront correction using Optical Eigenmodes

To account for optical aberrations, the theoretical SLM masks used in this study were corrected, using an eigenmode wavefront correction algorithm. This approach is based on the above Equations (C.1), (C.2) transposed in the experimental setting. In a first step, the intensity operator $M_{kj}^{(0)}$ was measured, describing the linear transfer between the SLM plane and imaging plane. This is done by interfering a reference beam (E_{ref}) with each single probe beam E_j (in this instance the probe beams were chosen to correspond to transversal deflection in the SLM plane giving rise to transversal displacement in the image plane) and retrieving the relative phase and amplitude of the probe field in the image plane. Both beams, reference and probe are encoded on the SLM using random phase encoding technique. The phase between the two beams is varied in four steps of $\pi/2$ and the complex field is retrieved via:

$$F_j = \frac{1}{4} \sum_{p=0}^{3} e^{i2\pi p/4} f(E_{ref} + e^{-i2\pi p/4} E_j) \qquad \text{(C.3)}$$

where the term *f(E)* corresponds to intensity measured on the detector when illuminated by field *E*. This procedure can be seen as a phase sensitive lock-in technique where the reference beam E_{ref} corresponds to a reference signal with respect to which the phase and amplitude of E_j is measured. Using these measures the intensity operator $M_{kj}^{(0)} = F_k^* F_j$ is defined. Its principal eigenvector defines the

optical eigenmode that delivers the largest intensity on the detector maintaining the total power in the system. The phase only part of the SLM mask implementing this eigenmode delivers the wavefront correction mask (see Ref. [155, 156] for a discussion on the number of probes used).